



HAL
open science

Optical spectroscopy of boron nitride heterostructures

Phuong Vuong

► **To cite this version:**

Phuong Vuong. Optical spectroscopy of boron nitride heterostructures. Physics [physics]. Université Montpellier, 2018. English. NNT : 2018MONT075 . tel-02152566

HAL Id: tel-02152566

<https://tel.archives-ouvertes.fr/tel-02152566>

Submitted on 11 Jun 2019

HAL is a multi-disciplinary open access archive for the deposit and dissemination of scientific research documents, whether they are published or not. The documents may come from teaching and research institutions in France or abroad, or from public or private research centers.

L'archive ouverte pluridisciplinaire **HAL**, est destinée au dépôt et à la diffusion de documents scientifiques de niveau recherche, publiés ou non, émanant des établissements d'enseignement et de recherche français ou étrangers, des laboratoires publics ou privés.

**THÈSE POUR OBTENIR LE GRADE DE DOCTEUR
DE L'UNIVERSITÉ DE MONTPELLIER**

En : Physique

École doctorale : Information, Structures, Systèmes (I2S)

Unité de recherche : UMR 5221

Optical spectroscopy of boron nitride heterostructures

Présentée par Phuong Vuong

Le 24 Octobre, 2018

**Sous la direction de Guillaume CASSABOIS
et Bernard GIL**

Devant le jury composé de

Tatiana V. SHUBINA, Professeur,

Lucyna FIRLEJ, Professeur,

Giorgia FUGALLO, Chargée de Recherches-CNRS,

LLuís ARTÚS, Professeur,

Abdallah OUGAZZADEN, Professeur,

Julien BARJON, Maître de conférences,

Hai Son NGUYEN, Maître de conférences,

Membre Invité

Président

Examineur

Rapporteur

Rapporteur

Examineur

Examineur



**UNIVERSITÉ
DE MONTPELLIER**

Acknowledgements

I am indebted to all those who have supported me over these three years.

Foremost, I would like to thank my thesis director Prof. Guillaume Cassabois, who I have my privileges to work under his supervision, knowledge and experience. His guidance helped me in all the time of research and writing of this thesis. Thank you for your advice and inspiration.

I would like to express my sincere gratitude to my thesis co-director Prof. Bernard Gil who gives me the opportunity to carry out this work and supports for my Ph.D study and research. Thank you not only for your patience, motivation, enthusiasm, and immense knowledge but also for your treatment to me as a second daughter. I really appreciate.

I would like to thank Prof. Tatiana Shubina, Dr. Giorgia Fugallo, Prof. Lluís Artús, Prof. Abdallah Ougazzaden, Dr. Julien Barjon, and Dr. Hai Son Nguyen for accepting to be part of my thesis jury, and Prof. Lucyna Firlej for having chaired it.

My sincere thanks also goes to the optical engineer Pierre Valvin, who taught me all the “magical aspects” of the experiments, and helped me to perform the photoluminescence spectroscopy in the lab. Similarly, profound gratitude goes to Prof. Thierry Michel for teaching me the Raman spectroscopy and C. L’Henoret for his technical support at the mechanics workshop.

Many thanks to the group of Prof. Taniguchi - National Institute for Materials Science, Japan; to the group of Prof. Edgar - Kansas State University, USA; and to the group of Prof. Novikov - Nottingham University, UK for growing the high quality samples.

I am also hugely appreciative to Prof. Arie Van der Lee - Institut Européen des Membranes, UMR 5635, Montpellier who has performed the X-ray diffraction. I would like to thank Prof. Lluís Artús and Prof. Ramon Cuscó - Institut Jaume Almera, Barcelona, Spain, for performing the Raman spectroscopy with high-resolution. Similarly, thank to Prof. Novikov and his co-workers who have performed Atomic force microscopy. Their

experiments give strong complementary to my photoluminescence experiments.

I gratefully acknowledge the network GaNeX (ANR-11-LABX-0014) that financially supported my Ph.D.

I am also grateful to the following L2C staffs: Jean-Christophe Art kindly organized my participation to scientific conferences. Thank you for sending me so far away from Montpellier; Christelle Eve has brought her help at anytime I have been needed. Thank you for always being in your desk for me.

A big thank to my colleagues, past and present, in particular, Tianlin Wang who shared all three years in L2C with me. I really enjoyed your presence.

I would like to thank my close friend, Ngo Thi Huong, who gave me the information of this project and was always beside me not only in the scientific area, but also on a personal level, in the first two years. Many thanks for that, Huong.

Last but not least, I would like to express my gratitude to my beloved mother and father and the rest of my family.

Contents

Introduction	1
1 Fundamentals of hexagonal boron nitride	5
1.1 Materials	5
1.1.1 The allotrope forms of boron nitride	6
1.1.2 Crystal structure of hexagonal Boron Nitride	7
1.2 Selection rules	11
1.2.1 General considerations	11
1.2.2 Symmetry of electronic states	13
1.3 Modern calculations of electronic band structure of boron nitride	21
1.4 Phonon symmetries and dispersion relations	22
1.4.1 Normal modes	23
1.4.2 Phonon dispersion relation	25
1.5 Selection rules for the optical transitions	27
2 Experiments	31
2.1 Samples	31
2.1.1 NIMS samples	32
2.1.2 HQ Graphene samples	32
2.1.3 KSU samples	33
2.1.4 MBE samples	34
2.2 Photoluminescence	35
2.2.1 Principle of photoluminescence.	35
2.2.2 Experimental setup	37

3	Phonon-assisted transitions	40
3.1	Identification of phonon-assisted recombination.	40
3.2	The polarization of the photoluminescence of BN	43
3.2.1	The impact of the phonon symmetries on the optical response in a real BN crystal	43
3.2.2	Missing phonon mode	49
3.2.3	The emission diagram of the indirect exciton iX line	52
3.3	Fine structure of phonon-assisted transitions in BN	53
3.3.1	The origin of the fine structure of phonon-assisted transitions . . .	53
3.3.2	Theoretical model for PL spectrum	56
3.4	Exciton-phonon interaction in a strong coupling regime	65
3.4.1	Comparison between Gaussian and Lorentzian functions	65
3.4.2	Excitonic absorption line-shape of BN	66
3.4.3	Temperature dependence of vibrational line-width	67
3.5	Conclusions.	71
4	Isotope engineering in boron nitride	74
4.1	Isotope effect on the optical properties of BN	76
4.1.1	Phonon energy	76
4.1.2	Electronic bandgap	80
4.2	Influence of boron isotope on Van der Waals interactions	85
4.2.1	Interlayer shear mode	85
4.2.2	Interlayer breathing mode	89
4.3	X-ray measurements	92
4.4	Conclusions	95
5	BN epilayers grown by molecular beam epitaxy (MBE)	97
5.1	BN grown on sapphire substrate	102
5.1.1	Atomic force microscopy (AFM)	102
5.1.2	Photoluminescence measurements	103
5.2	BN grown on highlyordered pyrolytic graphite (HOPG) substrate	105
5.2.1	Atomic force microscopy (AFM)	105
5.2.2	Photoluminescence measurements	106

5.3 Conclusions	110
Conclusion	112
A Character table for point group	136
A.1 Character table for point group D_{2h}	136
A.2 Character table for point group D_{3h}	136
A.3 Character table for point group D_{6h}	137
A.4 Character table for point group C_{3h}	137
A.5 Character table for point group C_{2v}	138
A.6 Character table for point group D_2	138
A.7 Character table for point group D_6	138
B Power-law dependence of the shear mode energy	139
C Phonon-photon mapping in a color center in boron nitride	141
Résumé en français	150

List of Figures

1.1	Schematic diagram of fundamental crystal structures of boron nitride (cubic and wurtzite phase)	6
1.2	Schematic diagram of fundamental crystal structures of boron nitride . . .	7
1.3	Maximum entropy method derived electron density for the structure of BN projec.	8
1.4	Two-dimensional structure and Brillouin zone of BN.	9
1.5	Three-dimensional structure and Brillouin zone of BN.	10
1.6	Symmetries of σ and π states under σ_h operator	14
1.7	Electronic band-structure of 2D BN using simple tight binding method and modern approach	17
1.8	Electronic band-structure of 3D BN for p_z states using simple tight binding method	20
1.9	Calculated and experimental electronic band structure for bulk hexagonal boron nitride	21
1.10	Acoustic phonon modes of BN	23
1.11	Raman active optical modes at low and high energies at center of Brillouin zone	24
1.12	InfraRed active optical modes at at center of Brillouin zone	24
1.13	Silent modes at low and high energies at center of Brillouin zone	25
1.14	Phonon dispersion relations calculation of BN along a high symmetry . .	26
1.15	Orientations relatively to the hexagon	29
2.1	Typical image of the BN crystal from National Institute for Materials Science - NIMS, Japan	32
2.2	Typical image of the BN crystal from HQ Graphene company	33

2.3	Typical image of the BN crystal from Kansas State University, USA	33
2.4	Typical image of the epitaxial BN from University of Nottingham, United Kingdom	34
2.5	Principle of photoluminescence spectroscopy (PL)	35
2.6	Illustration of a photon emission process in (left side) the direct and (right side) the indirect band gap semiconductors	36
2.7	Scheme of our experimental setup devoted to measurements in boron nitride at 8K, under (a) two-photon excitation and (b) one-photon excitation	37
2.8	Scheme of our experimental setup devoted to measurements in boron nitride at 8K, under two-photon excitation. Depending on the sample position, two configurations of detection are probed, with an emission wavevector either perpendicular or parallel to the c-axis	38
2.9	Rochon polarizer	39
3.1	Cathodoluminescence spectrum of BN at room temperature	40
3.2	Photoluminescence (PL) spectrum of BN at 8K with the identification of the PL lines as phonon-assisted recombination lines in BN	41
3.3	Photoluminescence spectrum of BN plotted at the same scale as the phonon dispersion relations	42
3.4	Polarization-resolved photoluminescence spectroscopy in bulk BN at 8 K for a Poynting vector parallel to c-axis for two orthogonal orientations of the linear polarization of analysis	44
3.5	Polarization-resolved photoluminescence spectroscopy in bulk BN at 8K for a Poynting vector perpendicular to the c-axis	45
3.6	Normalized photoluminescence signal intensity and the fits of LA/LO ₁ (blue) and ZO ₁ (red) phonon replicas as a function of polarization angles.	47
3.7	(a) Ideal case of a perfect BN monocrystal, (b) real case of a polycrystalline bulk BN sample with a distribution of thick multilayer segments, each one having a c-axis orientation rotated by an angle around a direction parallel to the sample edge.	48
3.8	Photoluminescence signal intensity of the LA/LO ₁ and ZO ₁ phonon replicas as a function of polarization angle	49

3.9	Polarization intensity differential emission spectrum corresponding to the difference of the polarization-resolved photoluminescence spectra	50
3.10	Comparison between our PL spectrum and the phonon dispersion relations	51
3.11	Polarization-resolved photoluminescence spectroscopy in bulk BN at 8K for a Poynting vector perpendicular to c-axis in the energy range of the fundamental indirect exciton iX around 5.95 eV	53
3.12	Photoluminescence spectrum of BN at 8K in linear scale	54
3.13	Schematic representations, in the single-particle picture of the electronic band structure, of the phonon-assisted recombination processes	55
3.14	Experimental data and fits in four cases of the phonon-assisted emission spectrum in BN	60
3.15	Photoluminescence spectrum in HQ Graphene BN in the deep ultraviolet under two-photon excitation at 3.03 eV, at 8 K together with the theoretical fit	63
3.16	Normalized weight A of the overtones of the interlayer shear modes as a function of overtone index n	64
3.17	PL spectrum at 100K and the fits using two functions in a model:Gaussian and Lorentzian	67
3.18	Temperature dependence of the PL spectrum in BN as a function of temperature, from 8 to 300K	68
3.19	Temperature dependence of the full width at half maximum of the phonon replicas	70
4.1	Honeycomb lattice in natural hexagonal boron nitride (N^a BN) showing the isotopic mixture of boron-10 (red) and boron-11 (green) atoms bound to nitrogen-14 (blue)	75
4.2	Isotope mass dependence of vibrational excitations	77
4.3	Schematic diagrams of the optical dispersion relation in Si, Ge, diamond, compared to phonon dispersion relation of BN	79
4.4	Photoluminescence spectra for ^{10}BN , $^{N^a}\text{BN}$ and ^{11}BN at 8K under excitation at 6.3 eV	81

4.5	Energy of phonon replicas versus calculated isotope-dependent phonon energy at 8K	83
4.6	Temperature dependence of the indirect bandgap	85
4.7	High-resolution Raman spectra for the E_{2g}^{low} interlayer shear mode in ^{11}BN , $^{\text{Na}}\text{BN}$ and ^{10}BN at 300K.	86
4.8	Temperature dependence of the frequency shift for the E_{2g}^{low} interlayer shear mode in ^{10}BN , $^{\text{Na}}\text{BN}$ and ^{11}BN	87
4.9	Phonon-assisted broadening Δ of the PL spectra in ^{10}BN , $^{\text{Na}}\text{BN}$ and ^{11}BN : experimental data (symbols), fits of the thermally-induced broadening (solid lines).	90
4.10	Electron density distribution in ^{10}BN and ^{11}BN using the maximum entropy method against X-ray data	93
4.11	Expanded view of figure 4.10(a&d) for (a) ^{10}BN and (b) ^{11}BN	94
5.1	Photoluminescence spectrum in HQ Graphene BN at 8K	98
5.2	PL and CL spectra of BN epilayers	101
5.3	Atomic force microscopy images of two BN samples grown on sapphire	102
5.4	PL spectra in the four BN samples grown on sapphire, were recorded at 8K under excitation at 6.3 eV	103
5.5	PL spectrum of S1690 over a larger spectral range, recorded at 8K under excitation at 6.3 eV	105
5.6	Atomic force microscopy images of BN grown on HOPG	106
5.7	PL spectra in the four BN samples grown on HOPG (solid lines), compared to the PL spectrum of HQ Graphene sample (dashed line), were recorded at 8K under excitation at 6.3 eV	107
5.8	PL spectrum of G1390 over a larger spectral range were recorded at 8K under excitation at 6.3 eV	109

List of Tables

1.1	The relationship between the notations of the symmetries.	15
1.2	Symmetrized combination of Bloch function for 2D BN at Γ , K and M points in BZ.	16
1.3	The relationship between the notations of the symmetries for 3D BN at Γ , K and M points in BZ.	18
1.4	Symmetrized combinations of Bloch function for 3D BN at Γ , K , M , H , A and L points in BZ.	19
1.5	Correlation table for D_{6h} and C_{2v} point groups.	27
1.6	Summary the phonon modes of BN	30
3.1	Phonon energy and group velocities of phonon modes at T point of BZ. . .	58
4.1	Isotopes concentration of boron and nitrogen ^{10}BN , ^{11}BN , and ^{10}BN together with their reduced mass.	75
5.1	Average film thickness of BN samples grown on sapphire, in units of monolayer (ML), after 3h of growth as a function of the growth temperature. 1ML = 0.33nm.	103
5.2	Average film thickness of BN samples grown on HOPG, in units of monolayer (ML), after 3h of growth as a function of the growth temperature. 1ML = 0.33nm.	106

Introduction

Semiconductor, sit at the connection between insulators and metals. Their physics is probably one of the most important topics for both academic and industrial research in the area of the science of materials. For over more than 70 years, their science and the questions of applications have been nonstop developing. Since many decades silicon transistors and silicon chips have replaced vacuum tubes in computers and semiconductor technology is driving most of the societal innovations. Reduction of the size of these basic elements of computers has required the invention and developments of modern growth techniques, susceptible to allow deposition of very thin layers of different materials, namely the epitaxial growth approaches. They permit to control atom by atom the amount of a given deposited material at the surface of a target substrate and they led to the development of semiconductors applications, beyond the simple case of transistors, and assembling III-V compounds led to realization of efficient light emitting devices among which were first light emitting diodes and later semiconductor laser diodes. This gave birth to optoelectronics and the modern information technology.

It is worthwhile reminding that light emitting diodes (LEDs) based on SiC were invented and described by Oleg Vladimirovich Losev as early as in 1921 [1], but they were produced a few decades later. In 1961, James Robert Biard and Gary E. Pittman working at Texas, USA demonstrated the earliest LEDs emitting a low-intensity infrared light, based on utilization of GaAs as active material [2]. In 1962, the first visible-spectrum (red) LED was developed by Nick Holonyak Jr. [1]. Long term efforts followed and sophisticated stackings of different nanometer-thin arsenides were realized, thus leading to creation of new materials and new devices with enhanced light emission efficiency of the new generations of LEDs. Heterostructures based on enlarged series of alternate III-V compounds (antimonides, phosphides) were grown to engineer the wavelength of the emitted light and stimulated emission was realized giving birth to compact solid state lasers

and digital information storage and exchanges. Compact solid state lasers diodes (LDs) operating at $1.3 \mu\text{m}$ or $1.5 \mu\text{m}$ are used for long-haul communications through optical fiber and they were the mandatory components allowing for the development of internet. However, the wavelength that could be produced by using the materials saturated to short wavelengths of orange colour for reasons linked to the intrinsic properties of these III-V compounds. Further reducing the wavelength tantalized researchers during many years until 1986, when at the Meijo University, Japan, Prof. Isamu Akasaki and his master student Hiroshi Amano, managed to grow high quality wurtzitic GaN. Then, they could make both n-type and p-type doping, opening the door toward short wavelength LEDs and paving the way to the realization of the efficient white light emitter based on such LEDs. Such devices are everywhere among us nowadays. Shuji Nakamura and they were together awarded the Nobel Prize in physics 2014 for *the invention of efficient blue light-emitting diodes which has enabled bright and energy-saving white light sources*.

The development of semiconductor light sources operating at even shorter wavelengths, in the deep ultra-violet (UV) region is now motivating the researchers in relation with a wide variety of applications. For instance, deep UV LEDs with emission wavelength in the range 230-350 nm, are expected to be used in sterilization applications, water purification, medicine, biochemistry, sensing field, fluorescence analytical system, and so on [3]. Thus, the next step is now to realize DUV compact solid-state emitters. One of the basic building block for the development of this technology is wurtzitic AlN, which has a wide band-gap around 6 eV [4]. An alternate to it is hexagonal boron nitride (h-BN) which has also a band-gap value sitting at 6 eV.

Boron Nitride (BN) was discovered very early in 1842 [5] and synthesized as white powders. This material is simultaneously an old one and a fairly new one. BN preferentially grows in the hexagonal system similarly to graphite. B and N atoms are alternatively connected via strong covalent bonds forming planar hexagonal rings, a honeycomb layer if seen from the top. Adjacent layers stacked by weak van der Waals forces, form a three-dimensional (3D) crystal. The similarity between the graphite and h-BN lattices are so strong that chemists named h-BN as "white graphite". In relation with its stability in the context of high temperatures densified powders are used at large industrial scales to realize crucibles for the growth of advanced materials. This material is intensively produced but as a powder or as a ceramics.

Little attention was paid to the optical properties of h-BN and to using it as a semiconductor until Japanese researchers at NIMS, Tsukuba, Japan kicked the ball by growing high quality single crystals in 2004 [6, 7]. The band-gap of these single crystals was established to sit near 6 eV and the material was found to be p-type when non-intentionally doped (in contrast to AlN which is always n-type).

The physical properties of this material, even the nature of the band-gap, were in turn not well-enough understood as required by semiconductor technology. In particular, the indirect band-gap of h-BN occur between the top of the valence band at the K point of the Brillouin zone and the bottom of the conduction band at M [8–11]. This stimulated a large number of the measurements that are presented in this thesis, which aim to offer a better understanding of the opto-electronic properties of h-BN and in particular electron-phonon interaction, beyond the scope of the Born-Oppenheimer approximation. This is even more interesting as the fabrication of isotopically purified h-BN crystals is also possible. Boron is available as forms of isotopically purified ^{10}B and ^{11}B . Such isotopic purification is motivated by the different interactions of ^{10}B and ^{11}B with neutrons and the possibility to realize neutron detectors having many applications in nuclear energy industries [12] and cancer treatment by boron neutron capture therapy [13]. In our case, advantage will be of this 10 percent change in the atomic mass of boron to study subtle effects related to the physics of isotopic purification in solids among which are the changes in phonon energies, the changes of interatomic force constants and renormalization of the bandgap. Besides this, the development of interest for two-dimensional (2D) materials like graphene or transition metal dichalcogenides (TMD), such as MoS_2 , WSe_2 makes it the ad hoc candidate for bridging the mature technology of III-V nitrides to the fascinating world of 2D materials. Such van der Waals heterostructure have recently been fabricated and investigated, revealing unusual properties and new phenomena [14].

This thesis is structured as follow:

In the first chapter we will introduce the fundamental properties of hexagonal BN. We will describe the construction of the electronic band structures of the 2D and 3D h-BN and we will compare the predictions of the old and of the modern calculations. Besides this, we will calculate the selection rules for the optical processes. Then, in the last section, we will describe the symmetries and wavefunctions of the normal phonon modes and we will give their dispersion relations. Chapter two will be dedicated to the presentation of

the samples which come from the four different sources from Japan, HQ Graphene company, Kansas State University or Nottingham University, and which have been grown using different methods. we will review the basic principles of photoluminescence and describe the experimental set up we used.

Along the next three chapters we will present my results and we will discuss them. In chapter three, we will investigate the impact of the phonon symmetry on the optical response of h-BN by performing polarization-resolved PL measurements. From them, we will measure the contribution of the missing phonon-assisted recombination which was not detected before this thesis. In a following section, we will address the origin of the fine structure of the phonon-assisted recombinations in h-BN which arises from overtones involving up to six low-energy interlayer shear modes, with a characteristic energy of about 6.8 meV. In the last section, we will show the signature of the strong-coupling regime of exciton-phonon interaction in h-BN. In chapter four we will record Raman and photoluminescence measurements to quantify the influence of isotope effects on optical properties of h-BN as well as the modifications of Van de Waals interactions linked to utilization of ^{10}B and ^{11}B or natural Boron for the growth of bulk h-BN crystals. The fifth chapter will focus on the h-BN thin epilayers grown by Molecular Beam Epitaxy at Nottingham University. Atomic force microscopy (AFM) images and photoluminescence features will be combined to confirm the first observation of phonon-assisted recombination in high quality thin h-BN epilayers grown on c-plane sapphire and Highly Ordered Pyrolytic Graphite.

At the end of this thesis are offered conclusions and appendixes.

Chapter 1

Fundamentals of hexagonal boron nitride

1.1 Materials

By using the reaction of melted boric acid and cyanide potassium, Balmain discovered boron nitride in 1842 [5]. However, at that time, and roughly speaking, until 2004, only boron nitride powders or very tiny single crystals were synthesized. The ball for motivating in depth physical investigations, including this thesis, was kicked in Japan in 2004 when large size single crystals were grown and published [6, 7]. Nowadays, many methods have been used for synthesizing boron nitride under various forms (powder, nanotube, bulk crystal). Finally although BN has been used in the industry for a long time in correlation with its interesting macroscopic physical properties, the interest for understanding the reason for them more intimately, that is to say from a more quantum mechanical point of view, is only very recent. We will examine in this thesis, the optical properties of bulk crystals and we will use our understanding of them to calibrate the performances of hetero-epitaxial layers: thin BN films that people now try to grow coherently at large scale on various substrates, with the perspective of developing a BN-related technology in the area of deep ultra-violet (UV) emission or for realizing advanced electronic devices.

1.1.1 The allotrope forms of boron nitride

Boron Nitride is a binary III-V compound (it consists of equal numbers of two light atoms: Boron ($Z = 5$) and Nitrogen ($Z = 7$)). Natural boron is a mixture of 20 at% ^{10}B and 80 at% ^{11}B , which makes thus very interesting to compare the optical properties of natural BN and isotopically purified BN, that will be discussed in chapter 4. BN exists under four main crystalline phases: cubic (c-BN), wurtzite (w-BN), rhombohedral (r-BN), and hexagonal (h-BN). In figures 1.1 and 1.2 are reproduced the atomic stackings of boron and nitrogen atoms that lead to these structural arrangements [15]. Their general properties between them are excellent thermal, chemical stabilities, and wide bandgaps ($> 5\text{eV}$). However, because of the differences in the arrangement of the atoms, each of these four phases of BN has individual properties and characteristics. Among that, c-BN and h-BN are the most interesting of the four.

c-BN and w-BN are four-fold coordinated crystals with perfect AB_3 tetrahedron for the cubic crystal and a distortion of one bond to form trigonal pyramid in case of the wurtzite crystal. The cubic phase of BN is similar to the one of diamond but the crystals are harder, the wurtzite phase of BN is metastable and thus of very poor interest. The 2s and 2p orbitals of boron and nitrogen atoms hybridize under the sp_3 scheme in case of these crystals.

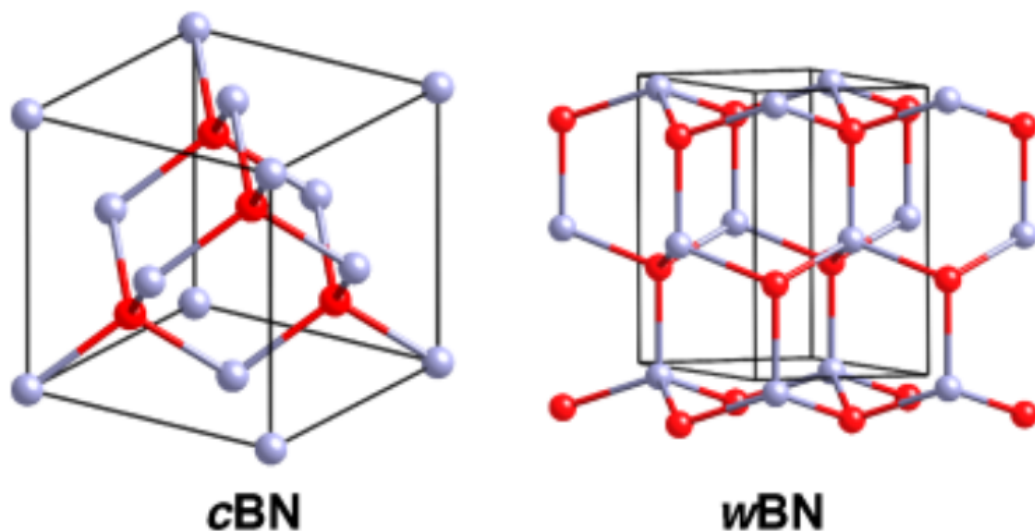


Figure 1.1: Schematic diagram of fundamental crystal structures of boron nitride (cubic and wurtzite phase [15]).

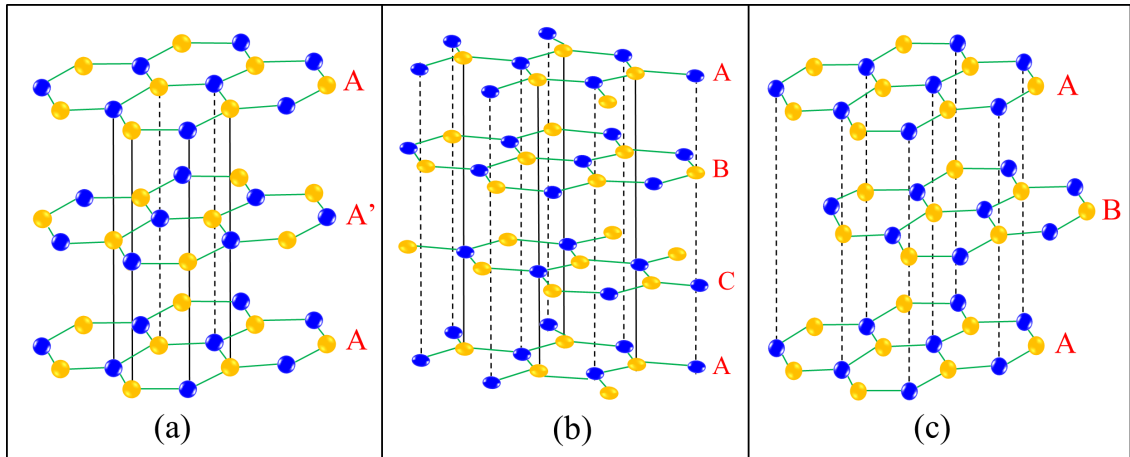


Figure 1.2: Schematic diagram of fundamental crystal structures of boron nitride: (a) h-BN in AA' stacking [16], (b) r-BN with ABC stacking, and (c) BN in AB stacking as proposed in [17].

The cases of both h-BN and r-BN are different, the 2s and 2p orbitals of boron and nitrogen atoms hybridize under the sp_2 scheme in case of these crystals which are stacked along a high symmetry direction, to form piles of hexagons made by alternating planar bonding of boron and nitrogen atoms located at the nodes of a two-dimensional (2D) honeycomb lattice. The main difference to emphasize here is the perfect superposition of boron and nitrogen atoms from a given BN sheet to another one in case of three-dimensional (3D) h-BN. This is called AA' stacking (see figure 1.2 (a)). Besides this, there are two intermediately twisted stackings for the rhombohedral layer (ABC stacking - figure 1.2 (b)), and the lattice parameter along the stacking direction is about 3/2 the value for h-BN. Distinguishing these different crystallographic stackings has been very challenging.

1.1.2 Crystal structure of hexagonal Boron Nitride

The geometric structure of h-BN (that we will just write BN in the rest of this thesis) has been investigated with X-rays in the beginning of twentieth century with the initial studies by Hassel [17] until a more consolidated one was proposed by Pease [16]. Their initial works led to proposing two distinct structures with the important difference coming from the existence (or not) of a center of symmetry in BN. Hassel alleged the stacking AB (figure 1.2 (c)) of the 2D layers of the honeycomb structure, while Pease alternatively evidenced an AA' stacking. This AA' stacking was since confirmed by a lot of complementary studies, either theoretical calculations or experimental investigations [18–20].

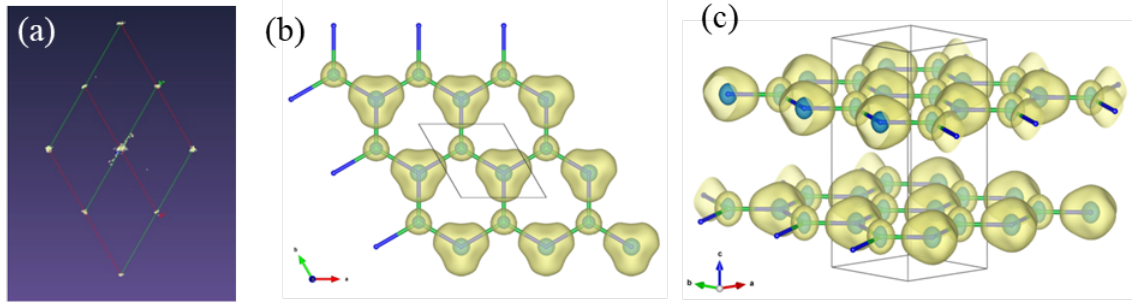


Figure 1.3: (a) Collapsed view of reciprocal space of h-BN; the maximum entropy method derived electron density for the structure of BN projection: (b) along the c -axis and (c) side view [21].

We have performed our own X-rays measurements in the Institut Européen des Membranes (UMR-5635 CNRS) at Montpellier where Dr. Arie Van der Lee uses a high resolution X-ray diffraction platform [21]. In figure 1.3 (a) is represented a plot of the diffraction spots (a projection of the 3D reciprocal lattice of BN) recorded on a single BN crystal. According to the theory of X-ray diffraction by crystals, the intensity of each of the diffraction spots in the reciprocal space is depending on the nature of the diffraction centers (atoms) and on their position in the lattice via a structure factor. After some kind of Fourier transformation of the data (called the maximum entropy method - MEM) one can reproduce the density of the electron cloud that diffracts the X-ray [21]. This is illustrated in figures 1.3 (b&c) that present the electronic densities plotted in three-dimension with both views from top (a) or side (b).

From these figures, it is clear that there exists a six-fold rotation axis (c -axis) that is orthogonal to the plot in figure 1.3 (b). Moreover, it strongly confirms the AA' stacking of BN with a perfect superposition of the reticular nodes of the adjacent planes stacked along the c direction with an exact superposition of B and N atoms from one plane to another one. The layers are stacked together by the weak Van der Waals (vdW) interactions and thus BN can be easily exfoliated into 2D layers. The distance between two nearest boron and nitrogen atoms in the c direction is $c_0 = 0.33$ nm (it is called interlayer distance). Within each layer, boron and nitrogen atoms are bound by strong covalent bonds, with the distance between boron and nitrogen atoms being $a_0 = 0.144$ nm (intra-layer distance). The crystal space group of BN is named $P6_3mc$, the point group of the crystal is D_{6h} . This indicates that the hexagonal Bravais lattice of the three dimensional stacking is a primitive one, with the main symmetry operation being the joint product of a $2\pi/6$

rotation with a $3c/6 = c/2$ translation along the c-axis of the crystal.

We will go further in the details of this crystal structure by starting from the simpler case of 2D BN and after that, by coupling such 2D BN layers to form 3D BN.

2D BN structure

In figure 1.4 (a) is plotted a top view of one boron nitride monolayer. Boron and nitrogen atoms are distinguished from each other using spheres of different colors. Red vectors represent the primitive translation vectors of the hexagonal lattice. With our notation here, the positions of boron and nitrogen atoms are $(0,0)$ and $(0, a_0)$. Relatively to the cartesian axes (x,y) , the primitive lattice vectors are $\tau_1 = a(1/2, \sqrt{3}/2)$ and $\tau_2 = a(-1/2, \sqrt{3}/2)$, where $a = a_0\sqrt{3}$ is the lattice parameter. We have constructed the reciprocal lattice, that is represented, the coordinates of the fundamental vectors of which are: $R_1 = \frac{2\pi}{a}(1, 1/\sqrt{3})$ and $R_2 = \frac{2\pi}{a}(-1, 1/\sqrt{3})$ relatively to the cartesian basis. We remind that, by definition $\tau_i R_j = 2\pi\delta_{ij}$ is the Kronecker symbol.

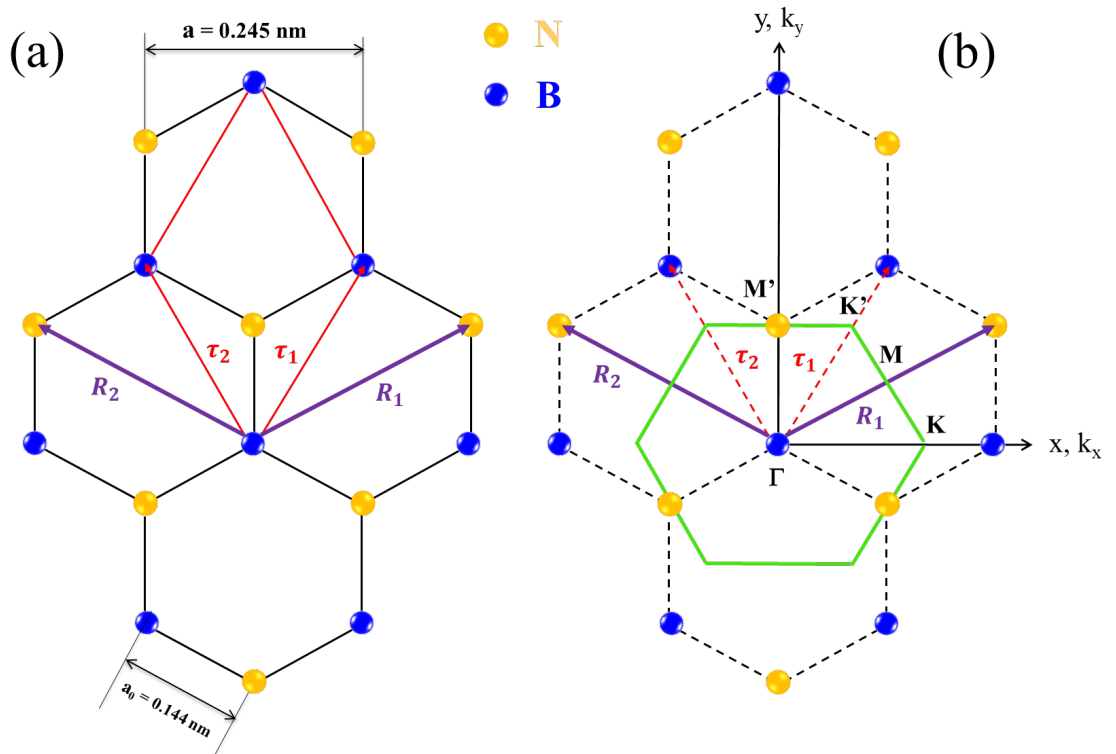


Figure 1.4: Two-dimensional structure (a) and Brillouin zone (b) of BN.

The Brillouin zone (BZ) of 2D BN is reported in figure 1.4 (b) involving three critical points Γ , M and K. We have to remark periodic chains of identical atoms oriented along the ΓK direction with the distance of a . Chains of blue atoms alternate with chains of orange atoms in the direction orthogonal to ΓK . Now considering the ΓM , there are chains of boron and nitrogen atoms with different interatomic spacings a_0 and $2a_0$, The chains of atoms in the KM direction are similar to those in the ΓK direction because ($\text{M}'\text{K}'$) is parallel to (ΓK) and it is equivalent to $1/2 \Gamma\text{K}$. **This result also holds for 3D BN and it will be of paramount importance for the interpretation of the photoluminescence properties of BN.**

3D BN structure

The 3D BN structure is obtained by a periodic AA' stacking of 2D BN layers with the third vector of the primitive cell $\tau_3 = c(0,0,1)$ obtained by adding $\tau_3 = \tau_3 \perp (\tau_1, \tau_2)$ where $c = 2c_0$ is the lattice constant in the z direction. Similarly, the third fundamental vector of the reciprocal lattice is $R_3 = \frac{2\pi}{c}(0,0,1)$. The schematic diagram of the structure for 3D BN is represented in figure 1.5. The BZ of 3D BN is also reported in the inset of figure 1.5

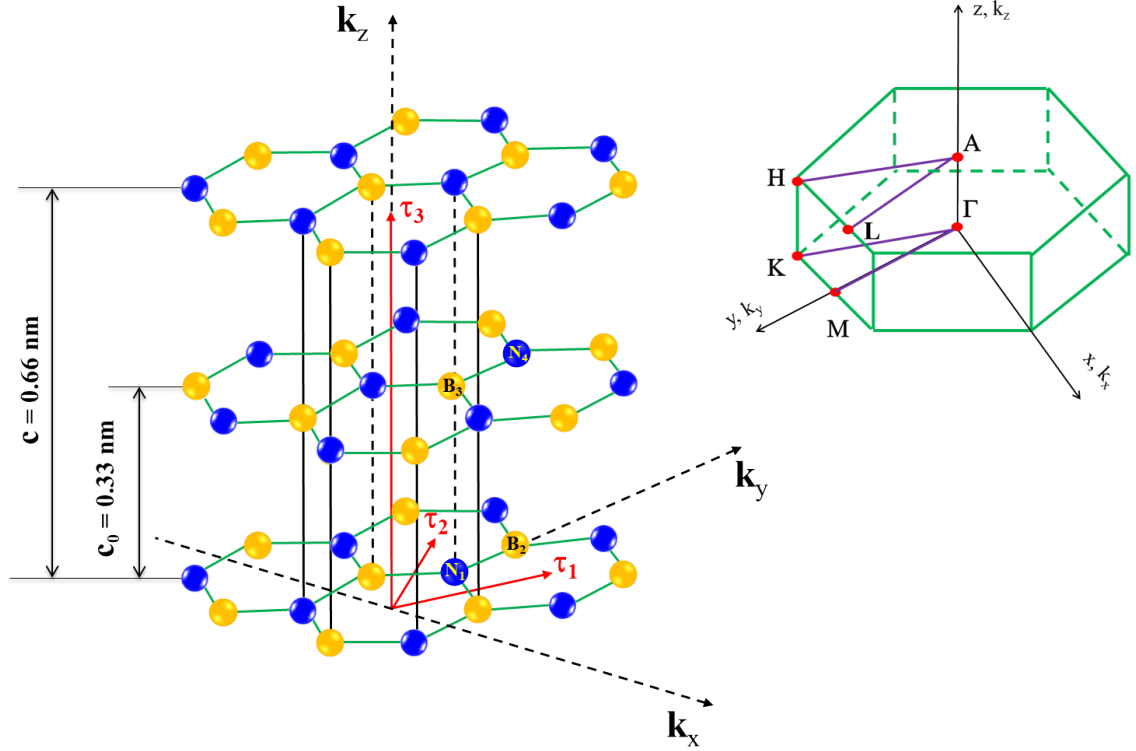


Figure 1.5: Three-dimensional structure and Brillouin zone of BN.

involving six critical points Γ , M, K, A, L and H. The group of \mathbf{k} at the Γ point and also the one of the crystal BN is D_{6h} and it will be determined at different points of the BZ according to the symmetry at these specific points.

1.2 Selection rules

1.2.1 General considerations

Time-dependent perturbation theory teaches us that the important quantity ruling the transition rate Γ_{if} between an initial state $|i\rangle$ and a final state $|f\rangle$ is giving by the Fermi's Golden rule:

$$\Gamma_{if} = \frac{2\pi}{\hbar} \sum_{k_i, k_f} |M_{if}|^2 \delta(E_f - E_i - \hbar\omega) \quad (1.1)$$

where M_{if} is a **matrix element**, E_i and E_f are the energies of an initial state $|i\rangle$ and a final state $|f\rangle$, \mathbf{k}_i and \mathbf{k}_f the wave vectors of these states and $\hbar\omega$ represents the photon energy. In **direct** bandgap semiconductors, this matrix element is written:

$$M_{if} = \langle \mathbf{n}_{VB}, \mathbf{k}_i | V_{photon} | \mathbf{n}_{CB}, \mathbf{k}_f \rangle \quad (1.2)$$

where $|\mathbf{n}_{VB}, \mathbf{k}_i\rangle$ and $|\mathbf{n}_{CB}, \mathbf{k}_f\rangle$ are the initial and final states with n_{VB} and n_{CB} the valence and conduction band indices, V_{photon} is the light-matter interaction term.

At first order, \mathbf{k} -conservation rules requires that $\mathbf{k}_i = \mathbf{k}_f$ when one makes the usual approximation that both the exciton-polariton effects and the wave number of the photon are neglected [22].

Then, for every \mathbf{k} -vector, $|\mathbf{n}_{VB}, \mathbf{k}_i\rangle$ and $|\mathbf{n}_{CB}, \mathbf{k}_f\rangle$ can be attributed a given symmetry, according to the symmetry of the small group of the wave vector at this specific \mathbf{k} , and in agreement with the theory of the representation of the wave functions of solids in terms of irreducible representations (IRs). Group theory permits to establish if such transitions between states of given wave vectors are allowed or forbidden, depending on the non-vanishing or vanishing value of such matrix element.

Let $S(|\mathbf{n}_{VB}, \mathbf{k}_i\rangle)$ and $S(|\mathbf{n}_{CB}, \mathbf{k}_f\rangle)$ represent the symmetries of the valence and conduction bands at the \mathbf{k} point. We suppose that we also know the symmetry $S(V_{photon})$ of the photon interaction. Then, the matrix element $\langle \mathbf{n}_{VB}, \mathbf{k}_i | V_{photon} | \mathbf{n}_{CB}, \mathbf{k}_f \rangle$ will not vanish under the strict condition that the direct product of symmetries $S(|\mathbf{n}_{VB}, \mathbf{k}_i\rangle)$, $S(|\mathbf{n}_{CB}, \mathbf{k}_f\rangle)$

and $S(V_{photon})$ contains the symmetry of the identity $S(E)$. This we can write as:

$$S(|\mathbf{n}_{VB}, \mathbf{k}_i\rangle) \otimes S(V_{photon}) \otimes S(|\mathbf{n}_{CB}, \mathbf{k}_f\rangle) \subset S(E) \quad (1.3)$$

In case of **indirect** transitions, the light-matter interaction process will involve a phonon. Therefore, calculation of the selection rules is much more complicated. The matrix element in this case is written:

$$M_{if} = \langle \mathbf{n}_{VB}, \mathbf{k}_i | V_{photon} | \mathbf{n}_{int}, \mathbf{k}_p \rangle \langle \mathbf{n}_{int}, \mathbf{k}_p | V_{e-phonon} | \mathbf{n}_{CB}, \mathbf{k}_f \rangle \quad (1.4)$$

where $|\mathbf{n}_{int}, \mathbf{k}_p\rangle$ represents an intermediate state and $V_{e-phonon}$ is the electron-phonon interaction term. We note that $\mathbf{k}_i = \mathbf{k}_p$, as mentioned above for a first order, so that $\mathbf{k}_f - \mathbf{k}_p = \mathbf{p}$ which is phonon wave vector. In BN, the maximum of the valence band sits at K point of BZ and the minimum of the conduction band is at M point in BZ (that will be discussed in details later) so the phonon wave vector of BN is $\mathbf{k}_p = \mathbf{MK}$.

Identically to the condition described above for direct bandgap semiconductors that hold for the first term of the matrix element, we have:

$$S(|\mathbf{n}_{VB}, \mathbf{k}_i\rangle) \otimes S(V_{photon}) \otimes S(|\mathbf{n}_{int}, \mathbf{k}_p\rangle) \subset S(E) \quad (1.5)$$

Similarly, one has to calculate the condition for having a non-vanishing second term:

$$S(|\mathbf{n}_{int}, \mathbf{k}_p\rangle) \otimes S(V_{e-phonon}) \otimes S(|\mathbf{n}_{CB}, \mathbf{k}_f\rangle) \subset S(E) \quad (1.6)$$

which requires knowing: (i) the symmetry of the different phonon modes having wave number \mathbf{q} , (ii) the symmetry of state $|\mathbf{n}_{CB}, \mathbf{k}_f\rangle$ which is sitting at \mathbf{k}_f . According to Basani and Hassan [23], and perturbations' theory, equation 1.6 is calculated at the \mathbf{k} point of the lowest symmetry. It is therefore mandatory to establish the compatibility relations between all IRs of small groups of \mathbf{k} at different locations inside the BZ.

Within the framework of the dipolar interaction, the symmetry of the photon $S(V_{photon})$ is given by the symmetry of the electric field of the photon [24]. Depending on its polarization we know from the compatibility tables that it transforms like x , y or z . V_{photon} is thus odd in real space. Which means that $|\mathbf{n}_{VB}, \mathbf{k}_i\rangle$ and $|\mathbf{n}_{int}, \mathbf{k}_p\rangle$ or $|\mathbf{n}_{CB}, \mathbf{k}_f\rangle$ have differ-

ent parities in real space. $V_{e-phonon}$ represents the interaction operator with the phonon field that transfers some momentum via the electron - phonon interaction. It is even in real space [23].

To get a full understanding of the electronic band structure of BN, it is mandatory to know the symmetry properties of the complicated band structure of BN and also the symmetries of the different phonon modes at the different points of the BZ.

1.2.2 Symmetry of electronic states

The electronic configurations of the B and N atoms are respectively: B ($1s^2, 2s^2, 2p^1$) and N ($1s^2, 2s^2, 2p^3$). We will limit the discussion here to a tight-binding analysis restricted to the atomic states that contribute to the chemical bond, namely states of the $n = 2$ shell of boron and nitrogen atoms, and we will neglect couplings with the empty states of the $n \geq 3$ shells. Each state of BN is thus described by Bloch functions formed from the atomic orbitals: $2s, 2p_x, 2p_y$ and $2p_z$. As mentioned above, 2D BN has 2 atoms in the unit cell and 3D BN has 4 atoms, we should expect $2 \times 4 = 8$ bands in 2D case and $4 \times 4 = 16$ bands in 3D case. Therefore, we have to solve an 8×8 matrix eigenvalue equation in the 2D case, and 16×16 one in the 3D case to find the energies at each wave vector k . Now, we will consider the symmetry of electronic states in two didactical cases, beginning by considering the 2D BN case and by further coupling these layers along the c direction to build the electronic states of 3D BN.

a. Symmetry of electronic states of 2D Boron nitride

In order to obtain simple description of energy bands of BN and to understand experimental optical data, we first consider just one single layer (2D BN).

At center of BZ (Γ point), the point group of 2D BN is D_{3h} which has only twelve symmetry operators: $E, 2C_3, 3C'_2, \sigma_h, 2S_3$ and $3\sigma_\nu$, inversion symmetry does not exist at the center of the hexagon in contrast to graphene. Among that, E is the identity operator, C_n is noted for rotation operators following $\frac{2\pi}{n}$ ($n = 1, 2, 3, 4, 6$). C_2 and C_3 are thus rotations by 180° and 120° which are called two-fold and three-fold rotations, respectively. Operators σ are reflection about a plane with the under-script ν or \bar{h} defined for a plane parallel or perpendicular to the rotation axis. Finally, S_3 is an improper operator which composes a C_3 operator followed by an σ_h operator. These twelve symmetry operations

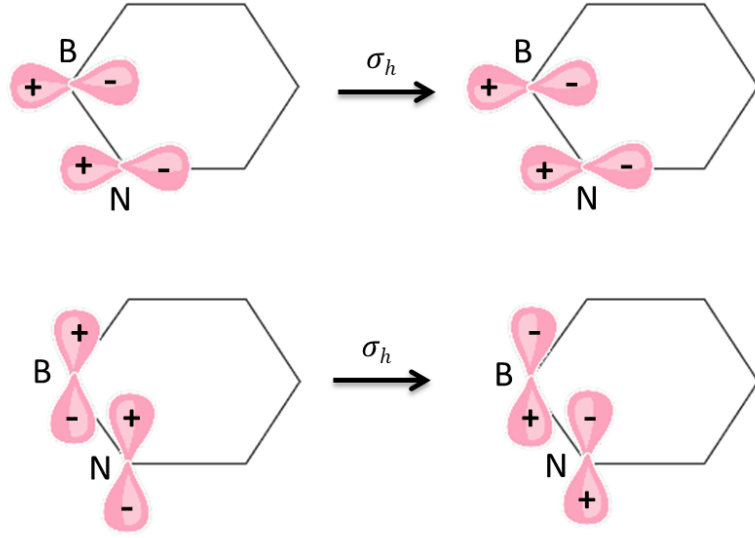


Figure 1.6: Symmetries of σ and π states under σ_h operator.

are gathered into 6 different classes, four of them being unidimensional, two of them being two-dimensional. At zone center, because of the presence of the symmetry operation σ_h , the determinant can be factorized into a determinant of order six formed with the Bloch functions s , p_x and p_y (σ -states) that are invariants under σ_h , and a determinant of order two formed with the Bloch functions p_z (π -states) that are changed of sign under σ_h (figure 1.6).

Therefore, we can distinguish the energy states as even or odd ones with respect to the symmetry operator σ_h . Their symmetries will be noted as S^+ in case of invariance under σ_h and S^- for the other case.

At the relevant points of high symmetry of the BZ, as calculated by Doñi and Parravicini [19], these determinants may be further reduced by using as basic functions, linear combinations of Bloch functions that are symmetrized according to the compatibility relations between the group of \mathbf{k} at the center of the BZ, and the small group of \mathbf{k} at the point under consideration. To do so, the symmetry of the point group at this specific point should be established and the procedure described above should be reproduced *mutatis mutandis*.

As mentioned above, the point group is D_{3h} at the center of BZ, it becomes C_{3h} at K point and C_{2v} at M point of BZ. The irreducible tables of D_{3h} , C_{3h} and C_{2v} point groups are given in **Appendix A**. There, symmetry operators are noted using different notations depending on people studying lattice vibrations or electronic states. For example, people studying phonons note them C'_i if their generic wave functions are invariant under σ_h ,

C_i'' in the other case. As usual, two-dimensional representations are labelled using E , and letter A is used for mono-dimensional representations, with under-script 1 and 2. Under-script 1 is used for the purely symmetric representation in the absence of σ_h , 2 in the other case. At the Γ point the relationships between the notations that are used are:

$$\Gamma_1^+, \Gamma_1^-, \Gamma_2^+, \Gamma_2^-, \Gamma_3^+, \Gamma_3^- = A_1', A_1'', A_2', A_2'', E', E''$$

where the superscripts + and - represent parity against action of symmetry operation σ_h following Doñi and Parravicini notation [19]. Basis functions of each of these irreducible representations of interest for us are shown in the right column of tables shown in **Appendix A**. The relationship between the notations are shown in tables 1.1 and 1.3 which are followed by Doñi and Parravicini *et al.* [19], George F. Koster *et al.* [25] and Cotton *et al.* [26]. They are not explicitly offered in the other, more compact notations.

At **K** point, the point group is C_{3h} which has six symmetry operators: $E, C_3, C_3^{-1}, \sigma_h, 2S_3$ and S_3^{-1} . The symmetry elements in addition to the identity are C_3 and C_3^{-1} rotations with axis along z , the symmetry plane σ_h and two S_3 and S_3^{-1} operations (rotations C_3 and C_3^{-1} respectively) further followed by a reflection in a plane perpendicular to the rotation axis). At **M** point, the point group C_{2v} has four symmetry operators: $E, C_2, 2\sigma_v$. There is a vertical symmetry plane, for example (y,z) that is orthogonal to the plane of σ_h , the intersection of both being a two-fold symmetry axis (parallel to y) in addition to identity. We note that the tables generally label "z" the orientation of the two-fold axis but here the C_2 axis lies along the y direction of the crystal. Using the classical labelling

D_{3h}	D_{3h}	D_{3h}	$C_{2v}(y)$	$C_{2v}(y)$	$C_{2v}(y)$	$C_{3h}(z)$	$C_{3h}(z)$	$C_{3h}(z)$
Doñi	Koster	Cotton	Doñi	Koster	Cotton	Doñi	Koster	Cotton
Γ_1^+	Γ_1	A_1'	M_1^+	M_1	$B_1(x)$	K_1^+	K_1	A'
$\Gamma_1^-(z)$	Γ_4	$A_2''(z)$	M_1^-	M_4	$B_2(x)$	K_1^-	$K_4(z)$	$A''(z)$
Γ_2^+	Γ_2	A_2'	M_2^+	M_2	$A_1(y)$	K_2^+	K_2	A'
Γ_2^-	Γ_3	A_1''	M_2^-	M_3	A_2	K_2^-	K_3	A''
Γ_3^+ (x,y)	Γ_6	E' (x,y)	$M_1^+ + M_2^+$	$M_1 + M_2$	$A_1(y) +$ $B_1(x)$	$K_1^+ + K_2^-$	$K_1 + K_2$ (x,y)	$E' + E'^*$ (x,y)
Γ_3^-	Γ_5	E''	$M_1^- + M_2^-$	$M_3 + M_4$	$A_2 + B_2$	$K_1^- + K_2^-$	$K_3 + K_4$	$E'' + E''^*$

Table 1.1: The relationship between the notations of the symmetries.

Point Γ (D_{3h})	Point M (C_{2v})	Point K (C_{3h})
Γ_1^+ s_N	M_1^+ s_N	K_1^+ s_N
s_B	s_B	$p_{xB} + ip_{yB}$
Γ_3^+ p_{xN}	p_{yN}	K_2^+ $p_{xN} + ip_{yN}$
p_{yN}	p_{yB}	s_B
p_{xB}	M_2^+ p_{xN}	K_3^+ $p_{xN} - ip_{yN}$
p_{yB}	p_{xB}	$p_{xB} - ip_{yB}$
Γ_2^- p_{zN}	M_2^- p_{zN}	K_1^- p_{zN}
p_{zB}	p_{zB}	K_2^- p_{zB}

Table 1.2: Symmetrized combination of Bloch function for 2D BN at Γ , K and M points in BZ.

of tables, the two planes are vertical ones and the specificity of σ_h that we emphasize since the beginning of this section could be lost if care were not taken. The compatibility relations between γ , K and M points are shown in table 1.1.

The energy levels in BN are obtained by expanding the Bloch states in terms of a linear combination of atomic orbitals. The symmetrized linear combinations of the atomic states for Γ , M , K points are shown in table 1.2, where one can see that all IRs are mono-dimensional away from zone center due to the lack of inversion symmetry. Specifically, **at Γ point** we have: $2\Gamma_1^+$ Bloch states that are formed from the linear combination of s states of B and N atoms, $2\Gamma_2^-$ Bloch states are given by the linear combinations of states p_z , and the $2\Gamma_3^+$ doubly-degenerate Bloch states are the linear combination of p_x, p_y states. These are summarized in the left column of table 1.2. The 8x8 matrix that we have to solve is reduced into four 1x1 ones (for the two $2\Gamma_1^+$ and the two $2\Gamma_2^-$ Bloch states) and two 2x2 ones ($2\Gamma_3^+$ Bloch states). **At K point** (middle column of table 2), now we have to solve (i) two non-degenerated 2x2 matrices with an initial state s state of one kind of atom and an equally weighted linear combination of p_x and p_y states of the other kind of atom; (ii) a 2x2 matrix with coupling of both kind of atoms via linear combination of complex conjugates of the previously cited ones of their p_x and p_y states; (iii) two 1x1 matrices as the p_z states of the N and B atoms have different symmetries. **At M point** (right hand column

of table 2), one has to solve a 4x4 matrix starting for s and p_y states of the two atoms (y is chosen arbitrarily), a 2x2 matrix for the p_x ones (x label derives from the preceding choice of y), and again a 2x2 matrix for the p_z states.

In the left part of figure 1.7 is the typical band structure for the BN monolayer that was calculated by a simple tight-binding method [19] compared with a modern approach published in 2014 (right part) [27]. The dispersion relations arising from p_z states of boron and nitrogen atoms are highlighted in red and green colors, respectively. The different interaction parameters in the models lead to different results: for instance, the energy of p_z state of N atom is lower than p_x and p_y states at Γ point in the modern calculations, in opposition to the old calculation. However, in the old calculations, the physics resulting from the symmetry is kept: the p_z states of both atoms are decoupled from the others, the first energy band exhibits a minimum in Γ and is gapped at the edges of the BZ at K and M before the second band is out of any extra coupling away from high symmetry points where, is maximized again at Γ . It is obvious that even if shapes are changed, the physics has been framed by the simple tight-binding approach and symmetry considerations. This simplified 2D model is very convenient for approaching the 3D description of the band structure of BN and for calculating the selection rules for the optical transitions.

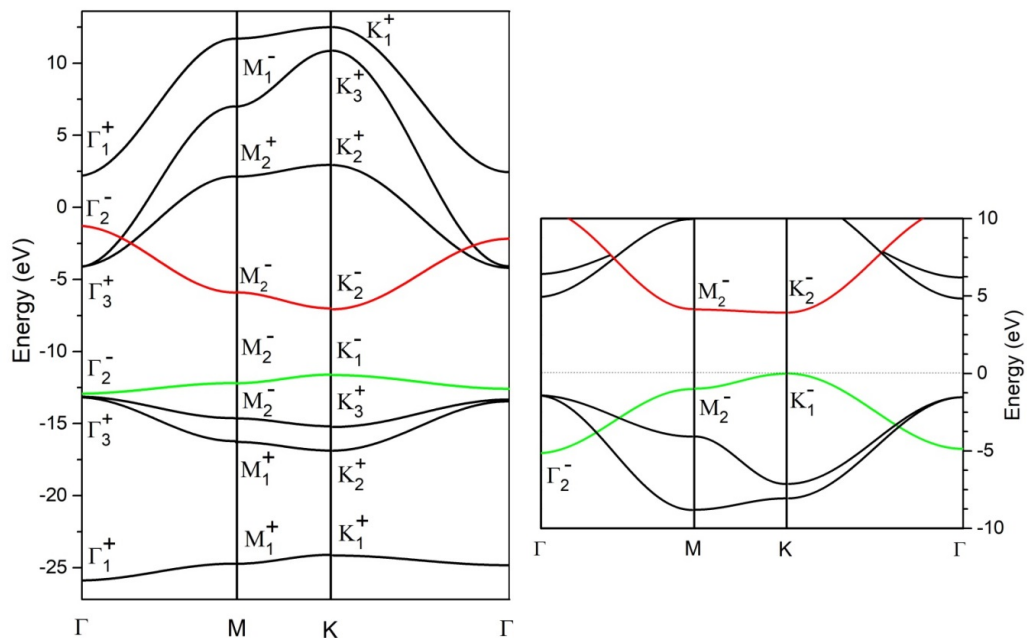


Figure 1.7: Electronic band-structure of 2D BN using simple tight binding method (left) [19] and modern approach (right) [27].

b. Symmetry of electronic states of 3-D Boron nitride

In case of 3D BN, we have to consider the full 16x16 matrix as mentioned above in line with having two nitrogen atoms and two boron ones in the unit cell of the crystal, one pair for each layer of the AA' stacking. These atoms are noted N_1, N_4, B_2, B_3 (figure 1.5). As pointed out by Doñi and Parravicini [19], a good approximation for calculating the band structure of 3D BN consists in coupling layers of 2D BN. Thanks to the high value of the interlayer distance along the z direction, and as only p_z atomic orbitals peak along the z direction, they proposed to calculate the band structure of 3D BN by simple coupling of the p_z states of the N and B atoms belonging to adjacent layers of the AA' stacking. Thus, by doing so, interlayer couplings between intra-layer σ states are neglected. In the context of this approximation, the modification of the band structure only occurs from 2D BN to 3D BN thanks to new interactions between the π states (formed with p_z orbitals of both kinds of atoms). We restrict our discussion here to the AA' coupling of

D_{6h}	D_{6h}	D_{6h}	$D_{2h}(y)$	$D_{2h}(y)$	$D_{3h}(y)$	$D_{3h}(y)$	$C_{2v}(y)$	$C_{2v}(y)$
Doñi	Koster	Cotton	Koster	Cotton	Koster	Cotton	Koster	Cotton
	Γ_1^+	A_{1g}	M_1^+	A_g	K_1	A_1'	T_1	A_1
Γ_{2g}^-	Γ_2^+	A_{2g}	M_3^+	B_{2g}	K_2	A_2'	T_2	B_1
	Γ_3^+	B_{1g}	M_2^+	B_{3g}	K_4	A_2''	T_3	B_2
	Γ_4^+	B_{2g}	M_4^+	B_{1g}	K_3	A_1''	T_4	A_2
	Γ_5^+	E_{1g}	$M_3^+ + M_4^+$	$B_{1g} + B_{3g}$	K_5	E'	$T_3 + T_4$	$A_2 + B_2$
	Γ_6^+	E_{2g}	$M_1^+ + M_2^+$	$A_g + B_{2g}$	K_6	E''	$T_1 + T_2$	$A_1 + B_1$
	Γ_1^-	A_{1u}	M_1^-	A_u	K_3	A_1''	T_3	A_2
$\Gamma_{2u}^-(z)$	$\Gamma_2^-(z)$	$A_{2u}(z)$	M_3^-	$B_{2u}(z)$	$K_4(z)$	$A_2''(z)$	$T_4(z)$	$B_2(z)$
	Γ_3^-	B_{1u}	M_2^-	B_{3u}	K_2	A_2'	T_1	B_1
	Γ_4^-	B_{2u}	M_4^-	B_{1u}	K_1	A_1'	T_2	A_1
	Γ_5^-	E_{1u}	$M_3^- + M_4^-$	$B_{3u}(x) +$ $B_{1u}(y)$	K_6	E'	$T_1 + T_2$ (x,y)	$A_1 + B_1$ (x,y)
	Γ_6^-	E_{2u}	$M_1^- + M_2^-$	$A_u + B_{2u}$	K_5	E''	$T_3 + T_4$	$A_2 + B_2$

Table 1.3: The relationship between the notations of the symmetries for 3D BN at Γ, K and M points in BZ.

Point Γ (D_{3h})	Point M (C_{2v})	Point K (C_{3h})
Γ_{2g}^- $p_{zN1} - p_{zN4}$ $p_{zB2} - p_{zB3}$	M_{2g}^- $p_{zN1} - p_{zN4}$ $p_{zB2} - p_{zB3}$	K_2^- p_{zN1} p_{zN4} p_{zB2} p_{zB3}
Γ_{2u}^- $p_{zN1} + p_{zN4}$ $p_{zB2} + p_{zB3}$	M_{2u}^- $p_{zN1} + p_{zN4}$ $p_{zB2} + p_{zB3}$	
Point A	Point H	Point L
A_1 p_{zN1} p_{zN4} p_{zB2} p_{zB3}	H_3 p_{zN1} p_{zN4}	L_1 p_{zN1} p_{zN4} p_{zB2} p_{zB3}
	H_2 p_{zB2} p_{zB3}	

Table 1.4: Symmetrized combinations of Bloch function for 3D BN at Γ , K, M, H, A and L points in BZ.

the π states of 2D BN. Linear combinations that are **even (gerade) and odd (ungerade) regarding the inversion center located at the middle of the interlayer spacing** can be constructed. The group of \mathbf{k} is D_{6h} at center of BZ, the small groups of \mathbf{k} are D_{3h} at K point, D_{2h} at M point and C_{2v} at T point. The irreducible tables of the point groups are given in **appendix A**. The compatibility relations between Γ , K, M and T points are shown in table 1.3 with different notations followed by Doñi and Parravicini, George F. Koster and Cotton as mentioned above. We note that, the (+,-) superscript in Koster corresponds to (g, u) underscripts in the notations of Doñi and Cotton.

In table 1.4 are given the symmetrized combinations of Bloch functions derived from atomic states p_z for 3D BN at the Γ , M and K, as well as in the direction of the stacking A, H and L are indicated.

In figure 1.8 are reported the dispersion relations that result from the coupling between p_z atomic states of the different layers [19]. Similar to the 2D case, the dispersion relations of the p_z states of boron and nitrogen atoms are plotted in red and green, respectively. Considering M and Γ points, each state M_2^- (respectively Γ_2^-) of the 2D case is split into M_{2g}^- and M_{2u}^- (respectively Γ_{2g}^- and Γ_{2u}^-) due to the interaction between different layers. Now considering the K and L points, there is no splitting, as a straightforward consequence of

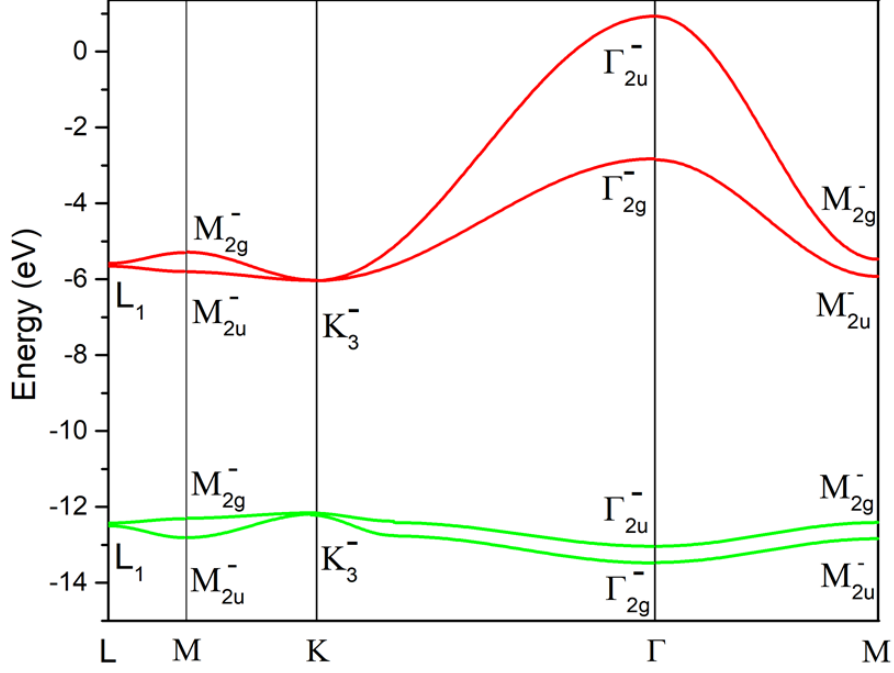


Figure 1.8: Electronic band-structure of 3D BN for p_z states using simple tight binding method [19].

the expressions of the symmetrized combinations of atomic orbitals and the possibility offered by group theory to have two-fold degeneracy in case of D_{3h} symmetry. Slightly moving away from K along the $\Gamma\mathbf{K}$ direction, the symmetry is lowered to C_{2v} and this degeneracy is lifted. We stress the lack of splitting and the twofold degeneracy in the \mathbf{KL} , \mathbf{LA} , \mathbf{KH} and \mathbf{LH} directions.

In fact the complicated dispersion relations in the high energy conduction band levels could be accounted for by the inclusion of more atomic orbital states corresponding to the $n \geq 3$ shells. The price to pay should be to increase the number of empirical tight-binding parameters. The limit of old tight-binding calculations to atomic states of the $n = 2$ shell leads to a wrong result when comparing with the modern calculations that will be referenced later, who went beyond this limit. Specifically, the band structure for p_z states of Doñi and Parravicini indicated a direct fundamental bandgap of BN at K point as shown in figure 1.8 whereas, in the modern calculations, the fundamental bandgap of BN is indirect because the minimum of conduction band is at M point.

However, we know the symmetry of the top most valence band state and of the bottom conduction state which knowledge will be of value for computing the selection rules for the phonon-assisted radiative recombination processes.

1.3 Modern calculations of electronic band structure of boron nitride

The band structure of BN has been already calculated from the beginning of the 1950s until nowadays. Many approaches have been used for calculations such as: tight binding; density functional theory (DFT), local density approximation (LDA) [10, 19, 28–34]. A quite accurate and detailed calculation was published in 2006 by Arnaud *et al.* [30] using the GW approximation which was studied before by Blase *et al.* [31]. Their calculations (figure 1.9 (top, left)), indicate that BN is unambiguously an indirect bandgap semiconductor with the extrema of the fundamental conduction and valence bands respectively sitting at the M and near K point (T_1 point) in the ΓK direction of Brillouin zone. The minimum of the direct bandgap is located at H point. The value of the indirect bandgap

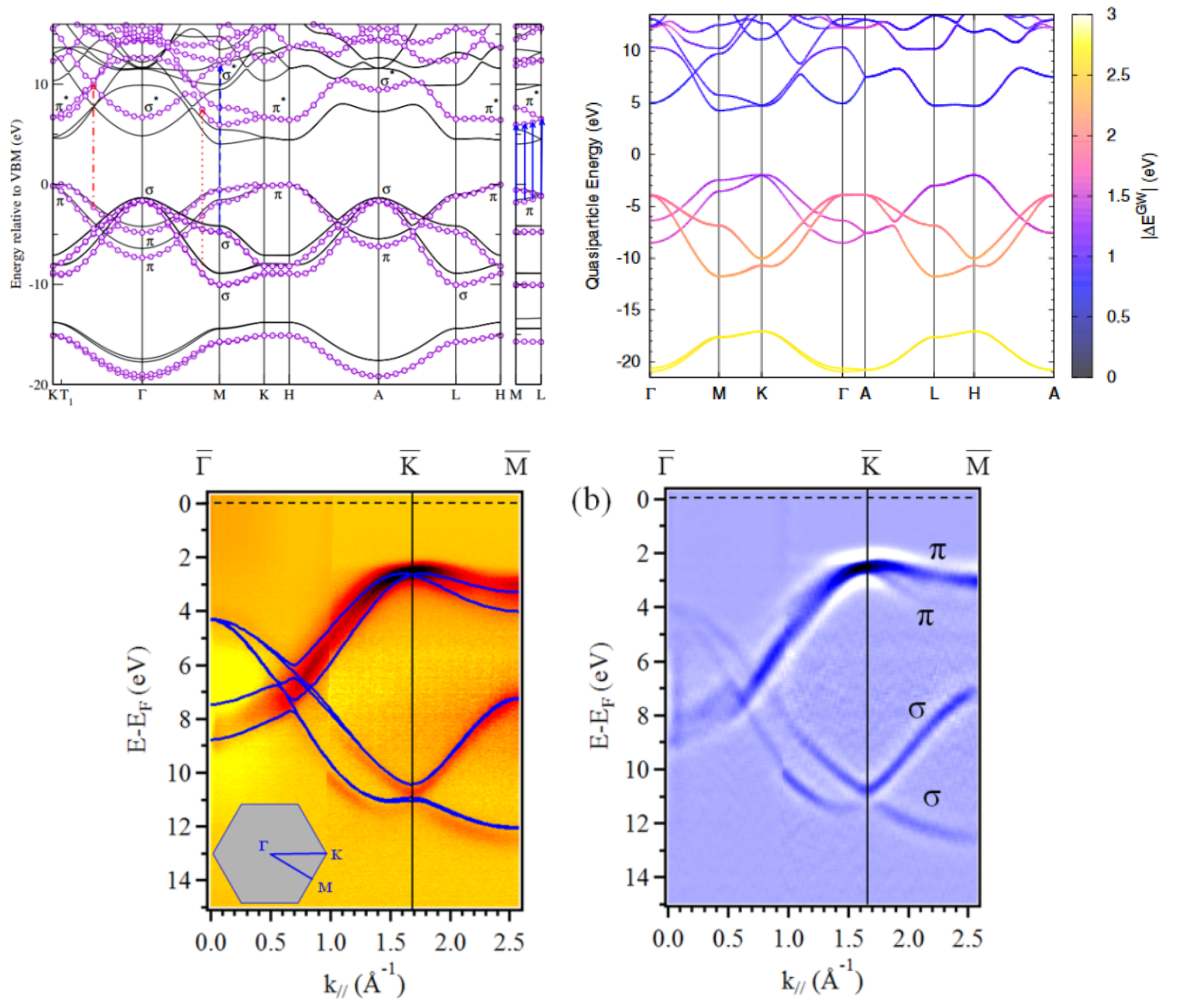


Figure 1.9: Calculated (top) and experimental (bottom) electronic band structure for bulk hexagonal boron nitride [10, 31, 34].

transition between T_1 and M is around 5.95 eV and is 6.5 eV for the direct bandgap between M valence and conduction band states. This calculation has been reproduced in several publications with excellent agreements [10, 33, 34]. The sitting of the maximum of the valence band in the neighborhood of K point has been confirmed through the interesting calculation published in 2015 [33]. The most recent calculation by Vinson *et al.* [10] also asserted the indirect bandgap of BN, with the fundamental gap of 6.34 eV and direct gap of 6.8 eV located at H ($1/3, 1/3, 1/2$) (Figure 1.9 (top, right)). They find that the extrema of the conduction and valence bands are at M ($1/2, 0, 0$) with an energy of 4.3 eV and near K at an energy of -2.038 eV or -2.042 eV, -2.054 eV depending on the position: M, Γ or H points, respectively.

From the experimental point of view, Henck *et al.* [34] published the measurements of the valence band by Nano ARPES (angle-resolved photoemission spectroscopy) in 2017. This work indicates that the maximum of the valence band locates away from K point in the Γ K direction (Figure 1.9 (bottom)) in agreement with the calculations mentioned above.

In summary, recent theoretical calculations all predict that BN is an indirect bandgap semiconductor with a minimum of the conduction band at the M point of the first Brillouin zone and a maximum of the valence band peaking a little bit away from the K point of the first Brillouin zone in the Γ K direction.

1.4 Phonon symmetries and dispersion relations

With four atoms per unit cell in BN, there are twelve phonon modes that are gathered at the center of the Brillouin zone. To determine the symmetries associated with atomic displacements, each atom is attributed a set of cartesian vectors, which leads the computation of phonon modes in a 12-dimensional representation basis. The 12x12 matrices that represent the action of the symmetry operators of D_{6h} on this basis are expressed. This permits to determine the characters of this reducible representation for all the classes of the group. Then one can expand this reducible representation along the irreducible representations of our group. This having been done, the matrices representing the symmetry elements are assembled in order to form the projector operators of the symmetries that appear during the decomposition of the irreducible representation. This permits to obtain

the symmetrized combination of the atomic displacements: the phonon eigen-vectors. Computing the phonon modes is much more complicated as interactions between the nuclei of the different atoms need to be included in the expression of the dynamical matrix, the eigen-values of which will give the phonon energies. This is fairly difficult, the textbook models of linear chain of atoms are over simplified regarding the resolution of our 3D problem.

1.4.1 Normal modes

Although the nature of the fundamental bandgap of BN led to controversial literature it was not the case of phonon modes thanks to Raman and far InfraRed measurements that were published as early as in 1966 [18]. In their pioneering work, Geick and Perry also proposed the symmetrized atomic displacements that could explain twelve phonon modes from 4 atoms in a unit cell. Depending on the movement direction of atoms (interlayer or intra-layer), we also divide these modes into two types: in plane and out-of plane modes.

There are three **acoustic phonon modes** (E_{1u} and A_{2u} symmetries at BZ center). Two of the three are in-plane translation modes that will be further noted LA and TA, and the third is an out-of plane mode which we will note ZA. There are shown in figure 1.10.

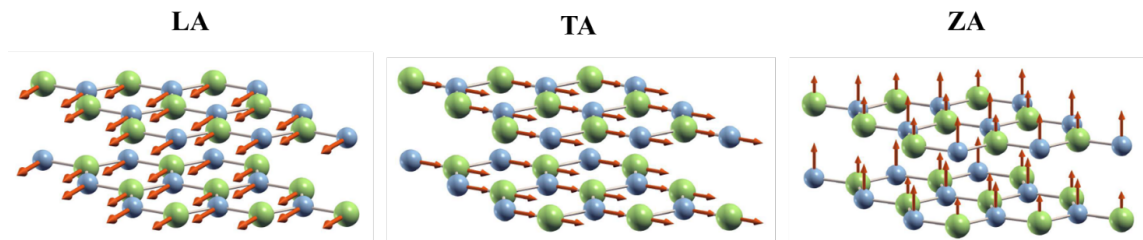


Figure 1.10: Acoustic phonon modes of BN.

Nine remaining modes are **optical phonon modes**, including two twice degenerated Raman active modes, three InfraRed active modes and two inactive modes (silent modes). The value of the high frequency Raman-active (E_{2g}^{high}) phonon mode of E_{2g} symmetry was measured at 169.8 meV at room temperature (RT) by Geick and Perry [18]. Though they could not find the second Raman-active phonon mode (E_{2g}^{low}) because of difficult experimental conditions, they predicted this mode to have an eigen-frequency smaller than 18.6 meV. In figure 1.11 is the schematic representation of atomic motion for the two Raman active phonon modes at high and low frequencies. We emphasize here that both

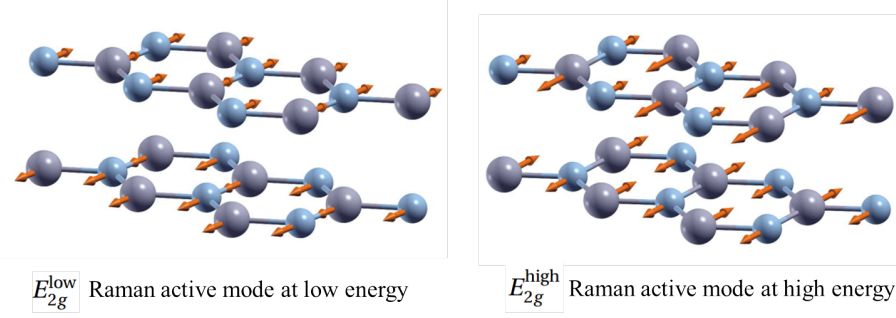


Figure 1.11: Raman active optical modes at low and high energies at center of Brillouin zone.

of them are in-plane modes. For the E_{2g}^{high} mode, boron and nitrogen atoms move in the opposite directions in the layer, whereas the movement of them for the second one is in a same direction in the plane but different directions with adjacent planes. Because of a weak interaction along c-axis and a strong dependence on interlayer force constant, the second Raman active mode (**interlayer shear mode**) is difficult to obtain as said above. However, in 1978, this low frequency mode was independently observed for the first time by two groups: namely by Nemanich *et al.* [20] and by Kuzuba *et al.* [35] with an energy of about 6.5 meV at room temperature. Then studies were published regarding the dependence of this mode with hydrostatic pressure [36], crystal size and temperature [20]. Regarding InfraRed active modes, there are two modes of E_{1u} symmetry and a single mode of A_{2u} symmetry as shown in figure 1.12. The A_{2u} mode is an out-of plane mode with the energy of 96.4 meV at RT, whilst the E_{1u} in-plane modes split into E_{1u}^{TO} and E_{1u}^{LO} at center of BZ with energies of 169.4 and 199.6 meV respectively, due to the long-range Coulomb interactions as pointed out by Michel and Verberck [37]. In their paper, they compared two phonon dispersion relations were calculated without and with the long-range Coulomb force, respectively. The difference between two calculation is the LO-TO splitting with the splitting energy of $\Delta\omega_{E_{1u}} = \omega_{E_{1u}^{LO}} - \omega_{E_{1u}^{TO}} = 30.2$ meV. Because of the

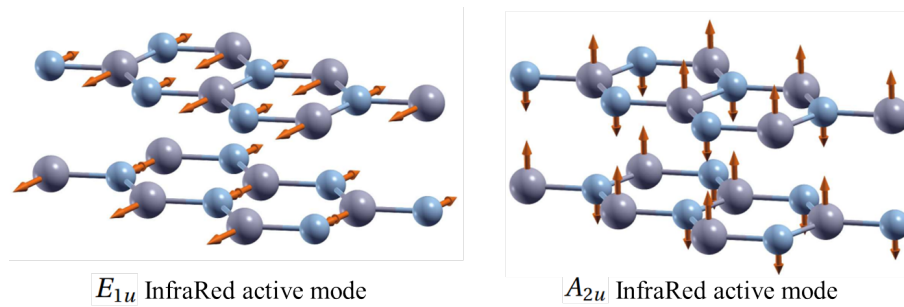


Figure 1.12: InfraRed active optical modes at center of Brillouin zone.

Coulomb interaction which breaks the symmetry field in BN leading to the split of the longitudinal and transverse optical phonons.

Finally, there are two silent modes of symmetries B_{1g} , which eigen-vectors are given in figure 1.13 and that correspond to the interlayer breathing mode. This B_{1g} mode is an out-of plane mode with the boron and nitrogen atoms movement along the c -axis. Specifically, the boron and nitrogen atoms move in the same direction (c -axis) within a plane, but different directions in adjacent planes. Their eigen-energies are 14.8 meV and 100.8 meV at zone center.

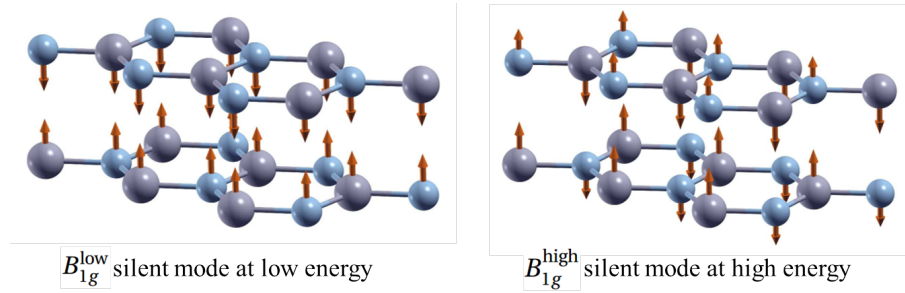


Figure 1.13: Silent modes at low and high energies at center of Brillouin zone

1.4.2 Phonon dispersion relation

These very much documented series of experimental results stimulated the production of theoretical calculations using various theoretical approaches (DFT, LDA) [8, 9, 18, 37–39]. The first calculation of phonon dispersion relations of bulk BN was done by Kern *et al.* [8] using a first principle force constant method in 1999. This calculation was confirmed by many works by Wirtz *et al.* [9], Serrano *et al.* [38], Michel and Verberck [37], Vinson *et al.* [10]. Almost all the calculations have a good agreement with each other and with experiment data.

In the figure 1.14 is shown the most detailed phonon band structure, which was calculated recently by Cuscó *et al.* [39] with more accuracy than in previous calculations. In this phonon band structure 12 phonon branches are clearly identified. Cuscó *et al.* have labeled the three acoustic phonons LA (E_{1u}^{LA}), TA (E_{1u}^{TA}), ZA (A_{2u}^{ZA}) and the nine optical branches are labeled TO₁ (E_{2g}^{1low}), LO₁ (E_{2g}^{2low}), TO₂ (E_{2g}^{1high}), LO₂ (E_{2g}^{2high}), LO₃ (E_{1u}^{LO}), TO₃ (E_{1u}^{TO}), ZO₁ (B_{1g}^{low}), ZO₂ (A_{2u}), ZO₃ (B_{1g}^{high}). In the blue notations, eigenvectors of the different modes may appear several times and for that reason they are distinguished using a superscript to indicate their energy (low or high). Along ΓK direction, Raman-active

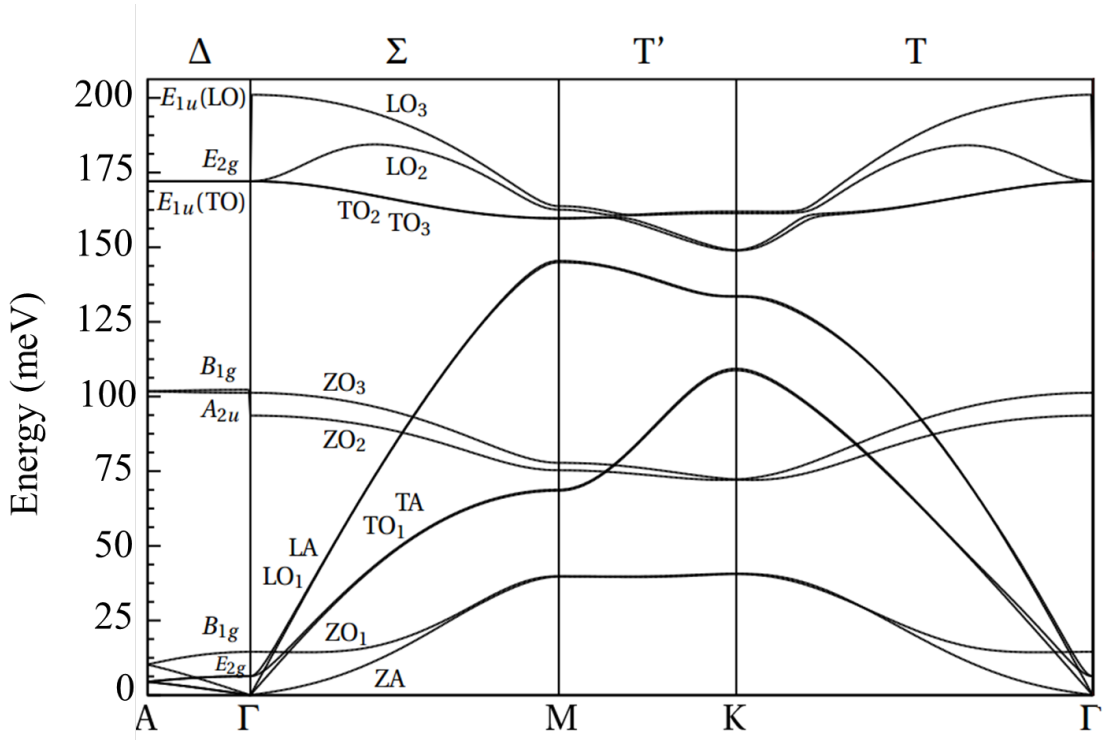


Figure 1.14: Phonon dispersion relations calculation of BN along a high symmetry [39]

modes with E_{2g} symmetry (for both high and low energies) split into $TO_1 - LO_1$ and $TO_2 - LO_2$ branches. Similarly, InfraRed-active mode E_{1u} splits into $TO_3 - LO_3$ branches. The frequencies for the three pairs of branches TO_1 - TA ; LO_1 - LA ; TO_2 - TO_3 are very close but they are not degenerated. This is summarized in table 1.6.

We have to remark that the notations of the different symmetries depend on the language used in the community of people that are using a given experimental technique. It may sometimes become a nightmare if it is required to bridge these different languages of the literature.

To understand what the symmetries of these phonon modes are, and how they transform at any point of the BZ, it is important to determine the compatibility relations between the phonon modes at zone center, and at any point of the BZ, in order to calculate the selection rules for the optical processes. In our case, we know that the phonon-assisted recombination of electron and holes will have a \mathbf{KM} wave number, which is equivalent to $1/2 \Gamma\mathbf{K}$. Therefore we will have to determine the compatibility relations between the vibration modes in a crystal of D_{6h} symmetry (Γ point in BZ) and a crystal of C_{2v} symmetry ($\Gamma\mathbf{K}$ direction at T point) as explained earlier in that chapter.

At Γ point (D_{6h}), a cartesian basis is following (x,y,z) with z axis colinear to the 6-fold

symmetry axis, while at T point (C_{2v}), the two-fold rotation axis is collinear to ΓK direction (x) which is chosen to transform like A_1 symmetry. ΓM (y) and ΓA (z) directions are chosen to transform like B_1 and B_2 symmetries, respectively (Figure 1.5). A summary of the correlation between IRs of D_{6h} and C_{2v} is obtained by comparing two character tables of D_{6h} and C_{2v} point groups (**Appendix A**), as shown in the correlation table 1.5 below.

D_{6h}	C_{2v}
B_{1g}	B_2
A_{1g}	A_1
E_{2g}	$A_1 + B_1$
E_{1u}	$A_1 + B_1$
A_{2u}	B_2

Table 1.5: Correlation table for D_{6h} and C_{2v} point groups.

From this table, we have the transformation of the phonon modes with different symmetries.

For acoustic phonons:

- $E_{1u} + A_{2u} \Rightarrow A_1 + B_1 + B_2$ (LA, TA, ZA branches respectively).

For optical phonons:

- $E_{2g} \Rightarrow A_1 + B_1$ (TO_1, LO_1, TO_2, LO_2 branches)
- $E_{1u} \Rightarrow A_1 + B_1$ (TO_3, LO_3 branches).
- $A_{2u} \Rightarrow B_2$ (ZO_2 branch).
- $B_{1g} \Rightarrow B_2$ (ZO_1 and ZO_3 branches).

1.5 Selection rules for the optical transitions

We have to distinguish two cases here.

In case 1: the photon emitted or absorbed propagates in the direction of the six-fold symmetry axis of 3D boron nitride. The electric field of this photon is orthogonal to it and it will be taken either parallel to x or to y. Its symmetry is similar to the symmetry of x or y.

We now consider matrix element of Fermi's Golden rule:

$$M_{if} = \langle \mathbf{n}_{VB}, \vec{\Gamma T}_1 | V_{photon} | \mathbf{n}_{int}, \vec{\Gamma T}_1 \rangle \langle \mathbf{n}_{int}, \vec{\Gamma T}_1 | V_{e-phonon} | \mathbf{n}_{CB}, \vec{\Gamma M} \rangle \quad (1.7)$$

We consider the phonon-assisted transition from the top valence band at T_1 (the compatibility tables indicate the symmetry of the valence band state is $A_1(T) + B_1(T)$) towards the bottom of the conduction band at M (the compatibility tables indicate the symmetry of the conduction band is $B_{1u}(M) + B_{3u}(M)$). The symmetry of the photon is in the most general case written $A_1(T) + B_1(T)$. The symmetry of the electric field being odd in real space (it is the symmetry of a polar vector), initial and final states have different spatial parities. $|\mathbf{n}_{int}, \overrightarrow{\Gamma T_1}\rangle$ represents all intermediate virtual or real states that satisfy k -conservative selection rule, and it must be even in real space. From the multiplication tables, the symmetry of $|\mathbf{n}_{int}, \overrightarrow{\Gamma T_1}\rangle$ has to be written $A_1(T) + B_1(T)$ to make sure that matrix element $\langle \mathbf{n}_{VB}, \overrightarrow{\Gamma T_1} | V_{photon} | \mathbf{n}_{int}, \overrightarrow{\Gamma T_1} \rangle$ does not vanish. We note that parity does not explicitly appear in this very compact notation and that $A_1(T) + B_1(T)$ notations do not give any information about parity.

In case 2 the photon emitted or absorbed propagates orthogonally to the direction of the six-fold symmetry axis of 3D boron nitride. The symmetry of the electric field is $B_2(T)$, and is aligned parallel to c which is the case of interest here if one wishes to make a discriminative experiment (chapter 3). We again consider the phonon-assisted transition from the top valence band $A_1(T)$ (resp. $B_1(T)$), then intermediate state $|\mathbf{n}_{int}, \overrightarrow{\Gamma T_1}\rangle$ must have symmetry $B_2(T)$ (resp. $A_2(T)$).

The virtual states involved in the k -conservative selection rules being different in the two cases, this should impact the non-vanishing conditions of the second matrix element $\langle \mathbf{n}_{int}, \overrightarrow{\Gamma T_1} | V_{e-phonon} | \mathbf{n}_{CB}, \overrightarrow{\Gamma M} \rangle$ and we expect to probe different phonon modes by doing experiments in case 1 and case 2 of the experimental configurations that we will use in the chapter 3.

We now consider the different possible symmetries for the $V_{e-phonon}$ exciton-phonon interaction and again apply group theory following the method initiated by Bassani and Hassan [23]. The symmetry of the exciton-phonon interaction $V_{e-phonon}$ is the product of the symmetry of the phonon under consideration with the symmetry of the excitonic envelope function obtained by using Wannier function for exciton wave function which has to be even in real space so that $\langle \mathbf{n}_{int}, \overrightarrow{\Gamma T_1} | V_{e-phonon} | \mathbf{n}_{CB}, \overrightarrow{\Gamma M} \rangle$ does not vanish for parity reasons. This restricts exciton envelope functions to those with $A_1(T)$ symmetry.

Let us consider an experiment done in the experimental configuration we called case 1 before. Then one finds that matrix element involving $V_{e-phonon}$ vanishes when the phonon

symmetry is $B_2(T)$. This selection rule states that emission (or absorption) of a ZO_1 or a ZO_3 phonon (which both derive from the phonon modes with B_{1g} symmetry at zone center) is forbidden in the context of the dipole interaction as well as emission of a ZA or a ZO_2 phonon mode (which both derive from the phonon modes with A_{2u} symmetry at zone center). However phonon-assisted processes with $A_1(T)$ and $B_1(T)$ phonons are allowed. These selection rules can be changed if performing the experiments in the context of another experimental configuration, **namely case 2**. Let us choose the Poynting vector of the photon perpendicular to the z axis of the crystal and let us choose it to transform like $A_1(T)$ for carrying on the demonstration of selection rules for the phonon assisted process within the context of the group theory analysis. There are two possible symmetries for the electric field of the photon: (either the electric field of the photon is colinear with the z axis of the crystal, then the relevant symmetry is $B_2(T)$) or it is of $B_1(T)$ symmetry (then the electric field of the photon is orthogonal to the $(B_2(T), A_1(T))$ plane). We have indicated these orientations relatively to the hexagon in figure 1.15.

In context of the $B_2(T)$ polarization of the photon, non-vanishing matrix elements $\langle \mathbf{n}_{VB}, \vec{\Gamma T}_1 | V_{photon} | \mathbf{n}_{int}, \vec{\Gamma T}_1 \rangle$ occur for a transition from a valence band state of symmetry $A_1(T)$ (resp. $B_1(T)$) to an intermediate state of symmetry $B_2(T)$ (resp. $A_2(T)$).

Regarding selection rules for, $\langle \mathbf{n}_{int}, \vec{\Gamma T}_1 | V_{e-phonon} | \mathbf{n}_{CB}, \vec{\Gamma M} \rangle$ non-vanishing elements are $\langle B_2(T) | B_2(T) | A_1(T) \rangle$ and $\langle A_2(T) | B_2(T) | B_1(T) \rangle$, which indicates that emission or absorption of one ZO_1 or one ZO_3 phonon (which both derive from the phonon modes with B_{1g} symmetry at zone center) is a priori allowed in the context of the dipole interaction, with this polarization of the photon, as well as emission of a ZA or a ZO_2 phonon mode

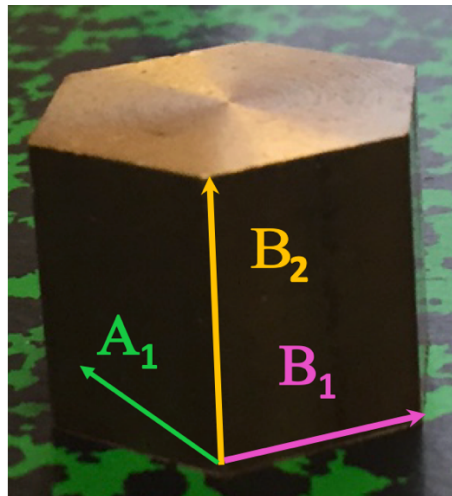


Figure 1.15: Orientations relatively to the hexagon.

(which both derive from the phonon modes with A_{2u} symmetry at zone center. We just have to keep in mind that B_{1g} mode are silent at the center of the BZ, whilst A_{2u} ones are InfraRed active. Therefore, the optical feature recorded in case 2 of the experimental configuration among that B_{1g} is an even mode whilst A_{2u} is an odd one. Therefore, phonon B_2 should be even so that $\langle \mathbf{n}_{VB}, \vec{\Gamma T}_1 | V_{photon} | \mathbf{n}_{int}, \vec{\Gamma T}_1 \rangle$ does not vanish for odd nature of the integration. So, ZO_1 and ZO_3 is phonon modes to consider.

Before moving to second chapter, I would like to present the summary of all phonon modes of BN as shown in table 1.6.

Phonon mode name	Phonon mode type	Symmetry at Γ point	Selection rules considering	
			$E \perp c$ -axis	$E \parallel c$ -axis
LA	Acoustic/In-plane	E_{1u}	allowed	forbidden
TA	Acoustic/In-plane	E_{1u}	allowed	forbidden
ZA	Acoustic/Out-of plane	A_{2u}	forbidden	forbidden
LO ₁	Optical/In-plane	E_{2g}	allowed	forbidden
LO ₂	Optical/In-plane	E_{1u}	allowed	forbidden
LO ₃	Optical/In-plane	E_{1u}	allowed	forbidden
TO ₁	Optical/In-plane	E_{2g}	allowed	forbidden
TO ₂	Optical/In-plane	E_{1u}	allowed	forbidden
TO ₃	Optical/In-plane	E_{1u}	allowed	forbidden
ZO ₁	Optical/Out-of plane	B_{1g}	forbidden	allowed
ZO ₂	Optical/Out-of plane	A_{2u}	forbidden	forbidden
ZO ₃	Optical/Out-of plane	B_{1g}	forbidden	allowed

Table 1.6: Summary the phonon modes of BN

Chapter 2

Experiments

This chapter introduces our BN samples (bulk and epilayers) grown by different growth methods in addition to the concept of the photoluminescence (PL) measurements.

High-purity BN samples play an important role for studying the physical properties of this material, however, the synthesis of large crystals with high quality was a difficult task. After the success in growing large, high-purity BN crystals by the group of Prof. Taniguchi in Japan in 2004 [6, 7], researchers started paying more attention to this semiconductor. Nowadays, many methods have been popularly used for synthesizing boron nitride such as a temperature gradient method under high-pressure and high-temperature method (HP-HT) [7], Ni-Cr flux method for 3D BN [40] or molecular beam Epitaxy (MBE) [41, 42], CVD [43–49] for 2D BN.

Besides, PL spectroscopy is one of the main fundamental and technologically important tools for characterising materials. It does not only help to confirm the quality of crystals but also to understand the underlying physics of the materials. In this thesis, we focus on understanding the fundamental opto-electronic properties of BN by performing the PL measurements. This chapter will explain the principle of PL and display the experimental setup of our measurements.

2.1 Samples

In this thesis, we use four samples from four sources: NIMS - Japan, HQ Graphene company, KSU - USA, and Nottingham - UK using HP-HT, Ni-Cr flux, and MBE methods to check the intrinsic optical properties of BN. Three of them are bulk crystals, while the

remaining one is an epitaxy BN samples. The details of each sample will be presented below.

2.1.1 NIMS samples

The first successful synthesis of large sized BN bulk crystal was reported in 2004 by Taniguchi and co-worker at the National Institute for Materials Science, NIMS - Japan [6, 7]. This process basically consists in high pressure (4-5 GPa) and high temperature (1500°C- 1650°C) growth for 20-80 hours using the barium boron nitride ($\text{Ba}_3\text{B}_2\text{N}_4$) solvent. The crystal size was obtained until few millimeters in three dimensions (Figure 2.1). The quality of crystals was analyzed by secondary ion mass spectrometry (SIMS) and cathodoluminescence (CL). High-purity level of such crystals reflects in the absence of any impurities absorption in the optical spectrum [6, 7].

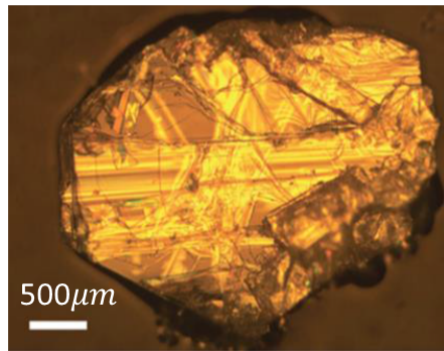


Figure 2.1: Typical image of the BN crystal from National Institute for Materials Science - NIMS, Japan.

2.1.2 HQ Graphene samples

The second series of samples was bought from HQ Graphene Company [50]. HQ Graphene is a manufacturer of high quality 2D single crystal such as: WSe_2 , MoSe_2 , MoWSe_2 and etc. Their products are being sold directly to a large of number of universities, laboratories and companies. The BN crystals from this commercial company have a typical lateral size is around 1 mm (Figure 2.2). The synthesis details remain still protected, the high qualities of crystals, however, were verified by many studies and publications [11, 51].

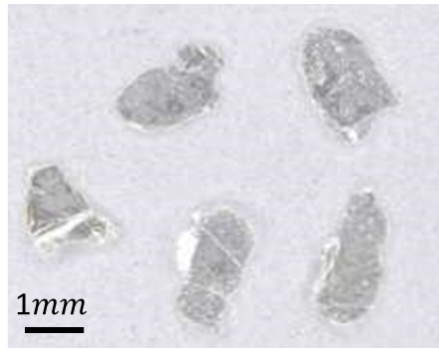


Figure 2.2: Typical image of the BN crystal from HQ Graphene company [50].

2.1.3 KSU samples

Isotopic ^{10}B and ^{11}B enriched BN crystals were synthesized by our colleagues working at Department of Chemical Engineering, Kansas State University, USA using the Ni-Cr flux method [40]. High purity elemental ^{10}B (99.22 at %) or ^{11}B (99.41 at %) powders were mixed with Ni and Cr powders to give overall concentrations of 4 at % B, 48 at% Ni and 48 at% Cr. The mixed Ni-Cr-B powder was loaded into an alumina crucible and placed in the furnace. The reaction tube was evacuated, and then filled with N_2 and forming gas (5% hydrogen in balance argon) to a constant pressure of 850 Torr. During the reaction process, the N_2 and forming gases continuously flowed through the system at rates of 125 sccm and 25 sccm, respectively. In this experiment, all nitrogen in the hBN originated from the flowing N_2 gas. The forming gas was used to minimize oxygen and carbon impurities that are recognized as the main contaminants in BN crystals. The liquid solution was formed by heating the furnace up to and holding at 1550°C for a dwell time of 24 hours. The BN crystals were precipitated by cooling at a rate of $1^\circ\text{C}/\text{h}$ to 1500°C . After growth, the system was quickly quenched to room temperature.

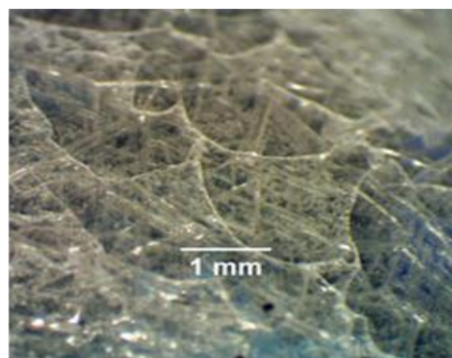


Figure 2.3: Typical image of the BN crystal from Kansas State University, USA [40].

2.1.4 MBE samples

The last series of samples comes from our colleagues - the group of Prof. Sergei Novikov working at the School of Physics and Astronomy, University of Nottingham, Nottingham, United Kingdom. These samples are grown by high temperature Molecular beam epitaxy (MBE) at substrate temperatures between 1200°C and 1700°C (thermocouple temperatures). The MBE system is a dual-chamber Veeco GENXplor specially modified to achieve growth temperatures of up to 1850°C and is capable of growth on rotated substrates of up to 3 inches in diameter [41]. The BN layers were all grown using a boron cell temperature of 1875°C and the nitrogen source operated at 550 W with a nitrogen flow rate of 2 standard cubic centimeters per minute (sccm). Epitaxial BN was grown on two substrate with a size of 10x10 mm²: sapphire (0001) and highly ordered pyrolytic graphite (HOPG). Before introduction into the MBE growth chamber the HOPG substrates were cleaned by exfoliation using adhesive tape to obtain a fresh surface for growth. Following exfoliation, substrates were further cleaned by immersion in toluene (CHROMASOLV for HPLC, Sigma-Aldrich) for 24h and after that, thermally cleaned in a tube furnace at 200°C in a flow of Ar:H₂ gas (0.15 standard litres per minute for 4h) to remove any remaining polymer residue.

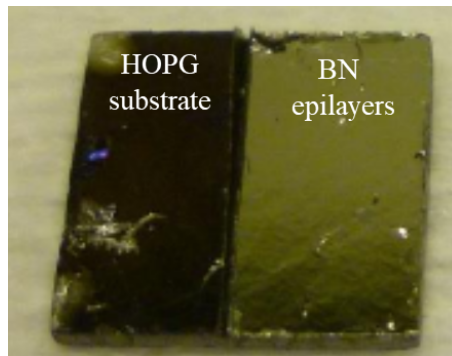


Figure 2.4: Typical image of the epitaxial BN from University of Nottingham, United Kingdom

2.2 Photoluminescence

2.2.1 Principle of photoluminescence.

Photoluminescence occurs after electrons have been excited by a high energy photon (similar to cathodoluminescence with high energy electrons). In this excitation process, the electron passes from a state E_i to another one E_f . The initial state may be called the ground state while the final state may be called the excited state. These electrons remain in the excited state for a short time (around 10^{-12} s) because they relax to lower states by phonon emission. Finally, radiative recombination may occur (figure 2.5).

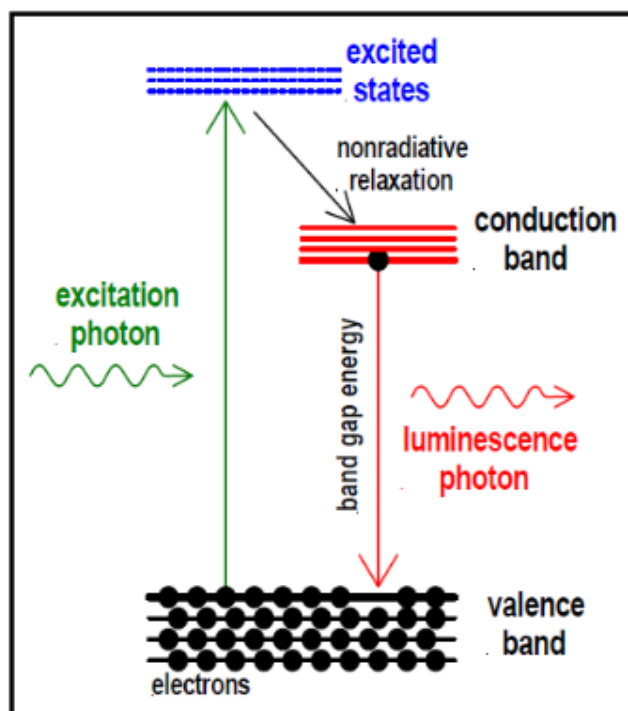


Figure 2.5: Principle of photoluminescence spectroscopy (PL).

Practically, in case of a semiconductor, the most common radiative transition is between states located at the conduction and valence band extrema. The difference in energy between the conduction and valence bands is called the bandgap.

Depending on the position in k -space of the conduction and valence band extrema, the band gap of a semiconductor is of two types: a direct band gap or an indirect band gap. The radiative recombination processes for direct-bandgap and indirect bandgap semiconductors are sketched in figure 2.6.

- In case of direct bandgap semiconductors, electrons and holes sit at the same po-

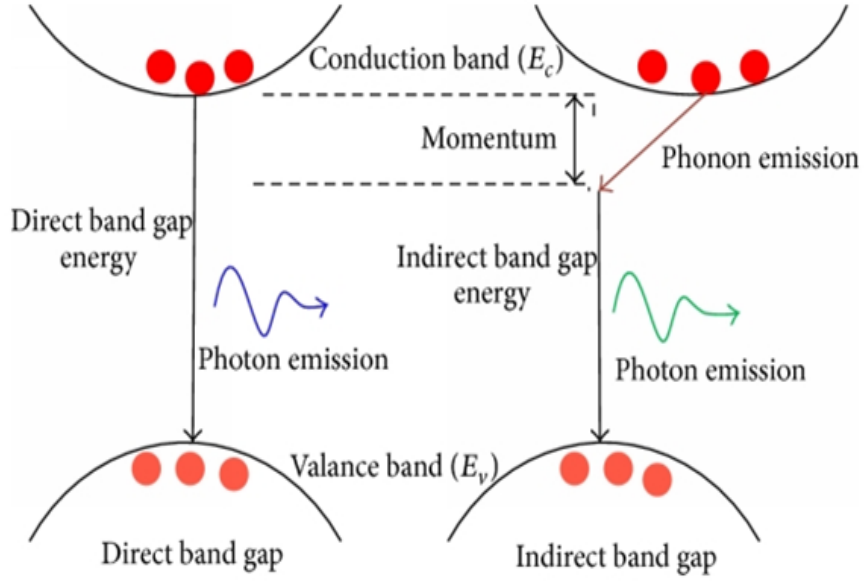


Figure 2.6: Illustration of a photon emission process in (left side) the direct and (right side) the indirect band gap semiconductors [52].

sition in both the conduction band and the valence band: the Bloch states have identical wave numbers k_h and k_e in the first Brillouin zone. Therefore, an electron can directly emit a photon. Examples of direct bandgap material include some III-V materials such as InAs, GaAs, GaN.

- In case of indirect bandgap semiconductors, the extrema of the conduction and valence band do not occur at the same point of the Brillouin zone. In that specific situation, emission or absorption of a phonon of ad-hoc vector is required to fulfill k conservation rule. Therefore, a phonon wave vector k_p is needed as a third particle to emit a photon and the photons can only be recorded at energies given by $E_{CB}(k) - E_{VB}(k') - \hbar\omega(k_p)$. Such recombination processes are less favorable than direct transition as the probability of phonon emission. Examples of indirect bandgap materials include Si, Ge, AlAs, AlP, AlSb, GaP.

Radiative transitions in semiconductors may also involve localized defects or impurity levels. Therefore, the analysis of the PL spectrum helps in the identification of specific defects or impurities in semiconductors.

The PL spectroscopy have been performed for all four samples (NIMS, HQ Graphene, KSU and MBE) in order to: (i) check the quality of BN samples; (ii) understand the intrinsic the optical and electronic properties of this BN material.

2.2.2 Experimental setup

In our experimental setup, all BN samples are held on the cold finger of a closed-circle cryostat for temperature-dependent measurements from 10K to room temperature. Depending on each sample and the purpose of each PL measurement, two-photon excitation spectroscopy and one-photon excitation spectroscopy were performed. In case of two-photon excitation, the excitation beam is provided by the second harmonic of a Ti:Sa oscillator, tuned at 408 nm in resonance with the sharp peak in the two-photon excitation spectrum. The spot diameter is of the order of $100 \mu\text{m}$, with a power of 50 mW. In case of one-photon excitation, the excitation beam is provided by the fourth harmonic of a cw mode-locked Ti:Sa oscillator with a repetition rate of 82 MHz. The spot diameter is $300 \mu\text{m}$ with a power of $40 \mu\text{W}$.

As demonstrated in Ref.[11], at high energy of around 6 eV, using two-photon excitation spectroscopy can avoid a stray light coming from laser light scattering, in contrast to one-photon excitation spectroscopy. However, in some cases, for instance the thickness of sample is too thin, an absorption can occur when using two-photon excitation spectroscopy, leading to an observation of no signal. That reason why we have to switch to one-photon excitation spectroscopy.

The setup of our PL experiments is described in figure 2.7. The excitation beam goes through a lense and is focused on the samples. The PL signal is collected by two parabolic

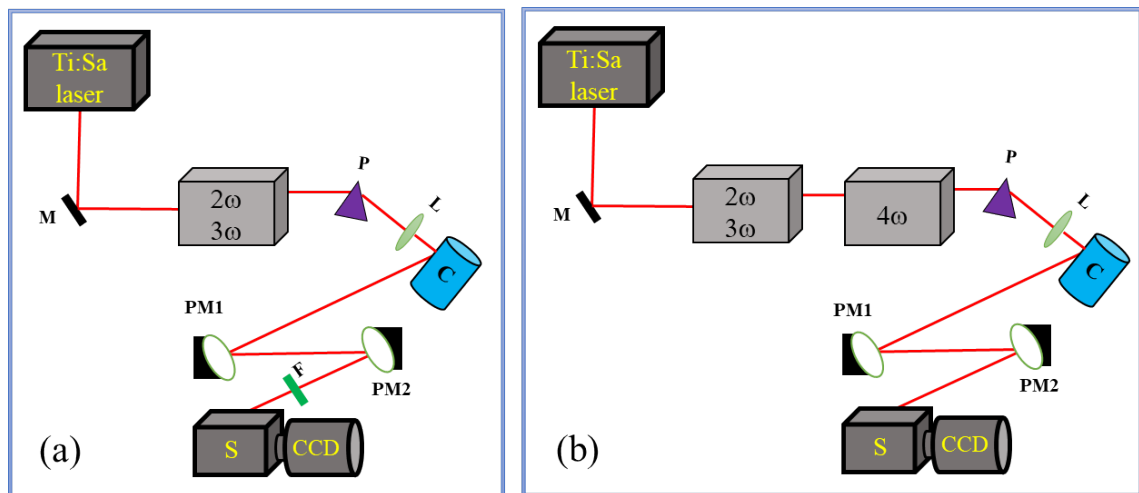


Figure 2.7: Scheme of our experimental setup devoted to measurements in boron nitride at 8K, under (a) two-photon excitation and (b) one-photon excitation. (M) = mirror, (P) = prism, (L) = lense, (C) = cryostat, (PM) = parabolic mirror, (F) = band-pass filter, (S) = spectrometer.

mirrors with the focused PL signals. The PL signals are directed to a $f = 500$ mm Czerny-Turner monochromator, equipped with a back-illuminated charge-coupled device (CCD) camera (Andor Newton 920), with a quantum efficiency of 50% at 210 nm. The monochromator is equipped with three diffraction gratings: a 1800 grooves/mm grating blazed at 250 nm, a 1200 grooves/mm grating blazed at 250 nm, and a 300 grooves/mm grating blazed at 250 nm. In case of two-photon excitation spectroscopy, we use a band-pass filter around 200 nm with a low transmission at 400 nm in front of the spectrometer for complete laser stray light rejection. The integration time is varied (from a minute to 10 minutes) depending on each sample and each measurement.

Polarization-resolved photoluminescence measurements

The large and thick sample using the growth method developed at NIMS was used for polarization-resolved PL measurement. The two-photon excitation spectroscopy was performed for these measurements. The setup of our PL experiments is described in figure 2.8. In this polarization-resolved PL measurements, the sample holder comprises two positions, which are either parallel or perpendicular to the cold finger for collect-

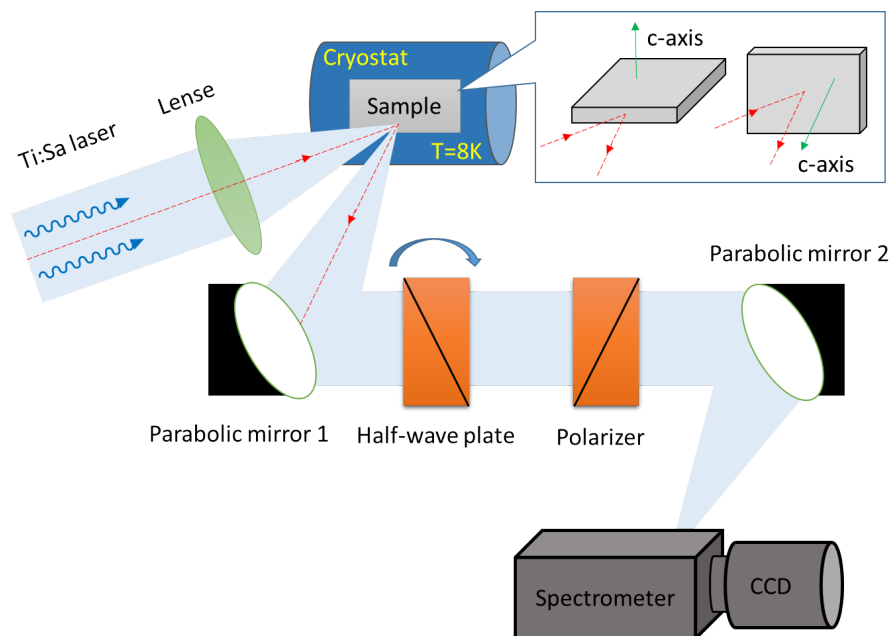


Figure 2.8: Scheme of our experimental setup devoted to measurements in boron nitride at 8K, under two-photon excitation. Depending on the sample position, two configurations of detection are probed, with an emission wave-vector either perpendicular (inset, left) or parallel (inset, right) to the c-axis.

ing along or perpendicular to the c-axis (Figure 2.8, inset), respectively. Between two parabolic mirrors, there are polarization optics consisting of MgF_2 components fabricated by Kogakugiken: a fixed Rochon polarizer, and a rotating half-wave plate.

- **Rochon polarizer** is made of two birefringent prisms cemented together. When an incident beam passes this polarizer, the beam will separate into ordinary and extraordinary rays. Both of ordinary and extraordinary rays propagate linearly the optic axis in the first prism under the ordinary refractive index. However, upon entering the second prism, the ordinary ray is continued to transmit straight through, while extraordinary is transmitted with a deviation angle of $2\hat{A}$ as shown in figure 2.9.

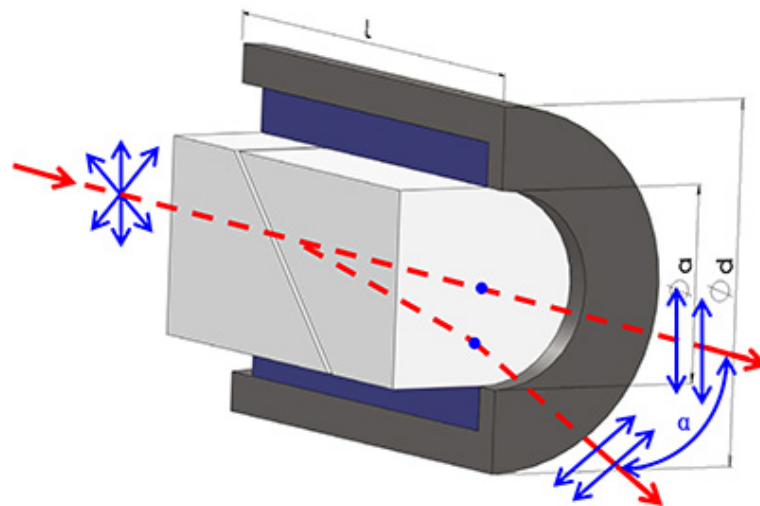


Figure 2.9: Rochon polarizer [53].

- **Half-wave plate** which is achromatic in the spectral range 180-240 nm, rotates linearly polarized light to any desired orientation. The rotation angle is twice the angle between the incident polarized light and optical axis.

All of results observed from our PL measurements will be discussed in the next chapters.

Chapter 3

Phonon-assisted transitions

3.1 Identification of phonon-assisted recombination.

Almost all calculations of the band structure of BN, and at least all the recent and accurate ones, lead to an indirect configuration for the fundamental bandgap of BN, as reviewed in the first chapter of this thesis. In 2004, the experimental measurement of an unexpected intense photoluminescence (PL) spectrum that displayed a documented series of features was reported by Watanabe *et al.* [6] in high-quality crystals.

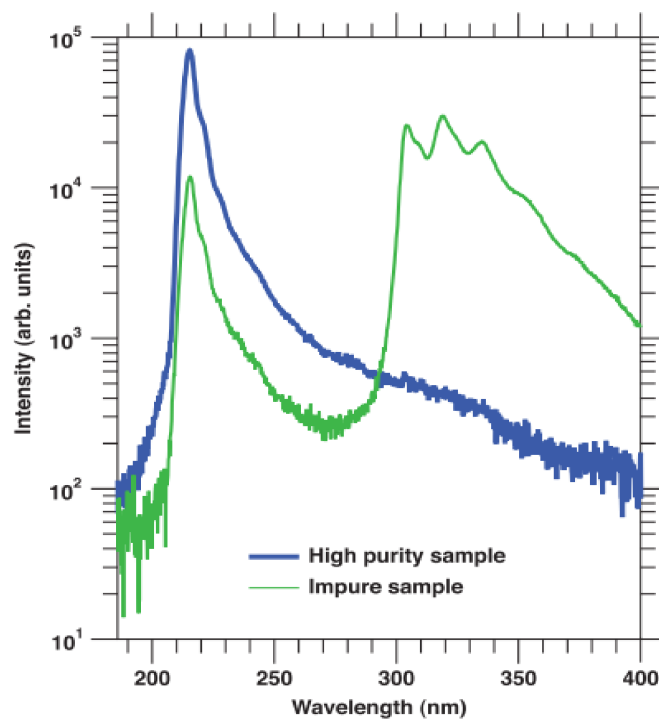


Figure 3.1: Cathodoluminescence spectrum of BN (high purity and impure samples) at room temperature [6, 15].

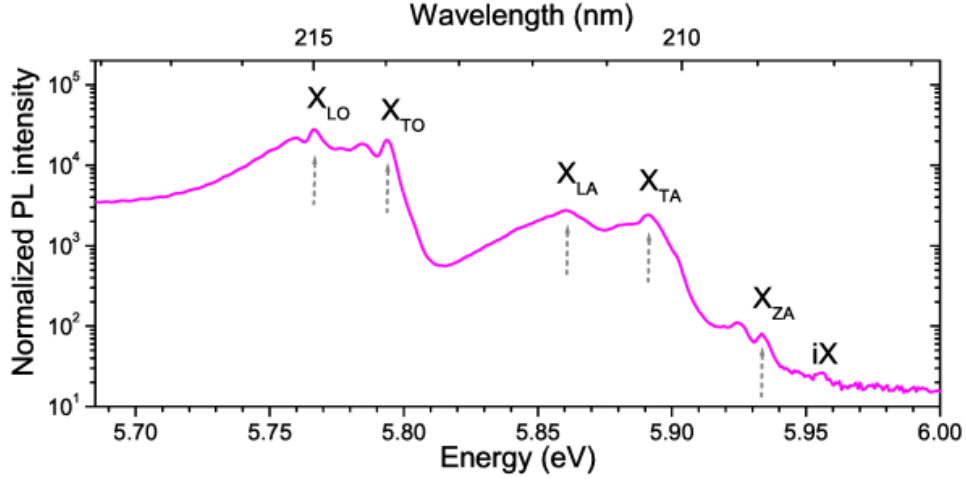


Figure 3.2: Photoluminescence (PL) spectrum of BN at 8K with the identification of the PL lines as phonon-assisted recombination lines in BN [11].

Based on the efficiency of the observed emission, and having in mind the efficiency of light-matter interaction in traditional indirect semiconductors (with cubic zinc blende or diamond structures), they alleged from this intense emission the direct nature of the bandgap of BN. Their study also showed in particular, that cathodoluminescence (CL) spectra at room temperature, which were obtained from high quality crystals, presented a series of sharp lines with light emission extending up to wavelength sitting around 215 nm (5.765 eV) (Figure 3.1 - blue line), while CL of defective crystals were giving a broad band centered around 320 nm (3.87 eV) instead (Figure.3.1 - green line).

This controversy between such a direct bandgap claim, which is now identified as being an allegation, and the theoretical calculations lasted during more than ten years in a context of numerous and nontrivial inconsistencies and a lack of global understanding. In 2016, our group brought the experimental evidence to support the indirect nature of the bandgap of BN. This result was published in Nature Photonics [11]. It was demonstrated that the PL spectrum consists of several emission lines corresponding to phonon-assisted recombination (**phonon replicas**) involving phonons at T point of the BZ (Figure 3.2) which confirming what was discussed in chapter 1. The phonon-assisted transitions have the following energies: 5.76 eV, 5.79 eV, 5.86 eV, 5.89 eV, and 5.93 eV, and the phonons that contribute to activate the radiative recombination were called LO, TO, LA, TA, and ZA respectively. Based on more accurate recent calculations, they will be now more precisely labeled LO_3 , TO_3/TO_2 , LA/LO_1 , TA/TO_1 , and ZO_1 in this thesis following the classification performed in Ref. [39].

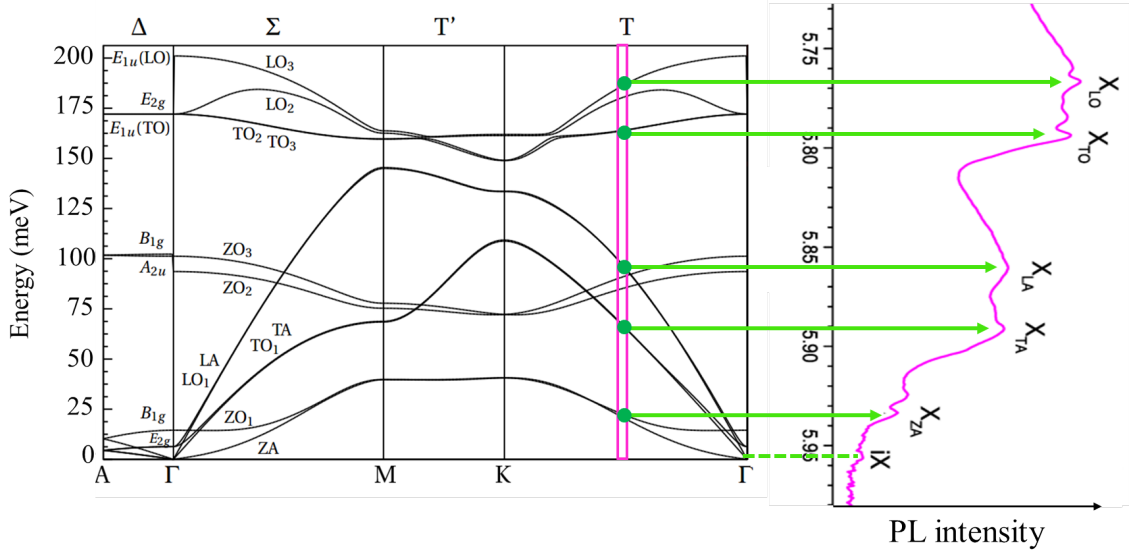


Figure 3.3: Photoluminescence spectrum of BN (right side) [11] plotted at the same scale as the phonon dispersion relations (left side) [39]. The energy of photoluminescence line iX is taken as the zero for the two plots.

Moreover, it was also reported the new observation of an additional, very tiny peak at a higher energy of 5.955 eV. This weak PL signal corresponds to the forbidden indirect exciton transition LO_1 (now called iX). This iX line has a very weak intensity because, as no phonon is emitted, its observation violates the selection rule of momentum conservation for the radiative recombination process. We believe that the imperfect surface of the crystal with defects produces localized potentials having non-vanishing Fourier transform components $V(T) = V(K-M)$ that permit to overcome the lack of \mathbf{k} -conservative selection rule, thus giving rise to the weak iX radiative recombination.

Our previous detailed examinations of the symmetry of the lattice of BN, of the symmetry of the phonon modes, and of the symmetry of the Bloch states at different points of the Brillouin zone and for different energy bands, have led us to conclude in the existence of selection rules for the light-matter interaction process and for light emission out of the crystal. To consolidate the determination of the indirect nature of the bandgap of BN, we have analyzed the polarization of the light emitted under different conditions of propagation out of the crystal in order to probe the contributions of more phonon modes than in Ref.[11].

We reproduce in figure 3.3 the method used in Ref.[11] to demonstrate that the series of sharp lines mentioned above are phonon-assisted transitions. To obtain such conclusion, the 8K PL spectrum of BN was plotted at the same scale as the phonon band structure that

was calculated by Cuscó *et al.* [39], taking the zero of the phonon energies as the energy of the iX recombination line. The energy detuning of the emission lines respect to the iX line is found to be 20, 60, 90, 160 and 190 meV, respectively. This displays an excellent matching with phonon energies at the T point of the phonon dispersion curves, giving an experimental proof for the indirect nature of the bandgap of BN. We remark that the larger the phonon energy, the larger the energy detuning with the indirect bandgap at around 5.95 eV, and thus the lower the energy of the phonon replicas.

In the PL spectrum, besides the observation of the phonon replicas, we also measure a series of lower energy companion replicas that involve several phonons, corresponding to complementary multiple energy relaxation processes as we shall demonstrate later in this chapter.

3.2 The polarization of the photoluminescence of BN

3.2.1 The impact of the phonon symmetries on the optical response in a real BN crystal

The method for measuring a polarization-resolved PL was described in detail in chapter 2 in two specific cases, for two experimental configurations that will lead to different PL shapes, unraveling the contributions of phonons of different symmetries. The Poynting vector $\vec{\omega}$ of the photon is the product $\vec{E} \otimes \vec{H}$ where \vec{E} and \vec{H} represent the electric and magnetic fields, respectively. We remind that, together with $\vec{\omega}$, the orientation of \vec{E} rules the selection determines, as indicated in chapter 1.

In figures 3.4 and 3.5 are displayed these results recorded at low temperature (8K) for different orientations of $\vec{\omega}$ and \vec{E} .

- **Case 1:** the Poynting vector of the emitted photons $\vec{\omega}$ is oriented along the c-axis, when collecting light from the sample top surface. In that case, the emitted light is polarized in the (x,y) plane, and four main emission lines that correspond to the phonon replicas LO_3 , TO_2/TO_3 , LA/LO_1 , and TA/TO_1 were distinctly recorded. A residual PL could be detected that is interpreted in terms of the ZO_1 phonon replica. It is hardly observable, but it is possible to detect it. When rotating the linear polarizer in the (x, y) plane, the PL spectrum does not change as shown for two typical spectra recorded with different polarization angles (figure 3.4). This

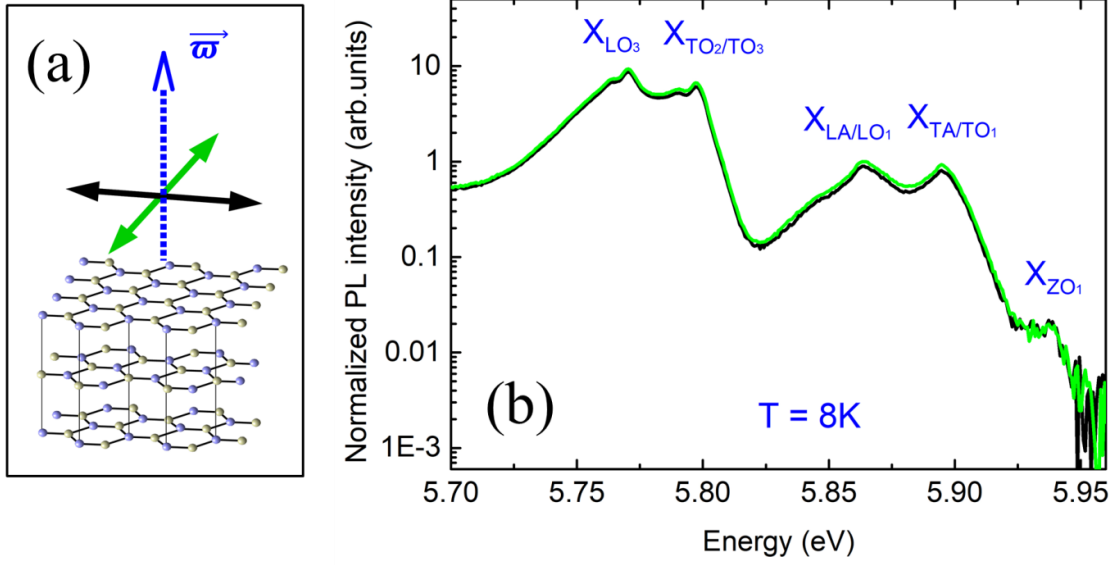


Figure 3.4: (a) The experimental geometry for a Poynting vector $\vec{\omega}$ parallel to c-axis. (b) Polarization-resolved photoluminescence spectroscopy in bulk BN at 8 K for a Poynting vector $\vec{\omega}$ parallel to c-axis for two orthogonal orientations of the linear polarization of analysis.

result is not surprising and it is predicted in text books of classical optics in case of uniaxial crystals when an experiment is realized in such conditions, that is to say for light propagation along the main axis of the crystal. Using a more sophisticated language and in the frame work of a semi-classical description, that involves symmetry of conduction and valence band states as detailed in chapter 1, this result is recovered, but it requires to calculate the selection rules, and prescripts to add for the calculation of the allowed transitions. The contributions of phonons with symmetrized displacements lying in the (x,y) plane, leading to the vibrational modes LO_3 , TO_2/TO_3 , LA/LO_1 , TA/TO_1 with symmetries $A_1(T)$ or $B_1(T)$. We remind that, as it was calculated in chapter 1, transitions involving out-of plane vibrational modes ZA or ZO_i are forbidden for different reasons: banal spatial parity for ZA and $B_2(T)$ symmetry for ZO_i . The observation of the weak line at 5.93 eV which corresponds to the emission of a ZO_1 phonon is attributed to the conditions of the experiments and to the un-perfect shape of the crystal which makes selection rules to slightly depart from ideality.

- **Case 2:** the Poynting vector of the emitted photons $\vec{\omega}$ is perpendicular to c-axis (let us call its orientation x here), photons can be detected having their electric field parallel (red) to the c-axis or orthogonal to it (black) as illustrated in the figure 3.5(a).

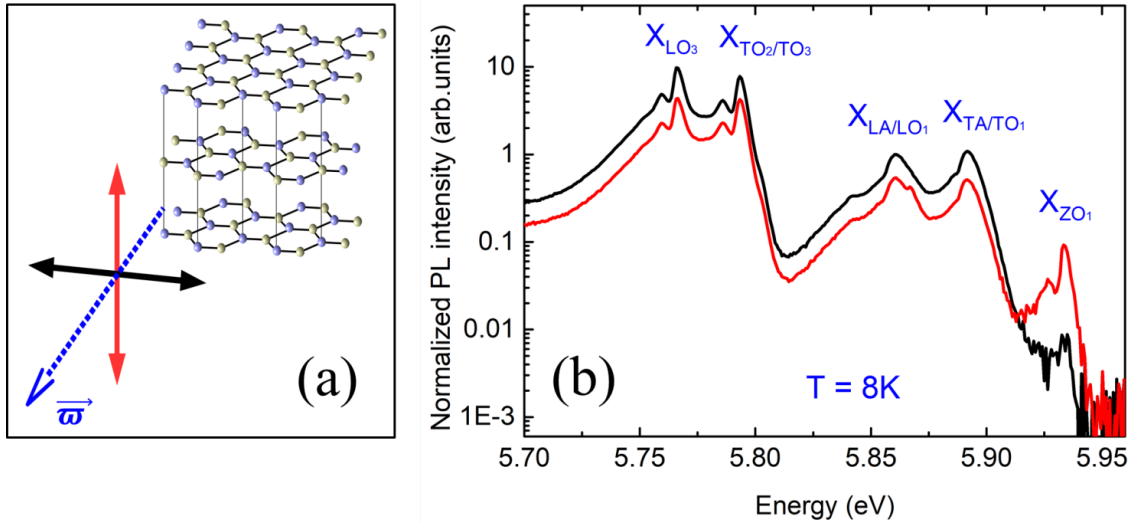


Figure 3.5: (a) The experimental geometry for a Poynting vector $\vec{\omega}$ perpendicular to c-axis. (b) Polarization-resolved photoluminescence spectroscopy in bulk BN at 8K for a Poynting vector $\vec{\omega}$ perpendicular to the c-axis for a linearly-polarized detection, either parallel (red line) or perpendicular (black line) to the c-axis.

Recording PL emitted from the sample edge with such a Poynting vector $\vec{\omega}$, and choosing the polarization of the photon in the appropriate directions, one expects to see the impact of selection rules according to our group theory analysis of chapter 1. As reported in figure 3.5(b), the result is different from what was recorded in the configuration named **case 1**. We still obtain a PL composed of the five emission lines corresponding to the phonon replicas LO_3 , TO_2/TO_3 , LA/LO_1 , TA/TO_1 and ZO_1 . However, the intensities of all phonon replicas depend strongly on the orientation of the polarizer in the (y, z) plane as found when comparing the red and black spectra in the figure 3.5(b). For the emission polarized perpendicular to c-axis (Figure 3.5(b)-black line), the ZO_1 line, again is hardly observed with a weak intensity, while intensities of PL lines involving other phonons replicas have strong intensities. The ratio between the intensities of the LA/LO_1 and ZO_1 phonon replicas is approximately two hundreds. Rotating the polarizer around the x-axis (Figure 3.5(b)-red line), the intensity of the ZO_1 phonon-assisted PL increases whereas, the intensities of the four remain transitions all reduce in concert. The ratio between the intensities of the LA/LO_1 -assisted and ZO_1 -assisted phonon replicas now is five. According to chapter 1, the ZO_1 phonon replica is allowed and the others are forbidden in the conditions of the Poynting vector of the emitted photons $\vec{\omega}$ is perpendicular to c-axis and the polarized detection parallel to c-axis because of se-

lection rules. This discussion is in agreement with what we observe as shown in 3.5(b)-red line, but the reduction of the intensities by factor two is only for the LO₃, TO₂/TO₃, LA/LO₁, TA/TO₁ phonon replicas.

We will go further to understand more the polarization-dependence of these phonon replicas in the two case of the Poynting vector $\vec{\omega}$.

Interpretation of the incomplete extinction of the phonon replicas in case of the Poynting vector $\vec{\omega}$ perpendicular to the c-axis.

The PL signal intensities of LA/LO₁ (blue spheres) and ZO₁ (red spheres) phonon replicas as a function of polarization angles are plotted in figure 3.6. We observe a clear an anti-correlation relatively to the polarization of the emitted photons. **We note an incomplete extinction of LA/LO₁ phonon replicas when analyzing along the c-axis, while the ZO₁ phonon replica is maximally contrasted as a function of polarization angle.** We interpret this phenomenon as due to orientation disorder at sample edges leading to the imperfect selection rules in our experiment.

A quantitative interpretation of the reduced contrast is presented below. The intensity of the emission lines when rotating a polarizer is written:

$$I(E, \theta) = I_V(E) \cos^2(\theta) + I_H(E) \sin^2(\theta) \quad (3.1)$$

where I_V and I_H are the intensities of the emission signal for two linear orthogonal polarizations of analysis, θ is the polarization angle, it is the angle between the orientation of the electric field of the photon and the c-axis of the crystal.

Before going to discuss our experiment, we first describe the case of a perfect BN single crystal with an ideal shape and $\vec{\omega} \parallel x$ as sketched in figure 3.7(a). When we consider a ZO₁ phonon replica, selection rules indicate that $I_V(E_{ZO_1}) \neq 0$ and $I_H(E_{ZO_1}) = 0$, so that the emission diagram is given by $I_V(E_{ZO_1}) \cos^2(\theta)$, while for an in-plane vibrational mode, like LA/LO₁ for instance, it is $I_H(E_{LA/LO_1}) \sin^2(\theta)$ and the contrast of polarization is 100% for both cases.

In our real crystal, we assume that the sample edge is made of a collection of facets each one having its normal direction rotated by an angle α around a direction parallel to the sample edge, as schematically shown in figure 3.7(b). The analysis in this case is the same

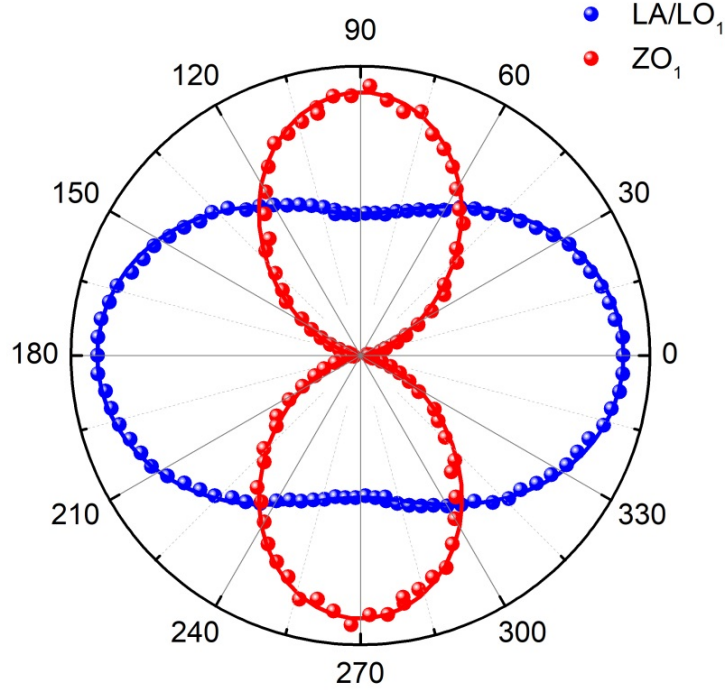


Figure 3.6: Photoluminescence signal intensity and the fits of LA/LO₁ (blue) and ZO₁ (red) phonon replicas as a function of polarization angles.

as in the former one but for each facet represented by its orientation α we write:

$$I_{\alpha}(E, \theta) = I_V^{\alpha}(E) + I_H^{\alpha}(E) \quad (3.2)$$

The emission diagram is obtained after integration over the distribution of α probed by the laser spot in the crystal under consideration. Without any assumption on the distribution, we can draw several important conclusions about the polarization dependence of the emission lines :

- For a dipole oriented along the c-axis of the crystal, i.e. ZO₁ line, the contrast is still 100 % as for the perfect BN monocrystal, in agreement with our data.
- For a dipole oriented orthogonal to the c-axis of the crystal, i.e. LA/LO₁ line, that is to say in the two-dimensional (x,y) plane, the integration process is different, and distribution of orientations slightly impacts the polarization of the emission diagram in such a way that how the ratio I_H/I_V equals:
 - $I_H/I_V = 1/2$ is obtained for all possible orientations are probed by the laser spot. This value is close to our experimental value, thus indicating a highly

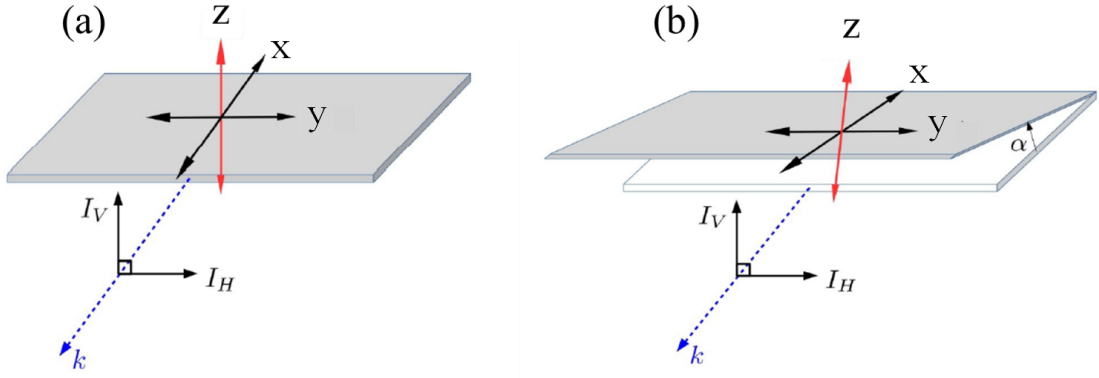


Figure 3.7: (a) Ideal case of a perfect BN monocrystal, (b) real case of a polycrystalline bulk BN sample with a distribution of thick multilayer segments, each one having a c-axis orientation rotated by an angle around a direction parallel to the sample edge.

disordered sample edge in terms of the c-axis orientation respect to the sample edge direction.

- $I_H/I_V = 4/7$ is obtained when only few multi-layer segments are probed by the laser spot. This value shows that the consideration of a continuous distribution of orientation α is not essential for retrieving a-value close to our experimental one of about $1/2$.

Interpretation of the impact of the position of the laser spot on the polarization of the photoluminescence in case of the Poynting vector $\vec{\omega}$ parallel to the c-axis.

In this section we examine the universality of the anti-correlation between the maxima of the emission diagram for ZO_i phonon replicas, for which the associate atomic displacements produce an on-axis dipole, while for other phonons the corresponding dipole is oriented in the plane of the hexagonal stacking. We perform these other experiments with the Poynting vector $\vec{\omega}$ parallel to the c-axis and we scanned the position of the laser spot from the middle towards the two edges of the sample. The positions of the laser spot are indicated for each measurement in the inset of figures 3.8 (a-f). In figure 3.8 below, we display the photoluminescence signal intensity of the LA/ LO_1 (a,c,e) and ZO_1 (b,d,f) phonon replicas as a function of the polarization angle. The measurements in the middle of the sample display a weak dependence of the polarization of analysis for both phonon replicas (see figure 3.8 (a,b)). For the measurements by collecting from the sample edges (figure 3.8 (c-f)), we obtain a pronounced polarization-dependence of the emission spectrum with the anti-correlation of ZO_1 and LA/ LO_1 phonon replicas as

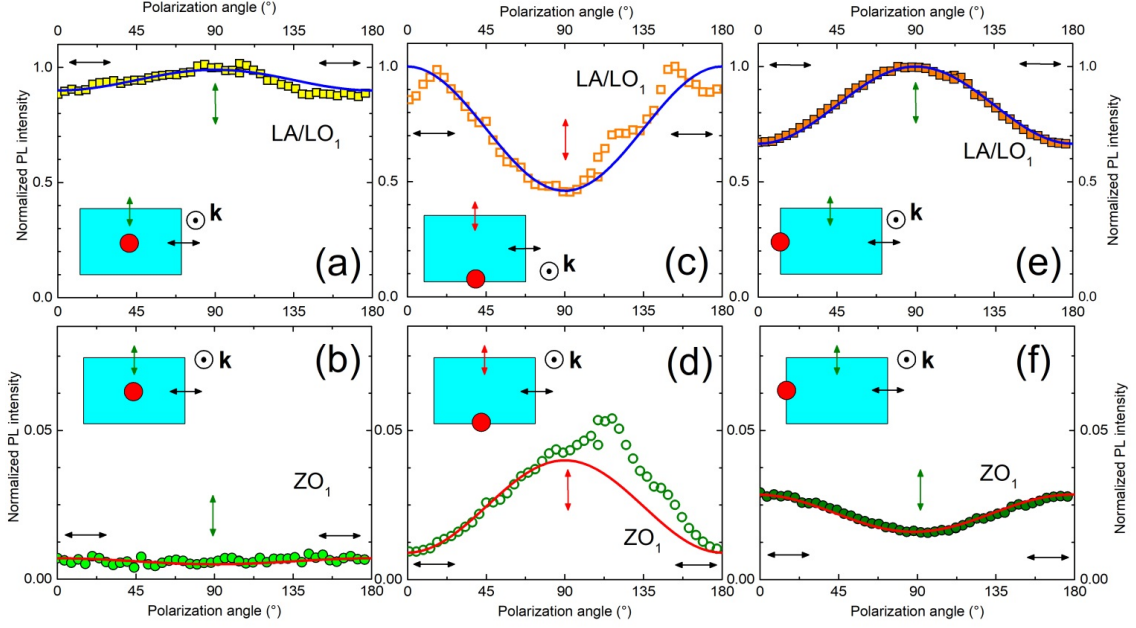


Figure 3.8: Photoluminescence signal intensity of the LA/LO₁ and ZO₁ phonon replicas as a function of polarization angle for a Poynting vector \vec{w} parallel to c axis, for laser excitation spot located in three positions (red spots) located at sample middle and sample edges.

expected. If orientation disorder was averaged by excitation at the center of the crystal it is no longer the case when we probe the edge of the sample. We thus conclude that the additional measurements displayed in figure 3.8 provide a definite cross-check of our model based on orientation disorder at the sample edges, thus fully validating our quantitative interpretation of the incomplete extinction of the phonon replicas when collecting from the sample edge.

3.2.2 Missing phonon mode

As discussed in the previous sections, five phonon-assisted emissions (LO₃, TO₂/TO₃, LA/LO₁, TA/TO₁, and ZO₁) were identified in Ref.[11] from the energy spacing of the PL lines matching the one of phonon modes at T point of the BZ. However, we have demonstrated the impact of the phonon symmetries on the optical response of BN by polarization-resolved measurements with the different polarization dependence for the two types of phonon modes: in-plane or out-of plane vibrational modes because of selection rules. In particular, for Poynting vector \vec{w} perpendicular to the c axis and polarizer along c axis, out-of plane phonons replicas are allowed as shown by the maximum inten-

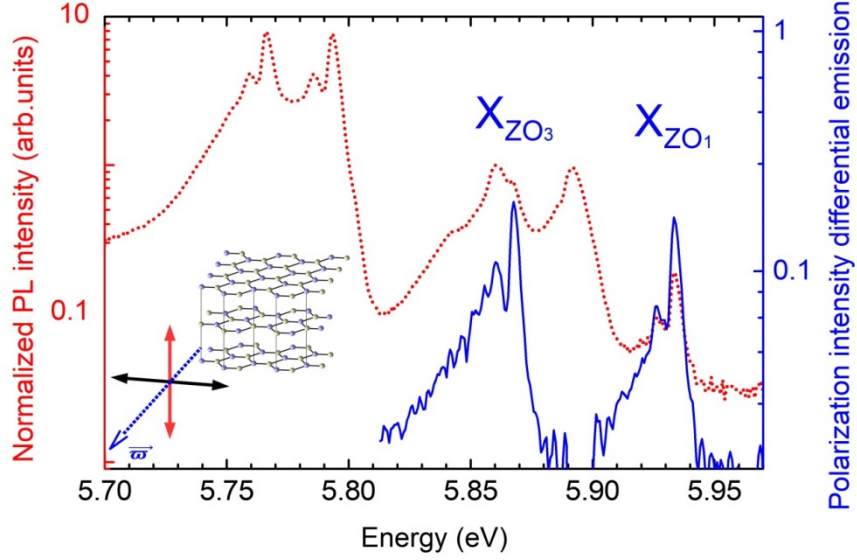


Figure 3.9: Polarization intensity differential emission spectrum corresponding to the difference of the polarization-resolved photoluminescence spectra displayed in figure 3.5(b) (blue solid line). The dashed red line is the photoluminescence spectrum of BN at 8K for a Poynting vector \vec{s} perpendicular to c-axis and the polarization detected parallel to c-axis.

sity of the PL line at 5.93 eV that corresponds to the ZO_1 phonon replica. In this condition, we should also obtain the ZO_3 phonon replica which has the same B_{1g} symmetry as the ZO_1 phonon replica, and of course they thus have the same selection rules. The raising question here is where this phonon replica is.

Regarding the phonon dispersion relations of BN (figure 1.14 and figure 3.3), we remark that at the T point of the BZ, the energy of the ZO_3 phonon mode is close to the one of LA/ LO_1 phonon mode with a down shift in energy of 10 meV. We realize in figure 3.5(b) in case of the emission polarized parallel to c-axis (red line) that there is a very tiny peak close to the LA/ LO_1 phonon replica, 10 meV at lower energy. This value coincides exactly with the LA/ LO_1 - ZO_3 energy splitting as pointed out before from the dispersion relations.

To confirm our interpretation, we have subtracted the two PL spectra in figure 3.5(b) after normalizing both spectra to the maximum intensity of the PL line corresponding to the LA/ LO_1 phonon replica. We get a new spectrum with two striking emission lines as shown in figure 3.9 in blue solid line together with the PL spectrum obtained for the emission polarized parallel to the c-axis (dashed red line). One of them, as we know, corresponds to the ZO_1 phonon replica lying at 5.93 eV. The other one at 5.87 eV has the

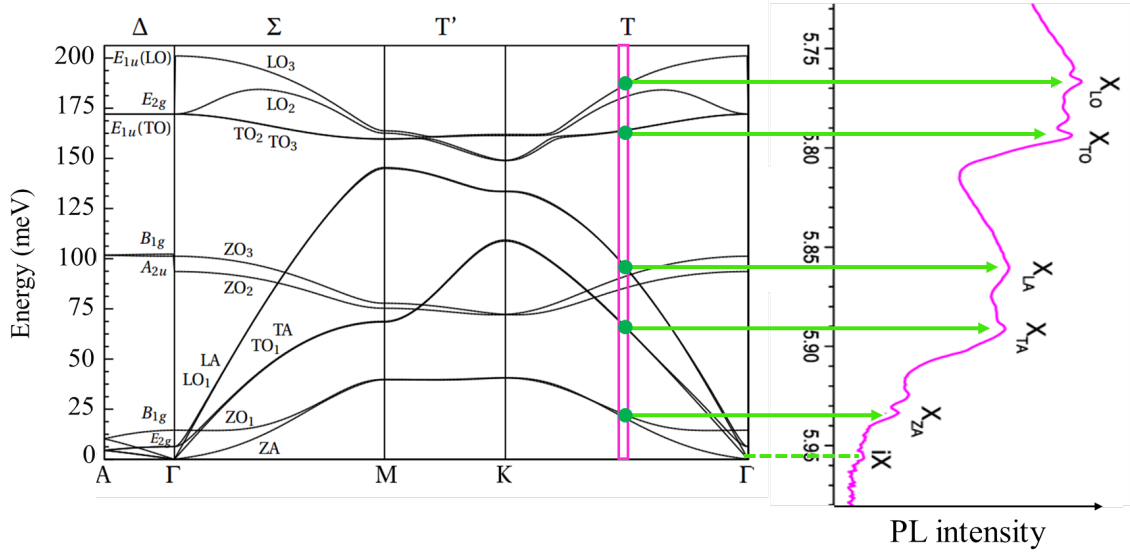


Figure 3.10: Photoluminescence spectra of BN from figure 3.9 (right side) plotted at the same scale as the phonon dispersion relations (left side) [39]. The energy of photoluminescence line iX at 5.955 eV coincides with the zero phonon-energy.

same profile as the identified phonon replicas. It lies at the expected position of the ZO_3 phonon-assisted transition.

To demonstrate that the PL line at 5.87 eV corresponds to ZO_3 phonon-assisted transition, we reproduce again in figure 3.10, the comparison between theoretical calculations and our data. The PL spectrum in figure 3.10 is plotted at the same scale as the phonon dispersion relations that were calculated by Cuscó *et al.* [39], taking again for the zero of the phonon energies the energy of the iX recombination line. We have an excellent matching between the emission line at 5.87 eV (blue solid line) with the energy of the ZO_3 phonon mode at the T point of the phonon dispersion curves (highlighted in pink color) in addition to the excellent agreement for all phonon replicas of PL spectrum (red dash line) as pointed out before. This agreement confirms our identification of the missing ZO_3 phonon replica due to the optical out-of plane phonon mode.

In summary, by means of polarization-resolved PL spectroscopy, the identification of the missing ZO_3 out-of plane phonon replica together with the other phonon replicas gives a comprehensive understanding of the phonon-assisted transitions as well as the originality of the optical properties in this material, besides a strong confirmation for the initial work reported in Ref.[11] about the indirect nature of the bandgap in BN.

3.2.3 The emission diagram of the indirect exciton iX line

Measuring the signature of the forbidden indirect exciton which gives a tiny PL signal at an energy of 5.955 eV, was first achieved in Ref. [11]. No phonon assists this recombination which is strictly forbidden in line with \mathbf{k} -selection rule, which is a severe rule. To the best of our knowledge, signature of shallow impurity-bound excitons were reported in PL spectra of Ge, Si, GaP, AlP, AlAs, AlSb, or Diamond, but the observation of indirect free exciton was not reported. To observe this emission line, it is required that \mathbf{k} -selection rule is broken, which we believe it occurs at the BN-air interface when a defect creates a localized variation of potential with ad-hoc component of its Fourier transform that relax the forbidden nature of the radiative electron-hole recombination. The binding energy of the indirect exciton is high in BN. It was measured to be about 130 meV [11], which means that electron and hole are strongly interacting and that a weak and localized surface perturbation may break the selection rule without significantly altering the value of this binding energy. This having been accepted, the question of the orientation of the electron-hole dipole arises, which we have targeted to solve. We have thus performed polarization-resolved PL measurements, for a Poynting vector $\vec{\omega}$ orthogonal to the c -axis with a much longer acquisition time (the integration time of each PL spectrum is 50 minutes) than for the polarization-resolved PL measurements with Poynting vector $\vec{\omega}$ parallel to the c -axis (5 minutes for the integration time of the PL spectrum). Figure 3.11 (a) shows the polarization-resolved PL experiments presenting the iX line and ZO_1 phonon replica. We observe a strong dependence of the intensity of the iX line with the orientation of the polarizer, in addition to the one of the ZO_1 line as found when comparing the red and black spectra in this figure. For the emission polarization parallel to c -axis (figure.3.11(a) - red line) the ZO_1 phonon replica has a strong intensity, while the iX line is hardly observed with a weak intensity. Rotating the polarizer, the ZO_1 intensity decreases whereas the iX intensity increases as shown in a black line of figure 3.11(a). Figure 3.9(b) plots the intensities of iX and ZO_1 as a function of polarization angle (green and red spheres, respectively) together with their fits as presented in solid lines. We reach the maximum value of the intensity of ZO_1 for the emission polarizer along c -axis, whilst the iX line has a minimum intensity. The vice versa phenomenon is obtained for the emission polarization perpendicular to c -axis. We find again, the anti-correlation of the polarization dependence of the iX line and ZO_1 phonon replica proves that the dipole

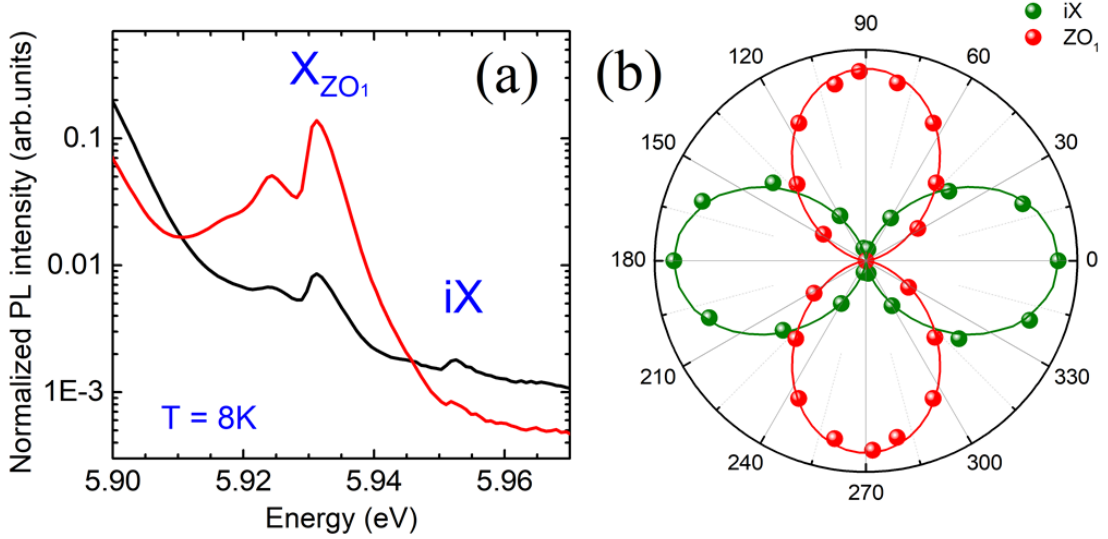


Figure 3.11: (a) Polarization-resolved photoluminescence spectroscopy in bulk BN at 8K for a Poynting vector $\vec{\omega}$ perpendicular to c-axis in the energy range of the fundamental indirect exciton iX around 5.95 eV. (b) Photoluminescence signal intensity of the ZO_1 phonon replica and iX line as a function of polarization angle, for a Poynting vector $\vec{\omega}$ perpendicular to c-axis.

of the fundamental indirect exciton is predominantly aligned in the layer plane.

Since BN is an anisotropic material, there is a strong contrast between the in-plane covalent binding and the inter-layer vdW coupling. The anti-correlation shown in 3.11 proves that the exciton dipole lies in layer plan, as expected from the strong binding in the layer plane.

In conclusion, we have succeeded in the challenging measurements of the polarization-dependence of the iX emission intensity giving the result for the dipole of the exciton in a predominant in-plane orientation.

3.3 Fine structure of phonon-assisted transitions in BN

3.3.1 The origin of the fine structure of phonon-assisted transitions

We reproduce our PL spectrum in a linear scale as shown in figure 3.12. There are five emission lines at 5.76, 5.79, 5.86, 5.89 and 5.93 respectively, corresponding to LO_3 , TO_2/TO_3 , LA/LO_1 , TA/TO_1 , and ZO_1 phonon replicas. We remark that the intensities of the LO_3 and TO_2/TO_3 optical phonon replicas are higher than the remains phonon ones because of the larger electron-phonon coupling for these modes [24]. As discussed in the previous section, the intensity of the ZO_1 phonon replica is very weak because it is

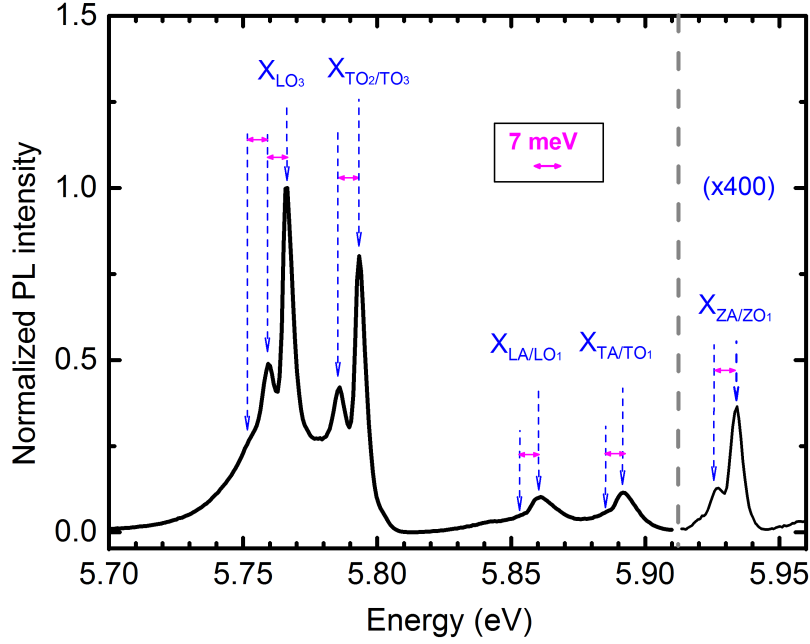


Figure 3.12: Photoluminescence spectrum of BN at 8K in linear scale.

forbidden due to selection rules. Therefore, it is multiplied by factor 400 in this figure for a better visibility. Besides five identified phonon replicas, we also obtain additional PL emission lines sitting at the low-energy side of each phonon replica. Specially, these PL lines are found to be shifted toward lower energy by a value of around 7 meV (pink arrows in figure 3.12). In general, the phonon replicas together with the additional PL lines have the same multiplet structure giving a fine structure of the PL spectrum in BN. In particular, there are three identical doublet structures for LO_3 , TO_2/TO_3 and ZO_1 phonon replicas while it is hardly observable for the other ones. This phenomenon relates directly to the phonon group velocities that will be discussed in details later. We note that the energy splitting between these emission lines (~ 7 meV) exactly matches the energy of the Raman active mode at low energy (E_{2g}^{low}) at the zone center which corresponds to the shear movement of boron and nitrogen atoms between adjacent planes as discussed in chapter 1, page 27. We will prove later that these additional PL lines arise from this interlayer shear mode.

The origin of the fine structure of BN can be interpreted simply from figure 3.13 which presents the schematic of the phonon-assisted recombination process. BN is an indirect bandgap semiconductor, so in the recombination process, we need phonon emission

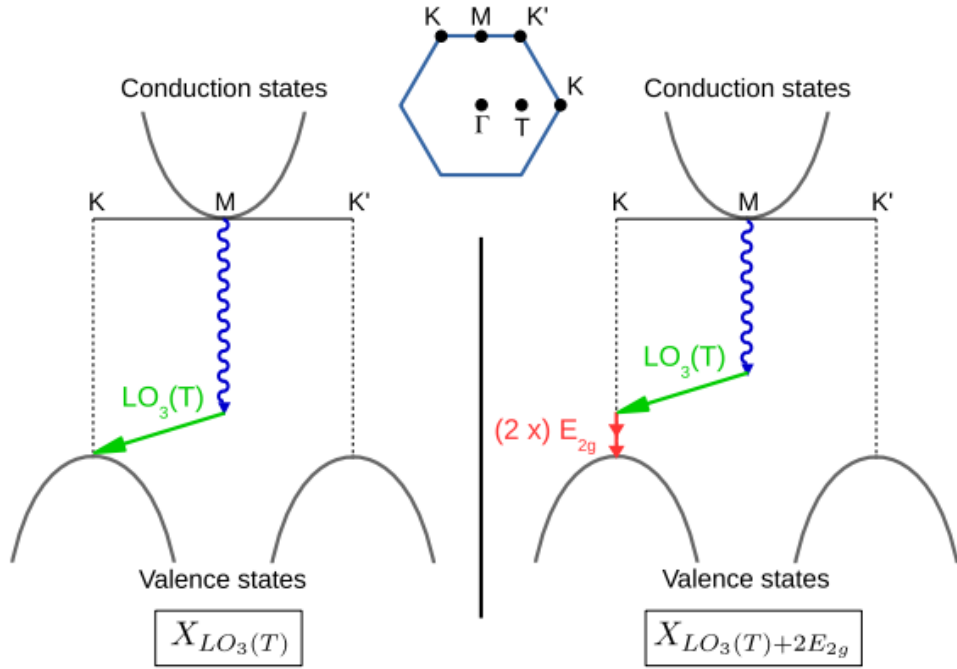


Figure 3.13: Schematic representations, in the single-particle picture of the electronic band structure, of the phonon-assisted recombination processes of the LO_3 line (left part), and of the LO_3+2E_{2g} one (right part).

(green arrow) due to the momentum conservation, in addition to a photon emission (blue arrow). This process is presented in the left side of figure 3.13.

In the right side of this figure, we show a different process with the contribution of another phonon (red arrows) in addition to the phonon and photon emitted previously (figure 3.13, left side). These phonons sit at the center of BZ without modifying the momentum balance, thus many of these phonons can be emitted in addition to the one at the T point, which is mandatory for the conservation of \mathbf{k} .

Therefore, the origin of the fine structure of the phonon-assisted transitions in BN would derive from the phonon replicas (at T point) combined with overtones of the interlayer shear mode (at zone center). The splitting between these overtones is small (about 6.8 meV) and independent of the phonon replica under consideration. What changes is the strong (or weak) contrast between the fundamental phonon replica and its overtones. The origin of the varying contrast will be quantitatively correlated to the values of the group velocity at the T point. This will be detailed further in this section. We will first demonstrate the origin by presenting our theoretical model for the PL spectrum of BN. We will show you later the overtones of the interlayer shear mode up to six phonons

and the relation between the phonon group velocity with the full width half maximum (FWHM).

3.3.2 Theoretical model for PL spectrum

a. Emission spectrum profile

On the basis of Ref.[11], the emission spectrum used in our theoretical model can be written:

$$H_{m,n}(E) = \rho(E - E_{m,n})(E - E_{m,n})e^{-\frac{E - E_{m,n}}{k_B T}} F \quad (3.3)$$

where the energy $E_{m,n}$ is given by $E_{m,n} = E_{iX} - E_m - nE_{2g}^{low}$ with E_{iX} the indirect exciton energy, E_m the energy of phonon-assisted recombination at T point of BZ ($m = LO_3, TO_2/TO_3, LA/LO_1, TA/TO_1, \text{ and } ZO_1$, respectively) and n is the number of the overtones of the interlayer shear mode E_{2g}^{low} .

The first term, ρ is the **joint density of state** which is proportional to the square root of energy for indirect transitions following Elliot [54] with the equation:

$$\rho(E - E_{m,n}) = \left(\frac{2M_n}{\hbar^2} \right)^{\frac{3}{2}} \sqrt{E - E_{m,n}} \quad (3.4)$$

where M_n is the reduced mass.

The second term $e^{-\frac{E - E_{m,n}}{k_B T}}$ comes from our assumption of a full thermal equilibrium and nondegenerate conditions, since we have the relation between the transition probability of emission (W_{emi}) and absorption (W_{abs}) [55, 56]i:

$$W_{emi} = W_{abs} e^{-\frac{E - E_{m,n}}{k_B T}} \quad (3.5)$$

The last term F is a **form factor** that depends on the exciton-phonon matrix element. According to Ref.[11] the matrix element of exciton-phonon interaction depends on two terms. The first one is the nature of phonon and its coupling for instance: piezo-electric coupling and deformation potential for acoustic phonon or Fröhlich interaction for optical phonon. The second one describes the dependence with phonon wave vector of the exciton-phonon matrix element (called form factor). This dependence is usually neglected in other semiconductors but it plays an important role for the interpretation of the optical response of BN because BN is a peculiar indirect bandgap semiconductor with the

extrema of both valence and conduction bands sitting away from the center of BZ. This form factor is written:

$$F(E - E_{m,n}) = \frac{1}{\left(4 + a^2 \left(k_T + \frac{E - E_{m,n}}{\hbar v_g^m}\right)^2\right)^4} \quad (3.6)$$

where a is the Bohr radius, k_T is the phonon wave vector at T point, \hbar is the reduced Planck's constant, v_g^m is phonon group velocity of the m phonon branch around T points. From equation 3.6, there are two quantities we would like to stress here:

- First, there is a cut-off phonon wave-vector (q_c) which is given by the inverse of the Bohr radius ($q_c \sim \frac{1}{a}$). It impacts the emission profile through the modified rate of phonon-assisted emission. It means that, for phonon-assisted recombination in semiconductors with a phonon wave-vector larger than q_c , the emission intensity varies rapidly with \mathbf{k} leading to the appearance of a peak in the spectrum. As far as BN is concerned, we have the phonon wave vector $k_T = \Gamma K/2 = 0.87 \cdot 10^{-10} m^{-1}$ while the Bohr radius was estimated at $a = 3 \text{ \AA}$ according to Ref. [11]. Therefore, BN has a low q_c due to $k_T > \frac{1}{a}$ and it is possible to observe sharp peaks in the emission profile of this semiconductor as pointed out in Ref.[11], and in contrast to all other indirect semiconductors studied.
- Second, one has to pay attention to the phonon group velocity defined as the speed of propagation of energy along a specific direction, which can be calculated following the equation:

$$v_g = \frac{\partial w}{\partial k} \quad (3.7)$$

Because the extrema of the valence and conduction bands of BN sit at K and M of BZ, the involved phonons are at T point of BZ in the recombination processs (chapter 1). Therefore, we have to take into account phonon group velocity in the form factor of BN as presented in equation 3.6. In case of other indirect semiconductors such as diamond, silicon, germanium that have a maximum of valence band sitting at zone center and the minimum of conduction band around high symmetry point of BZ, the phonon-assisted recombination involve phonons located around the same high symmetry points, thus their group velocity is zero.

The values of phonon group velocities were calculated together with the phonon

energy of modes at T point of BZ by Cusco *et al.* [39]. Their result is shown in table 3.1 below:

Phonon type	Phonon energy at T point of BZ (meV)	Group velocities v_g ($10^4 m s^{-1}$)
ZA	20	0.57
ZO ₁	21.7	0.43
TA	64.6	1.08
TO ₁	65.1	1.1
LO ₁	94.3	1.29
LA	94.4	1.27
TO ₂	162.6	0.18
TO ₃	162.7	0.17
LO ₃	185.4	0.57
LO ₂	179	0.365
ZO ₃	85	0.362
ZO ₂	76	0.3

Table 3.1: Phonon energy and group velocities of phonon modes at T point of BZ.

The fit of our spectra was performed step by step by increasing the complexity of the model. We present here our model in four cases by focusing on LO₃ and TO₂/TO₃ phonon replicas because of the larger visibility of the multiple structure in these phonon replicas. For all the calculated profiles, we take $a = 3\text{\AA}$, $k_T = 0.87 \cdot 10^{-10} m^{-1}$. For the Boltzmann distribution in equation 3.3, we take for T an effective electronic temperature of 50K, following our analysis of the incomplete thermalization of the excitonic gas with the lattice at a sample temperature of 10K [11].

b. The comparison of the models in four cases

- **Case (a): no additional broadening**

The equation used for reproducing our data reads:

$$I(E) = \sum_m \sum_{n=0} A_n^m H_{m,n}(E) \quad (3.8)$$

where A_n^m is a fitting parameter corresponding to the amplitude of the $H_{m,n}(E)$ line. The number of interlayer shear modes n is $n = 0 \mapsto 6$ for LO_3 phonon replica and $n = 0 \mapsto 3$ for TO_2/TO_3 one. Because the energy splitting of $LO_3 - TO_2/TO_3$ is 27 meV while the energy of the interlayer shear mode is 6-7 meV, there is an overlap between the low-energy tail of TO_2/TO_3 phonon replica with high energy of LO_3 phonon replica (figure 3.12), thus explaining the lower value of n for TO_2/TO_3 phonon replica.

The result of the first model is presented in figure 3.14(a) in pink solid line. We obtain an ensemble of the peaks for $H_{m,n}(E)$ components. The two high-intensity peaks (X_m components) correspond to the LO_3 and TO_2/TO_3 phonon replicas while the other ones with lower intensities ($X_{m+n}E_{2g}^{low}$ components) arise from the overtones of the interlayer shear modes. As seen in this figure, these peaks are too sharp compared to the experimental data even in the case $n=0$. Consequently, this model gives a poor agreement with the experimental data, meaning we have to switch to a second one. We remark however that the line-width of LO_3 phonon replica is larger than the one of TO_2/TO_3 phonon replica that relates to their group velocities ($v_g^{LO_3} > v_g^{TO_2/TO_3}$). When we enhance the group velocity, the form factor varies, the line-width of the phonon replica increases. We can say that the larger the phonon group velocity, the larger the line-width of the phonon replica.

- **Case (b): constant Gaussian broadening**

We try to improve the result of case (a) by doing the convolution of this emission spectrum with a Gaussian function. The theoretical emission spectrum is:

$$I(E) = \left(\sum_m \sum_{n=0} A_n^m H_{m,n}(E) \right) \otimes G_0(E) \quad (3.9)$$

where the Gaussian function is given by:

$$G_0(E) = \exp\left(-\frac{E^2}{\sigma_0^2}\right) \quad (3.10)$$

In this approximation, we kept the same amplitudes A_n^m as in case (a), and the width of the Gaussian function $\sigma_0 = 2$ meV. Such a value leads to a full width at half maximum (FWHM) of the Gaussian function $G_0(E)$ of $\Delta = 2\sqrt{\ln 2}\sigma_0 = 3.3$ meV. We

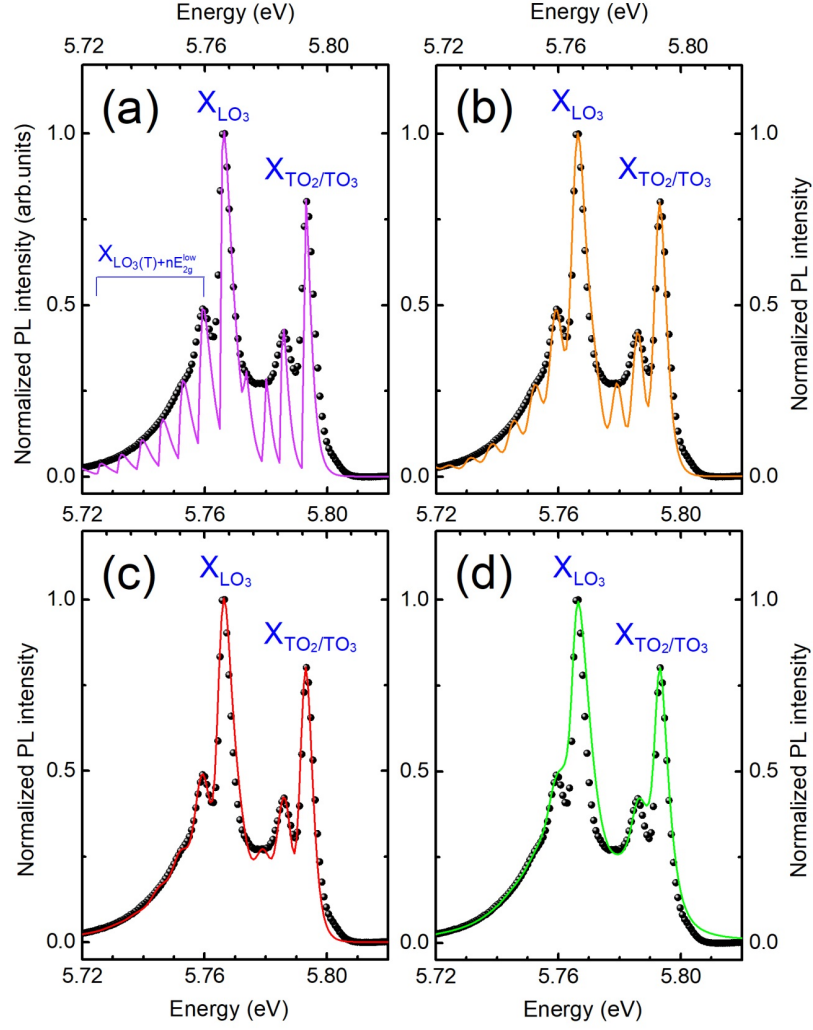


Figure 3.14: Experimental data (symbols) and fit (solid line) of the phonon-assisted emission spectrum in BN: (a) without any linebroadening, (b) with a Gaussian broadening identical for each overtone, (c) with a Gaussian cumulative broadening, and (d) with a Lorentzian cumulative broadening.

note that this width of the Gaussian function is fixed and is totally independent on the number of the interlayer shear modes.

The result is shown in figure 3.14 (b) in orange solid line. Similarly to case (a), we observe the peaks for the $H_{m,n}(E)$ components but these peaks are not as sharp as the ones in the previous case presented in figure 3.14 (a). Specifically, our theoretical model leads to a doublet structure for X_{LO_3} and $X_{LO_3+E_{2g}^{low}}$ components in good agreement with the prominent doublet structure measured for the LO_3 phonon replica. However, the first overtones appear too sharp for the TO_2/TO_3 phonon replica. Moreover, increasing the number of the interlayer shear modes, the

$X_{m+nE_{2g}^{low}}$ components provide too sharp peaks again. On the whole, this model gives a better agreement with the experiments compared to the previous case especially for case $n = 0$, but it is still not good enough for the interpretation of the fine structure observed in PL spectrum of BN.

- **Case (c): cumulative Gaussian broadening**

The theoretical emission spectrum in this case differs from case (b) because the width of the Gaussian function increases with the index n . The theoretical model in case (c) reads:

$$I(E) = \sum_m \sum_{n=0} A_n^m H_{m,n}(E) \otimes G_n(E) \quad (3.11)$$

where the amplitudes A_n^m were kept the same as in case (a) and the Gaussian function is:

$$G_n(E) = \exp\left(-\frac{E^2}{\sigma_n^2}\right) \quad (3.12)$$

with $\sigma_n^2 = (n + 1)\sigma_0^2$ and $\sigma_0 = 2$ meV was kept the same as for the previous case. σ_n was taken with the assumption of a cumulative Gaussian broadening that means the linewidth of $H_{m,n}(E)$ component increases with the number of interlayer shear mode n . This is the only different point between this cumulative Gaussian broadening case and the case of the constant Gaussian broadening. As far as the Gaussian function is concerned, the convolution of two Gaussian functions of widths σ_1 and σ_2 is a Gaussian with a width $\sqrt{\sigma_1^2 + \sigma_2^2}$. In case (b) of identical broadening processes, the linewidth of the $X_{m+nE_{2g}^{low}}$ components (overtones) is the same as the one of the phonon-replicas (which varies with each phonon-replica according to the group velocities). In the present case relying on adding each linewidth squared and then taking the square of the sum, we expect the enhancement of the linewidth of the overtones to lead to a better result.

The corresponding theoretical spectrum provides an excellent agreement with our experimental data as seen in figure 3.14 (c) in red solid line. The model exactly matches not only for the prominent doublet structure but also for the low-energy side of the phonon replicas. Because the linewidth of the $H_{m,n}(E)$ component increases with n , instead of the sharp peaks in previous cases, we obtain broader ones, especially for high index n providing an excellent agreement with the data. The larger the index n , the broader the line of the $X_{m+nE_{2g}^{low}}$ components, as seen

for the peaks at 5.766, 5.759 eV and the shoulder at 5.751 and 5.747 eV. We note that these linewidths increase approximately linearly with the number of the interlayer shear modes. This effect was predicted by Krummheuer *et al.* [57] and the observation of such effect was also reported, on ZnO by Sahoo *et al.* [58] and CdS by Schreder *et al.* [59].

In summary, by taking the assumption of a cumulative Gaussian broadening, this model gives the best fit for the PL spectrum of BN compared to the case (a) and case (b). Before showing the fit of the full spectrum using this model, we will present another case in order to get more insight.

- **Case (d): cumulative Lorentzian broadening**

The last case is given by the equation below where the convolution is taken with the Lorentzian function.

$$I(E) = \sum_m \sum_{n=0} A_n^m H_{m,n}(E) \otimes L_n(E) \quad (3.13)$$

where the amplitude A_n^m were kept the same as the previous cases and the Lorentzian function reads:

$$L_n(E) = \frac{(\Gamma_n/2)^2}{E^2 + (\Gamma_n/2)^2} \quad (3.14)$$

with $\Gamma_n = (n + 1)\Gamma_0$, and the value of $\Gamma_0 = 3.3$ meV leads to the same FWHM as the Gaussian function for the X_m components. Unlike the Gaussian function, the convolution of two Lorentzian functions of widths Γ_1 and Γ_2 has a width $\Gamma_1 + \Gamma_2$.

Figure 3.14(d) shows in green solid line the result of this case with a global degradation of the data fitting. In particular, for case of $n = 0$ and $n = 1$, we completely lost the two prominent doublet structure arising from the X_m and $X_{m+E_{2g}^{low}}$ components. Still, the contribution of higher-order components provide a good fit as in case (c), as can be seen in this figure on the low-energy side of LO_3 and TO_2/TO_3 phonon replicas. This theoretical model as the whole gives a poorer agreement with the experimental data compared to case (c). It raises the question of the physical mechanisms underlying the Gaussian and Lorentzian profiles for the fit of the phonon-assisted broadening that will be discussed in the next section.

c. Fit of the full spectrum

The best model (case c) is presented again, but for the full PL spectrum of BN (excluding the ZO_3 phonon replica) as shown in solid line in figure 3.15 together with the experimental data (black sphere). We stress again that our model uses only one parameter which is phonon group velocity arising from the nature of each phonon replica. We obtain an excellent fit not only for the two LO_3 , LA/LO_1 phonon replicas (as displayed above), but also for the two remaining TO_2/TO_3 , TA/TO_1 ones. Moreover, we present two fits of the weak PL emission line at 5.93 eV, taking the group velocity of the ZA phonon (green solid line) and the ZO_1 phonon (red solid line) (figure 3.15 (b)) for the purpose of further confirming the origin of this PL line. As seen in figure 3.15 (b), the linewidth of the green solid line is larger than the one of the red solid line due to $v_g^{ZA} > v_g^{ZO_1}$ [39], thus reducing the agreement with the data by taking v_g^{ZA} compared to $v_g^{ZO_1}$. We conclude that the fit taking the ZO_1 group velocity provides a better result compared to the other one, further confirming our discussion above, where the PL line at 5.93 eV was assigned to the phonon replica involving ZO_1 phonon mode at T point in BZ.

Now, we comment the LA/LO_1 and TA/TO_1 phonon replicas where the prominent doublet structure are not observed clearly. As seen in figure 3.15, there is the an excel-

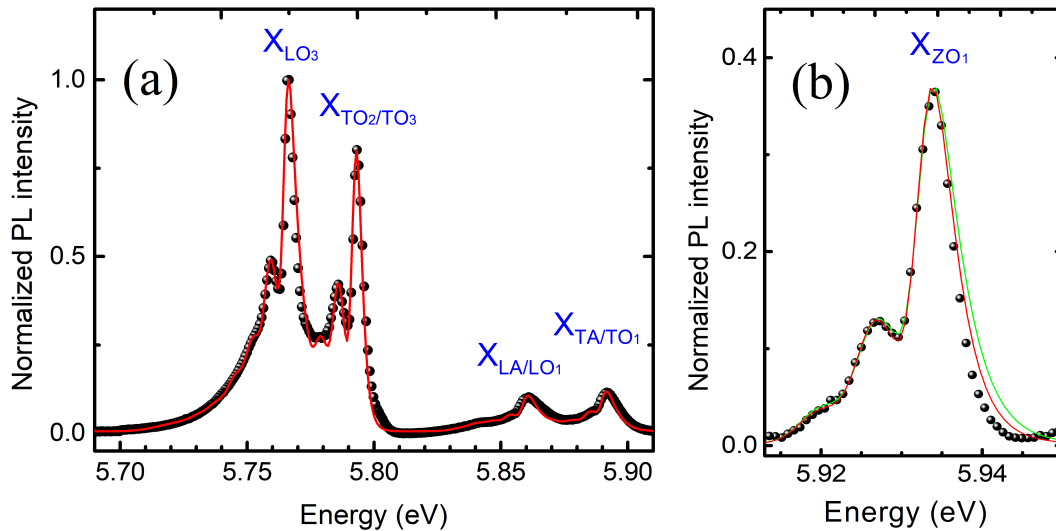


Figure 3.15: Photoluminescence spectrum in HQ Graphene BN in the deep ultraviolet under two-photon excitation at 3.03 eV, at 8 K. Experimental data are displayed in symbols, theoretical fit in solid line: (a) LO_3 , LA/LO_1 , TO_2/TO_3 , TA/TO_1 phonon replicas; (b) ZO_1 phonon replica.

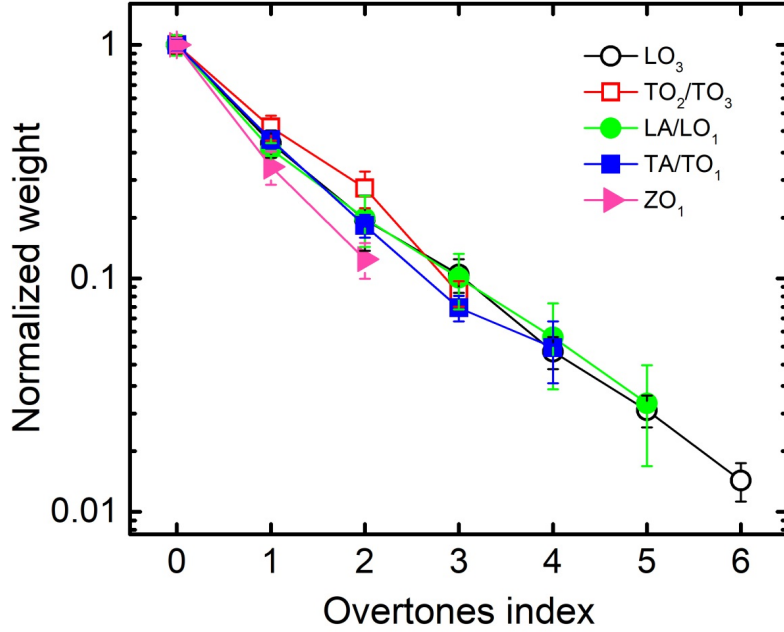


Figure 3.16: Normalized weight A of the overtones of the interlayer shear modes used in figure 3.15, as a function of overtone index n .

lent agreement between the X_m components and the data. The broader linewidth comes from the larger group velocity of LA/LO₁ and TA/TO₁ phonon replicas (Table 3.1). This makes the doublet structure of these two phonon replicas hardly observable. This observation supports the impact of the phonon group velocity on the linewidth of the phonon replicas as mentioned before. Therefore, the visibility of the fine structure of the phonon replicas varies as a function of the phonon group velocity.

Figure 3.16 displays the amplitude of each component of the phonon replicas as a function of the number of the interlayer shear mode n in semilog scale. We take $n = (0:6), (0:5), (0:4), (0:3), (0:2)$ for LO₃, LA/LO₁, TO₂/TO₃, TA/TO₁, ZO₁, respectively. We observe an exponential decrease of the amplitude A_n^m with the index n whatever the phonon nature m as seen in the figure 3.16. As expected, the higher the order of the electron-phonon interaction process, the smaller its probability. A quantitative interpretation of the decrease of the amplitude with index n would give a direct insight into the physics of the electron-phonon coupling in BN.

In conclusion, our theoretical model reveals the peculiar origin of the fine structure of the PL spectrum in BN. Among that, the group velocity plays a vital role directly controlling the line-width of the phonon replicas. The larger the phonon group velocity, the

broader the line of the phonon replica. The comparison between our model and the data provides a detailed insight into the origin of the fine structure of phonon replicas in BN as well as it raises a new question about the different profile between the two Gaussian and Lorentzian functions. We will discuss this in the next section.

3.4 Exciton-phonon interaction in a strong coupling regime

3.4.1 Comparison between Gaussian and Lorentzian functions

The optical response of solid state systems is affected by two kinds of broadening, which are described in terms of homogeneous and inhomogeneous broadenings. The first one is dynamically broadened by rapid variations in the amplitude, phase, or orientation of dipoles that can come from carrier-carrier interactions, electron-phonon coupling, and spectral diffusion. In contrast, the second one reflects a static distribution of resonance frequencies, and the width of the line represents the distribution of frequencies, which arise, for instance, from disorder, extended or point defects, and more generally any inhomogeneity in the sample structure.

The different line-shape of each kind of broadening leads to different function for line-shape fitting. Homogeneous broadening is usually considered to be characterized by a Lorentzian line profile, whereas inhomogeneous broadening by more complex distribution functions, the most generic one being the Gaussian statistics.

However, even in the case of a purely homogeneously-broadened or purely inhomogeneously broadened system, the line profile is not necessarily a Lorentzian or Gaussian functions, some system can be described by two of them, for instance, spectral diffusion [60]. This process can be described by Gaussian or Lorentzian profile as limiting form for the correlation function through the product of the spectral fluctuation amplitude Δ and fluctuation correlation time τ . If $\Delta\tau \ll 1$ that corresponds to the fast modulation, limit the optical response takes a Lorentzian profile. This is called the motional narrowing and it is commonly observed in nuclear magnetic resonance, for example. On the contrary, if $\Delta\tau \gg 1$, the modulation is slow, and the optical response takes a Gaussian profile.

We thus conclude that the Gaussian broadening leading to the best description of the emission spectrum in BN can be of homogeneous nature as the result of an intrinsic interaction process, namely the electron-phonon coupling in BN. In this part, we will

demonstrate the strong coupling regime in BN case with two evidences that are the excitonic line-shape and the temperature dependence of linewidth.

In fact, the same phenomenology applies to the phonon-assisted broadening, as discussed by Toyozawa in Ref.[61]. Theoretical predictions of Toyozawa demonstrated that there are two regimes for exciton-phonon interaction with different temperature-dependence of the exciton line and width. The first one is called weak coupling regime: it occurs when the exciton-phonon interaction is weak, the effective mass of exciton is small or the temperature is not too high. In this regime, the line-shape of exciton is Lorentzian and its line-width increases linearly with temperature due to the motional narrowing. On the contrary, the second regime is called strong coupling regime, describing a strong interaction between exciton and phonon, a large exciton effective mass, and a high temperature. The excitonic lineshape of this regime is Gaussian and its line-width is proportional to the square root of temperature.

3.4.2 Excitonic absorption line-shape of BN

The first evidence for the strong coupling regime of the exciton-phonon interaction is the Gaussian profile that we already presented at low temperature in the previous section. The comparison between Gaussian and Lorentzian functions in our fits of the PL spectrum at low temperature (8K) was displayed in figure 3.14. As discussed above, with the same FWHM for the $n = 0$ component, the fit using a Lorentzian function does not lead to good agreement with experimented data because of the slow decay of Lorentzian wings, smearing the doublet structure at low temperature (figure 3.14 (c and d)).

More generally, we show in figure 3.17 (black spheres) the PL spectrum of BN at high temperature where the LO_3 - TO_2 / TO_3 splitting due to longitudinal and transverse phonons is now hardly observable. The comparison of Gaussian and Lorentzian functions is also presented in red and green solid lines in this figure. We obtain a better fit when using Gaussian function (figure 3.17(a)) while, the broad emission bands centered at 5.77 decay too rapidly to be accounted for by a Lorentzian function (figure 3.17(b)).

By comparing Gaussian and Lorentzian functions in our model at low and high temperatures, we demonstrate that the PL spectrum of BN has a Gaussian nature that is the first signature for the strong-coupling regime of the exciton-phonon interaction following Toyozawa's theory.

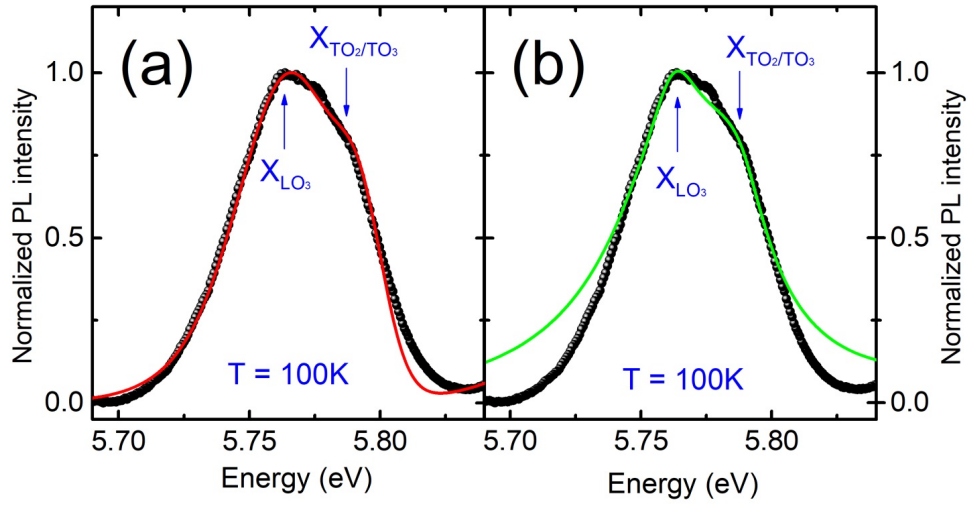


Figure 3.17: PL spectrum at 100K and the fits using two functions in a model: (a) Gaussian function, (b): Lorentzian function

3.4.3 Temperature dependence of vibrational line-width

The second evidence for the strong-coupling regime of the exciton-phonon interaction relies on the temperature-dependent line-width. We have thus performed temperature-dependent photoluminescence from 8K to 300K as shown in figure 3.18 (black spheres) where a few temperatures are selected. On raising the temperature, the line-width of the phonon replicas as well as their overtones increases leading to a reduced visibility of the doublet fine-structure of LO_3 and TO_2/TO_3 phonon replicas. Specifically, above 20K this doublet is hardly observed and it disappears above 60K, indicating that the line-width is larger than the doublet splitting energy of 6-7 meV. Above 100K, the line-width becomes larger than the splitting energy of 27 meV between LO_3 and TO_2/TO_3 phonon replicas (figure 3.12), we cannot thus easily distinguish the two pairs of phonon replicas LO_3 - TO_2/TO_3 and LA/LO_1 - TA/TO_1 . From 100K up to 300K, the shape of the BN spectrum does not change so much and the enhanced line-width of phonon-assisted emission lines increases more slowly with temperature.

The different increase of the line-width at low temperature ($T < 60K$) and high temperature ($T > 100K$) suggests a non-linear dependence of the line-width with temperature, as expected for a strong coupling regime of the exciton-phonon interaction with the square root dependence of linewidth on temperature in Toyozawa's theory.

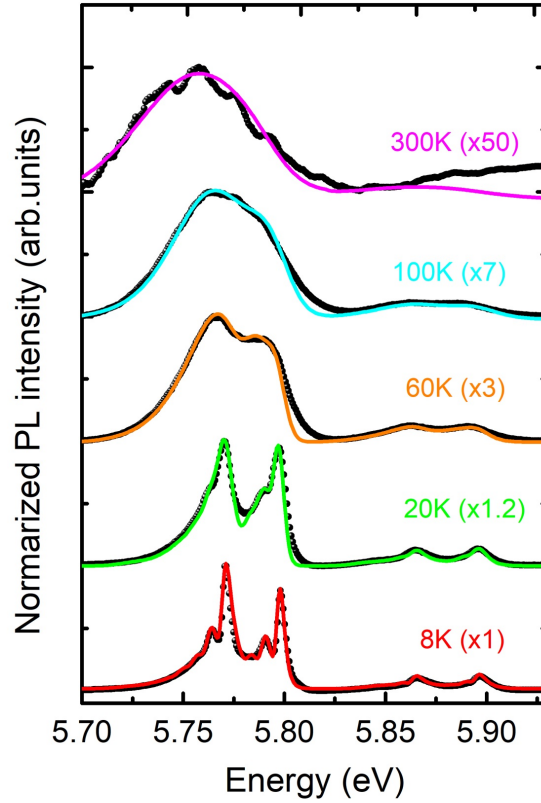


Figure 3.18: Temperature dependence of the PL spectrum in BN as a function of temperature, from 8 to 300 K under an excitation of 6.3 eV: experimental data (symbols); theoretical fit (solid line)

We now go further by a quantitative analysis of the phonon replicas broadening.

To do that, **first**, we fit all the spectra using the theoretical model presented in the previous section. The results are shown in solid line in figure 3.18 with an excellent agreement with the experimental data. For each fit of the PL spectrum, the only varying parameter is the FWHM (Δ) that is obtained by varying σ_0 in the Gaussian function (equation 3.14). Increasing the temperature, σ_0 is larger, thus the FWHM is larger following the equation $\Delta = 2\sqrt{\ln 2}\sigma_0$.

Second, from these fits, we extract the variations of the parameter Δ and plot them as a function of temperature. The result is presented in figure 3.19 as a black sphere. As seen in this plot, the temperature dependence is not as straightforward as a pure square root of T broadening revealing several contributions in the phonon-assisted broadening.

As far as the scattering processes are concerned, there are scatterings by impurities and

scattering by phonons (both acoustic and optical phonons). The scattering by acoustic phonon is nearly elastic (quasi-elastic) scattering because of the small energy transfer involved, whilst the scattering by optical phonon is inelastic [24]. The scattering by impurities, which is elastic scattering is not mentioned here because of the high quality of the samples and also because this scattering does not depend on temperature. In the phonon-assisted broadening processes of BN, both acoustic and optical phonon scatterings exist depending on which terms of these scatterings dominate. According to Cardona [24], at low temperature ($T < 50\text{K}$), the optical phonon scattering processes are negligible because the thermal occupation factor of optical phonon is low, thus the phonon-assisted broadening is dominated by acoustic phonon scattering. On the contrary, when the temperature is higher, the thermal energy is high enough to allow efficient optical phonon absorption, leading to be dominated by inelastic scattering.

The theoretical fits corresponding to the strong and weak coupling regimes for the temperature dependence of the phonon replicas broadening is shown in figure 3.19. First, we discuss the fit in the weak coupling regime using the standard equation taken from Ref.[62]:

$$\Gamma = \Gamma_0 + aT + \frac{b}{e^{\frac{E_0}{k_B T}} - 1} \quad (3.15)$$

with k_B is Boltzmann constant, a, b are the strength of the coupling to phonons, E_0 is the optical phonon energy.

The first term Γ_0 in equation 3.15 corresponds to the scattering by impurities and/or radiative broadening. The second term is broadening due to the acoustic phonon scattering. The last term is broadening arising from optical phonon scattering that is proportional to the Bose-Einstein function for the optical phonon. When the temperature is low, this term is small and can be neglected. The broadening increases linearly with temperature with the contribution of acoustic phonon scattering. The best fit for this regime is shown in the green dashed line in figure 3.19 giving a poor agreement with the data for temperature above 100K. We find $a = 0.1 \pm 0.02\text{meV/K}$, $b = 150 \pm 80\text{meV}$ and $E_0 = 25 \pm 10\text{meV}$. The large discrepancy between this fit and our data supports our assertion before, and it demonstrates that the exciton-phonon interaction is not in the weak coupling regime in BN.

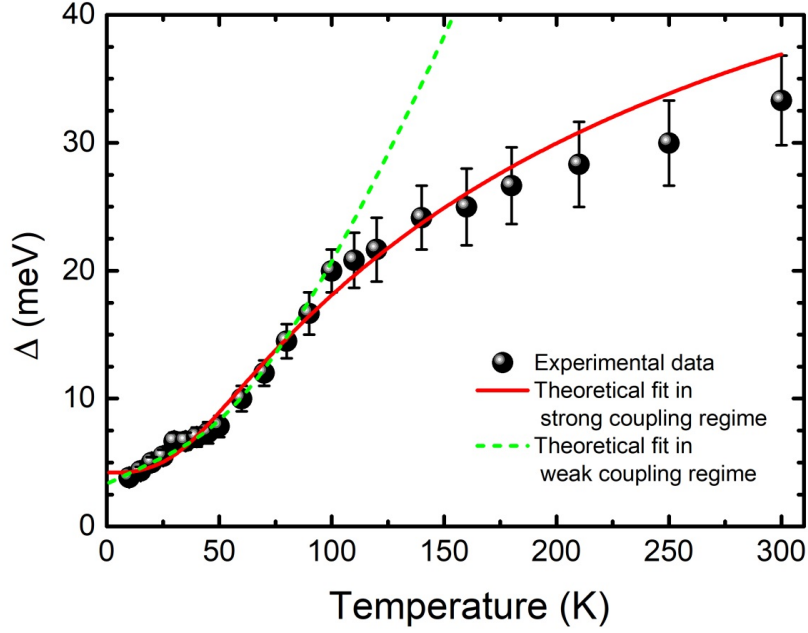


Figure 3.19: Temperature dependence of the full width at half maximum of the phonon replicas, estimated from the quantitative interpretation performed in figure 3.18: experimental data (symbols); theoretical fit in the strong-coupling regime (red solid line), or in the weak-coupling regime (dashed green line).

Now, we discuss the fit in the strong coupling regime where the equation is given by [24, 63]:

$$\Delta = \sqrt{\Delta_A^2 + \Delta_O^2} = \sqrt{(S_A E_A \coth(\frac{E_A}{2k_B T}))^2 + (S_O E_O \frac{b}{e^{\frac{E_O}{k_B T}}})^2} \quad (3.16)$$

Similarly to the fit in the weak coupling regime, we have here the first term Δ_A and the second term Δ_O due to the broadening by acoustic and phonon optical phonon scatterings. Among that, S_A and S_O are the strength of the coupling to phonons, E_A and E_O are the acoustic and optical phonon energies, respectively.

In the red solid line of figure 3.19, we reach an excellent agreement with our data by taking $E_A = 4 \pm 2$ meV, $S_A = 4.5 \pm 1.5$ meV, $E_O = 15 \pm 5$ meV, and $S_O = 65 \pm 8$ meV. This is an additional proof for the strong coupling regime of the exciton-phonon interaction in BN.

At low temperature ($T < 50$ K) the quasi-elastic scattering is dominating with the acoustic phonon energy of $E_A = 4 \pm 2$ meV that corresponds to the mean energy of the acoustic phonon mode ZA which has A_{2u} symmetry at the center of the BZ. It means that the origin of this broadening at low temperature derives from the ZA mode at center of BZ. We

stress that there is no offset term in equation 3.16, equivalent to the Γ_0 term for Lorentzian lines. Here, the finite value of the linewidth at low temperature arises from Δ_A itself because of the quasielastic nature of the scattering processes involving ZA phonons.

As far as the high temperature regime ($T > 50\text{K}$) is concerned, the inelastic scattering is dominating by the optical phonon energy of $E_O = 15 \pm 5 \text{ meV}$. This estimation exactly matches the energy of the silent mode at low energy ZO_1 with B_{1g} symmetry at the zone center, thus proving the contribution of this optical phonon mode to the broadening of phonon replicas at high temperature. We remark that both ZA and ZO_1 are out-of-plane phonon modes (chapter 1) with the atomic displacement in the c-axis direction. It would mean that the van der Waals structure of BN has a strong influence on the phonon-assisted broadening below 300K.

Studying the temperature-dependent PL measurements of HQ Graphene sample from 8K to 300K, gives the second evidence for the strong-coupling regime of the exciton-phonon interaction. The square root dependence of line-width with temperature was obtained as in Toyozawa's theory of this regime. By fitting our data, we interpreted the temperature dependence of the line-width on the basis of quasi-elastic scattering by acoustic phonons, and inelastic scattering by absorption of optical phonons corresponding to the ZA and ZO_1 phonon modes in BN.

3.5 Conclusions.

Based on the previous results of BN published by our group [11, 64], in this chapter, we go further to elucidate the fundamental optical properties of BN by performing the PL spectroscopy in the two samples (NIMS and HQ Graphene).

First, we have performed the polarization-resolved PL measurements for the two experimental configurations of the large NIMS sample.

- The different PL signals, including phonon replicas involving the phonon modes at T point of BZ because of the indirect band-gap semiconductor [11, 30, 33], were observed in the two cases of Poynting vector $\vec{\omega}$ parallel or perpendicular to the c-axis due to the selection rules. In particular, in case of Poynting vector $\vec{\omega}$ parallel to the c-axis, four main emission lines that correspond to the phonon replicas LO_3 , TO_2/TO_3 , LA/LO_1 , TA/TO_1 were recorded. Furthermore, their intensity do not

change when rotating the linear polarizer. On the contrast, in the case of Poynting vector $\vec{\omega}$ perpendicular to the c-axis, in addition to four phonon replicas, ZO_1 phonon replica at 5.93 eV were also observed. Moreover, there is a strong dependence of the intensity of phonon replicas with the polarizer angle. The intensities ratio of LA/ LO_1 and ZO_1 changes from 200 to 5 when rotating a linear polarizer. These results demonstrate the impact of the phonon symmetries on the optical emission spectrum in bulk BN.

- Besides the phonon replicas mentioned above, the ZO_3 phonon replica at 5.87 eV, which has the same B_{1g} symmetry as the ZO_1 phonon replica, was obtained by subtracting the two different PL spectra in case of a Poynting vector $\vec{\omega}$ perpendicular to the c-axis. This ZO_3 phonon replica was confirmed by the comparison between the phonon dispersion relations [39] with our PL spectrum, giving a comprehensive understanding of the phonon replicas in h-BN, and further pointing out the originality of the optical properties in this layered compound where the extrema of the conduction and valence bands lie in different high symmetry points which are both away from the zone center.
- Outstandingly, we have succeeded in the challenging measurements of the polarization-dependence of the forbidden indirect exciton emission intensity giving the orientation of the dipole of the exciton in a predominantly in-plane orientation. As a matter of fact, the results obtained by mean of polarization-resolved PL spectroscopy provides a strong confirmation, and a definite proof for the indirect nature of the bandgap in h-BN that was investigated in Ref.[11].

Second, we have demonstrated that the origin of the fine structure of the PL spectrum in BN arises from overtones of interlayer shear modes in the phonon-assisted emission spectrum of h-BN. These lattice vibrations are specific to layered compounds since they correspond to the shear rigid motion between adjacent layers, with a characteristic energy of about 6.8 ± 0.5 meV in h-BN at 8 K. Our theoretical model, based on calculations of the phonon energy and group velocity at T points of the Brillouin zone, reveals that the differences observed for the various phonon replicas in h-BN only come from the variations of the phonon group velocity at T points of the Brillouin zone. The larger the phonon group velocity, the broader the line of the phonon replica. An excellent fit of the

multiplet observed in each phonon replica is obtained by taking the assumption of a cumulative Gaussian broadening. The comparison between our model and the data raises a new question about the different profile between the two Gaussian and Lorentzian functions.

Third, following the theoretical predictions of Toyozawa of the line-shape of the exciton absorption band [61], we have brought the two evidences for the strong-coupling regime of the exciton-phonon interaction in h-BN, that had never been previously observed since the paper of Toyozawa. The first evidence comes from the comparison between Gaussian and Lorentzian functions in the fits of the PL spectrum at low temperature (8 K) as well as at high temperature. The excellent fit obtained with the Gaussian profile suggests that the exciton-phonon interaction is in the strong coupling regime in BN [61]. The second evidence was observed by performing the temperature-dependent PL measurements from 8K to 300K. We obtain the square root dependence of the line-width with temperature as in Toyozawa's theory for the strong-coupling regime. By fitting our data, we interpreted the temperature dependence of the line-width on the basis of quasi-elastic scattering by acoustic phonons, and inelastic scattering by absorption of optical phonons corresponding to the ZA and ZO₁ phonon modes in h-BN. The strong-coupling regime and the bright emission in this indirect band-gap semiconductor are unusual properties, calling for a microscopic understanding of the exciton-phonon coupling in this van der Waals crystal with fascinating properties.

Chapter 4

Isotope engineering in boron nitride

Isotopes were discovered in the previous century by Soddy [65], and in the same year Thomson [66] confirmed it. According to them, isotopes of a given element have the same number of electrons, but their different numbers of neutrons lead to difference atomic mass and nuclear spin. Following this discovery, the number of researches on isotopes in different materials rapidly increased in addition to the developing of methods for separating isotopes. Many applications of isotopes of different materials have been used, such as for diagnostic purpose in the pharmaceutical and biomedical industries, for military during the World War II, and etc. Among them, it is worth to mention the studies of the modification in the reaction rate of a chemical reaction when one of the atoms in the reactants is replaced by one of its isotopes. This phenomenon is well-known as the **kinetic isotope effect** [67, 68].

As a matter of fact, due to isotopes, the electronic and optical properties of the semiconductors change dramatically, for instance, the lattice parameter, thermal conductivity, the phonon frequency or the linewidth, and the electronic bandgap. These variations were investigated in the series of special papers through the works of many materials such as Ge [69], Diamond [70, 71], Si [72, 73], ZnSe [74]. Manuel Cardona is a major contributor to the field of studies with isotopically controlled semiconductors in recent years. Two famous papers of his group [75, 76] bring a comprehensive understanding about the isotope effect on the optical spectra of the semiconductor and they are a guideline for our study which will be presented in this chapter.

As far as BN is concerned, we know that boron nitride in nature (^{Na}BN) makes up about 20 at% ^{10}B , 80 at% ^{11}B and 99.6 at% ^{14}N and it is also one of many materials with high

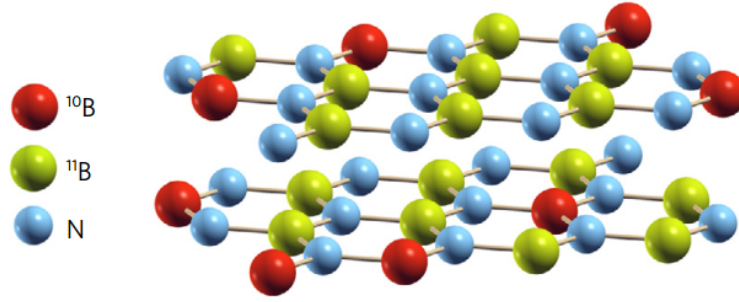


Figure 4.1: Honeycomb lattice in natural boron nitride (^{Na}BN) showing the isotopic mixture of boron-10 (red) and boron-11 (green) atoms bound to nitrogen-14 (blue)

potential for application. For example, the ^{10}B and ^{11}B isotopes are strong and weak thermal neutron absorbers respectively, hence ^{10}B has many applications in nuclear energy industries [12] and cancer treatment by boron neutron capture therapy [13].

Based on these publications, in this chapter, we are going to discuss the isotope effect in BN by performing the Raman and PL measurements of three controlled boron isotopic samples ^{10}BN , ^{Na}BN and ^{11}BN (KSU samples) that are synthesized in KSU using high-purity elemental boron nitride of 99.2 at% ^{10}B and 99.4 at% ^{11}B by the Ni-Cr flux method as presented in detail in chapter 2. The schematic of natural BN is shown in figure 4.1.

The variation in the isotope of boron leads to the variation in the boron mass and also of the reduced mass of BN that is calculated by the equation 4.1 below:

$$\frac{1}{\mu} = \frac{1}{10(1-x) + 11x} + \frac{1}{14} \quad (4.1)$$

where μ is the reduced mass, x the ^{11}B -concentration, and $(1-x)$ the ^{10}B -concentration. The calculations of the reduced masses of three controlled boron isotopic samples (^{10}BN , ^{Na}BN and ^{11}BN) are shown in table 4.1. The difference in the reduced mass of three KSU samples due to isotope of boron contributes to the modification of the optical properties

Samples	^{10}BN	^{Na}BN	^{11}BN
Boron Isotopes	99.2% at ^{10}B	20% at ^{10}B and 80% at ^{11}B	99.4% at ^{11}B
Nitrogen Isotopes	99.6% at ^{14}N	99.6% at ^{14}N	99.6% at ^{14}N
Reduced mass (amu)	5.834	6.0975	6.1728

Table 4.1: Isotopes concentration of boron and nitrogen ^{10}BN , ^{Na}BN , and ^{11}BN together with their reduced mass.

of BN that will be discussed in details later.

In our work, we focus on the conspicuous effects of the isotope that are: (i) the dependence of the phonon frequencies and the linewidths with the isotopic composition; (ii) renormalization of the energy of the electronic states through the electron-phonon interaction. Furthermore, we will discuss the influence of the isotope on the weak van der Waals (vdW) interactions in this material. That will be obtained by analyzing the temperature dependence results of the shear and breathing modes of the adjacent layers.

4.1 Isotope effect on the optical properties of BN

4.1.1 Phonon energy

We have performed the Raman scattering measurements in the back-scattering configuration from the c-face of ^{10}BN , $^{\text{Na}}\text{BN}$ and ^{11}BN samples at room temperature. The results are shown in figure 4.2. We observe three Raman lines at 168.2 meV (1357 cm^{-1}) for ^{11}BN (red line), 169.3 meV (1365.6 cm^{-1}) for $^{\text{Na}}\text{BN}$ (green line) and 172.5 meV (1392 cm^{-1}) for ^{10}BN (blue line). The Raman peak at 169 meV of $^{\text{Na}}\text{BN}$ corresponds to the Raman-active mode at high energy (E_{2g}^{high}). This mode presented in chapter 1, page 27 correspond to an in-plane direction of the movement of the boron and nitrogen atoms; its observation was reported in many publications [18, 20, 36, 39, 77] with the energy value of 169.8 meV at low temperature. The Raman peaks in ^{10}BN and ^{11}BN display a shift of 3.8 meV at higher energy for ^{10}BN and 1.1 meV at lower energy for ^{11}BN .

According to Cardona [76], the frequency of a given phonon corresponding to the wavevector \mathbf{k} and branch i is given by:

$$\omega = \sqrt{\frac{f(\mathbf{k}, i)}{\mu}} \sim \mu^{-1/2} \quad (4.2)$$

where ω is the frequency of phonon, $f(\mathbf{k}, i)$ a restoring force constant, and μ the reduced mass.

Therefore, the frequency of the phonon is proportional to the reduced mass, like $\mu^{-1/2}$. It means that the smaller the reduced mass, the higher the frequency of the phonon. As shown in table 4.1, the reduced mass of ^{11}BN is larger than the one of $^{\text{Na}}\text{BN}$, there is thus a shift of the Raman line to the lower energy. An opposite phenomenon is observed in

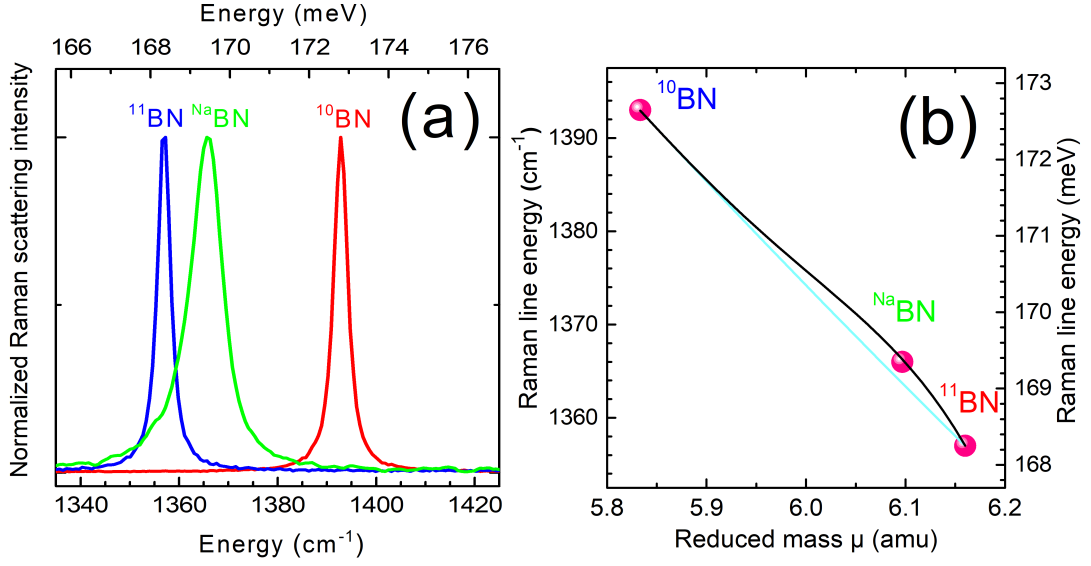


Figure 4.2: (a) Raman scattering spectra in ¹⁰B_N, ^{Na}B_N and ¹¹B_N, at room temperature. (b) Raman mode energy vs reduced mass μ in BN: $\mu^{-1/2}$ mass dependence in the virtual crystal approximation (dashed line), energy shift due to isotopic mass disorder + $\mu^{-1/2}$ mass dependence (solid line).

¹⁰B_N whose reduced mass is smaller than the one of ^{Na}B_N, so the Raman peak shifts to the higher energy. The equation 4.1 can be used to estimate the shift of the phonon energy when varying isotope.

The energy of the Raman-active optical phonon (E_{2g}^{high}) of ¹⁰B_N, ^{Na}B_N and ¹¹B_N is plotted as a function of the reduced mass in BN as shown in figure 4.2 (b) (pink spheres), in addition to the two fits presented in black and cyan solid lines.

The first fit (cyan solid line in figure 4.2 (b)) reproduces the mass dependence as $\mu^{-1/2}$ in the Virtual Crystal Approximation (VCA), including a small ad hoc correction of $1.5x$ cm⁻¹ to account for the in-plane lattice contraction, as in Ref.[26]. Specifically, the equation used for this fit is written:

$$\omega = \omega_{\alpha} \sqrt{\frac{\mu_{\alpha}}{\mu}} + 1.5x \quad (4.3)$$

where ω is the frequency of phonon, μ the reduced mass, x the ¹¹B-concentration, and α indicates the isotopic composition.

As seen in figure 4.2 (b), the fit does not give a good agreement with our data. In particular, the phonon energy of ^{Na}B_N shifts toward a higher energy of around 2.5 cm⁻¹ compared to the dashed line making a 'parabolic bowing'. Consequently, the dependence of the phonon energy of the isotopic samples with the reduced mass is not well

reproduced by VCA plus the ad hoc correction.

The 'bowing' is attributed to a mass disorder-induced self-energy arising from the elastic scattering of phonons. This phenomenon was interpreted in several studies such as Hass *et al.* [78], Gobel *et al.* [74], and Cardona *et al.* [75]. As their explanation, the isotopic mixture leads to mass disorder that breaks the translational invariance. Therefore, the crystal momentum does not need to be strictly conserved leading to the elastic scattering of phonons. This isotope disorder induced self energy has real and imaginary parts. While the real part is the energy shift, the imaginary part is the linewidth broadening. Both of them display the same variations as a function of mass disorder.

To illumine this phenomenon in our isotopic samples, we thus switch to the second fit presented in black solid line in figure 4.2(b). Compared to the first one, we take into account the energy shift due to static isotopic mass disorder, which expression is taken proportional to the simple form of the scattering rate given in [75]. The fitting equation now reads:

$$\omega = \omega_{\alpha} \sqrt{\frac{\mu_{\alpha}}{\mu}} + 1.5x + \Lambda x(1-x) \left(\frac{11x + 10(1-x) - 10}{10} \right)^2 \quad (4.4)$$

where Λ is a characteristic energy giving the amplitude of the shift due to mass disorder. We obtain a fair agreement with our experimental data for $\Lambda = 2500$ meV. This value leads to a maximum energy shift of 2.5 cm^{-1} (0.3 meV). By adding the contribution of the mass disorder effect in our fit, the dependence of the phonon energy of the isotopically pure samples with the reduced mass is well reproduce, proving the impact of the mass disorder on the frequency of phonons in BN.

The mass disorder effects become even more pronounced when we consider the full width at half maximum (FWHM) of these Raman lines. We now come back to figure 4.2 (a). We remark that the FWHM of the isotopically pure samples ^{11}BN and ^{10}BN is around 3.2 cm^{-1} while it is 7.2 cm^{-1} in $^{\text{Na}}\text{BN}$. This broadening of the Raman line in $^{\text{Na}}\text{BN}$ comes from a mass disorder-induced self-energy. We stress that our samples have the same growth conditions, thus the difference in the linewidths of these Raman lines due to the defects is negligible. In particular of BN, there is 3 cm^{-1} broadening of the Raman linewidth in $^{\text{Na}}\text{BN}$ that can be comparable to the energy shift of $^{\text{Na}}\text{BN}$ obtained from the fit as presented before.

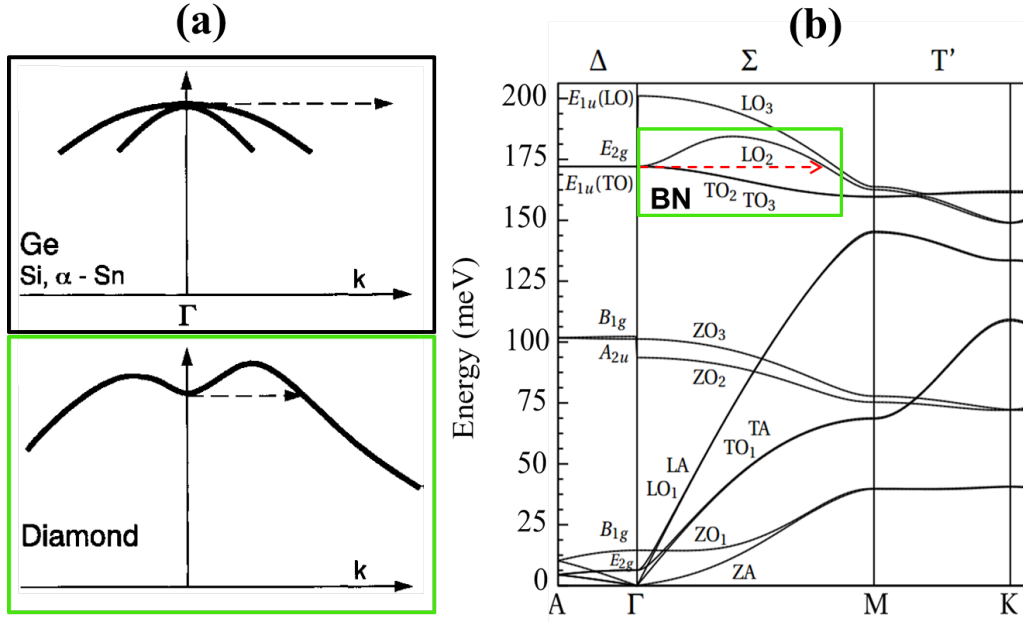


Figure 4.3: Schematic diagrams of the optical dispersion relation in Si, Ge, diamond [76], compared to phonon dispersion relation of BN [39].

As far as other semiconductors are concerned, there is the same phenomenon in diamond but not in Ge, Si or α -Sn. It means that the isotopic disorder does not significantly affect the linewidth of Raman line in Ge, Si or α -Sn, while it plays an important role in the variation of the linewidth of Raman line in Diamond or BN. The reason for this is the difference of the phonon dispersion relations in materials where the highest phonon energy is at zone center for Ge, Si, and α -Sn, but it is away from the center of BZ for Diamond and BN. To illustrate for that, we show the schematic diagrams of the optical dispersion relation in Si, Ge, diamond [75, 76], compared to phonon dispersion relation of BN [39] in figure 4.3. We can see the contrast between the curvature of the dispersion relations of diamond and Si, Ge: one is concave while the other one is convex at zone center of BZ (figure 4.3(a)). In case of the E_{2g}^h mode of BN, its curvature of the phonon dispersion relations is similar to the case of diamond (figure 4.3(b)). Therefore, the elastic scattering process (is represented in dashed lines in figure 4.3) induced by the isotopic mass disorder is allowed in case of diamond and BN, but not in case of Si or Ge (no final state for such process) [75, 76].

In conclusion, by performing Raman measurements, we observe the dependence of the phonon energy with the reduced mass of BN. The lower the reduced mass, the higher the phonon energy. Besides this effect, there is the impact of the isotopic mass disorder

displaying an energy shift and a line-width broadening of ^{Na}BN compared to isotopically pure BN (^{11}BN and ^{10}BN).

4.1.2 Electronic bandgap

Besides the vibrational excitations, the isotope mass also impacts the electronic properties because of the electron-phonon interaction. A well-known effect concerns the zero-point renormalization of the bandgap. The electronic states are renormalized to second order in the phonon amplitude u because of the so-called Fan and Debye-Waller terms in second-order perturbation theory, but also because of anharmonic terms responsible for thermal expansion in first-order perturbation. At zero temperature, the bandgap energy eventually depends on the zero-point vibrations $\langle u^2 \rangle$, the average value being calculated over all phonon modes. The renormalization of the bandgap at low temperature is thus a true quantum effect related to the zero-point vibrations. Since the renormalization energy δE_g scales as $\mu^{-1/2}$, isotopic substitution changes the bandgap of a semiconductor at low temperature, as demonstrated for instance in silicon, germanium and diamond [75]. This phenomenon was investigated in our isotopically purified BN crystals by PL spectroscopy. This phenomenon was investigated in our isotopically purified BN crystals by PL spectroscopy.

The photoluminescence spectra of ^{10}BN , ^{Na}BN and ^{11}BN at 8K are shown in figure 4.4 in a linear scale. For each sample, we observe PL lines corresponding to the phonon-assisted recombination LO_3 , TO_2/TO_3 , LA/LO_1 , TA/TO_1 and ZO_1 . The ZO_1 phonon replica at 5.93 eV is only observable in log scale because of its weak intensity. As seen in this figure, there are energy shifts in the PL spectra of the isotopically pure samples (^{10}BN and ^{11}BN) compared to ^{Na}BN . In particular, the PL spectrum is red-shifted for ^{10}BN (red line), while it is blue-shifted for ^{11}BN (blue line) compared to ^{Na}BN .

Because the PL spectrum consists of phonon-assisted recombination lines, the energy of the emitted photon is given by:

$$h\nu = E_{iX} - E_p \quad (4.5)$$

where $h\nu$ is the energy of the emitted photons, E_{iX} the indirect exciton bandgap energy and E_p the phonon energy.

The first term E_{iX} in the equation 4.5 is the indirect exciton bandgap energy. Accord-

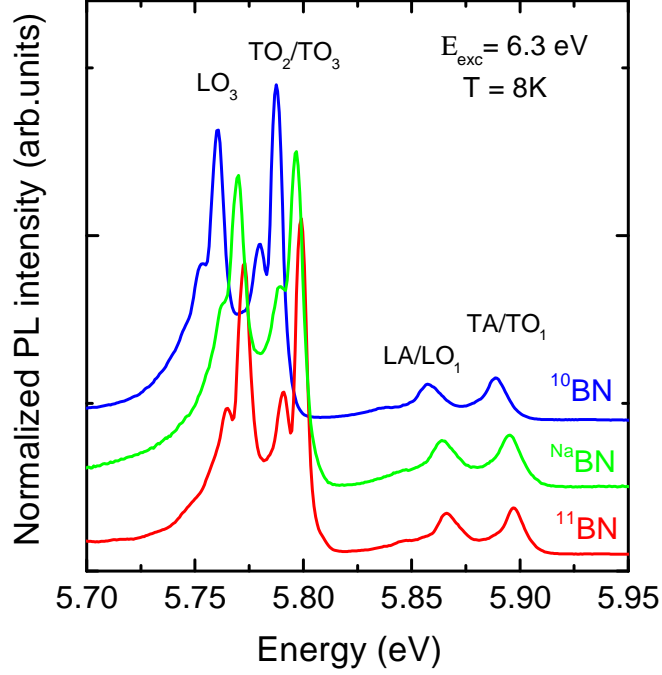


Figure 4.4: Photoluminescence spectra for ^{10}BN , ^{Na}BN and ^{11}BN at 8K under excitation at 6.3 eV.

ing to Cardona and Thewalt [75], the bandgap varies with reduced mass, like $-\mu^{-1/2}$. It means the larger the reduced mass, the lower the renormalization of the bandgap.

The second term E_p in equation 4.5 is the phonon energy that roughly depends on the reduced mass, like $\mu^{-1/2}$, as discussed in the previous section. The larger the reduced mass, the lower the phonon energy, the lower the phonon detuning energy and thus the higher the energy of the phonon replicas (chapter 3). When decreasing the mass, the energy of phonon increases, the energy of phonon replica shifts thus toward a higher energy and vice versa.

We remark that the two terms in the equation 4.5 have a same sign, the two contributions to the energy shift of PL spectra thus go in the same direction.

Moreover, the lower the energy of the phonon replicas, the higher the splitting among ^{11}BN , ^{Na}BN , and ^{10}BN . For example, the red-shift energies of four phonon replicas LO_3 , TO_2/TO_3 , LA/LO_1 and TA/TO_1 in ^{10}BN are 90, 80, 50 and 30 meV, respectively, compared to the ones in ^{Na}BN . A similar observation is in ^{11}BN , but it is in blue-shift. This effect is the result of the isotope mass dependence of the phonon energy as discussed above. Since the absolute isotopic shift of a phonon mode increases with its energy, the

splitting of the phonon replicas is more pronounced for the emission lines lying at lower energy.

Consequently, a global red-shift from ^{11}BN to ^{10}BN is observed in the PL spectra of the our BN samples because the electronic bandgap renormalization and the phonon energy, both depend on the boron isotope mass.

We will now go further for analyzing these two contributions.

We plot in figure 4.5 (a) the energy of the phonon replica at 8K of ^{10}BN , $^{\text{Na}}\text{BN}$, and ^{11}BN versus the phonon energy at T point of the BZ that are calculated by Cuscó *et al.* [39] (^{10}BN , $^{\text{Na}}\text{BN}$ and ^{11}BN are presented in red, green and blue, respectively). The shift in the x direction in this figure (called horizontal shift) relates to the isotope dependence of the phonon energy (second term in equation 4.5). This horizontal shift is observed more clearly for LO_3 and TO_2/TO_3 phonon modes because of their higher phonon energy. On the other hand, there is also a shift in the y direction (called vertical shift) that relates to the electric bandgap renormalization.

We present the linear fit of our data in solid lines in figure 4.5 (a) using the equation 4.5 taking an isotope-dependent bandgap energy E_{iX}^α , where α indicates the isotopic composition. Equation 4.5 now is rewritten:

$$h\nu = E_{iX}^\alpha - E_p \quad (4.6)$$

with $E_{iX}^\alpha = E_g + \delta E_g^\alpha - E_b$, where E_g is the single-particle bandgap, E_b the exciton binding energy and δE_g^α the band-gap renormalization due to zero-point fluctuations [75].

In our fit, we take the isotope-dependent E_{iX}^α equal to 5.960, 5.9585, and 5.954 meV in ^{11}BN , $^{\text{Na}}\text{BN}$, and ^{10}BN , respectively. For better visibility, we present in figure 4.5(b) the energy shift of the phonon replicas in ^{10}BN (blue chart) and ^{11}BN (red chart) compared to $^{\text{Na}}\text{BN}$, after subtracting the isotopic shift of the corresponding phonon mode. As seen in this figure, all charts of ^{11}BN sit at higher energy while all charts of ^{10}BN sit at lower energy. The average values of the energy shift of the five types of phonon replicas are estimated to 1.6 ± 0.2 in ^{11}BN and -4.4 ± 0.2 in ^{10}BN compared to $^{\text{Na}}\text{BN}$, as shown by the dashed lines in figure 4.5(b). These values are precisely the variations of the bandgap renormalization δE_g with the isotope mass, namely $\delta E_g^{11} - \delta E_g^{\text{Na}} = 1.6 \pm 0.2$ meV and $\delta E_g^{10} - \delta E_g^{\text{Na}} = -4.4 \pm 0.2$ meV.

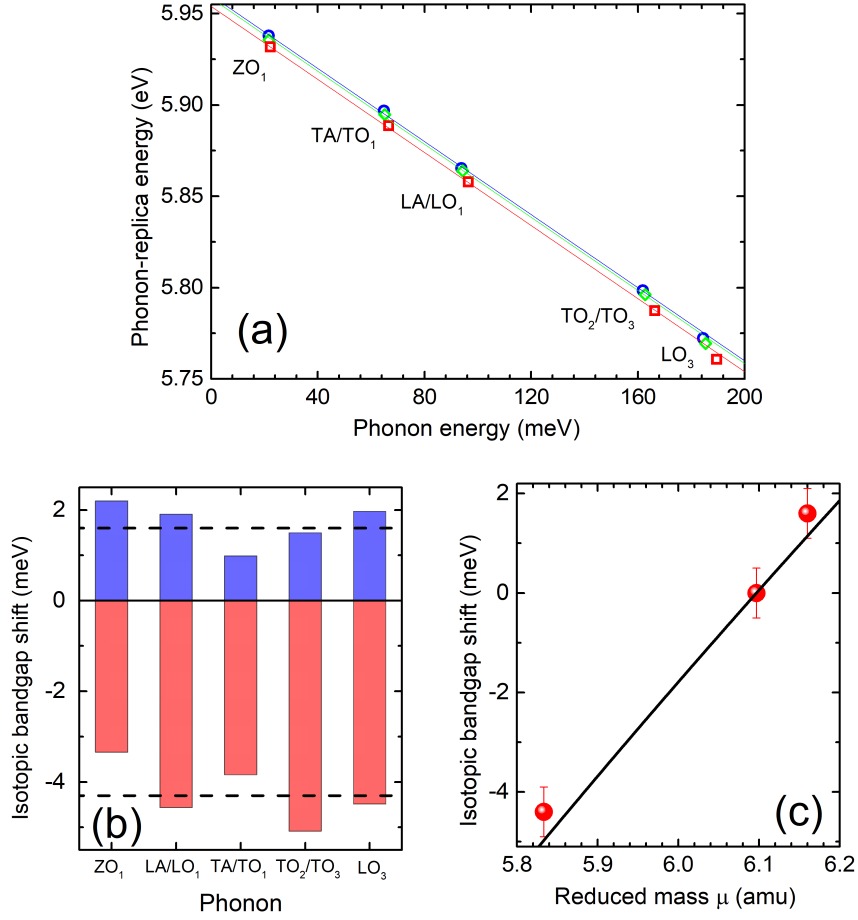


Figure 4.5: (a) Energy of phonon replicas versus calculated isotope-dependent phonon energy at 8K. (b) Energy shift of the phonon replica in ¹⁰BN (blue bars) and ¹¹BN (red bars) compared to ^{Na}BN, after subtraction of the isotopic shift of the phonon modes. (c) Isotopic dependence of bandgap renormalization.

In the purpose of an estimation of the band-gap renormalization, in figure 4.5(c), we plot the average values of the energy shifts discussed above as a function of the reduced mass (symbols). Since, the band-gap renormalization is proportional to $\mu^{-1/2}$ [75], it reads:

$$\delta E_g^\alpha = \delta E_g^{\text{Na}} \sqrt{\frac{\mu^\alpha}{\mu^{\text{Na}}}} \quad (4.7)$$

From equation 4.7, we can find that the variations of the band-gap renormalization compared to ^{Na}BN given by:

$$\delta E_g^\alpha - \delta E_g^{\text{Na}} = \delta E_g^{\text{Na}} \left(\sqrt{\frac{\mu^\alpha}{\mu^{\text{Na}}}} - 1 \right) \quad (4.8)$$

Equation 4.8 is used for the fit displayed in solid line in figure 4.5(c), with the only parameter being the bandgap renormalization in NaBN . We obtain a value $\delta E_g^{\text{Na}} = 225 \pm 10$ meV. Now, we are going to analyze the temperature dependence of the bandgap E_g .

As mentioned in the beginning of this section, at zero temperature, the renormalization of the electronic bandgap is proportional to the zero-point vibrations. While the zero-point renormalization energy δE_g involves all phonon modes, there is a phenomenological ansatz approximating the full phonon dispersion with a single Einstein oscillator of energy Ω . At high temperature ($k_B T \gg \hbar\Omega$), ΔE_g is linear in temperature reflecting the lattice expansion, according to Refs. [75, 76]. In contrast, at low temperature ($k_B T \ll \hbar\Omega$), ΔE_g deviates from the linear decrease of the bandgap by a quantity $-\delta E_g$, which is proportional to $\mu^{-1/2}$ that relates to the renormalization of the bandgap. Then, the temperature dependent of an interband gap energy can be written [75, 79]:

$$\Delta E_g(T) = -\delta E_g \left(1 + \frac{2}{e^{\hbar\Omega/k_B T} - 1} \right) \quad (4.9)$$

In figure 4.6, we display using red spheres the experimental data of the temperature dependent PL measurements from 10 to 800K, taken from Du *et al.* [80]. Fit in solid line, displayed in figure 4.6, using equation 4.9 presents the renormalization of the bandgap, while fit in dashed line is the extrapolation low temperature of the linear in T dependence found at high temperatures. Applying the value of the bandgap renormalization in NaBN ($\delta E_g^{\text{Na}} = 225$ meV), we obtain $\hbar\Omega = 68 \pm 2$ meV. Compared to the absolute maximum of the phonon dispersion of 200 meV in BN [39], we obtain a ratio of 0.34, significantly lower than the usual one-half found in cubic semiconductors [75]. Since the Einstein parameter Ω in layer BN is rather low, this indicates that the interlayer vibrations (which have lower energies than the intralayer ones) make a significant contribution to the electron-phonon bandgap renormalization. Still, one can not exclude that the acoustic phonons might play a more important role in layered compounds than in the cubic crystals discussed by Cardona and Thewalt [75]. The elucidation of this novel phenomenology will require microscopic calculations of the Einstein parameter Ω in the framework of the theoretical approaches developed in Refs. [81, 82].

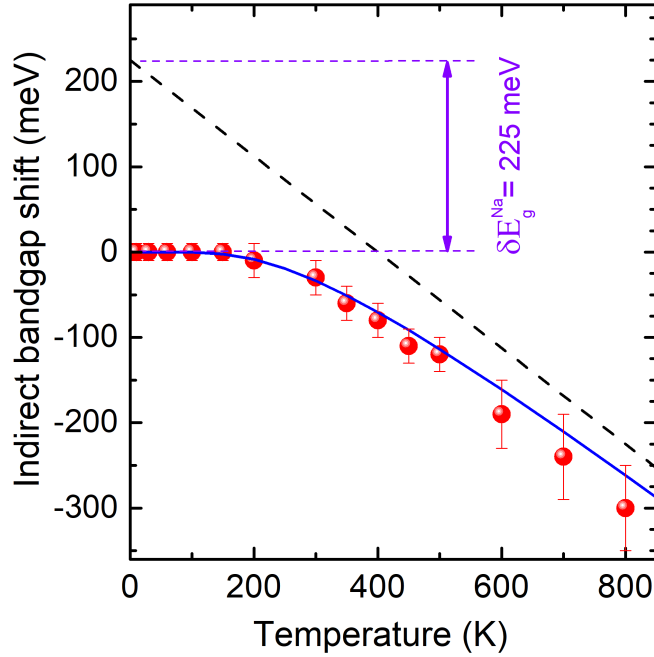


Figure 4.6: Temperature dependence of the indirect bandgap: data from Ref.[80] (symbols, where error bars indicate the standard deviations for least-squares fitting of the emission spectrum), single oscillator fit (solid line), and high-temperature asymptotic linear limit of the single oscillator fit (dashed line).

4.2 Influence of boron isotope on Van der Waals interactions

In the first section of this chapter, we discussed the impacts of isotope purification on the phonon energy as well as on the value of the band gap in BN. Besides these variations, we will see that the isotopes also impact the peculiar lattice vibrations of Van der Waals crystals that will be studied in this section by analyzing the temperature-dependent results of the shear and breathing modes between adjacent layers.

4.2.1 Interlayer shear mode

We first address the interlayer shear mode (E_{2g}^{low}). This mode was detailed in chapter 1, page 27 with the movements of boron and nitrogen atoms are in a different directions for adjacent planes and the energy of 6.8 meV (54cm^{-1}) at low temperature. *Therefore, this E_{2g}^{low} mode directly relates to vdW interaction because of the rigid movement of adjacent mode.*

Raman measurements with high-resolution have been performed for the E_{2g}^{low} at Institut Jaume Almera, Consejo Superior de Investigaciones Científicas (ICTJA-CSIC), Barcelona,

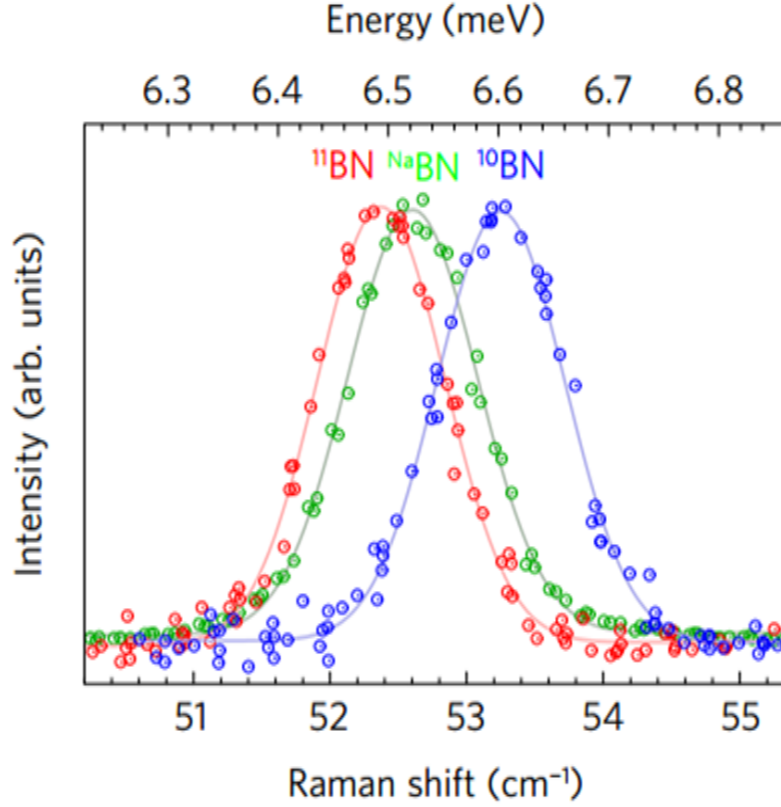


Figure 4.7: High-resolution Raman spectra for the E_{2g}^{low} interlayer shear mode in ^{11}BN , $^{\text{Na}}\text{BN}$ and ^{10}BN at 300K (taken in Institut Jaume Almera, Consejo Superior de Investigaciones Científicas, Barcelona by our colleagues).

Spain by our colleagues Prof. Cuscó and Prof. Artús. Figure 4.7 shows the Raman spectra at room temperature (RT) for ^{11}BN (red), $^{\text{Na}}\text{BN}$ (green), and ^{10}BN (blue) at energies of 6.49 meV (52.2 cm^{-1}), 6.51 meV (52.6 cm^{-1}), and 6.6 meV (53.3 cm^{-1}), respectively. These Raman lines correspond to the interlayer shear modes of the BN. Similar to the E_{2g}^{high} mode, we observe the E_{2g}^{low} phonon energy dependence with the reduced mass of the boron nitride, as $\mu^{-1/2}$. In particular, the energy of the interlayer shear mode in ^{10}BN shifts to the higher energy, whereas the one in ^{11}BN shifts to lower energy compared to the one in $^{\text{Na}}\text{BN}$. Generally, we have a global decrease of the interlayer shear mode energy from ^{10}BN to ^{11}BN due to increasing of the reduced mass.

The temperature-dependent Raman measurements have also been performed for the E_{2g}^{low} mode from 10K to 600K. The Raman line energy as the function of temperature is presented in figure 4.8 for ^{10}BN (red spheres), $^{\text{Na}}\text{BN}$ (green sphere), and ^{11}BN (red sphere). We first observe the red-shift of the energy of the interlayer shear mode in the three samples as the function of the temperature. This is due to the fact that the phonon

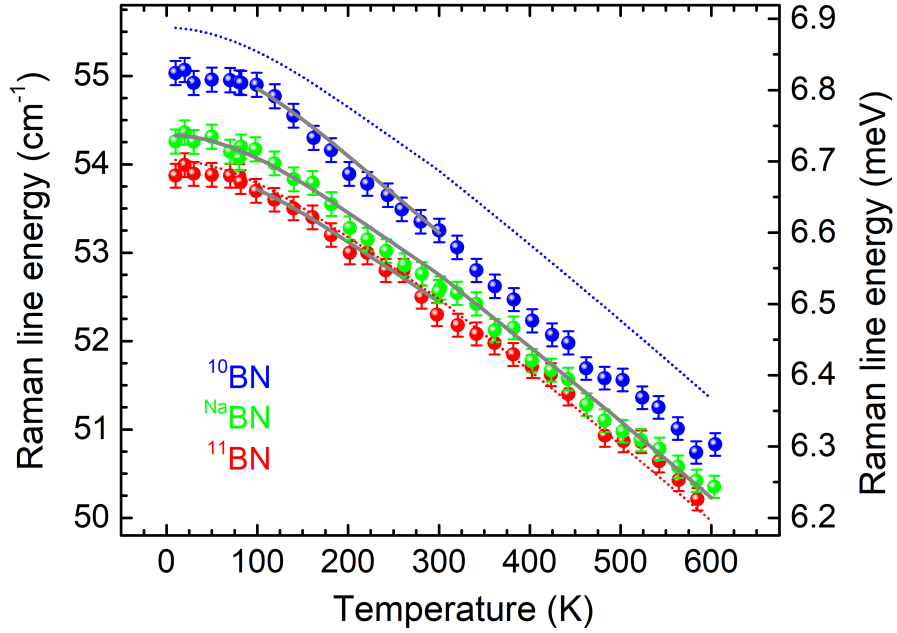


Figure 4.8: Temperature dependence of the frequency shift for the E_{2g}^{low} interlayer shear mode in ^{10}BN , $^{\text{Na}}\text{BN}$ and ^{11}BN : experimental data (symbols), fits with a $1/c^p$ power-law dependence of the E_{2g}^{low} interlayer shear mode energy with the c -lattice parameter (solid lines). The dotted lines correspond to a trivial mass scaling as $\mu^{-1/2}$ of the energy of the interlayer shear mode in $^{\text{Na}}\text{BN}$.

energy is proportional to an inverse of the lattice parameter which increases with temperature.

However, this red-shift does depend on the isotopic composition, with the highest (lowest) variations for ^{10}BN (^{11}BN). In particular, the energy splitting between ^{10}BN and $^{\text{Na}}\text{BN}$ at low temperature ($T < 150$ K) is larger than the one at high temperature ($T > 150$ K) as seen in figure 4.8. A similar phenomenon was observed in ^{11}BN .

To go further for the interpretation of this effect, it is meaningful to analyze the power-law dependence of the interlayer shear mode energy with the c -lattice parameter in our temperature-dependent measurements. The power law dependence was studied by Valentin N. Popov and Christian Van Alsenoy [83], using a tight-binding model with matrix elements derived within the density functional theory, in order to study the interplay between the repulsive interlayer band energy and the weak attractive vdW interactions. In their calculations, they found that two exponents of $n=3$ and 4 are the dominant contributions in graphite. To the best of our knowledge, a power-law dependence of the thermal shift of the interlayer shear mode in BN has never been addressed in the litera-

ture.

For that purpose, we fit our data using equation 4.10 below:

$$\omega(T) = \omega_0 \left(\frac{c_0}{c(T)} \right)^p \sim \frac{1}{c(T)^p} \quad (4.10)$$

where T is the temperature, ω the interlayer shear mode energy, ω_0 the interlayer shear mode for a lattice parameter c_0 , and p an exponent.

In case of ^{Na}BN , the thermal expansion along the c -axis of ^{Na}BN was studied between 10 and 600K by Yates *et al.* [84] and Paszkowicz *et al.* [85]. Following their results of the dependence of the c -lattice parameter on temperature, we obtain the best fit (gray solid line in figure 4.8) for the temperature dependence of the interlayer shear mode in ^{Na}BN with the p -exponent value of $p = 3.7 \pm 0.1$.

In case of ^{10}BN and ^{11}BN , the thermal expansion along the c -axis was studied between 125 and 275 K, by our colleague Dr. Arie Van der Lee, in the Institut Européen des Membranes (UMR-5635 CNRS) at Montpellier. The results have not a significant difference between the isotopically pure samples and the natural one [86]. Between 125 and 275K, we fit the thermal expansion along the c -axis with a linear regression $c(T) = c + aT$, where $a = 1.7$ and $2.3 \times 10^{-4} \text{ \AA}/K$ in ^{10}BN and ^{11}BN , respectively. Then, we apply these results for the fit of the temperature dependence of the interlayer shear mode in ^{10}BN and ^{11}BN as shown in gray solid lines in figure 4.8. Unfortunately, we have to restrict our analysis to the temperature range from 125 to 275K, so that the fits are not performed for the full temperature range (10 to 600K) as it is the case of ^{Na}BN . The best fits are obtained with $p = 3.6 \pm 0.3$ and $p = 5.7 \pm 0.3$ in ^{11}BN and ^{10}BN , respectively. The larger error value of ± 0.3 in ^{11}BN and ^{10}BN is due to the limited temperature range.

In ^{11}BN , the thermal shift of the interlayer shear mode is slightly smaller than in ^{Na}BN . It is in a good agreement with the p -exponent value of 3.6 estimated from our fits compared to the value of 3.7 in ^{Na}BN . In contrast, in ^{10}BN , the thermal shift of the interlayer shear mode is larger than in ^{Na}BN . The p -exponent in ^{10}BN ($p = 5.7$) that we obtain is indeed larger than the one in ^{Na}BN .

Comparing to Ref.[83], we find that the p -exponent in BN is approximately $n + 1$ in graphite. The explanation for this investigation is presented in **Appendix B**.

In summary, the p -exponent does present a striking dependence on the isotopic com-

position. The quantitative analysis of our measurements in isotopically-purified BN crystals concludes to a variation of the $1/c^p$ power-law dependence of the interlayer shear mode, with modifications of the p -exponent from one sample to another. While $p=3.6\pm 0.3$ in ^{11}BN , it increases to 5.7 ± 0.3 in ^{10}BN , as a result of the larger thermal red-shift observed in figure 4.8. This is the first indication that the weak, non-local vdW coupling varies with the isotopic composition.

4.2.2 Interlayer breathing mode

We now address the B_{1g} mode, which corresponds to the interlayer breathing mode. As mentioned in chapter 1, pages 28-29, this B_{1g} mode is an out-of plane mode with the boron and nitrogen atoms movement along the c -axis. Specifically, the boron and nitrogen atoms move in the same direction (c -axis) within a plane, but different directions in adjacent planes. Importantly, this interlayer breathing mode is also called a silent mode because it is not observably by symmetry neither in Raman nor in InfraRed spectroscopy, so that the direct investigation of this silent mode is not possible by optical spectroscopy [87]. The energy of the B_{1g} interlayer breathing mode (~ 15 meV) is higher than the one of the E_{2g}^{low} interlayer shear mode (~ 6.8 meV), since the latter is related to the C_{44} shear elastic constant while the former to the C_{33} compression one, with the natural hierarchy $C_{44} < C_{33}$ in graphitic systems [88].

The contribution of the B_{1g} interlayer breathing phonon mode to the thermal broadening of the phonon replicas in HQ Grapheren BN sample has already studied by temperature-dependent line-width in PL spectroscopy as discussed in chapter 3. Here, we have performed again temperature-dependent PL measurements in our three controlled boron isotopic samples ^{10}BN , ^{Na}BN and ^{11}BN from 8K to 300K. All spectra are fitted using the theoretical model presented in chapter 3 (pages 64-67). We stress again that there is only one varying parameter for reproducing the full PL spectrum of BN, the FWHM (Δ), which is identical for all phonon replicas. After extracting the variations of Δ versus temperature, we plot these values as a function of temperature in ^{10}BN , ^{Na}BN , and ^{11}BN as shown in figure 4.9 (symbols). At low temperature, the line-width of the phonon replicas is not significantly different in our three samples. However, by increasing the temperature, the phonon replicas broadening Δ is the highest for ^{10}BN and it is the lowest for ^{11}BN . The solid lines in this figure are the theoretical fits of the temperature dependence

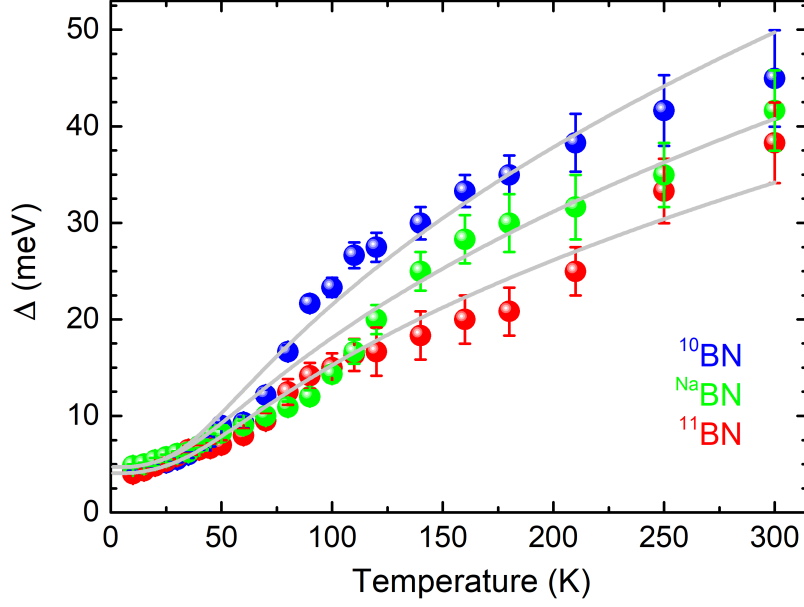


Figure 4.9: Phonon-assisted broadening Δ of the PL spectra in ^{10}BN , $^{\text{Na}}\text{BN}$ and ^{11}BN : experimental data (symbols), fits of the thermally-induced broadening (solid lines).

of the phonon replicas broadening according to equation 3.16:

$$\Delta = \sqrt{\Delta_A^2 + \Delta_O^2} = \sqrt{(S_A E_A \coth(\frac{E_A}{2k_B T}))^2 + (S_O E_O \frac{b}{e^{\frac{E_O}{k_B T}}})^2}$$

As discussed in chapter 3, the first term Δ_A is the broadening due to the quasi-elastic scattering involving ZA phonons while the second term Δ_O is the broadening due to the inelastic scattering arising from ZO_1 optical branch that corresponds to the B_{1g} at the zone center (chapter 1). S_A and S_O are the strength of the coupling to phonons, E_A and E_O are the mean acoustic and optical phonon energies, respectively. In figure 4.9, we obtain a good agreement with the experimental data. We find the optical phonon energy is constant within our fitting error $E_O = 15 \pm 5$ meV, in contrast the coupling strength increases from 50 ± 10 , 65 ± 10 to 115 ± 10 meV in ^{11}BN , $^{\text{Na}}\text{BN}$, and ^{10}BN , respectively. The values of $S_A = 1.5 \pm 0.3$ and $E_A = 4 \pm 1$ meV are the same in the three KSU samples.

We remark that all fitting parameters in $^{\text{Na}}\text{BN}$ are exactly the same (within the fitting error) as the ones in the HQ Graphene sample (chapter 3, pages 78-80). This further confirms the intrinsic origin of the linewidth broadening of the emission lines in BN and also supports that the zero temperature linewidth is exclusively limited by phonon-assisted broadening in BN. Moreover, above 70 K, where Δ_O prevails, the same value of the optical phonon energy of $E_O = 15 \pm 5$ meV was found in three fits of the three KSU samples

(also equals to HQ Graphene sample) confirms the contribution of the B_{1g} phonon mode to the line-width broadening. The fitting error for ± 5 meV of the phonon energy is at least one order of magnitude larger than the isotopic shift of the interlayer breathing mode, in the range of 0.15 meV, by assuming 1%-variations of the phonon energy as for the Raman modes. This means that the larger broadening observed in PL spectroscopy in ^{10}BN is not due to the isotopic shift of the interlayer breathing mode. According to the equation 3.16 and the discussion in chapter 3, the larger the phonon energy, the larger the line-width broadening. It means that the line-width broadening should be smallest in ^{10}BN and biggest in ^{11}BN . That is totally in opposition to our experimental findings. The variations of the coupling strength is the only way to reproduce our data, with the highest (lowest) value in ^{10}BN (^{11}BN). Moreover, like in case of interlayer shear mode, the value of the coupling strength in ^{10}BN is close to the one in ^{11}BN while it is much smaller compared to the one in ^{10}BN .

As a matter of fact, the coupling strength thus captures the impact of isotopic engineering on the thermally-assisted broadening of the PL lines. Following Sumi *et al.* [63], the expression of the coupling strength indicates that it is proportional to the square modulus of the matrix element describing the exciton-phonon interaction. This expression is written:

$$S_O = \frac{1}{2} \sum_k \frac{|V_k|^2}{\omega_k^2} \quad (4.11)$$

where S_O the coupling strength, ω_k the phonon energy, and V_k the matrix element describing the exciton-phonon interaction. This matrix element can be described by the optical deformation potential (D_0) [24]: $V_k = D_0$.

On the other hand, the energy shift due to exciton-phonon interaction have been calculated using tight binding model. The equation giving the energy shift reads:

$$\delta E = 8 \left(\frac{\gamma}{E_g} \right) \delta \gamma \quad (4.12)$$

where δE is the energy shift, γ is the matrix element describing the interlayer hopping, E_g the bandgap energy. Besides, according to Pötz and Vogl [89], the power-law dependence of the matrix element γ with the interlayer distance reads:

$$\gamma = \eta \frac{1}{c^{2n}} \quad (4.13)$$

where $2n$ is the exponent.

Combining Equations 4.12 and 4.13, we obtain the optical deformation potential in the case of the interlayer breathing mode in BN:

$$D_0 = 8(2n) \frac{\gamma^2}{E_g} \quad (4.14)$$

As discussed in Appendix 4, the Van der Waals potential can be expanded in power series of the interatomic distance ($-C_6/r^6 + -C_8/r^8 \dots$). It means that the exponent n can be 3 or 4. Consequently, we obtain the relation between the quantities:

$$S_O \sim |D_0|^2 \sim |\gamma|^4 \sim c^{-8n}$$

According to our analysis of the thermal red-shift of the interlayer shear mode, we take an approximate value $n = 4$ in BN, so that $S_O \sim c^{-32}$. This huge value indicates a dramatic sensitivity of the exciton-phonon interaction with the c-lattice parameter in the case of the interlayer breathing mode. We thus conclude that the increase of the coupling strength between ^{11}BN and ^{10}BN goes beyond standard models of the exciton-phonon interaction. Similar to the case of the shear motion of adjacent layers, we infer that isotope engineering in BN impacts the lattice vibrations controlled by the weak vdW coupling between adjacent layers.

By studying the temperature-dependent PL measurements of interlayer shear mode and interlayer breathing mode in BN gives two signatures for the modification of vdW due to boron isotopes. The two signatures bring a very new phenomenon of isotopes effect in BN relating to the vdW heterostructure. These results also open a question about the direct observation of the modification of vdW due to boron isotopes. An answer were solved by performing X-rays measurements that will be presented in next section.

4.3 X-ray measurements

The X-rays measurements were performed, with a high resolution X-ray diffraction platform, in the Institut Européen des Membranes (UMR-5635 CNRS) at Montpellier by by our colleagues Prof. Van der Lee (see more details in supplementary in Vuong *et al.* [86]. Figure 4.10 displays electronic density distribution in ^{10}BN (top, (a-c)) and ^{11}BN (bottom,

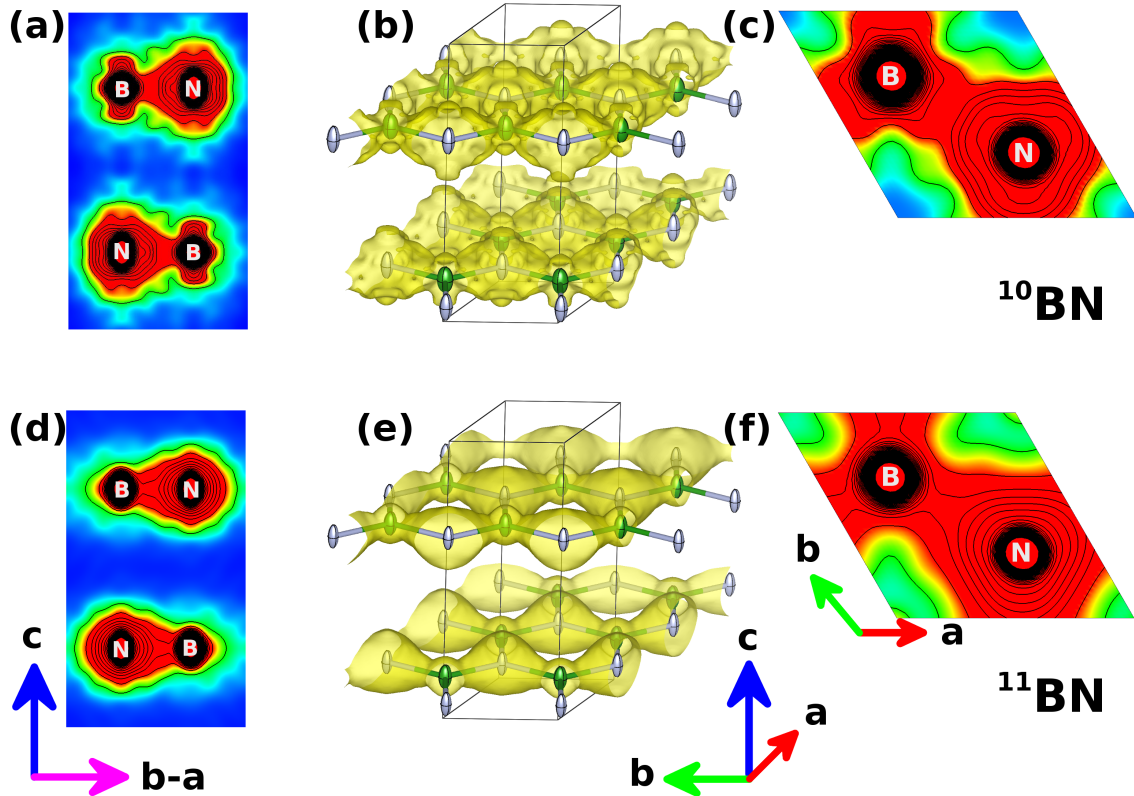


Figure 4.10: Electron density distribution in ^{10}BN (top, (a-c)) and ^{11}BN (bottom, (d-f)) using the maximum entropy method against X-ray data collected at 125K to 0.4 \AA resolution. (a&d) 2D contour plots in a plane parallel to the c-axis, (b&e) side view of 3D contour plots with an iso-contour level at 1 e. \AA^{-3} , (c&f) 2D contour plots in a plane perpendicular to the c-axis. The iso-contour levels range from 1 to 30 e. \AA^{-3} in steps of 0.5 e. \AA^{-3} .

(d-f)) using the maximum entropy method (MEM) against X-ray data collected at 125K. We have 3D maps of electronic distribution for ^{10}BN and ^{11}BN showing in figures 4.10 (b and e).

Whereas, figures 4.10 (a,c, d, and f) show the 2D maps of electronic density distribution of the two samples ^{10}BN and ^{11}BN in a plane parallel or perpendicular to the c-axis. From these figures, we can see the modification of electronic distribution between ^{10}BN and ^{11}BN . This modification can be seen more clear in figure 4.11 that is presenting the expansion of figures 4.10 (a&d) for ^{10}BN and ^{11}BN . Along the c-axis, the out-of-plane electron density is more spread out around both nuclei in ^{10}BN , while in ^{11}BN , it is more dilocalized. It means the electron is less strong bound in ^{10}BN than in ^{11}BN .

The different neutron numbers of isotopes are expected to induce slight modifications in the electronic wavefunction. In accordance with Ref.[90], for a point-like nucleus, the

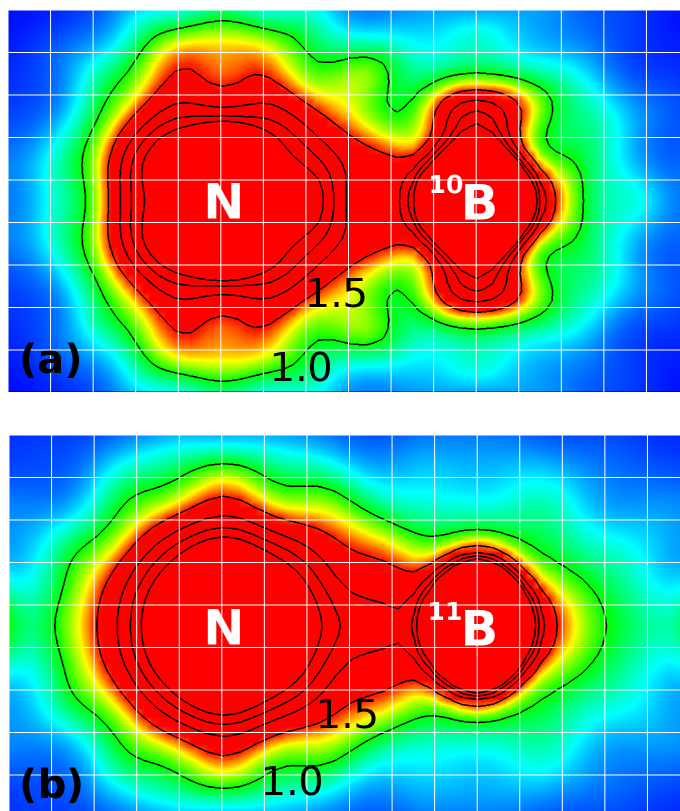


Figure 4.11: Expanded view of figure 4.10(a&d) for (a) ^{10}BN and (b) ^{11}BN . The orientation is identical to figure 4.10(a&d), but the vertical section is between $z=0.585$ and $z=0.915$ in crystallographic units of the c -lattice parameter ($c \sim 6.6 \text{ \AA}$). Contour levels are from 1 to 3 e.\AA^{-3} in steps of 0.5 e.\AA^{-3} . Squares in the white grids have a size of 0.242 \AA .

Coulomb potential experienced by electrons approaches $-\infty$ at the center. When increasing size of the nucleus, this potential deviates because of the finite nucleus size. This effect is called Field shift which increases with nucleus size. The hyperfine effect due to the deformation of the nuclear charge distribution is however in the GHz range [90], i.e. three orders of magnitude lower than the characteristic spectral shifts discussed here. The most plausible interpretation for the deformation of the electron wavefunctions in-between the layers of isotopically-purified BN crystals goes back to the mass variations in ^{10}B and ^{11}B nuclei.

By performing X-ray diffraction experiments, we demonstrate that the interlayer electronic distribution itself is affected by the isotopic substitution, giving a direct observation for the modification of vdW interaction in BN due to isotopes.

4.4 Conclusions

In this chapter, we study on the isotope engineering of lamellar BN crystals with nearly pure boron isotopes (^{10}B and ^{11}B) compared to those with the natural distribution of boron (20 at% ^{10}B and 80 at% ^{11}B) by performing the Raman and PL measurements.

In the first section, based on the publication of Cardona and his co-worker, we we have focused on the two conspicuous effects of the isotope that are:

The dependence of the phonon frequencies and the linewidths with the isotopic composition:

Raman measurements of three controlled boron isotopic samples of the phonon mode at high energy of BN, which were performed by our colleagues, evidenced the dependence of the phonon energy with the reduced mass of BN. We observed the shift of Raman lines of ^{11}BN and ^{10}BN compared to $^{\text{Na}}\text{BN}$ with amount of 1.5 and 3.5 meV. Besides this effect, there is the impact of the isotopic mass disorder leading to an energy shift and a linewidth broadening of $^{\text{Na}}\text{BN}$ compared to isotopically pure BN (^{11}BN and ^{10}BN).

Renormalization of the energy of the electronic states through the electron-phonon interaction:

The PL measurements have been performed for the three KSU samples. We observed the global red-shift from ^{11}BN to ^{10}BN due to both the phonon energy effect and the electronic bandgap renormalization. The band-gap renormalization is estimated at 225 meV by analyzing our data. This value is in fair agreement with the temperature dependent PL measurements done in Ref. [80]. From which, we extract a single Einstein oscillator of energy $\hbar\Omega = 68\pm 2$ meV. This value is is rather low compared to the absolute maximum of the phonon dispersion of 200 meV in h-BN [39], indicating the interlayer vibrations make a significant contribution to the electron-phonon bandgap renormalization.

In the second section, we have focused on the impact of isotopes on the weak van der Waals interactions in BN that is obtained by analyzing the temperature-dependent results of the shear and breathing modes of adjacent layers.

Temperature-dependent Raman measurements of the phonon mode at low energy (inter-layer shear mode) were performed from 10 to 600K. Increasing temperature, the Raman energy decreases due to the dependence of phonon energy with the c-lattice parameters that increases with temperature. A power-law dependence was used to analyze our data.

We obtain a modification of the exponent of the power-law from one sample to another: it is 3.6 ± 0.3 in ^{11}BN , and it increases to 5.7 ± 0.3 in ^{10}BN . This is the first evidence for the weak, non-local van de Waals coupling varying with the isotopic composition. The second evidence was obtained by studying the line-width broadening of PL lines due to the contribution of the interlayer breathing mode. Similar to the case of the interlayer shear mode, we obtain an increase of the coupling strength to the interlayer breathing mode from 50 ± 10 , to 70 ± 10 , and then 115 ± 10 meV in ^{11}BN , ^{10}BN , and ^{10}BN . We infer that isotope engineering in BN impacts the lattice vibrations controlled by the weak van der Waals coupling between adjacent layers.

Besides, X-ray diffraction was performed for ^{11}BN to ^{10}BN by our colleague to observe directly the difference between them. The result is the electron density distribution is more diffuse between adjacent layers in ^{11}BN than in ^{10}BN crystals. Therefore, we can conclude that the interlayer electronic distribution itself is affected by the isotopic substitution, giving a direct observation for the modification of the van de Waal interaction in BN due to isotopic purification.

Chapter 5

BN epilayers grown by molecular beam epitaxy (MBE)

In the previous chapters, we have studied the electronic and optical properties of different bulk crystals, so called NIMS, HQ Graphene or KSU. They were grown by different methods discussed in details in chapter 2. All of them present the same PL spectrum with three emission bands centered at 4, 5.5, and 5.8 eV respectively, corresponding to the signature of point defects, stacking faults, and phonon replicas [64, 91–94]. In figure 5.1, we show the PL spectrum in a larger scale from 3.5 eV to 6 eV of a sample bought from HQ Graphene company. Three areas are distinguished by different colors. The first one shown in green corresponds to electronic states localized in point defects. This PL signal was studied in detail and the interpretation was published in Physics Review Letters (PRL) in 2016. We will not further discuss the result of this area in this chapter, more details can be found in **Appendix C**. The second area (red) comes from extended defects or stacking faults, which were in particular characterized with a nanometric resolution in a transmission electron microscope [64, 95]. This emission spectrum exhibits various peaks at 5.62, 5.56, 5.47, and 5.3 eV, the so-called D lines (figure 5.1) [64, 93]. The D_2 and D_6 lines at energy of 5.27eV and 5.56 eV were tentatively assigned to the boron nitride divacancy [64], while the D_1 , $D_{3,4}$, and D_5 lines are phonon replicas involving real excitonic states due to the presence of defects in BN [64]. The last one using textured blue includes five emission lines at 5.76, 5.79, 5.86, 5.89, and 5.93 eV corresponding to the phonon-assisted emissions, namely LO_3 , TO_3/TO_2 , LA/LO_1 , TA/TO_1 , and ZO_1 that were previously discussed.

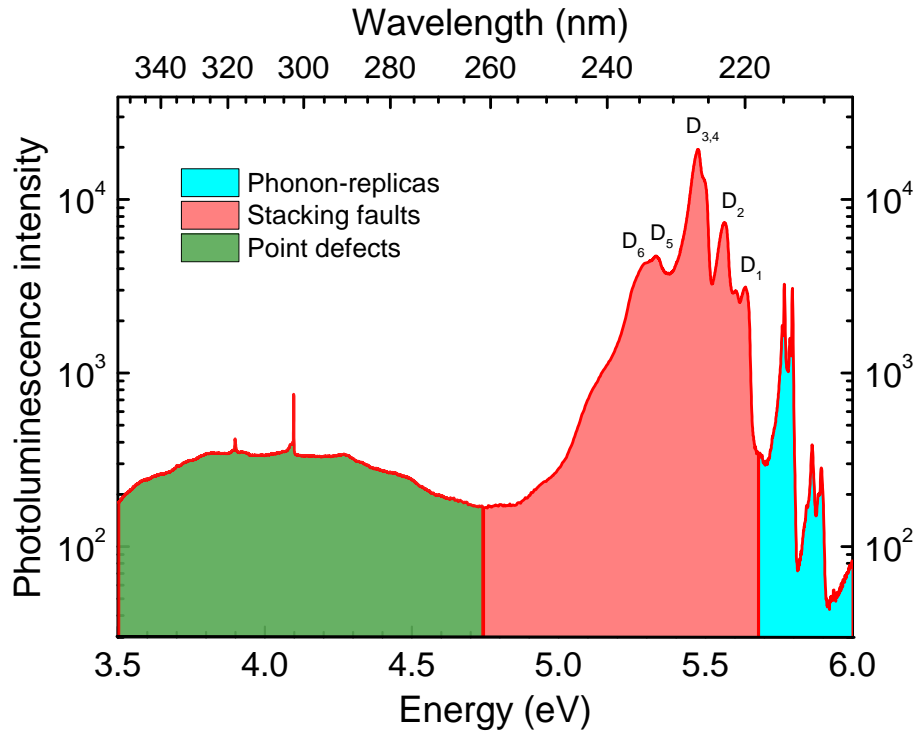


Figure 5.1: Photoluminescence spectrum in HQ Graphene BN at 8K, under excitation at 6.3 eV.

Such crystals are very appropriate for the establishment of basic quantities that indicate what the performances of BN are. Developing a large scale production of BN-based devices using such tiny crystals cannot be seriously envisioned as the worldwide need requires production of much higher amounts of materials than the growth methods used to get these tiny crystal will ever allow. As an example to reinforce the statement above, let us consider the GaN parent material. Although the first GaN mono-crystals grown by taking into advantages of the thermodynamics were published in 1938 [96], it was necessary to wait more than 30 complementary years to have the first demonstration of an operating device obtained by an alternative growth method, using chemical precursors that were made to react to form GaN, based on chemical processes out of equilibrium. These methods offer the possibility to deal with higher growth rate than the solidification processes, and they permit to realize junctions of different doping with controlled interfaces. One further had to wait till 1986 to be able to obtain high quality GaN material by such epitaxial methods and 1989 was the year when was published the first GaN-AlGaN light emitting diode (LED) with 'appropriate' electrical injection conditions [97–99].

The epitaxial crystal growth methods consist of depositing a monocrystalline film on a mono-crystalline substrate forming an epitaxial film or an epitaxial layer. The substrates, such as sapphire, SiC, GaAl₂O₄ act as a seed crystal. The first difficulty lies in the lack of lattice matching of the different materials used to grow the device, and the second one is the lack of the substrate lattice matched with materials such as GaN, BN, AlN, the main components of these devices. In line with bondings in such crystals, a lot of dislocations are created to relax the elastic energy stored in the strained layers. Shaded layer epitaxy is thus very challenging through the managing of defect for nature. Defects have such deleterious influence on the performances lifetime of devices. For compound semiconductor processes, impurities will affect the electrical characteristics through compensation of dopant or unintentional doping, shift the intended emission wavelength in lasers or LEDs, and reduce device lifetime by degrading the interface and introducing imperfections in the crystal lattice. Epitaxy makes use of a variety of gases for growth and doping.

There are two main epitaxial growth approaches for materials in general, and for BN in particular: the Chemical Vapour Deposition (CVD) and the molecular beam Epitaxy (MBE). In all cases, the epitaxial layer is formed by the coherent deposition of the atoms on the substrate surface. The only differences are the conditions in which growth occurs.

Molecular beam epitaxy (MBE)

MBE is realized in high vacuum conditions, in metallic chambers to which can be adapted a lot of different in-situ growth control instruments (Auger probes, Rheed oscillation probes) [100]. Atomic beams target the substrate surface where growth can thus be controlled in real time. Among all the critical quantities is the management of the very high temperature needed at the surface of the substrate for the growth of BN. The intrinsic properties of metals (a high thermal conductivity making the thermal exchanges with the substrate holder and the rest of the metallic growth chamber softening substantially in the very high temperature range) are hurdling the development of this growth technology in the high temperature range. A specific and expensive design has been realized in Nottingham to overcome these difficulties and to grow BN at high temperature, with, as will be demonstrated further, optical performances that teach us what is the state of the art at the time of writing.

The high-purity BN epilayers grown by MBE, however, have not been recorded so far.

Chemical Vapour Deposition (CVD)

CVD is practiced in a variety of formats, for instance Atomic-layer CVD (ALCVD), Hybrid Physical-Chemical Vapor Deposition (HPCVD), Metal Organic chemical vapor deposition (MOCVD), Combustion Chemical Vapor Deposition (CCVD), and etc . Among that, MOCVD, also known as organometallic vapour phase epitaxy (OMVPE) or metalorganic Vapor-phase epitaxy (MOVPE) is more popular [101]. The atoms are brought on the surface by using gas flow after cracking of precursors that contain organic radicals. The gas flow can be N_2 or H_2 or a mixture of them, it is chosen based on criteria like its viscosity, chemical aggressiveness at the growth temperature. The growth pressure conditions can be tuned through a large range of values together with different partial pressures of the actors that contribute to the growth. Except an optical, laser-assisted control of the growth rate there are almost no in-situ growth control instruments. In contrast to MBE, high growth temperatures can be fairly easily achieved at a reasonable cost, but it is less precise. In these ranges of high growth temperatures, thermal exchanges mediated by the gas flow occur between the substrate and the quartz reactor which requires ad-hoc design to work under these severe conditions. We can anticipate from what is known concerning the high temperature growth of (Al,Ga)N-related compounds that the main drawback will from bonafide come from the thermal cracking of the boron precursors that may lead to efficient carbon incorporation or contamination of all residual impurities in the growth layer under these high temperature conditions. The doping of MOCVD-grown samples will be strongly correlated to the purity of the precursor for boron.

Unlike MBE, high-purity BN epilayers grown by CVD has been reported in many literatures such as [43–49, 102]. The high-purity of BN samples were demonstrated by various measurements, such as X-ray, Raman, CL, or PL. The PL and CL spectra of BN epilayers grown by MOCVD and MOVPE by Majety *et al.* [48, 103] and Li *et al.* [49] are shown in figure 5.2, respectively.

Figure 5.2(a) shows the PL spectra of $1\mu m$ BN epilayers grown on sapphire compared to the PL spectrum of AlN epilayers in Ref. [103]. They observed a strong band-edge PL emission centered at about 5.48 eV at 10K corresponding to the emission band related to

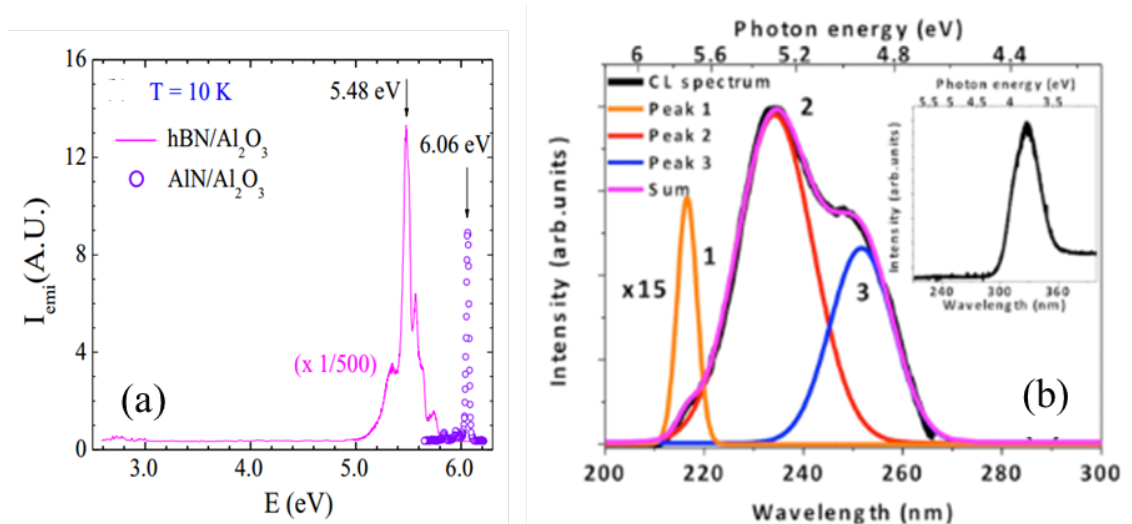


Figure 5.2: (a) PL spectra of BN and AlN epilayers at 10K [48, 103], (b) CL spectrum of BN grown on sapphire at wavelengths near bandgap at 77 K under excitation of 6 kV. Inset shows defect band emission [49].

extended defects in bulk samples. Besides, figure 5.2(b) displays the CL spectrum including three band edge PL peaks of 30 nm BN layer on sapphire grown by MOPVE by Li *et al.* [49]. They indicated that the tiny peak at 5.73 eV (peak 1, figure 5.2(b)) corresponds to the phonon replicas of BN (S series in their paper), while the two remaining peaks at 5.29 eV and 4.92 eV (peaks 2 and 3, figure 5.2(b)) correspond to the emission band related to extended defects in bulk samples. The inset of this figure displays a strong CL peak at around 3.9 eV corresponding the signature of point defects in bulk sample.

Based on all the discussion above, we would like to contribute to develop a technology based on BN that would be grown at large scale. To do that it is mandatory to be able to establish the epitaxial growth protocol on large scale and low-cost foreign substrates such as c-plane Al_2O_3 , c-plane SiC. In this chapter, we are going to evaluate the optical properties of two series BN epilayers grown by MBE (chapter 2). The first series of BN epilayers were grown on sapphire substrates (S series), while the second one were grown on highly ordered pyrolytic graphite (HOPG) substrates (G series). Besides PL measurements, atomic force microscopy (AFM) was performed in ambient conditions using an Asylum Research Cypher-S AFM, by our colleagues working at School of Physics and Astronomy, University of Nottingham, United Kingdom. Such experiments provide important information on the morphology as well as an estimate of the thickness of BN deposited during the growth of the two series of samples.

5.1 BN grown on sapphire substrate

We first address the first series of samples, grown on sapphire. These four samples are named S1390, S1480, S1560, and S1690 and they were grown at different temperatures of 1390 °C, 1480 °C, 1560 °C, and 1690 °C, respectively.

5.1.1 Atomic force microscopy (AFM)

The typical AFM images recorded on the first series of BN samples are presented in figure 5.3. We make here a comparison between samples S1390 and S1690. The morphology of the three BN samples with growth temperatures of 1390 °C, 1480 °C, and 1560 °C are very close to each other, so that, only data corresponding to S1390 and S1690 have been displayed in figure 5.2. In sample S1390 (and also S1480 and S1560), we observe a uniform nano-crystallite morphology with BN nanocrystallites covering the entire sapphire surface. Otherwise, in sample S1690, we observe the underlying terraces of the sapphire substrate that are visible through the BN deposits. It may be due to re-evaporation of BN from the sapphire substrate at these high temperatures, resulting in a thinner BN layer. The estimations of the average BN film thickness indicate a monotonic decrease, from ~ 17 nm to ~ 5 nm (from 53 to 15 in units of monolayer (ML) with $1\text{ML} = 0.33$ nm) with the growth temperature conditions shown in table 5.1. Specifically, the average thickness of S1390, S1480, S1560, and S1690 were estimated at 53 ± 3 ML, 40 ± 3 ML, 33 ± 3 ML, and 15 ± 3 ML, respectively. It means that when increasing the growth temperature, the average thickness of the samples decreases in the S series.

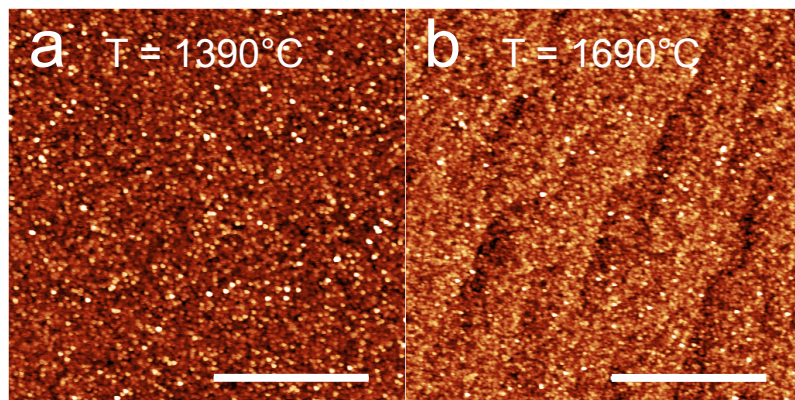


Figure 5.3: Atomic force microscopy images of two BN samples grown on sapphire for 3 h, (a) at 1390 °C, and (b) at 1690 °C. The scale bars in both images are $2 \mu\text{m}$

Growth temperature	1390 °C	1480 °C	1560 °C	1690 °C
BN/Sapphire	53±3	40±3	33±3	15±3

Table 5.1: Average film thickness of BN samples grown on sapphire, in units of monolayer (ML), after 3h of growth as a function of the growth temperature. 1ML = 0.33nm.

5.1.2 Photoluminescence measurements

Photoluminescence spectra recorded in the energy range from 5 to 6 eV for the S series at low temperature (8K) under an excitation at 6.3 eV are plotted in figure 5.4. At first sight, we observe an emission band centered at 5.4 eV (with a maximum PL peak around 5.4 eV and a secondary shoulder at a higher energy of 5.55 eV) and a full width at half maximum of the order of 300 - 400 meV in the four samples. The PL signal of the S1390 grown at the lowest temperature is tricky to observe in a linear scale because of its weak intensity. The emission line of BN epilayers centered at 5.4 eV match the emission band corresponding to stacking faults in bulk samples. Nevertheless, this band is unlike the case of high-quality BN crystals where it is composed of many lines (D series) as shown above in figure 5.1; it is more less similar to the PL spectrum of BN epilayers grown by MOVPE which consist in two broad lines (Figure 5.2(a)). In fact, for the BN grown on sap-

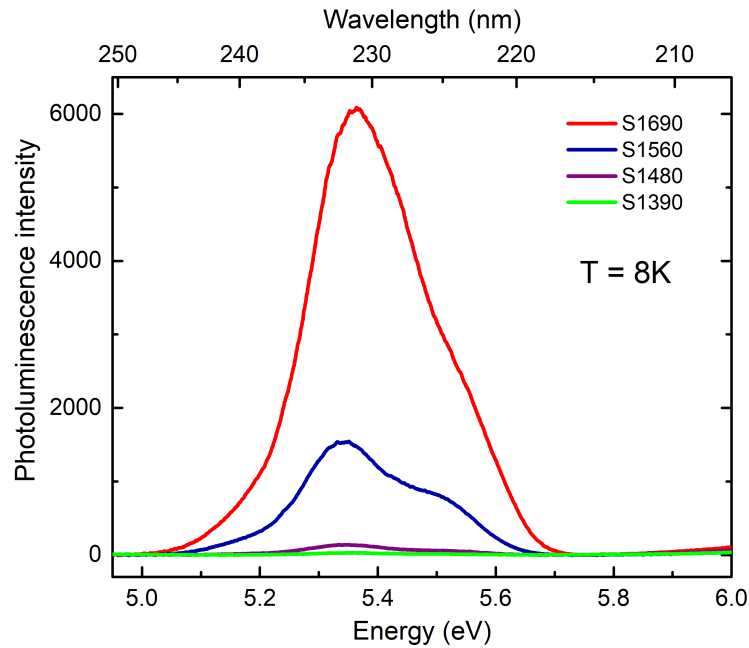


Figure 5.4: PL spectra in the four BN samples grown on sapphire were recorded at 8K under excitation at 6.3 eV, followed by the growth temperature in °C.

phire, the emission spectrum can only comprise the PL lines arising from point defects (D_2 and D_6 lines) which were identified as being related to shallow transitions involving presumable boron nitride divacancies. This is because the first series of BN consist of nanocrystalline domains (AFM image - figure 5.3) , so that extended defects cannot develop in this type of sample.

Furthermore, there is a strong dependence of the PL intensity of the MBE samples with their growth temperature. In particular, we observe the highest intensity for the sample grown at the highest temperature of 1690 °C (S1690). The PL intensities of S1560, S1480, and S1390 are reduced by a factor 4, 44, and 225, respectively, compared to the one of S1690. We can say that the higher the growth temperature of the MBE samples grown on sapphire, the higher the PL intensity. Still, the lower the growth temperature, the thicker the BN epilayer as indicated in table 5.1 and discussed in the previous section. *This means that the increase of the PL signal intensity is due to a higher quality of the epilayers.* However, we do not observe any signal at higher energy corresponding to the intrinsic phonon replicas, as shown by the blue area in figure 5.1. We believe that the quality of this first series is not good enough to observe the phonon-assisted recombination around the band gap. Finally, we plot the PL spectrum through a larger energy range (from 3.5 to 5.8 eV) for S1690 in figure 5.5. We note that we do not observe the two sharp peaks around 4 eV corresponding to point defects, like in other samples (HQ graphene, NIMS or KSU samples).

Nevertheless, a broad emission, comparable to the one highlighted in green in figure 5.1 is still observed. There is a good match between our result with the CL spectrum of BN epilayers grown on sapphire by MOVPE as shown in figure 5.2(a), inset. But, in this figure, the intensity of the defects band is much higher than the one of the S1690 BN sample. This proves that samples grown by MBE has a good control over defect density.

In conclusion, we have succeeded, *for the first time*, to record PL signal in the DUV on thin BN epilayers grown on sapphire substrates by MBE. The emission band around 5.4 eV of the first series of BN has been observed proving that high temperature MBE growth can produce BN layers of high optical quality. Furthermore, the quality of the sample increases when increasing the temperature. However, the quality of the series S is still not good enough to obtain a PL signal at high energy, near the bandgap. This rises the motivation to increase the quality of our samples. To do that, our colleagues working

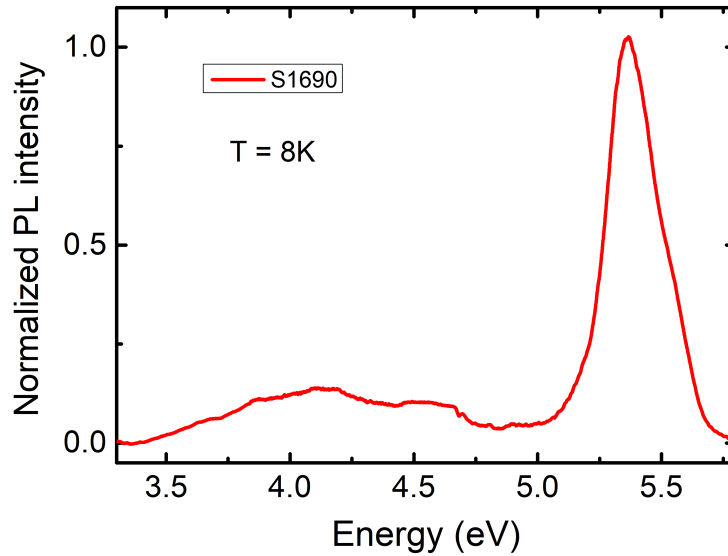


Figure 5.5: PL spectrum of S1690 over a larger spectral range, recorded at 8K under excitation at 6.3 eV.

at Nottingham University have deposited BN not only on sapphire, but also on highly ordered pyrolytic graphite (HOPG) substrates. HOPG is not a standard MBE substrate, but it is a good alternative to sapphire, because BN is closely lattice-matched to HOPG with a low lattice mismatch of $\sim 1.8\%$ [41]. The AFM and PL measurements recorded on this second series are plotted and interpreted in the next section.

5.2 BN grown on highlyordered pyrolytic graphite (HOPG) substrate

We now focus on the second series of samples grown on HOPG substrates. This series includes four samples, namely G1390, G1480, G1560, and G1690 which were grown at different temperatures of 1390 °C, 1480 °C, 1560 °C, and 1690 °C, respectively.

5.2.1 Atomic force microscopy (AFM)

The AFM images of the four BN samples of the G series are presented in figure 5.6. We find that the morphology of the BN epilayers grown on HOPG is markedly different from those grown on sapphire. In particular, we observe faceted BN islands nucleating from HOPG step edges, and bulk BN deposits. The BN islands form a near-complete mono-

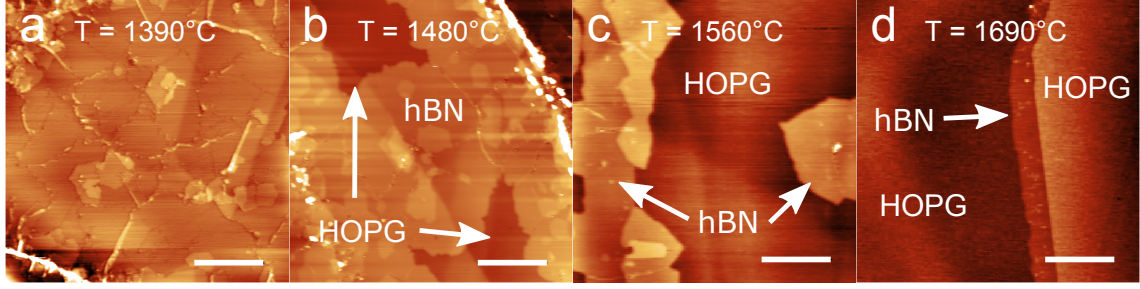


Figure 5.6: Atomic force microscopy images of BN grown on HOPG for 3h, at 1390 °C (a), 1480 °C (b), 1560 °C (c) and 1690 °C (d). The images show a gradual reduction in surface coverage from complete BN coverage in (a) to island growth ((b) and (c)), and finally only growth from HOPG step-edges (d). The arrows in images ((b)-(d)) indicate the regions corresponding either to the underlying HOPG substrate (b), or to the BN islands ((c) and (d)), following the comparative analysis detailed in [41]. The AFM images ((b)-(d)) were acquired using AC mode AFM, and image (a) was acquired in contact mode. The scale bars in images ((a)-(d)) are all 500 nm.

layer for the lowest growth temperature as shown in figure 5.6(a) (1390 °C), together with multi-layered regions. Defects and grain boundaries are also observed which indicate a laterally polycrystalline BN surface. We note that in the two samples grown at the highest temperatures (1580 °C and 1690 °C), the BN coverage of the HOPG surface is drastically decreased, compared to the two remaining ones because of BN sublimation, which will impact on the optical response (next section).

The estimations of the average BN thickness are shown in table 5.2. Similarly to the case of the S series, we obtain a monotonic decrease of the average thickness with the growth temperature. The thickness of the G series, however, is deeply smaller than the one of the S series. Specifically, the thickness of G1390, G1480, G1560, and G1690 were estimated at 1.15 ± 0.01 ML, 0.85 ± 0.01 ML, 0.38 ± 0.01 ML, and 0.09 ± 0.01 ML, respectively.

Growth temperature	1390 °C	1480 °C	1560 °C	1690 °C
BN/HOPG	1.15 ± 0.01	0.85 ± 0.01	0.38 ± 0.01	0.09 ± 0.01

Table 5.2: Average film thickness of BN samples grown on HOPG, in units of monolayer (ML), after 3h of growth as a function of the growth temperature. 1ML = 0.33nm.

5.2.2 Photoluminescence measurements

The PL spectra of the second series of BN samples have been recorded in the same experimental conditions as before. Figure 5.7 displays the results of the PL measurements for BN epilayers grown on HOPG focusing on a short energy range scaling from 5 eV

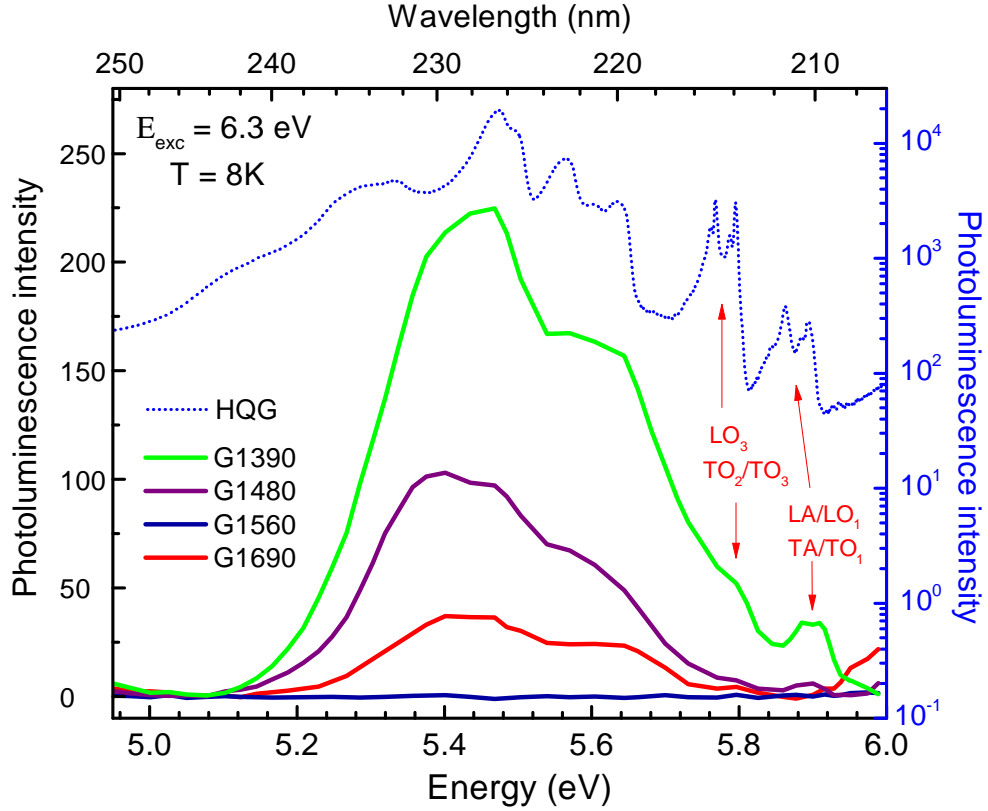


Figure 5.7: PL spectra in the four BN samples grown HOPG (solid lines), compared to the PL spectrum of HQ Graphene sample (dashed line), were recorded at 8K under excitation at 6.3 eV.

to 6 eV. Similarly to the PL spectra of the S series, we also observe the broad emission band around 5.4 - 5.5 eV with a full width at half maximum of 400-500 meV in the four samples that match the emission band corresponding to stacking faults in bulk samples (figure 5.1). In particular, these PL bands include a strong main peak at 5.45 eV and a secondary shoulder at 5.65 eV. We note that the intensity of G1560 is only observable in log scale because of its weak intensity. However, these PL bands are larger by approximately of 100 meV, and they shift toward higher energy by an amount of about 0.5 eV, compared to the ones of BN epitaxies grown on sapphire. This shift may be due to the smaller lattice mismatch between BN and graphite compared to the one of BN and sapphire. Furthermore, the shoulder of the emission band at 5.65 eV is more pronounced (compared to BN/sapphire), and it is close to the D_1 line in the PL spectrum of bulk samples, which corresponds to the first overtone arising from intervalley scattering assisted by the emission of one transverse optical phonon at the K point [64].

On the other hand, we also observe a pronounced dependence of the PL spectrum with

growth temperature for the BN layers grown on HOPG. Unlike the case of sapphire substrate, the evolution is reversed: the lowest substrate temperature (1390 °C) is displaying the most intense and rich signal. Moreover, the dependence of the PL signals with the growth temperature is not exactly monotonic, like in the case of the first set of BN samples. Specifically, the lowest PL signal is not recorded for the highest substrate temperature sample (G1690) but for the second highest one (G1580). The explanation for this comes from the coverage of the BN surface. Let us come back to AFM images (figure 5.6), we note that AFM data for the two BN samples G1580 and G1690 do not indicate complete surface coverage. Their PL signals are therefore not very strong and depend on the position of the laser spot on the surface of the samples.

In contrast to the first series of BN samples, at higher energy, we observe PL signals around 5.9 eV with a doublet structure at 5.88 and 5.91 eV in the two BN epilayers: G1390 and G1480 (figure 5.7 - green and purple lines). These PL lines are attributed to the contributions of two phonon replicas LA/LO₁ and TA/TO₁ with a small shift toward higher energy of 100 meV, respectively, compared to the PL spectrum of HQ Graphene sample (figure 5.1 - blue area). This blue-shift of phonon replicas may come from the modification of the intrinsic optical properties of BN when changing from bulk crystal to monolayer. A similar phenomenon has been observed in several literatures, such as Schué *et al.*, Du *et al.* [51, 80].

Looking more carefully at sample G1390, we also observe another peak at 5.8 eV, as a high-energy shoulder of the dominant emission band around 5.4-5.5 eV. This emission line may correspond to the other phonon replicas, labeled LO₃ and TO₂/TO₃. I would like to highlight that the phonon replicas have never been observed in **thin** BN epilayers grown either by MBE or MOCVD. Our PL signals give an evidence to confirm the high-purity of BN epilayers grown on HOPG by MBE.

According to Ref.[51] when reducing the thickness of BN samples from bulk down to few monolayer-samples, the intensity ratio of the LO₃ - TO₂/TO₃ and LA/LO₁ - TA/TO₁ phonon replicas decreases. It means that the LO₃ - TO₂/TO₃ optical phonon replicas dominate the intrinsic emission spectrum in bulk BN, whereas the PL spectrum is dominated by the LA/LO₁ - TA/TO₁ phonon replicas in BN few monolayers samples. This effect is also observed in our samples. In particular, the intensity ratio of the LO₃ - TO₂/TO₃ and LA/LO₁ - TA/TO₁ phonon replicas is equal to 8 in the bulk BN samples, while this

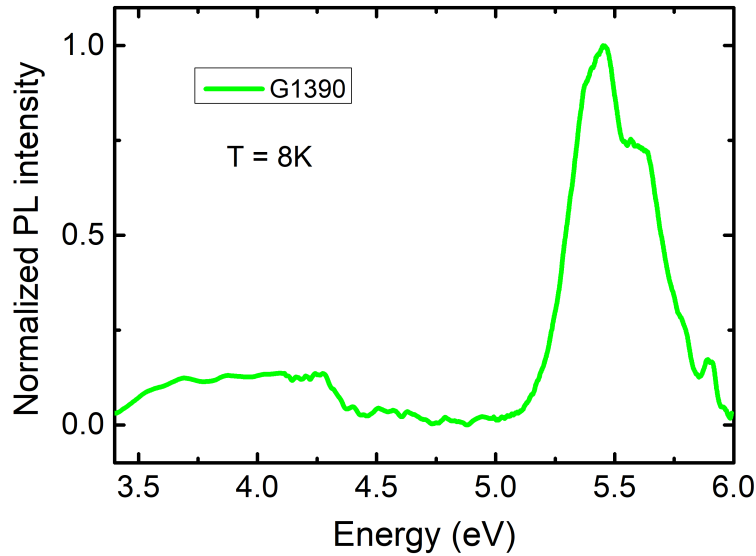


Figure 5.8: PL spectrum of G1390 over a larger spectral range were recorded at 8K under excitation at 6.3 eV.

ratio is 1/3 in the G1390 BN sample (after background correction). Comparing to the study of Ref.[51], the thickness of our sample G1390 was estimated of around 6 - 8 ML at the position of the laser spot on the surface of the sample. We remark that the AFM image for G1390 (Figure 5.6) indicates the complete surface coverage, however it is not homogeneous with the simultaneous existence of the BN monolayer and multi-layers. That explain the different between the average thickness of 1 ML estimated by AFM and the thickness of 6-8ML estimated by PL spectrum in G1390. In fact, it is very tricky to observe exactly the PL signal from the BN island monolayer with our experimental conditions, i.e the diameter of a laser spot. This fact raises a requirement for improving or changing our system such as a microscopy cryostat or laser.

Similarly to the S series, the PL spectrum on a larger energy range (from 3.5 to 5.8 eV) for G1390 displayed in figure 5.8 consists of a broad emission band centered around 5.4 - 5.5 eV discussed above, and another broad band around 4 eV corresponding to point defects. This band has been already discussed in the previous section.

In summary, the presence of the phonon replicas in the PL spectrum of G1390 is a direct signature of the excellent crystalline quality of our BN epilayers grown by high-temperature MBE. The quality of the BN samples enhances obviously by changing the substrate from sapphire to HOPG. The comparison between the PL spectra of two series (S series and G series) proves that the quality of the samples grown on HOPG substrates

is better than the one grown on sapphire substrates due to the lower lattice mismatch.

5.3 Conclusions

In this chapter, we have studied the two series of h-BN epilayers grown by MBE in different substrates: sapphire and Highly Ordered Pyrolytic Graphite (HOPG), with different growth temperature of 1390 °C, 1480 °C, 1560 °C, and 1690 °C.

The Atomic force microscopy (AFM) images show different results for the two series. In the series grown on sapphire of BN, AFM images show that the BN epilayers consist of nanocrystalline domains, while in the series grown on HOPG we observe faceted BN islands nucleating from HOPG step edges, and bulk BN deposits. The estimation of the average thickness by AFM of the two series decrease with the growth temperature. In particular, when increasing the growth temperature, the thickness of samples decreases. However, the average thickness of the series grown on HOPG (from 0.09 to 1.15 in units of monolayer (ML)) is deeply smaller than the one of the series grown on sapphire (from 15 to 53 ML).

As far as the PL measurements are concerned, for the first time, we have succeeded to recorded the PL signal in the deep ultra-violet (UV) in thin BN epilayers grown on sapphire and HOPG substrates by MBE. The emission bands around 5.4-5.5 eV match the emission band corresponding to stacking fault that were recorded in bulk BN crystal [6, 51, 64] and in BN epilayers [49, 103].

Moreover, PL spectra show that there is a strong dependence of the PL intensity of the series grown on sapphire with their growth temperature. The higher the growth temperature, the smaller the average thickness of the samples, the higher the PL intensity. From this, we conclude that the high temperature MBE growth can produce BN layers of high optical quality.

Furthermore, in the two samples grown on HOPG with the lowest growth temperatures of 1390 °C and 1480 °C, we observed the PL peaks at energy of 5.88 and 5.91 eV which correspond to the two phonon replicas LA/LO₁ and TA/TO₁, compared to the PL spectrum of bulk samples. These PL lines corresponding to the phonon replicas have never been observed in thin BN epilayers grown either by CVD or MBE. For the first time, we show the evidence of the phonon replicas in BN thin epilayers. This is a direct signa-

ture for the excellent crystalline quality of our samples grown by the high temperature MBE. The comparison between the PL spectra of the two series of BN epilayers proves that the quality of the samples grown on HOPG substrates is better than the ones grown on sapphire substrates due to the lower lattice mismatch. In conclusion, high purity BN epilayers grown by MBE pave the way to the launching of complementary growth which may trigger the entrance of epi-BN into the arena of both wide bandgap semiconductors with the possibility to bridge the technologies.

Conclusion

IN THIS THESIS, the optical properties of bulk and epilayers of hexagonal boron nitride (h-BN) were studied using the photoluminescence and Raman spectroscopies, X-ray diffraction, and Atomic force microscopy (AFM). We investigated samples from different sources: National Institute for Materials Science - Japan, HQ Graphene company, Kansas State University, and Nottingham University using different growth methods, such as high-pressure and high-temperature (HP-HT), Ni-Cr flux, and molecular beam Epitaxy (MBE). The purpose for that is to confirm the intrinsic optical properties of h-BN.

First, we have focused on the phonon-assisted recombinations of h-BN by performing polarization-resolved PL measurements.

- We have analyzed the two cases of a Poynting vector $\vec{\omega}$ parallel or perpendicular to the c-axis. In the case of a Poynting vector $\vec{\omega}$ parallel to the c-axis, we recorded four main emission lines that correspond to the phonon replicas LO_3 , TO_2/TO_3 , LA/LO_1 , TA/TO_1 . Their intensity did not change when rotating the linear polarizer of analysis. On the contrary, in the case of a Poynting vector $\vec{\omega}$ perpendicular to the c-axis, in addition to these four phonon replicas, the ZO_1 phonon replica at 5.93 eV was also observed. Moreover, there was a strong dependence of the intensity of all phonon replicas with the polarizer angle. The intensity ratio of LA/LO_1 and ZO_1 changes from 200 to 5 when rotating the linear polarizer. These results demonstrate the impact of the phonon symmetries on the optical emission spectrum in bulk h-BN. Besides the phonon replicas mentioned above, the ZO_3 phonon replica at 5.87 eV, which has the same B_{1g} symmetry as the ZO_1 phonon replica, was obtained by subtracting the two different PL spectra in case of a Poynting vector $\vec{\omega}$ perpendicular to the c-axis. This ZO_3 phonon replica was confirmed by the comparison between the phonon dispersion relations [39] with our PL spectrum, giving

a comprehensive understanding of the phonon replicas in h-BN, and further pointing out the originality of the optical properties in this layered compound where the extrema of the conduction and valence bands lie in different high symmetry points which are both away from the zone center. Outstandingly, we have succeeded in the challenging measurements of the polarization-dependence of the forbidden indirect exciton emission intensity giving the orientation of the dipole of the exciton in a predominantly in-plane orientation. As a matter of fact, the results obtained by means of polarization-resolved PL spectroscopy provide a strong confirmation, and a definite proof for the indirect nature of the bandgap in h-BN that was investigated in Ref.[11].

- We have demonstrated that the origin of the fine structure of the PL spectrum in BN arises from overtones of interlayer shear modes in the phonon-assisted emission spectrum of h-BN. These lattice vibrations are specific to layered compounds since they correspond to the shear rigid motion between adjacent layers, with a characteristic energy of about 6.8 ± 0.5 meV in h-BN at 8 K. Our theoretical model, based on calculations of the phonon energy and group velocity at T points of the Brillouin zone, reveals that the differences observed for the various phonon replicas in h-BN only come from the variations of the phonon group velocity at T points of the Brillouin zone. The larger the phonon group velocity, the broader the line of the phonon replica. An excellent fit of the multiplet observed in each phonon replica is obtained by taking the assumption of a cumulative Gaussian broadening. The comparison between our model and the data raises a new question about the different profile between the two Gaussian and Lorentzian functions.
- Following the theoretical predictions of Toyozawa of the line-shape of the exciton absorption band [61], we have brought the two evidences for the strong-coupling regime of the exciton-phonon interaction in h-BN, that had never been previously observed since the paper of Toyozawa. The first evidence comes from the comparison between Gaussian and Lorentzian functions in the fits of the PL spectrum at low temperature (8 K) as well as at high temperature. The excellent fit obtained with the Gaussian profile suggests that the exciton-phonon interaction is in the strong coupling regime in BN [61]. The second evidence was observed by performing the

temperature-dependent PL measurements from 8K to 300K. We obtain the square root dependence of the line-width with temperature as in Toyozawa's theory for the strong-coupling regime. By fitting our data, we interpreted the temperature dependence of the line-width on the basis of quasi-elastic scattering by acoustic phonons, and inelastic scattering by absorption of optical phonons corresponding to the ZA and ZO₁ phonon modes in h-BN. The strong-coupling regime and the bright emission in this indirect band-gap semiconductor are unusual properties, calling for a microscopic understanding of the exciton-phonon coupling in this van der Waals crystal with fascinating properties.

Second, we have studied the isotope engineering of lamellar BN crystals with nearly pure boron isotopes (¹⁰B and ¹¹B) compared to those with the natural distribution of boron (20 at% ¹⁰B and 80 at% ¹¹B) by performing the Raman and PL measurements.

- Based on the publication of Cardona and his co-worker, we have focused on the two conspicuous effects of the isotope that are:

(i) *The dependence of the phonon frequencies and the linewidths with the isotopic composition:*

Raman measurements of three controlled boron isotopic samples of the phonon mode at high energy of BN, which were performed by our colleagues, evidenced the dependence of the phonon energy with the reduced mass of BN. We observed the shift of Raman lines of ¹¹BN and ¹⁰BN compared to ^{Na}BN with amount of 1.5 and 3.5 meV. Besides this effect, there is the impact of the isotopic mass disorder leading to an energy shift and a linewidth broadening of ^{Na}BN compared to isotopically pure BN (¹¹BN and ¹⁰BN).

(ii) *Renormalization of the energy of the electronic states through the electron-phonon interaction*

The PL measurements have been performed for the three KSU samples. We observed the global red-shift from ¹¹BN to ¹⁰BN due to both the phonon energy effect and the electronic bandgap renormalization. The band-gap renormalization is estimated at 225 meV by analyzing our data. This value is in fair agreement with the temperature dependent PL measurements done in Ref. [80]. From which, we extract a single Einstein oscillator of energy $\hbar\Omega = 68 \pm 2$ meV. This value is rather low compared to the absolute maximum of the phonon dispersion of 200 meV in h-

BN [39], indicating the interlayer vibrations make a significant contribution to the electron-phonon bandgap renormalization.

- In the following of that, we have focused on the impact of isotopes on the weak van der Waals interactions in BN that is obtained by analyzing the temperature-dependent results of the shear and breathing modes of adjacent layers.

Temperature-dependent Raman measurements of the phonon mode at low energy (interlayer shear mode) were performed from 10 to 600K. Increasing temperature, the Raman energy decreases due to the dependence of phonon energy with the c-lattice parameters that increases with temperature. A power-law dependence was used to analyze our data. We obtain a modification of the exponent of the power-law from one sample to another: it is 3.6 ± 0.3 in ^{11}BN , and it increases to 5.7 ± 0.3 in ^{10}BN . This is the first evidence for the weak, non-local van de Waals coupling varying with the isotopic composition. The second evidence was obtained by studying the line-width broadening of PL lines due to the contribution of the interlayer breathing mode. Similar to the case of the interlayer shear mode, we obtain an increase of the coupling strength to the interlayer breathing mode from 50 ± 10 , to 70 ± 10 , and then 115 ± 10 meV in ^{11}BN , ^{10}BN , and ^{10}BN . We infer that isotope engineering in BN impacts the lattice vibrations controlled by the weak van der Waals coupling between adjacent layers.

- Besides, X-ray diffraction was performed for ^{11}BN to ^{10}BN by our colleague to observe directly the difference between them. The result is the electron density distribution is more diffuse between adjacent layers in ^{11}BN than in ^{10}BN crystals. Therefore, we can conclude that the interlayer electronic distribution itself is affected by the isotopic substitution, giving a direct observation for the modification of the van de Waal interaction in BN due to isotopic purification.

Third, we have studied the two series of h-BN epilayers grown by MBE in different substrates: sapphire and Highly Ordered Pyrolytic Graphite (HOPG), with different growth temperature of 1390 °C, 1480 °C, 1560 °C, and 1690 °C.

The Atomic force microscopy (AFM) images show different results for the two series. In the series grown on sapphire of BN, AFM images show that the BN epilayers consist of nanocrystalline domains, while in the series grown on HOPG we observe faceted BN is-

lands nucleating from HOPG step edges, and bulk BN deposits. The estimation of the average thickness by AFM of the two series decrease with the growth temperature. In particular, when increasing the growth temperature, the thickness of samples decreases. However, the average thickness of the series grown on HOPG (from 0.09 to 1.15 in units of monolayer (ML)) is deeply smaller than the one of the series grown on sapphire (from 15 to 53 ML).

As far as the PL measurements are concerned, for the first time, we have succeeded to record the PL signal in the deep ultra-violet (UV) in thin BN epilayers grown on sapphire and HOPG substrates by MBE. The emission bands around 5.4-5.5 eV match the emission band corresponding to stacking fault that were recorded in bulk BN crystal [6, 51, 64] and in BN epilayers [49, 103].

Moreover, PL spectra show that there is a strong dependence of the PL intensity of the series grown on sapphire with their growth temperature. The higher the growth temperature, the smaller the average thickness of the sample, and the higher the PL intensity. From this, we conclude that the high temperature MBE growth can produce BN layers of high optical quality.

Furthermore, in the two samples grown on HOPG with the lowest growth temperatures of 1390 °C and 1480 °C, we observed the PL peaks at energy of 5.88 and 5.91 eV which correspond to the two phonon replicas LA/LO₁ and TA/TO₁, compared to the PL spectrum of bulk samples. These PL lines corresponding to the phonon replicas have never been observed in thin BN epilayers grown either by CVD or MBE. For the first time, we show the evidence of the phonon replicas in BN thin epilayers. This is a direct signature for the excellent crystalline quality of our samples grown by the high temperature MBE. The comparison between the PL spectra of the two series of h-BN epilayers proves that the quality of the samples grown on HOPG substrates is better than the ones grown on sapphire substrates due to the lower lattice mismatch. In conclusion, high purity BN epilayers grown by MBE pave the way to the launching of complementary growth which may trigger the entrance of epi-BN into the arena of both wide bandgap semiconductors with the possibility to bridge the technologies.

Bibliography

- [1] Nikolay Zheludev. The life and times of the LED — a 100-year history, April 2007. URL <https://www.nature.com/articles/nphoton.2007.34>.
- [2] James R. Biard and Gary E. Pittman. Semiconductor radiant diode, December 1966. URL <https://patents.google.com/patent/US3293513A/en>.
- [3] Michael Kneissl and Jens Rass, editors. *III-Nitride Ultraviolet Emitters: Technology and Applications*. Springer Series in Materials Science. Springer International Publishing, 2016. ISBN 978-3-319-24098-5. URL [//www.springer.com/fr/book/9783319240985](http://www.springer.com/fr/book/9783319240985).
- [4] E. Silveira, J. A. Freitas, O. J. Glembocki, G. A. Slack, and L. J. Schowalter. Excitonic structure of bulk AlN from optical reflectivity and cathodoluminescence measurements. *Physical Review B*, 71(4):041201, January 2005. doi: 10.1103/PhysRevB.71.041201. URL <https://link.aps.org/doi/10.1103/PhysRevB.71.041201>.
- [5] W. H. Balmain. Bemerkungen über die Bildung von Verbindungen des Bors und Siliciums mit Stickstoff und gewissen Metallen. *Journal für Praktische Chemie*, 27(1):422–430. ISSN 1521-3897. doi: 10.1002/prac.18420270164. URL <https://onlinelibrary.wiley.com/doi/abs/10.1002/prac.18420270164>.
- [6] Kenji Watanabe, Takashi Taniguchi, and Hisao Kanda. Direct-bandgap properties and evidence for ultraviolet lasing of hexagonal boron nitride single crystal. *Nature Materials*, 3(6):404–409, June 2004. ISSN 1476-1122. doi: 10.1038/nmat1134. URL <http://www.nature.com/nmat/journal/v3/n6/abs/nmat1134.html?foxtrotcallback=true>.

- [7] Kenji Watanabe, Takashi Taniguchi, and Hisao Kanda. Ultraviolet luminescence spectra of boron nitride single crystals grown under high pressure and high temperature. *physica status solidi (a)*, 201(11):2561–2565, September 2004. ISSN 1521-396X. doi: 10.1002/pssa.200405188. URL <http://onlinelibrary.wiley.com/doi/10.1002/pssa.200405188/abstract>.
- [8] G. Kern, G. Kresse, and J. Hafner. \textbf{ \textit{Ab initio} } calculation of the lattice dynamics and phase diagram of boron nitride. *Physical Review B*, 59(13): 8551–8559, April 1999. doi: 10.1103/PhysRevB.59.8551. URL <http://link.aps.org/doi/10.1103/PhysRevB.59.8551>.
- [9] Ludger Wirtz, Angel Rubio, Raul Arenal de la Concha, and Annick Loiseau. Ab initio. *Physical Review B*, 68(4):045425, July 2003. doi: 10.1103/PhysRevB.68.045425. URL <https://link.aps.org/doi/10.1103/PhysRevB.68.045425>.
- [10] John Vinson, Terrence Jach, Matthias Müller, Rainer Unterumsberger, and Burkhard Beckhoff. Resonant x-ray emission of hexagonal boron nitride. *Physical Review B*, 96(20):205116, November 2017. doi: 10.1103/PhysRevB.96.205116. URL <https://link.aps.org/doi/10.1103/PhysRevB.96.205116>.
- [11] G. Cassabois, P. Valvin, and B. Gil. Hexagonal boron nitride is an indirect bandgap semiconductor. *Nature Photonics*, 10(4):262–266, January 2016. ISSN 1749-4885, 1749-4893. doi: 10.1038/nphoton.2015.277. URL <http://arxiv.org/abs/1512.02962>. arXiv: 1512.02962.
- [12] C. Subramanian, A. K. Suri, and T. S. R. Ch Murthy. Development of boron-based materials for nuclear applications. *BARC Newsletter*, pages 14–22, 2010. ISSN 0976-2108. URL http://inis.iaea.org/Search/search.aspx?orig_q=RN:45027141.
- [13] R. F. Barth, A. H. Soloway, R. G. Fairchild, and R. M. Brugger. Boron neutron capture therapy for cancer. Realities and prospects. *Cancer*, 70(12):2995–3007, December 1992. ISSN 0008-543X.
- [14] A. K. Geim and I. V. Grigorieva. Van der Waals heterostructures. *Nature*, 499(7459): 419–425, July 2013. ISSN 1476-4687. doi: 10.1038/nature12385. URL <https://www.nature.com/articles/nature12385>.

- [15] Kenji Watanabe and Takashi Taniguchi. Hexagonal Boron Nitride as a New Ultraviolet Luminescent Material and Its Application. *International Journal of Applied Ceramic Technology*, 8(5):977–989, September 2011. ISSN 1744-7402. doi: 10.1111/j.1744-7402.2011.02626.x. URL <http://onlinelibrary.wiley.com/doi/10.1111/j.1744-7402.2011.02626.x/abstract>.
- [16] R. S. Pease. An X-ray study of boron nitride. *Acta Crystallographica*, 5(3):356–361, May 1952. ISSN 0365-110X. doi: 10.1107/S0365110X52001064. URL <http://scripts.iucr.org/cgi-bin/paper?a00642>.
- [17] Hassel, T.Norsk Deutsch, Geol. J.Tidsskr. Appl. Phys. 9, 258 33,(1926) - Google Search, . URL https://www.google.com/search?client=firefox-b-ab&ei=BAE2W6nKNKOMgAbZ1LL4Dg&q=Hassel%2C+T.Norsk+Deutsch%2C+Geol.+J.Tidsskr.+Appl.+Phys.+9%2C+258+33%2C%281926%29&oq=Hassel%2C+T.Norsk+Deutsch%2C+Geol.+J.Tidsskr.+Appl.+Phys.+9%2C+258+33%2C%281926%29&gs_l=psy-ab.12...0.0.0.474592.0.0.0.0.0.0.0..0.0....0...1c..64.psy-ab..0.0.0....0.opxHsAqp1Zc.
- [18] R. Geick, C. H. Perry, and G. Rupprecht. Normal Modes in Hexagonal Boron Nitride. *Physical Review*, 146(2):543–547, June 1966. doi: 10.1103/PhysRev.146.543. URL <https://link.aps.org/doi/10.1103/PhysRev.146.543>.
- [19] E. Doni and G. Pastori Parravicini. Energy bands and optical properties of hexagonal boron nitride and graphite. *Il Nuovo Cimento B (1965-1970)*, 64(1):117–144, November 1969. ISSN 0369-3554, 1826-9877. doi: 10.1007/BF02710286. URL <https://link.springer.com/article/10.1007/BF02710286>.
- [20] R. J. Nemanich, S. A. Solin, and Richard M. Martin. Light scattering study of boron nitride microcrystals. *Physical Review B*, 23(12):6348–6356, June 1981. doi: 10.1103/PhysRevB.23.6348. URL <https://link.aps.org/doi/10.1103/PhysRevB.23.6348>.
- [21] T. Q. P. Vuong, G. Cassabois, P. Valvin, V. Jacques, A. Van Der Lee, A. Zobelli, K. Watanabe, T. Taniguchi, and B. Gil. Phonon symmetries in hexagonal boron nitride probed by incoherent light emission. *2D Materials*, 4(1):011004, 2017. ISSN

- 2053-1583. doi: 10.1088/2053-1583/4/1/011004. URL <http://stacks.iop.org/2053-1583/4/i=1/a=011004>.
- [22] F. Bassani and G. Pastori Parravicini. Band structure and optical properties of graphite and of the layer compounds GaS and GaSe. *Il Nuovo Cimento B (1965-1970)*, 50(1):95–128, July 1967. ISSN 0369-3554, 1826-9877. doi: 10.1007/BF02710685. URL <https://link.springer.com/article/10.1007/BF02710685>.
- [23] F. Bassani and A. E. Hassan. Analysis of indirect two-photon interband transitions and of direct three-photon transitions in semiconductors. *Il Nuovo Cimento B (1971-1996)*, 7(2):313–332, February 1972. ISSN 1826-9877. doi: 10.1007/BF02743603. URL <https://link.springer.com/article/10.1007/BF02743603>.
- [24] Peter YU and Manuel Cardona. *Fundamentals of Semiconductors: Physics and Materials Properties*. Graduate Texts in Physics. Springer-Verlag, Berlin Heidelberg, 4 edition, 2010. ISBN 978-3-642-00709-5. URL [//www.springer.com/gp/book/9783642007095](http://www.springer.com/gp/book/9783642007095).
- [25] George F. Koster. *Properties of the thirty-two point groups*. M.I.T. Press research monographs.no. 34. M.I.T. Press, Cambridge, Mass., 1963. URL <https://catalog.hathitrust.org/Record/001114463>.
- [26] W. Haase. F. A. Cotton: Chemical Applications of Group Theory, 2nd Edition. John Wiley & Sons Ltd., Baffins Lane 1971, 386 S. Preis: £ 6.50. *Berichte der Bunsengesellschaft für physikalische Chemie*, 76(2):173–173, February 1972. ISSN 0005-9021. doi: 10.1002/bbpc.19720760217. URL <http://onlinelibrary.wiley.com/doi/10.1002/bbpc.19720760217/abstract>.
- [27] Pere Miró, Martha Audiffred, and Thomas Heine. An atlas of two-dimensional materials. *Chemical Society Reviews*, 43(18):6537–6554, August 2014. ISSN 1460-4744. doi: 10.1039/C4CS00102H. URL <http://pubs.rsc.org/en/content/articlelanding/2014/cs/c4cs00102h>.
- [28] R. Taylor and C. A. Coulson. Studies in Graphite and Related Compounds III: Electronic Band Structure in Boron Nitride. *Proceedings of the Physical Society. Section A*, 65(10):834, 1952. ISSN 0370-1298. doi: 10.1088/0370-1298/65/10/307. URL <http://stacks.iop.org/0370-1298/65/i=10/a=307>.

- [29] A. Catellani, M. Posternak, A. Baldereschi, H. J. F. Jansen, and A. J. Freeman. Electronic interlayer states in hexagonal boron nitride. *Physical Review B*, 32(10):6997–6999, November 1985. doi: 10.1103/PhysRevB.32.6997. URL <https://link.aps.org/doi/10.1103/PhysRevB.32.6997>.
- [30] B. Arnaud, S. Lebègue, P. Rabiller, and M. Alouani. Huge Excitonic Effects in Layered Hexagonal Boron Nitride. *Physical Review Letters*, 96(2):026402, January 2006. doi: 10.1103/PhysRevLett.96.026402. URL <http://link.aps.org/doi/10.1103/PhysRevLett.96.026402>.
- [31] X. Blase, Angel Rubio, Steven G. Louie, and Marvin L. Cohen. Quasiparticle band structure of bulk hexagonal boron nitride and related systems. *Physical Review B*, 51(11):6868–6875, March 1995. doi: 10.1103/PhysRevB.51.6868. URL <https://link.aps.org/doi/10.1103/PhysRevB.51.6868>.
- [32] Ludger Wirtz, Andrea Marini, Myrta Gruning, and Angel Rubio. Excitonic effects in optical absorption and electron-energy loss spectra of hexagonal boron nitride. *arXiv:cond-mat/0508421*, August 2005. URL <http://arxiv.org/abs/cond-mat/0508421>. arXiv: cond-mat/0508421.
- [33] Giorgia Fugallo, Matteo Aramini, Jaakko Koskelo, Kenji Watanabe, Takashi Taniguchi, Mikko Hakala, Simo Huotari, Matteo Gatti, and Francesco Sottile. Exciton energy-momentum map of hexagonal boron nitride. *Physical Review B*, 92(16), October 2015. ISSN 1098-0121, 1550-235X. doi: 10.1103/PhysRevB.92.165122. URL <http://arxiv.org/abs/1508.01769>. arXiv: 1508.01769.
- [34] Hugo Henck, Debora Pierucci, Giorgia Fugallo, José Avila, Guillaume Cassabois, Yannick J. Dappe, Mathieu G. Silly, Chaoyu Chen, Bernard Gil, Matteo Gatti, Francesco Sottile, Fausto Sirotti, Maria C. Asensio, and Abdelkarim Ouerghi. Direct observation of the band structure in bulk hexagonal boron nitride. *Physical Review B*, 95(8):085410, February 2017. doi: 10.1103/PhysRevB.95.085410. URL <https://link.aps.org/doi/10.1103/PhysRevB.95.085410>.
- [35] T. Kuzuba, K. Era, T. Ishii, and T. Sato. A low frequency Raman-active vibration of hexagonal boron nitride. *Solid State Communications*, 25(11):863–865,

- March 1978. ISSN 0038-1098. doi: 10.1016/0038-1098(78)90288-0. URL <http://www.sciencedirect.com/science/article/pii/0038109878902880>.
- [36] Takashi Kuzuba, Yoichiro Sato, Shinobu Yamaoka, and Koh Era. Raman-scattering study of high-pressure effects on the anisotropy of force constants of hexagonal boron nitride. *Physical Review B*, 18(8):4440–4443, October 1978. doi: 10.1103/PhysRevB.18.4440. URL <https://link.aps.org/doi/10.1103/PhysRevB.18.4440>.
- [37] K. H. Michel and B. Verberck. Phonon dispersions and piezoelectricity in bulk and multilayers of hexagonal boron nitride. *Physical Review B*, 83(11):115328, March 2011. doi: 10.1103/PhysRevB.83.115328. URL <http://link.aps.org/doi/10.1103/PhysRevB.83.115328>.
- [38] J. Serrano, F. J. Manjón, A. H. Romero, A. Ivanov, M. Cardona, R. Lauck, A. Bosak, and M. Krisch. Phonon dispersion relations of zinc oxide: Inelastic neutron scattering and ab initio calculations. *Physical Review B*, 81(17):174304, May 2010. doi: 10.1103/PhysRevB.81.174304. URL <http://link.aps.org/doi/10.1103/PhysRevB.81.174304>.
- [39] Ramon Cuscó, Bernard Gil, Guillaume Cassabois, and Luis Artús. Temperature dependence of Raman-active phonons and anharmonic interactions in layered hexagonal BN. *Physical Review B*, 94(15):155435, October 2016. doi: 10.1103/PhysRevB.94.155435. URL <http://link.aps.org/doi/10.1103/PhysRevB.94.155435>.
- [40] T. B. Hoffman, B. Clubine, Y. Zhang, K. Snow, and J. H. Edgar. Optimization of Ni–Cr flux growth for hexagonal boron nitride single crystals. *Journal of Crystal Growth*, 393:114–118, May 2014. ISSN 0022-0248. doi: 10.1016/j.jcrysgr.2013.09.030. URL <http://www.sciencedirect.com/science/article/pii/S0022024813006313>.
- [41] Yong-Jin Cho, Alex Summerfield, Andrew Davies, Tin S. Cheng, Emily F. Smith, Christopher J. Mellor, Andrei N. Khlobystov, C. Thomas Foxon, Laurence Eaves, Peter H. Beton, and Sergei V. Novikov. Hexagonal Boron Nitride Tunnel Barriers Grown on Graphite by High Temperature Molecular Beam Epitaxy. *Scientific Re-*

- ports*, 6:srep34474, September 2016. ISSN 2045-2322. doi: 10.1038/srep34474. URL <https://www.nature.com/articles/srep34474>.
- [42] Zheng Zuo, Zhongguang Xu, Renjing Zheng, Alireza Khanaki, Jian-Guo Zheng, and Jianlin Liu. In-situ epitaxial growth of graphene/h-BN van der Waals heterostructures by molecular beam epitaxy. *Scientific Reports*, 5:14760, October 2015. ISSN 2045-2322. doi: 10.1038/srep14760.
- [43] Peter Sutter, Jayeeta Lahiri, Peter Albrecht, and Eli Sutter. Chemical Vapor Deposition and Etching of High-Quality Monolayer Hexagonal Boron Nitride Films. *ACS Nano*, 5(9):7303–7309, September 2011. ISSN 1936-0851. doi: 10.1021/nn202141k. URL <https://doi.org/10.1021/nn202141k>.
- [44] Amir Pakdel, Chunyi Zhi, Yoshio Bando, Tomonobu Nakayama, and Dmitri Golberg. A comprehensive analysis of the CVD growth of boron nitride nanotubes. *Nanotechnology*, 23(21):215601, 2012. ISSN 0957-4484. doi: 10.1088/0957-4484/23/21/215601. URL <http://stacks.iop.org/0957-4484/23/i=21/a=215601>.
- [45] Ki Kang Kim, Allen Hsu, Xiaoting Jia, Soo Min Kim, Yumeng Shi, Mario Hofmann, Daniel Nezich, Joaquin F. Rodriguez-Nieva, Mildred Dresselhaus, Tomas Palacios, and Jing Kong. Synthesis of Monolayer Hexagonal Boron Nitride on Cu Foil Using Chemical Vapor Deposition. *Nano Letters*, 12(1):161–166, January 2012. ISSN 1530-6984. doi: 10.1021/nl203249a. URL <https://doi.org/10.1021/nl203249a>.
- [46] Majharul Haque Khan, Hua Kun Liu, Xudong Sun, Yusuke Yamauchi, Yoshio Bando, Dmitri Golberg, and Zhenguo Huang. Few-atomic-layered hexagonal boron nitride: CVD growth, characterization, and applications. *Materials Today*, 20(10):611–628, December 2017. ISSN 1369-7021. doi: 10.1016/j.mattod.2017.04.027. URL <http://www.sciencedirect.com/science/article/pii/S1369702117301098>.
- [47] Mallikarjuna Gurram, Siddhartha Omar, Simon Zihlmann, Péter Makk, Qiucheng Li, Yanfeng Zhang, Christian Schönenberger, and Bart J. van Wees. Spin transport in two-layer-CVD-hBN/graphene/hBN heterostructures. *Physical Review B*, 97(4),

- January 2018. ISSN 2469-9950, 2469-9969. doi: 10.1103/PhysRevB.97.045411. URL <http://arxiv.org/abs/1712.00815>. arXiv: 1712.00815.
- [48] H. X. Jiang and J. Y. Lin. Review—Hexagonal Boron Nitride Epilayers: Growth, Optical Properties and Device Applications. *ECS Journal of Solid State Science and Technology*, 6(2):Q3012–Q3021, January 2017. ISSN 2162-8769, 2162-8777. doi: 10.1149/2.0031702jss. URL <http://jss.ecsdl.org/content/6/2/Q3012>.
- [49] Xin Li, Suresh Sundaram, Youssef El Gmili, Taha Ayari, Renaud Puybaret, Gilles Patriarche, Paul L. Voss, Jean Paul Salvestrini, and Abdallah Ougazzaden. Large-Area Two-Dimensional Layered Hexagonal Boron Nitride Grown on Sapphire by Metalorganic Vapor Phase Epitaxy. *Crystal Growth & Design*, 16(6):3409–3415, June 2016. ISSN 1528-7483. doi: 10.1021/acs.cgd.6b00398. URL <https://doi.org/10.1021/acs.cgd.6b00398>.
- [50] h-BN - Hexagonal Boron Nitride, . URL <http://www.hqgraphene.com/h-BN.php>.
- [51] Léonard Schué, Bruno Berini, Andreas C. Betz, Bernard Plaçais, François Ducastelle, Julien Barjon, and Annick Loiseau. Dimensionality effects on the luminescence properties of hBN. 8(13):6986–6993, March 2016. ISSN 2040-3372. doi: 10.1039/C6NR01253A. URL <http://pubs.rsc.org/en/content/articlelanding/2016/nr/c6nr01253a>.
- [52] Ashish Kumar Singh, Jahnvi Tiwari, Ashish Yadav, and Rakesh Kumar Jha. MATLAB User Interface for Simulation of Silicon Germanium Solar Cell, 2015. URL <https://www.hindawi.com/journals/jma/2015/840718/>.
- [53] Rochon Polarizer, . URL <http://laserstates.com/Rochon-Polarizer.html>.
- [54] R. J. Elliott. Intensity of Optical Absorption by Excitons. *Physical Review*, 108(6): 1384–1389, December 1957. doi: 10.1103/PhysRev.108.1384. URL <https://link.aps.org/doi/10.1103/PhysRev.108.1384>.
- [55] B. Segall and G. D. Mahan. Phonon-Assisted Recombination of Free Excitons in Compound Semiconductors. *Physical Review*, 171(3):935–948, July 1968.

- doi: 10.1103/PhysRev.171.935. URL <http://link.aps.org/doi/10.1103/PhysRev.171.935>.
- [56] S. J. Xu, G. Q. Li, S.-J. Xiong, and C. M. Che. Temperature dependence of the LO phonon sidebands in free exciton emission of GaN. *Journal of Applied Physics*, 99(7):073508, April 2006. ISSN 0021-8979. doi: 10.1063/1.2188034. URL <http://aip.scitation.org/doi/abs/10.1063/1.2188034>.
- [57] B. Krummheuer, V. M. Axt, and T. Kuhn. Theory of pure dephasing and the resulting absorption line shape in semiconductor quantum dots. *Physical Review B*, 65(19):195313, May 2002. doi: 10.1103/PhysRevB.65.195313. URL <http://link.aps.org/doi/10.1103/PhysRevB.65.195313>.
- [58] Satyaprakash Sahoo, V. Sivasubramanian, S. Dhara, and A. K. Arora. Excitation energy dependence of electron–phonon interaction in ZnO nanoparticles. *Solid State Communications*, 147(7):271–273, August 2008. ISSN 0038-1098. doi: 10.1016/j.ssc.2008.06.002. URL <http://www.sciencedirect.com/science/article/pii/S0038109808003128>.
- [59] B. Schreder, C. Dem, M. Schmitt, A. Materny, W. Kiefer, U. Winkler, and E. Umbach. Raman spectroscopy of II–VI semiconductor nanostructures: CdS quantum dots. *Journal of Raman Spectroscopy*, 34(2):100–103, February 2003. ISSN 1097-4555. doi: 10.1002/jrs.959. URL <http://onlinelibrary.wiley.com/doi/10.1002/jrs.959/abstract>.
- [60] Yoichi Kubota, Kenji Watanabe, Osamu Tsuda, and Takashi Taniguchi. Deep Ultraviolet Light-Emitting Hexagonal Boron Nitride Synthesized at Atmospheric Pressure. *Science*, 317(5840):932–934, August 2007. ISSN 0036-8075, 1095-9203. doi: 10.1126/science.1144216. URL <http://science.sciencemag.org/content/317/5840/932>.
- [61] Yutaka Toyozawa. Theory of Line-Shapes of the Exciton Absorption Bands. *Progress of Theoretical Physics*, 20(1):53–81, July 1958. ISSN 0033-068X. doi: 10.1143/PTP.20.53. URL <https://academic.oup.com/ptp/article/20/1/53/1937228/Theory-of-Line-Shapes-of-the-Exciton-Absorption>.

- [62] S. Rudin, T. L. Reinecke, and B. Segall. Temperature-dependent exciton linewidths in semiconductors. *Physical Review B*, 42(17):11218–11231, December 1990. doi: 10.1103/PhysRevB.42.11218. URL <http://link.aps.org/doi/10.1103/PhysRevB.42.11218>.
- [63] Hitoshi Sumi. Exciton-Phonon Interaction in the Coherent Potential Approximation with Application to Optical Spectra. *Journal of the Physical Society of Japan*, 32(3):616–628, March 1972. ISSN 0031-9015. doi: 10.1143/JPSJ.32.616. URL <http://journals.jps.jp/doi/10.1143/JPSJ.32.616>.
- [64] G. Cassabois, P. Valvin, and B. Gil. Intervalley scattering in hexagonal boron nitride. *Physical Review B*, 93(3):035207, January 2016. doi: 10.1103/PhysRevB.93.035207. URL <http://link.aps.org/doi/10.1103/PhysRevB.93.035207>.
- [65] Frederick Soddy. The Radio-Elements and the Periodic Law. *Nature*, 91(2264):57–58, March 1913. ISSN 1476-4687. doi: 10.1038/091057a0. URL <https://www.nature.com/articles/091057a0>.
- [66] Joseph John Thomson. Bakerian Lecture:—Rays of positive electricity. *Proc. R. Soc. Lond. A*, 89(607):1–20, August 1913. ISSN 0950-1207, 2053-9150. doi: 10.1098/rspa.1913.0057. URL <http://rspa.royalsocietypublishing.org/content/89/607/1>.
- [67] Jacob Bigeleisen and Maria Goeppert Mayer. Calculation of Equilibrium Constants for Isotopic Exchange Reactions. *The Journal of Chemical Physics*, 15(5):261–267, May 1947. ISSN 0021-9606. doi: 10.1063/1.1746492. URL <https://aip.scitation.org/doi/10.1063/1.1746492>.
- [68] Eric M. Simmons and John F. Hartwig. On the interpretation of deuterium kinetic isotope effects in C-H bond functionalizations by transition-metal complexes. *Angewandte Chemie (International Ed. in English)*, 51(13):3066–3072, March 2012. ISSN 1521-3773. doi: 10.1002/anie.201107334.
- [69] C. Parks, A. K. Ramdas, S. Rodriguez, K. M. Itoh, and E. E. Haller. Electronic band structure of isotopically pure germanium: Modulated transmission and reflectivity study. *Physical Review B*, 49(20):14244–14250, May 1994. doi: 10.1103/PhysRevB.49.14244. URL <https://link.aps.org/doi/10.1103/PhysRevB.49.14244>.

- [70] H. Holloway, K. C. Hass, M. A. Tamor, T. R. Anthony, and W. F. Banholzer. Isotopic dependence of the lattice constant of diamond. *Physical Review B*, 44(13):7123–7126, October 1991. doi: 10.1103/PhysRevB.44.7123. URL <http://link.aps.org/doi/10.1103/PhysRevB.44.7123>.
- [71] J. Spitzer, P. Etchegoin, M. Cardona, T. R. Anthony, and W. F. Banholzer. Isotopic-disorder induced Raman scattering in diamond. *Solid State Communications*, 88(7):509–514, November 1993. ISSN 0038-1098. doi: 10.1016/0038-1098(93)90039-P. URL <http://www.sciencedirect.com/science/article/pii/003810989390039P>.
- [72] F. Widulle, T. Ruf, M. Konuma, I. Silier, M. Cardona, W. Kriegseis, and V. I. Ozhigin. Isotope effects in elemental semiconductors: a Raman study of silicon. *Solid State Communications*, 118(1):1–22, March 2001. ISSN 0038-1098. doi: 10.1016/S0038-1098(01)00014-X. URL <http://www.sciencedirect.com/science/article/pii/S003810980100014X>.
- [73] R. B. Georg, B. C. Reynolds, M. Frank, and A. N. Halliday. Mechanisms controlling the silicon isotopic compositions of river waters. *Earth and Planetary Science Letters*, 249(3):290–306, September 2006. ISSN 0012-821X. doi: 10.1016/j.epsl.2006.07.006. URL <http://www.sciencedirect.com/science/article/pii/S0012821X06004973>.
- [74] A. Göbel, T. Ruf, J. M. Zhang, R. Lauck, and M. Cardona. Phonons and fundamental gap in ZnSe: Effects of the isotopic composition. *Physical Review B*, 59(4):2749–2759, January 1999. doi: 10.1103/PhysRevB.59.2749. URL <http://link.aps.org/doi/10.1103/PhysRevB.59.2749>.
- [75] Manuel Cardona and M. L. W. Thewalt. Isotope effects on the optical spectra of semiconductors. *Reviews of Modern Physics*, 77(4):1173–1224, November 2005. doi: 10.1103/RevModPhys.77.1173. URL <http://link.aps.org/doi/10.1103/RevModPhys.77.1173>.
- [76] M. Cardona. Isotopic Effects in the Phonon and Electron Dispersion Relations of Crystals. *physica status solidi (b)*, 220(1):5–18, July 2000. ISSN 1521-3951. doi: 10.1002/1521-3951(200007)220:1<5::AID-PSSB5>3.0.CO;2-K. URL <http://>

[//onlinelibrary.wiley.com/doi/10.1002/1521-3951\(200007\)220:1<5::AID-PSSB5>3.0.CO;2-K/abstract](https://onlinelibrary.wiley.com/doi/10.1002/1521-3951(200007)220:1<5::AID-PSSB5>3.0.CO;2-K/abstract).

- [77] S. Reich, A. C. Ferrari, R. Arenal, A. Loiseau, I. Bello, and J. Robertson. Resonant Raman scattering in cubic and hexagonal boron nitride. *Physical Review B*, 71(20):205201, May 2005. doi: 10.1103/PhysRevB.71.205201. URL <https://link.aps.org/doi/10.1103/PhysRevB.71.205201>.
- [78] K. C. Hass, M. A. Tamor, T. R. Anthony, and W. F. Banholzer. Lattice dynamics and Raman spectra of isotopically mixed diamond. *Physical Review B*, 45(13):7171–7182, April 1992. doi: 10.1103/PhysRevB.45.7171. URL <http://link.aps.org/doi/10.1103/PhysRevB.45.7171>.
- [79] Feliciano Giustino, Steven G. Louie, and Marvin L. Cohen. Electron-Phonon Renormalization of the Direct Band Gap of Diamond. *Physical Review Letters*, 105(26):265501, December 2010. doi: 10.1103/PhysRevLett.105.265501. URL <http://link.aps.org/doi/10.1103/PhysRevLett.105.265501>.
- [80] X. Z. Du, C. D. Frye, J. H. Edgar, J. Y. Lin, and H. X. Jiang. Temperature dependence of the energy bandgap of two-dimensional hexagonal boron nitride probed by excitonic photoluminescence. *Journal of Applied Physics*, 115(5):053503, February 2014. ISSN 0021-8979. doi: 10.1063/1.4863823. URL <http://aip.scitation.org/doi/full/10.1063/1.4863823>.
- [81] P. Lautenschlager, M. Garriga, L. Vina, and M. Cardona. Temperature dependence of the dielectric function and interband critical points in silicon. *Physical Review B*, 36(9):4821–4830, September 1987. doi: 10.1103/PhysRevB.36.4821. URL <https://link.aps.org/doi/10.1103/PhysRevB.36.4821>.
- [82] null Zollner, null Cardona, and null Gopalan. Isotope and temperature shifts of direct and indirect band gaps in diamond-type semiconductors. *Physical Review. B, Condensed Matter*, 45(7):3376–3385, February 1992. ISSN 0163-1829.
- [83] Valentin N. Popov and Christian Van Alsenoy. Low-frequency phonons of few-layer graphene within a tight-binding model. *Physical Review B*, 90(24):245429, December 2014. doi: 10.1103/PhysRevB.90.245429. URL <http://link.aps.org/doi/10.1103/PhysRevB.90.245429>.

- [84] B. Yates, M. J. Overy, and O. Pirgon. The anisotropic thermal expansion of boron nitride. *The Philosophical Magazine: A Journal of Theoretical Experimental and Applied Physics*, 32(4):847–857, October 1975. ISSN 0031-8086. doi: 10.1080/14786437508221624. URL <https://doi.org/10.1080/14786437508221624>.
- [85] W. Paszkowicz, J. B. Pelka, M. Knapp, T. Szyszko, and S. Podsiadlo. Lattice parameters and anisotropic thermal expansion of hexagonal boron nitride in the 10–297.5 K temperature range. *Applied Physics A*, 75(3):431–435, September 2002. ISSN 0947-8396, 1432-0630. doi: 10.1007/s003390100999. URL <http://link.springer.com/article/10.1007/s003390100999>.
- [86] Phuong VUONG, S. Liu, A. Van Der Lee, R. Cusco, L. Artus, Thierry MICHEL, Pierre VALVIN, J. Edgar, Guillaume CASSABOIS, and Bernard GIL. Isotope engineering of van der Waals interactions in hexagonal boron nitride. *Nature Materials*, 17:152, January 2018. URL <https://hal.archives-ouvertes.fr/hal-01698228>.
- [87] J. Serrano, A. Bosak, R. Arenal, M. Krisch, K. Watanabe, T. Taniguchi, H. Kanda, A. Rubio, and L. Wirtz. Vibrational Properties of Hexagonal Boron Nitride: Inelastic X-Ray Scattering and Ab Initio Calculations. *Physical Review Letters*, 98(9):095503, March 2007. doi: 10.1103/PhysRevLett.98.095503. URL <http://link.aps.org/doi/10.1103/PhysRevLett.98.095503>.
- [88] G. Savini, Y. J. Dappe, S. Öberg, J. C. Charlier, M. I. Katsnelson, and A. Fasolino. Bending modes, elastic constants and mechanical stability of graphitic systems. *Carbon*, 49(1):62–69, January 2011. ISSN 0008-6223. doi: 10.1016/j.carbon.2010.08.042. URL <http://www.sciencedirect.com/science/article/pii/S0008622310006159>.
- [89] W. Pötz and P. Vogl. Theory of optical-phonon deformation potentials in tetrahedral semiconductors. *Physical Review B*, 24(4):2025–2037, August 1981. doi: 10.1103/PhysRevB.24.2025. URL <http://link.aps.org/doi/10.1103/PhysRevB.24.2025>.
- [90] (13) Nuclear Charge Radii of Light Elements and Recent Developments in Collinear Laser Spectroscopy, . URL <https://www.researchgate.net/publication/>

263022548_Nuclear_Charge_Radii_of_Light_Elements_and_Recent_Developments_in_Collinear_Laser_Spectroscopy.

- [91] P. Jaffrennou, J. Barjon, J.-S. Lauret, B. Attal-Trétout, F. Ducastelle, and A. Loiseau. Origin of the excitonic recombinations in hexagonal boron nitride by spatially resolved cathodoluminescence spectroscopy. *Journal of Applied Physics*, 102(11):116102, December 2007. ISSN 0021-8979. doi: 10.1063/1.2821413. URL <https://aip.scitation.org/doi/10.1063/1.2821413>.
- [92] Luc Museur and Andrei Kanaev. Near band-gap photoluminescence properties of hexagonal boron nitride. *Journal of Applied Physics*, 103(10):103520, May 2008. ISSN 0021-8979. doi: 10.1063/1.2925685. URL <https://aip.scitation.org/doi/10.1063/1.2925685>.
- [93] Kenji Watanabe and Takashi Taniguchi. Jahn-Teller effect on exciton states in hexagonal boron nitride single crystal. *Physical Review B*, 79(19):193104, May 2009. doi: 10.1103/PhysRevB.79.193104. URL <http://link.aps.org/doi/10.1103/PhysRevB.79.193104>.
- [94] T. Q. P. Vuong, G. Cassabois, P. Valvin, A. Ouerghi, Y. Chassagneux, C. Voisin, and B. Gil. Phonon-Photon Mapping in a Color Center in Hexagonal Boron Nitride. *Physical Review Letters*, 117(9):097402, August 2016. doi: 10.1103/PhysRevLett.117.097402. URL <http://link.aps.org/doi/10.1103/PhysRevLett.117.097402>.
- [95] C. Attaccalite, M. Bockstedte, A. Marini, A. Rubio, and L. Wirtz. Coupling of excitons and defect states in boron-nitride nanostructures. *Physical Review B*, 83(14):144115, April 2011. doi: 10.1103/PhysRevB.83.144115. URL <https://link.aps.org/doi/10.1103/PhysRevB.83.144115>.
- [96] Robert Juza and Harry Hahn. Über die Kristallstrukturen von Cu₃N, GaN und InN Metallamide und Metallnitride. *Zeitschrift für anorganische und allgemeine Chemie*, 239(3):282–287. ISSN 1521-3749. doi: 10.1002/zaac.19382390307. URL <https://onlinelibrary.wiley.com/doi/abs/10.1002/zaac.19382390307>.
- [97] J. I. Pankove. Luminescence in GaN. *Journal of Luminescence*, 7:114–126, January

1973. ISSN 0022-2313. doi: 10.1016/0022-2313(73)90062-8. URL <http://www.sciencedirect.com/science/article/pii/0022231373900628>.
- [98] J. I. Pankove, E. A. Miller, and J. E. Berkeyheiser. GaN yellow-light emitting diodes. *Journal of Luminescence*, 6(1):54–60, January 1973. ISSN 0022-2313. doi: 10.1016/0022-2313(73)90094-X. URL <http://www.sciencedirect.com/science/article/pii/002223137390094X>.
- [99] Jacques I Pankove. GaN: from fundamentals to applications. *Materials Science and Engineering: B*, 61-62:305–309, July 1999. ISSN 0921-5107. doi: 10.1016/S0921-5107(98)00523-6. URL <http://www.sciencedirect.com/science/article/pii/S0921510798005236>.
- [100] Molecular beam epitaxy, April 2018. URL https://en.wikipedia.org/w/index.php?title=Molecular_beam_epitaxy&oldid=837979856. Page Version ID: 837979856.
- [101] Chemical vapor deposition, June 2018. URL https://en.wikipedia.org/w/index.php?title=Chemical_vapor_deposition&oldid=845156232. Page Version ID: 845156232.
- [102] K. Ahmed, R. Dahal, A. Weltz, James J. Q. Lu, Y. Danon, and I. B. Bhat. Metalorganic chemical vapor deposition of hexagonal boron nitride on (001) sapphire substrates for thermal neutron detector applications. *Vacuum*, 137:81–84, March 2017. ISSN 0042-207X. doi: 10.1016/j.vacuum.2016.12.023. URL <http://www.sciencedirect.com/science/article/pii/S0042207X16308806>.
- [103] S. Majety, X. K. Cao, J. Li, R. Dahal, J. Y. Lin, and H. X. Jiang. Band-edge transitions in hexagonal boron nitride epilayers. *Applied Physics Letters*, 101(5):051110, July 2012. ISSN 0003-6951. doi: 10.1063/1.4742194. URL <http://aip.scitation.org/doi/10.1063/1.4742194>.
- [104] Juan Restrepo, Cristiano Ciuti, and Ivan Favero. Single-Polariton Optomechanics. *Physical Review Letters*, 112(1):013601, January 2014. doi: 10.1103/PhysRevLett.112.013601. URL <https://link.aps.org/doi/10.1103/PhysRevLett.112.013601>.

- [105] Serge Haroche and Jean-Michel Raimond. *Exploring the Quantum: Atoms, Cavities, and Photons*. Oxford University Press, Oxford ; New York, 1 edition edition, October 2006. ISBN 978-0-19-850914-1.
- [106] J. M. Pirkkalainen, S. U. Cho, Jian Li, G. S. Paraoanu, P. J. Hakonen, and M. A. Sillanpää. Hybrid circuit cavity quantum electrodynamics with a micromechanical resonator. *Nature*, 494(7436):211–215, February 2013. ISSN 0028-0836, 1476-4687. doi: 10.1038/nature11821. URL <http://arxiv.org/abs/1207.1637>. arXiv: 1207.1637.
- [107] Martin V. Gustafsson, Thomas Aref, Anton Frisk Kockum, Maria K. Ekström, Göran Johansson, and Per Delsing. Propagating phonons coupled to an artificial atom. *Science (New York, N.Y.)*, 346(6206):207–211, October 2014. ISSN 1095-9203. doi: 10.1126/science.1257219.
- [108] Xiaoze Liu, Tal Galfsky, Zheng Sun, Fengnian Xia, Erh-chen Lin, Yi-Hsien Lee, Stéphane Kéna-Cohen, and Vinod M. Menon. Strong light-matter coupling in two-dimensional atomic crystals. *Nature Photonics*, 9(1):30–34, January 2015. ISSN 1749-4885, 1749-4893. doi: 10.1038/nphoton.2014.304. URL <http://arxiv.org/abs/1406.4826>. arXiv: 1406.4826.
- [109] S. Dufferwiel, S. Schwarz, F. Withers, A. a. P. Trichet, F. Li, M. Sich, O. Del Pozo-Zamudio, C. Clark, A. Nalitov, D. D. Solnyshkov, G. Malpuech, K. S. Novoselov, J. M. Smith, M. S. Skolnick, D. N. Krizhanovskii, and A. I. Tartakovskii. Exciton-polaritons in van der Waals heterostructures embedded in tunable microcavities. *Nature Communications*, 6:8579, October 2015. ISSN 2041-1723. doi: 10.1038/ncomms9579. URL <https://www.nature.com/articles/ncomms9579>.
- [110] V. Singh, S. J. Bosman, B. H. Schneider, Y. M. Blanter, A. Castellanos-Gomez, and G. A. Steele. Optomechanical coupling between a multilayer graphene mechanical resonator and a superconducting microwave cavity. *Nature Nanotechnology*, 9(10): 820–824, October 2014. ISSN 1748-3387, 1748-3395. doi: 10.1038/nnano.2014.168. URL <http://arxiv.org/abs/1403.5165>. arXiv: 1403.5165.
- [111] V. Miseikis, J. E. Cunningham, K. Saeed, R. O’Rourke, and A. G. Davies. Acoustically induced current flow in graphene. *Applied Physics Letters*, 100(13):133105, March

2012. ISSN 0003-6951. doi: 10.1063/1.3697403. URL <https://aip.scitation.org/doi/abs/10.1063/1.3697403>.
- [112] Yu-Ming He, Genevieve Clark, John R. Schaibley, Yu He, Ming-Cheng Chen, Yu-Jia Wei, Xing Ding, Qiang Zhang, Wang Yao, Xiaodong Xu, Chao-Yang Lu, and Jian-Wei Pan. Single quantum emitters in monolayer semiconductors. *Nature Nanotechnology*, 10(6):497–502, June 2015. ISSN 1748-3395. doi: 10.1038/nnano.2015.75.
- [113] M. Koperski, K. Nogajewski, A. Arora, V. Cherkez, P. Mallet, J.-Y. Veuillen, J. Marcus, P. Kossacki, and M. Potemski. Single photon emitters in exfoliated WSe₂ structures. *Nature Nanotechnology*, 10(6):503–506, June 2015. ISSN 1748-3395. doi: 10.1038/nnano.2015.67. URL <https://www.nature.com/articles/nnano.2015.67>.
- [114] Toan Trong Tran, Cameron Zachreson, Amanuel Michael Berhane, Kerem Bray, Russell Guy Sandstrom, Lu Hua Li, Takashi Taniguchi, Kenji Watanabe, Igor Aharonovich, and Milos Toth. Quantum Emission from Defects in Single-Crystalline Hexagonal Boron Nitride. *Physical Review Applied*, 5(3):034005, March 2016. doi: 10.1103/PhysRevApplied.5.034005. URL <http://link.aps.org/doi/10.1103/PhysRevApplied.5.034005>.
- [115] Audrius Alkauskas, Bob B. Buckley, David D. Awschalom, and Chris G. Van de Walle. First-principles theory of the luminescence lineshape for the triplet transition in diamond NV centres. *New Journal of Physics*, 16(7):073026, 2014. ISSN 1367-2630. doi: 10.1088/1367-2630/16/7/073026. URL <http://stacks.iop.org/1367-2630/16/i=7/a=073026>.
- [116] A. Albrecht, A. Retzker, F. Jelezko, and M. B. Plenio. Coupling of nitrogen vacancy centres in nanodiamonds by means of phonons. *New Journal of Physics*, 15(8):083014, 2013. ISSN 1367-2630. doi: 10.1088/1367-2630/15/8/083014. URL <http://stacks.iop.org/1367-2630/15/i=8/a=083014>.
- [117] A. Katzir, J. T. Suss, A. Zunger, and A. Halperin. Point defects in hexagonal boron nitride. I. EPR, thermoluminescence, and thermally-stimulated-current measurements. *Physical Review B*, 11(6):2370–2377, March 1975. doi: 10.1103/PhysRevB.11.2370. URL <http://link.aps.org/doi/10.1103/PhysRevB.11.2370>.

- [118] M. G. Silly, P. Jaffrennou, J. Barjon, J.-S. Lauret, F. Ducastelle, A. Loiseau, E. Obraztsova, B. Attal-Tretout, and E. Rosencher. Luminescence properties of hexagonal boron nitride: Cathodoluminescence and photoluminescence spectroscopy measurements. *Physical Review B*, 75(8):085205, February 2007. doi: 10.1103/PhysRevB.75.085205. URL <http://link.aps.org/doi/10.1103/PhysRevB.75.085205>.
- [119] Luc Museur, Eduard Feldbach, and Andrei Kanaev. Defect-related photoluminescence of hexagonal boron nitride. *Physical Review B*, 78(15):155204, October 2008. doi: 10.1103/PhysRevB.78.155204. URL <http://link.aps.org/doi/10.1103/PhysRevB.78.155204>.
- [120] Romain Bourrellier, Michele Amato, Luiz Henrique Galvão Tizei, Christine Giorgetti, Alexandre Gloter, Malcolm I. Heggie, Katia March, Odile Stéphan, Lucia Reining, Mathieu Kociak, and Alberto Zobelli. Nanometric Resolved Luminescence in h-BN Flakes: Excitons and Stacking Order. *ACS Photonics*, 1(9):857–862, September 2014. doi: 10.1021/ph500141j. URL <https://doi.org/10.1021/ph500141j>.
- [121] X. Z. Du, J. Li, J. Y. Lin, and H. X. Jiang. The origin of deep-level impurity transitions in hexagonal boron nitride. *Applied Physics Letters*, 106(2):021110, January 2015. ISSN 0003-6951. doi: 10.1063/1.4905908. URL <http://aip.scitation.org/doi/10.1063/1.4905908>.
- [122] Mark J. Holmes, Kihyun Choi, Satoshi Kako, Munetaka Arita, and Yasuhiko Arakawa. Room-Temperature Triggered Single Photon Emission from a III-Nitride Site-Controlled Nanowire Quantum Dot. *Nano Letters*, 14(2):982–986, February 2014. ISSN 1530-6984. doi: 10.1021/nl404400d. URL <https://doi.org/10.1021/nl404400d>.
- [123] Stefan Zollner, Sudha Gopalan, and Manuel Cardona. Intervalley deformation potentials and scattering rates in zinc blende semiconductors. *Applied Physics Letters*, 54(7):614–616, February 1989. ISSN 0003-6951. doi: 10.1063/1.100895. URL <https://aip.scitation.org/doi/10.1063/1.100895>.
- [124] Stefan Zollner, Sudha Gopalan, and Manuel Cardona. Microscopic theory of inter-

- valley scattering in GaAs: k dependence of deformation potentials and scattering rates. *Journal of Applied Physics*, 68(4):1682–1693, August 1990. ISSN 0021-8979. doi: 10.1063/1.346622. URL <https://aip.scitation.org/doi/10.1063/1.346622>.
- [125] Sudha Gopalan, P. Lautenschlager, and M. Cardona. Temperature dependence of the shifts and broadenings of the critical points in GaAs. *Physical Review B*, 35(11): 5577–5584, April 1987. doi: 10.1103/PhysRevB.35.5577. URL <https://link.aps.org/doi/10.1103/PhysRevB.35.5577>.
- [126] Kun Huang and Avril Rhys. Theory of light absorption and non-radiative transitions in F-centres. *Proc. R. Soc. Lond. A*, 204(1078):406–423, December 1950. ISSN 0080-4630, 2053-9169. doi: 10.1098/rspa.1950.0184. URL <http://rspa.royalsocietypublishing.org/content/204/1078/406>.
- [127] C. B. Duke and G. D. Mahan. Phonon-Broadened Impurity Spectra. I. Density of States. *Physical Review*, 139(6A):A1965–A1982, September 1965. doi: 10.1103/PhysRev.139.A1965. URL <https://link.aps.org/doi/10.1103/PhysRev.139.A1965>.
- [128] Takashi Kuzuba, Koh Era, Toshihiko Ishii, Tadao Sato, and Minoru Iwata. Electron-phonon interactions in layered hexagonal boron nitride. *Physica B+C*, 105(1):339–342, May 1981. ISSN 0378-4363. doi: 10.1016/0378-4363(81)90271-0. URL <http://www.sciencedirect.com/science/article/pii/0378436381902710>.
- [129] A. Bhattacharya, S. Bhattacharya, and G. P. Das. Strain-induced band-gap deformation of H/F passivated graphene and h-BN sheet. *Physical Review B*, 84(7): 075454, August 2011. doi: 10.1103/PhysRevB.84.075454. URL <https://link.aps.org/doi/10.1103/PhysRevB.84.075454>.
- [130] Romain Bourrellier, Sophie Meuret, Anna Tararan, Odile Stéphan, Mathieu Kociak, Luiz H. G. Tizei, and Alberto Zobelli. Bright UV Single Photon Emission at Point Defects in h-BN. *Nano Letters*, 16(7):4317–4321, July 2016. ISSN 1530-6984. doi: 10.1021/acs.nanolett.6b01368. URL <http://dx.doi.org/10.1021/acs.nanolett.6b01368>.

Appendix A

Character table for point group

A.1 Character table for point group D_{2h}

D_{2h}	E	$C_2(z)$	$C_2(y)$	$C_2(x)$	i	(xy)	(xz)	(yz)	linear functions, rotations
A_g	+1	+1	+1	+1	+1	+1	+1	+1	-
B_{1g}	+1	+1	-1	-1	+1	+1	-1	-1	R_z
B_{2g}	+1	-1	+1	-1	+1	-1	+1	-1	R_y
B_{3g}	+1	-1	-1	+1	+1	-1	-1	+1	R_x
A_u	+1	+1	+1	+1	-1	-1	-1	-1	-
B_{1u}	+1	+1	-1	-1	-1	-1	+1	+1	z
B_{2u}	+1	-1	+1	-1	-1	+1	-1	+1	y
B_{3u}	+1	-1	-1	+1	-1	+1	+1	-1	x

A.2 Character table for point group D_{3h}

D_{3h}		E	$2C_3(z)$	$3C_2'$	$\sigma_h(xy)$	$2S_3$	$3\sigma_v$	Linear functions rotations
Koster notation	Molecular notation							
Γ_1^+	A_1'	+1	+1	+1	+1	+1	+1	1s, 2s
Γ_2^+	A_2'	+1	+1	-1	+1	+1	-1	
Γ_3^+	E'	+2	-1	0	+2	-1	0	(x,y), (2p _x , 2p _y)
Γ_1^-	A_1''	+1	+1	+1	-1	-1	-1	
Γ_2^-	A_2''	+1	+1	-1	-1	-1	+1	z, 2p _z
Γ_3^-	E''	+2	-1	0	-2	+1	0	

A.3 Character table for point group D_{6h}

D_{6h}	E	$2C_6$ (z)	$2C_3$	C_2	$3C'_2$	$3C''_2$	i	$2S_3$	$2S_6$	h (xy)	$3d$	$3v$	linear functions, rotations
A_{1g}	+1	+1	+1	+1	+1	+1	+1	+1	+1	+1	+1	+1	-
A_{2g}	+1	+1	+1	+1	-1	-1	+1	+1	+1	+1	-1	-1	R_z
B_{1g}	+1	-1	+1	-1	+1	-1	+1	-1	+1	-1	+1	-1	-
B_{2g}	+1	-1	+1	-1	-1	+1	+1	-1	+1	-1	-1	+1	-
E_{1g}	+2	+1	-1	-2	0	0	+2	+1	-1	-2	0	0	(R_x, R_y)
E_{2g}	+2	-1	-1	+2	0	0	+2	-1	-1	+2	0	0	-
A_{1u}	+1	+1	+1	+1	+1	+1	-1	-1	-1	-1	-1	-1	-
A_{2u}	+1	+1	+1	+1	-1	-1	-1	-1	-1	-1	+1	+1	z
B_{1u}	+1	-1	+1	-1	+1	-1	-1	+1	-1	+1	-1	+1	-
B_{2u}	+1	-1	+1	-1	-1	+1	-1	+1	-1	+1	+1	-1	-
E_{1u}	+2	+1	-1	-2	0	0	-2	-1	+1	+2	0	0	(x, y)
E_{2u}	+2	-1	-1	+2	0	0	-2	+1	+1	-2	0	0	-

A.4 Character table for point group C_{3h}

C_{3h}	E	C_3 (z)	$(C_3)^2$	σ_h	S_3	$(S_3)^5$	Linear functions rotations
A'	+1	+1	+1	+1	+1	+1	R_z
E'	+1	$+\epsilon$	$+\epsilon^*$	+1	$+\epsilon$	$+\epsilon^*$	$x + iy$
	+1	$+\epsilon^*$	$+\epsilon$	+1	$+\epsilon^*$	$+\epsilon$	$x - iy$
A''	+1	+1	+1	-1	-1	-1	z
E''	+1	$+\epsilon$	$+\epsilon^*$	-1	$-\epsilon$	$-\epsilon^*$	$R_x + iR_y$
	+1	$+\epsilon^*$	$+\epsilon$	-1	$-\epsilon^*$	$-\epsilon$	

A.5 Character table for point group C_{2v}

C_{2v}	E	$C_2(z)$	$\sigma_v(xy)$	$\sigma_v(yz)$	Linear functions rotations
A_1	+1	+1	+1	+1	x
A_2	+1	+1	-1	-1	R_x
B_1	+1	-1	+1	-1	z, R_y
B_2	+1	-1	-1	+1	y, R_z

A.6 Character table for point group D_2

D_2	E	$C_2(z)$	$C_2(y)$	$C_2(x)$	linear functions, rotations
A	+1	+1	+1	+1	-
B_1	+1	+1	-1	-1	z, R_z
B_2	+1	-1	+1	-1	y, R_y
B_3	+1	-1	-1	+1	x, R_x

A.7 Character table for point group D_6

D_6	E	$2C_6(z)$	$2C_3(z)$	$C_2(z)$	$3C'_2$	$3C''_2$	linear functions, rotations
A_1	+1	+1	+1	+1	+1	+1	-
A_2	+1	+1	+1	+1	-1	-1	z, R_z
B_1	+1	-1	+1	-1	+1	-1	-
B_2	+1	-1	+1	-1	-1	+1	-
E_1	+2	+1	-1	-2	0	0	(x, y) (R_x , R_y)
E_2	+2	-1	-1	+2	0	0	-

Appendix B

Power-law dependence of the shear mode energy

Regarding the publication of Valentin N. Popov and Christian Van Alsenoy [83], the vdW interaction is described by power law in first- and second-order quantum-mechanical perturbation theory by an equation:

$$V(r) = - \sum_{n=3} \frac{C_{2n}}{r^{2n}} \quad (\text{B.1})$$

where r is the interaction separation and the C_{2n} coefficient were found with $n = 3$ and $n = 4$ in graphite.

Otherwise, the interlayer interacting potential $V(r)$ is presented as the sum of a repulsive $V_r(r)$ and attractive $V_a(r)$ parts and it can be written:

$$V(r) = V_r(r) + V_a(r) \quad (\text{B.2})$$

The first term is accounted for the interlayer band energy which is an exponentially decreasing function of the c -lattice parameter. And the second one is the contribution of the weak vdW interaction between the boron nitride layers. Around the equilibrium position $r = c$, the interlayer potential reads to second-order approximation:

$$V(r) \sim V(c) + (V_r'(r) + V_a'(r))(r - c) + \frac{1}{2}(V_r''(r) + V_a''(r))(r - c)^2 \quad (\text{B.3})$$

We have $V_r'(r) = -V_a'(r)$ due to $r = c$ (equilibrium position). Let assume $|V_r''(r)| \sim |V_a''(r)|$. So that the interlayer interacting potential $V(r)$ as well as the force constant k is now proportional to $V_a''(r)$. On the other hand, the phonon energy is proportional to the square root of the force constant $f(\mathbf{k}, i)$ [75], we have:

$$\omega \sim \sqrt{|V_a''(r)|} \quad (\text{B.4})$$

If we retains only one term $-C_{2n}/r^{2n}$ in the series expansion of the vdW potential (equation 4.7), we obtain:

$$\omega \sim \frac{\sqrt{C_{2n}}}{c^{n+1}} \quad (\text{B.5})$$

From all of that, we have a link between the power law dependence of the interlayer shear mode with the expansion of the vdW potential, that gives $p = n + 1$. This can explain our fit with the p -exponent ranges is found from 3.6 to 5.7. These values is in agreement with the expected range of $p = n + 1$ for $n=3$ or 4 , i.e. $-C_6/r^6$ and $-C_8/r^8$ as the two leading terms according to Popov *et al.* [83].

Appendix C

Phonon-photon mapping in a color center in boron nitride

Hybrid quantum systems aim at combining the electronic, vibronic and photonic degrees of freedom into tripartite excitations [104]. This novel field emerges at the intersection of cavity quantum electrodynamics [105] and opto-mechanics, with impressive recent developments such as the integration of superconducting qubits with micromechanical resonators [106], or the coupling of propagating phonons with an artificial atom [107].

In this context, the rising interest in two-dimensional (2D) atomic crystals and their Van der Waals heterostructures [14] has resulted in various experiments paving the way for the implementation of hybrid quantum systems in 2D materials. The strong coupling regime of the electronic-photonic interaction has been achieved by embedding transition metal dichalcogenide monolayers in an optical microcavity, enabling the observation of exciton-polaritons [108, 109]. The *vibronic-photonic* coupling has been explored in graphene, and the use of graphene membranes as a mechanical resonator has allowed the demonstration of its optomechanical coupling with a microwave cavity [110]. Although the propagation of surface acoustic waves was evidenced in graphene for acousto-electronics applications [111], there is however no work on the *electronic-vibronic* interaction in artificial atoms in 2D crystals, and more generally in layered materials, but only the report of quantum light emission in localized states in WSe₂ [112, 113] and hexagonal boron nitride (hBN) [114].

In this Letter, we report on the ultra-violet (UV) optical response of a color center in hBN. In the emission spectrum, we resolve a narrow zero-phonon line and phonon sidebands,

that remarkably map the bulk phonon dispersion in hBN. We show that the vibronic spectrum reflects the density of states of bulk phonons in hBN, with a striking suppression of the phonon-assisted emission signal at the energy of the hBN phonon gap. Moreover, we do not observe any signature related to local vibration modes, contrarily to other color centers in semiconductors, such as the prototype NV center in diamond [115]. By means of non-perturbative calculations of the electron-phonon interaction in a point defect, we reach a quantitative interpretation of the sidebands due to the long-wavelength bulk acoustic phonons, which are at the basis of side-band cooling protocols or coherent phonon manipulation [107, 116]. From this analysis, we also obtain the first estimation of the deformation potential in hBN, together with the characteristic spatial extension of the defect of $2 \pm 0.3 \text{ \AA}$. hBN is a wide-bandgap nitride semiconductor with a lamellar crystalline structure analog to graphite [6]. Its fundamental bandgap is indirect with a dim excitonic emission at 5.955 eV [11], and intense phonon replicas between 5.7 and 5.9 eV, as seen in Fig.C.1. In our measurements, a commercial hBN crystal from HQ Graphene is hold on the cold finger of a closed-cycle cryostat, and after non-resonant excitation at 6.3 eV by the fourth harmonic of a Ti:Sa oscillator, the PL signal is detected by an achromatic optical system [64]. The presence of defects in hBN leads to two additional emission bands centered at 5.5 eV and 4 eV [15, 91, 92, 117–119]. The former comes from extended defects or stacking faults (red shaded area in Fig.C.1), which were in particular characterized with a nanometric resolution in a transmission electron microscope [120]. It was also recently demonstrated that most of the lines observed in the broad emission spectrum between 4.8 and 5.7 eV consist in resonances of the phonon-assisted carrier relaxation rate, with an energy spacing reflecting intervalley scattering [64]. Below 4.8 eV, the emission spectrum in bulk hBN displays a band related to deep levels (green shaded area in Fig.C.1), corresponding to electronic states localized in point defects [117, 119, 121]. Moreover, we observe substructures, and in particular a sharp peak at 4.1 eV, a weaker one at 3.9 eV, and a third one at 3.7 eV barely observable atop the broad emission background, as shown in the inset of Fig. C.1 displaying a zoom around 3.9 eV. In contrast to previous studies focusing on this multiplet of peaks in hBN and concluding to the existence of phonon replicas in a point defect [118, 119, 121], we resolve here the complete vibronic spectrum by means of high-spectral resolution in PL experiments in hBN single crystals at 10K. We first demonstrate the presence of a previously

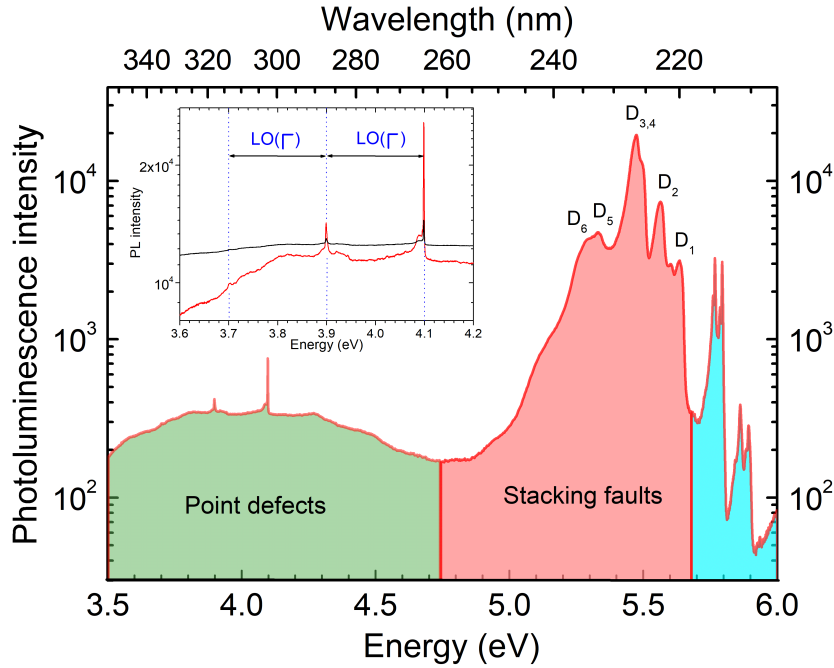


Figure C.1: Photoluminescence (PL) spectrum in bulk hBN at 10K (solid red line) on a 2.5-eV energy range, for an excitation at 6.3 eV. The vertical dotted blue line indicates the hBN bandgap at 5.95 eV. The green (red) shaded area corresponds to the emission of point defects (stacking faults, respectively). Inset: zoom around 3.9 eV.

unresolved zero-phonon-line (ZPL) in the emission spectrum, lying at 4.1 eV with a full width at half-maximum (FWHM) as narrow as 2 meV (Fig.C.1). Such a value is of the order of the linewidth measured in single quantum dots in state-of-the-art AlGaIn-based samples for single photon sources in the UV range [122]. The fact that we observe similar values by means of ensemble measurements is a strong indication for the well-defined, excellent structural properties of this UV color center. However, in Fig.C.1 the PL signal of the color center appears to be superimposed on the broad emission background, approximately at its maximum intensity, making difficult a further investigation of the color center optical properties, at least in this configuration where we perform above bandgap excitation at 6.3 eV.

We thus switch to below bandgap excitation in order to suppress the 4-eV broad emission background, following the excitation spectroscopy measurements performed below 4.75 eV and reported in Ref. [119]. In Fig.C.2, we display, on a semi-log scale, the PL signal intensity (solid red line) as a function of the energy detuning with the 4.1-eV energy of the ZPL. In this background-free configuration, we observe that the vibronic spectrum does not only consist in a low-energy sideband with a maximum intensity for a 10 meV

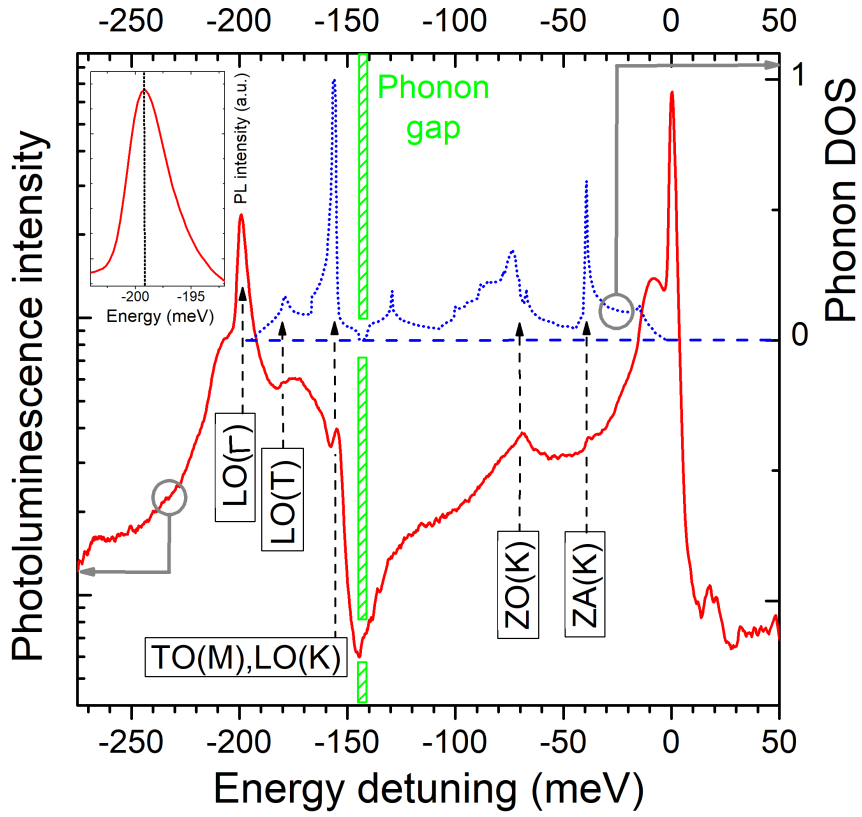


Figure C.2: Photoluminescence signal intensity at 10K (solid red line), on a semi-log scale, for an excitation at 4.6 eV, as a function of the energy detuning with the zero-phonon line of the color center emitting at 4.1 eV (figure.C.1), compared to the phonon density of states in hBN (blue dotted line) from Ref. [8]. Inset: zoom of the PL spectrum around 200 meV.

red-shift, and that secondary maxima are observable at -40 and -70 meV energy detunings. Moreover, the PL signal intensity decreases to the noise level for a detuning of -145 meV, that coincides with the phonon gap in hBN [8, 87]. For larger detunings, the PL signal intensity increases with a steep rise to a relative maximum at -155 meV, followed by a broader line until -180 meV, and finally a sharp asymmetric line at -200 meV, i.e. the absolute maximum of the optical phonon energy in hBN, corresponding to zone-center longitudinal optical phonons LO(Γ).

In the light of the vibronic spectrum inspection correlating with specific energies of the phonon bandstructure in hBN, we further compare the PL spectrum of our UV color center with the phonon density of states in hBN [8] (blue dotted line in Fig.C.2). We first observe that the peaks at -40, -70, -155, and -180 meV all correspond to extrema of the phonon density of states in different high-symmetry points of the Brillouin zone, and

related to ZA(K), ZO(K), TO(M)/LO(K), and LO(Γ) phonons, respectively. In the case of zone-edge phonons, the electron-phonon interaction via the deformation potential is known to be weakly dependent on the phonon wave-vector k [24], whereas at the zone-center, the deformation potential and the piezo-electric coupling scale like \sqrt{k} and $1/\sqrt{k}$, respectively, while the Fröhlich interaction varies like $1/k$. Such a weak k -dependence of the deformation potential at the zone-edge is well documented in the context of intervalley scattering in indirect and direct bandgap semiconductors [123–125]. As a matter of fact, the efficiency of the corresponding phonon-assisted recombination will mainly reflect the phonon density of states, provided that first-order processes involving only one phonon are dominant in the optical response. The one-by-one identification of the phonon sideband peaks with the extrema of the phonon density of states (Fig.C.2) indicates that we are, at low temperature, in the regime where one-phonon scattering processes dominate. This interpretation is further supported by the striking observation of a pronounced dip in the vibronic spectrum (down to our noise level) exactly in the 5 meV-spectral range of the phonon gap in hBN (green dashed area in Fig.C.2). To the best of our knowledge, it is the first evidence of such a suppression of the phonon sideband in the spectral region of a phonon gap, in point defects and more generally in semiconductor nanostructures. In contrast to phonons at the boundaries of the Brillouin zone, zone-center phonons couple to electrons through strongly k -dependent interactions [24]. In the case of optical phonons, the Fröhlich interaction scales like the inverse of the phonon wave-vector, resulting in a divergence of the electron-phonon matrix element for zone-center longitudinal optical phonons. This singularity accounts for the intense phonon sideband at -200 meV (Fig.C.2), despite the vanishing density of states at the energy of the LO(Γ) phonons in hBN. Interestingly, the usual negative curvature of the LO phonon branch around Γ is expected to result in a tail of the LO(Γ) sideband towards smaller energy detunings, which was never observed so far. The asymmetric line-profile around -200 meV in Fig.C.2(inset) provides a text-book example for this effect. As far as zone-center acoustic phonons are concerned, we present below a quantitative interpretation of the low-energy vibronic spectrum, which will allow us to extract estimations of the defect size and deformation potential, and to reproduce the temperature-dependent measurements up to room temperature, displayed in Fig.C.3. Phonon-assisted optical processes in point defects were described in the early years of solid-state physics, in particular in

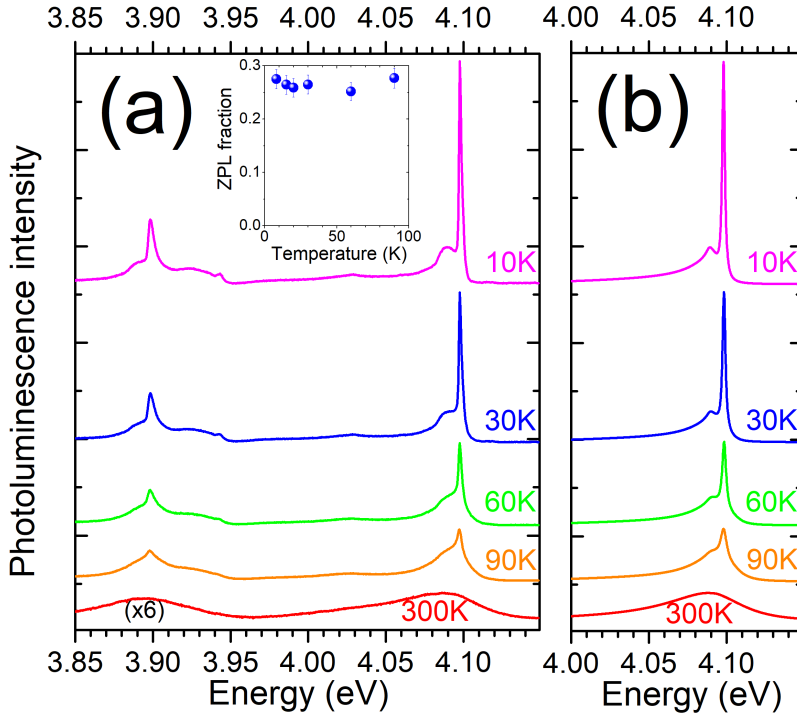


Figure C.3: (a) Photoluminescence spectrum of the 4.1-eV color center in hBN, for an excitation at 4.6 eV, from 10K to 300K. Inset: fraction of the emission in the ZPL as a function of temperature. (b) Calculations of the longitudinal acoustic phonon sidebands, from 10K to 300K, with a deformation potential $D=11$ eV and a point defect extension $\sigma = 2\text{\AA}$.

the pioneering study of Huang and Rhys [126]. In this paper, the authors analyzed the optical absorption of F-centres on the basis of the Franck-Condon principle. A description to all orders in the electron-phonon interaction was later developed by Duke and Mahan within a Green function formalism [127], with a renewed interest in the context of semiconductor quantum dots and nanocrystals. In order to interpret time-resolved experiments of the coherent nonlinear response in semiconductor quantum dots, Krummheuer *et al.* calculated the time-dependent polarization after pulsed excitation, and they derived an analytical expression of the non-perturbative optical response for the coupling to phonons [57]. Such a non-perturbative approach takes into account the coupling terms to all orders in the exciton-phonon interaction, thus accounting for the radiative recombination assisted by the emission of any phonon number. This aspect is particularly important on increasing the temperature where the phonon sidebands are no longer limited to the one-phonon processes, which usually dominate at low temperature [57], so that a non-perturbative approach becomes mandatory at high temperature.

In the framework of this theoretical approach, we have calculated the emission spectrum of the 4.1-eV color center in hBN in order to quantitatively account for our PL measurements (Fig.C.3). More specifically, we have computed the sidebands arising from the coupling to acoustic phonons. Close to the zone-center, the deformation potential interaction is allowed only for LA phonons, while piezoelectric coupling is allowed for both LA and TA phonons [57]. hBN being centro-symmetric and thus non-piezoelectric, the only remaining coupling is the deformation potential for LA phonons. The emission spectrum is thus obtained by taking the Fourier transform of the time-dependent linear susceptibility $\chi(t)$ given by [57]:

$$\chi(t) = \exp \left[\sum_{\mathbf{k}} |\gamma_{\mathbf{k}}|^2 \left(e^{-i\omega(\mathbf{k})t} - n(\mathbf{k}) \left| e^{-i\omega(\mathbf{k})t} - 1 \right|^2 - 1 \right) \right] \quad (\text{C.1})$$

where $\omega(\mathbf{k})$ is the energy of a LA phonon of wavevector \mathbf{k} , $n(\mathbf{k})$ the corresponding Bose-Einstein phonon occupation factor, and $\gamma_{\mathbf{k}}$ a dimensionless coupling strength. Importantly, we have taken into account the anisotropic sound dispersion in hBN resulting from the peculiar crystalline properties of this lamellar compound, so that $\omega(\mathbf{k})$ reads $\sqrt{(c_{s,\parallel}k_{\parallel})^2 + (c_{s,z}k_z)^2}$ where k_{\parallel} ($c_{s,\parallel}$) and k_z ($c_{s,z}$) are the in-plane and out-of-plane wavevectors (sound velocities, respectively), with the Oz direction along the c-axis of hBN, and $c_{s,\parallel}/c_{s,z} \sim 7.5$ [87].

In our calculations, we have three free parameters: the magnitude D of the deformation potential, the extension σ of the electronic wave-function in the color center, and the FWHM of the ZPL labelled Γ_{ZPL} . Γ_{ZPL} is a phenomenological broadening introduced in the model, since the latter does not account for the thermally-assisted broadening of the ZPL [57]. Its value is adjusted for each temperature in order to reproduce the ZPL. In Fig.C.3, we display the comparison between our temperature-dependent measurements from 10K to 300K (Fig.C.3(a)), and our calculations of the longitudinal acoustic phonon sidebands (Fig.C.3(b)) for fixed values of the deformation potential ($D=11$ eV) and point defect extension ($\sigma=2 \text{ \AA}$). We observe an excellent agreement for the complete set of data. In particular, we fully account for the smooth transition to a symmetric emission spectrum on raising the temperature. While phonon emission gives rise to a red-shifted emission after phonon-assisted recombination, phonon absorption leads on the contrary to a blue-shifted emission with respect to the ZPL. At low temperature, the probability

of phonon absorption is negligible compared to phonon emission, leading to an asymmetric vibronic spectrum (Fig.C.3, 10K). When raising temperature, phonon absorption becomes more and more probable, resulting in a high-energy sideband of growing intensity (Fig.C.3, 30-90K), up to a quasi-symmetric emission spectrum at room temperature (Fig.C.3, 300K). Furthermore, we note that the visibility of the ZPL decreases as a function of temperature. Nevertheless, as long as it is observable, i.e. below 100K, the fraction of the emission in the ZPL, often called Debye-Waller factor, remains constant (Fig.C.3(a), inset). The decreasing visibility of the ZPL arises in fact from its broadening, that reduces the maximum intensity of the ZPL on top of the Γ_{ZPL} -independent vibronic spectrum. Eventually, we highlight that the longitudinal acoustic phonon sidebands involve both in-plane and out-of-plane phonons, in contradiction to early studies on the electron-phonon interaction in a layered compound tentatively predicting the implication of only rigid-layer modes with a k_z wavevector [128]. In Eq.(C.1), the truncated sum to only $\{k_z\}$ wavevectors does lead to a drastic reduction of the sideband intensity, infirming the hypothesis of Ref.[128] and thus showing the combined action of in-plane and out-of-plane phonons in the sideband build-up.

In our model, the free intrinsic parameters are the defect extension σ and the deformation potential D . Although the latter can a priori be estimated from independent experiments [24] and is usually tabulated for a number of semiconductor compounds, the only recent synthesis of high-quality hBN crystals makes the literature completely inexistent on this topic. Nevertheless, the observation of the sideband maximum at an energy detuning of -10 meV in our low temperature measurements turns out to be decisive for reaching an accurate estimation of both fitting parameters. When varying the values of D and σ , the sideband maximum changes in energy and in intensity, the latter being directly related to the Debye-Waller factor. In order to reproduce both the energy and the intensity of the sideband maximum at 10K, we have to take $D=11\pm 0.5$ eV and $\sigma=2\pm 0.3$ Å. The 11-eV value of the deformation potential has to be compared with the absolute value of the difference D_e-D_h between the deformation potentials D_e and D_h for electrons and holes, respectively. From the theoretical estimations in the literature [129], we deduce that $|D_e-D_h|$ ranges from 1.7 to 8 eV. However, these calculations performed within the density functional theory without GW corrections underestimate the bandgap of hBN by 30%, and therefore possibly also the deformation potentials, so that corrected theoretical esti-

mations will have higher values with an upper bound close to our estimate. As far as the extension of the electronic wave-function is concerned, the $2\text{-}\text{\AA}$ value is of the order of the in-plane B-N bond length (1.4 \AA), but smaller than the interlayer distance in hBN (3.3 \AA), suggesting a ponctual alteration of the in-plane crystalline structure. The $2\text{-}\text{\AA}$ extension of the color center also corroborates the observation of zone-edge phonon replicas in the PL spectrum (Fig.C.2), requiring a defect extension comparable to the inverse of the phonon wave-vector in the form factor describing the electron-phonon coupling efficiency [57]. These results should stimulate further investigation by local probe techniques in order to achieve the chemical identification of this defect center. It might be a nitrogen vacancy V_N bound to a carbon or an oxygen atom [121], although Stone-Wales defects transforming two hexagons into a pentagon and a heptagon could also form preferential sites for adsorbates.

In summary, we have studied the vibronic spectrum in a color center in hexagonal boron nitride. We have shown that the vibronic spectrum reflects the density of states of bulk phonons in hexagonal boron nitride, with a striking suppression of the phonon-assisted emission signal at the energy of the phonon gap. By means of non-perturbative calculations of the electron-phonon interaction in a strongly anisotropic phonon dispersion, we reach a quantitative interpretation of the acoustic phonon sidebands from cryogenic up to room temperature, allowing us to estimate the deformation potential value and the spatial extension of the defect. These unique features of the electronic-vibronic interaction in this color center are supplemented by the recent success in isolating such a single color center, which displays bright single photon emission in anti-bunching experiments [130]. These results pave the way for the implementation of hybrid quantum systems in layered materials, using this color center as a fundamental building block.

Résumé en français

En utilisant la réaction de l'acide borique fondu et du cyanure de potassium, le chimiste Balmain a isolé le nitrure de bore (BN) dès 1842 [5]. A cette époque et durant de nombreuses décades, BN était obtenu sous forme d'une poudre blanche ou sous forme de céramique constituée de très petits monocristaux. La taille de ces cristaux rendra longtemps difficile la détermination de la structure cristalline de BN aux rayons X. Il faudra en effet attendre 1963, c'est à dire plus de quarante ans après les premières détermination de structure cristallines cubiques réalisées par les Bragg père et fils pour que des expériences de diffraction de rayons X indiquent sans ambiguïté l'empilement lamellaire hexagonal bien spécifique qui sera reconnu par les physiciens des solides sous le nom générique de « structure cristalline du nitrure de bore ». Cette structure lamellaire présente de nombreux intérêts technologiques, en particulier pour utilisation comme lubrifiant solide. Si la faible cohérence spatiale de l'arrangement cristallin rend la diffusion de la lumière visible complexe dans ce matériau qui devient absorbant dans l'ultra-violet (UV) profond et a fait des poudres de BN un matériau de choix pour l'industrie cosmétique, au vu de sa blancheur non nacree, le manque de contrôle de la pureté chimique du « graphite blanc » lui a longtemps barré la route de toute application industrielle dans le domaine optoélectronique. En 2004, le Professeur Taniguchi, du laboratoire NIMS à Tsukuba au Japon a réussi à croître des monocristaux BN de grande taille (l'adjectif grand est utilisé ici pour caractériser des confettis « circuloïdes » d' environ 1mm^2 de surface et de $200\mu\text{m}$ de hauteur) avec de hautes performances optiques dans l'ultraviolet profond, à 200 nm typiquement [6, 7]. Depuis ce jour, de nombreuses méthodes ont été utilisées pour synthétiser le nitrure de bore sous diverses formes, qu'il soit recherché de fabriquer de la poudre, des nanotubes, des monocristaux, des hétéro-épitaxies. Étonnement, bien que le BN soit depuis fort longtemps largement utilisé dans l'industrie en raison de ses propriétés physiques macroscopiques qui sont fort intéressantes pour des appli-

cations assez banales, la compréhension des mécanismes régissant l'interaction lumière matière et leur gestion dans BN n'a pas sollicité les vocations de nombreux expérimentateurs alors que la compétition a très tôt fait rage parmi les théoriciens de la structure de bande. Deux raisons peuvent être invoquées qui sont: i) la nécessité de s'approvisionner en cristaux de haute pureté chimique et de haute qualité structurale d'une part et ii) de développer des technologies expérimentales adaptées à des mesures optiques fines dans la zone de longueurs d'onde autour 200 nanomètres qui rassemble toutes les difficultés techniques envisageables pour empêcher de travailler facilement et à bon marché (pas de sources laser simple et bon marché, lampes à UV produisant de l'ozone, problèmes de composants optiques adaptés et qu'il faut parfois faire fabriquer à l'unité, nécessité de travailler en atmosphère contrôlée pour éviter les absorption par l'oxygène de l'air, ...). Dans l'équipe qui m'a accueillie, l'envie de relever ces défis expérimentaux ne fut pas une motivation plus subalterne pour entamer les investigations parmi lesquelles s'inscrit mon travail de thèse que celle de dire les performances optiques de BN.

Durant cette thèse, nous avons étudié les propriétés optiques de cristaux massifs et de couches hétéro-épitaxiales de nitrure de bore hexagonal (h-BN). Nous avons combiné les spectroscopies de photoluminescence et de diffusion inélastique Raman avec des mesures de diffraction de rayons X et de l'imagerie obtenue par microscopie à force atomique (AFM). Nous avons étudié des échantillons de différentes sources:

- Les cristaux massifs du Professeur Takashi Taniguchi du National Institute for Materials Science à Tsukuba au Japon,
- Les cristaux massifs achetés auprès du fournisseur Batave HQ Graphene,
- Les cristaux massifs du Professeur James Edgar de l'Université d'Etat du Kansas
- Les hétéro-épitaxies réalisées par le Professeur Sergueï Novikov à l'Université de Nottingham.

Ces cristaux ont été fabriqués en utilisant différentes méthodes de croissance, par exemple en conditions extrêmes combinant des hautes pressions et des hautes températures (HP-HT), des flux catalyseurs de Ni-Cr flux, ou par Epitaxie sous jets moléculaires (MBE pour Molecular Beam Epitaxy).

Nous pensons que cette variété de sources de cristaux fut déterminante pour nous permettre de mesurer sans ambigüité les propriétés optiques intrinsèques de h-BN.

La présentation des résultats est organisée en cinq parties. Nous commençons par rappeler un certain nombre de propriétés fondamentales de BN toutes corrélées à son arrangement cristallin. Le second chapitre deux présente les échantillons que nous avons étudiés et les techniques expérimentales que nous avons utilisées lors de nos campagnes de mesures. Les trois chapitres suivants sont consacrés à la présentation de nos résultats expérimentaux obtenus dans des conditions particulières qu'il s'agisse de configurations expérimentales permettant de nous concentrer sur les spécificités de l'interaction électron-phonon dans BN ou d'échantillons hors du commun : cristaux massifs purifiés isotopiquement en bore ou couches épitaxiales.

Les spécificités de l'interaction electron-phonon dans BN

Du point de vue de nos mesures, nous nous sommes d'abord concentrés sur les recombinaisons assistées par phonon (phonon replicas) du h-BN en effectuant des mesures de photoluminescence (PL) résolues par polarisation afin de compléter les études réalisées dans l'équipe d'accueil avant mon arrivée. Nous avons dans un premier temps calculé ce que la théorie des groupes dit de la structure fine du spectre de fluorescence de BN dans les deux cas où le vecteur de Poynting du photon émis $\vec{\omega}$ est parallèle ou perpendiculaire à l'axe c du cristal. Dans le cas d'un vecteur de Poynting parallèle $\vec{\omega}$ à l'axe c , nous avons prédit et enregistré quatre raies d'émission principales qui correspondent aux

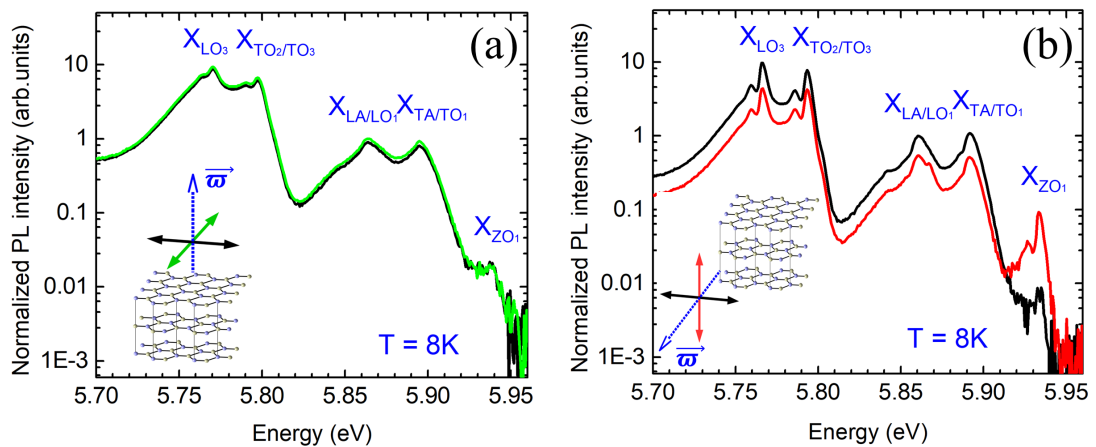


Figure R.1: Spectres en polarisation de la photoluminescence assistée par phonon de h-BN. Les spectres sont mesurés dans le cas d'un vecteur de Poynting $\vec{\omega}$ parallèle (a) ou perpendiculaire (b) à l'axe c .

recombinaisons radiatives assistées par émissions de phonons de types LO_3 , TO_3/TO_2 ,

LA/LO₁, et TA/TO₁ pour lesquels le calcul des modes normaux indique que les atomes vibrent dans un seul feuillet de BN. Leur intensité n'est pas altérée lorsqu'on analyse leur symétrie en intercalant entre le cristal et notre système de détection un polariseur linéaire dont on change continûment l'orientation la polarisation passante. Ceci n'est pas le cas dans la configuration expérimentale d'un vecteur de Poynting perpendiculaire à l'axe *c*: outre ces quatre répliques phonons une transition supplémentaire faisant intervenir le phonon de symétrie ZO₁ (mode normal de vibration des atomes orthogonal aux feuillets de BN) contribue à une raie supplémentaire détectée à 5,93 eV (figure R.1). Nous avons en outre mesuré dépendance spectaculaire de l'intensité de toutes les répliques phonons avec l'angle de polarisation dans le plan contenant la direction *c* du cristal.

Le rapport d'intensité entre les répliques phonons LA/LO₁ et ZO₁ passe de 200 à 5 quand la rotation du polariseur linéaire balaie le plan contenant *c*. L'analyse des données en polarisation nous permet d'envisager la contribution du phonon ZO₃ qui a la même symétrie que le phonon ZO₁, sur le spectre rouge de la figure R.1(b), à 5,87 eV sur le flanc à haute énergie de la recombinaison assistée par LA/LO₁. La présence d'une telle structure à cette énergie est compatible avec la théorie des groupes, notre spectre PL et la comparaison avec les relations de dispersion des phonons au centre de la zone de Brillouin. On obtiendra indirectement la forme de cette raie en soustrayant les deux spectres de PL obtenus pour des polarisations orthogonales dans le cas d'un vecteur de Poynting $\vec{\omega}$ perpendiculaire à l'axe *c*. Ce résultat expérimental difficile à obtenir en raison de la faible épaisseur des échantillons permet d'atteindre une compréhension complète des transitions assistées par émission d'un phonon dont le vecteur d'onde est situé au centre de la zone de Brillouin dans h-BN. Il apporte une preuve complémentaire à l'originalité des propriétés optiques de h-BN pour lequel la structure de bande électronique est originale avec les extrema fondamentaux des bandes de conduction et de valence qui sont tous les deux situés hors du centre de la zone de Brillouin.

Lors de cette campagne de mesures en polarisation nous avons réussi la mesure de la dépendance de l'intensité d'émission des excitons indirects interdits en polarisation. Clairement donnant l'orientation du dipôle de l'exciton indirect est dans le plan du feuillet BN (figure R.2).

Dans une seconde étude nous avons démontré que l'origine de la structure fine du spectre de PL provient pour chaque réplique phonon d'une diffusion complémentaire de

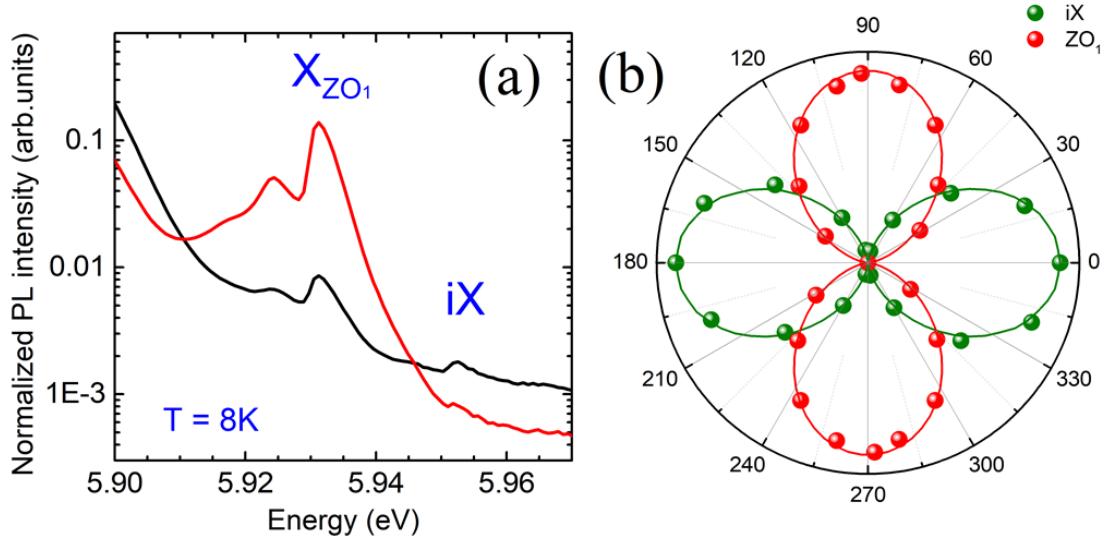


Figure R.2: Spectres de photoluminescence de l'exciton indirect interdit résolu en polarisation (a) et diagramme d'émission (intensité du signal de photoluminescence en fonction de l'angle de polarisation) (b) pour la fluorescence assistée par un phonon ZO_1 et pour celle de l'excitons indirect interdit h-BN dans le cas d'un vecteur de Poynting $\vec{\omega}$ perpendiculaire à l'axe c .

type Raman faisant intervenir le mode E_{2g} à basse énergie (mode de cisaillement interfeuillets) (figure R.3(a)). Plutôt que se recombiner après émission du phonon principal qui règle les problèmes de la règle de sélection en k , la paire électron-trou en interaction coulombienne transmet une partie de son énergie au réseau par émission d'un ou plusieurs phonons en centre zone. Ici c'est le mode mode E_{2g} à basse énergie et ses harmoniques qui contribuent. Ces vibrations de réseau correspondent au mouvement de cisaillement rigide entre couches adjacentes, avec une énergie caractéristique d'environ $6,8 \pm 0,5$ meV à 8 K. Nous avons développé un modèle théorique sophistiqué d'interprétation de la forme du spectre de PL dans lequel la largeur des raies de PL dépend pour chaque phonon considéré de sa vitesse de groupe calculée au points T de la zone de Brillouin. Le vecteur de longueur $\vec{\Gamma T}$ équivalent en longueur au vecteur \vec{KM} . C'est un phonon en T qui permet d'assurer la règle de conservation du moment pour rendre la recombinaison radiative. Ce modèle révèle que les différences observées pour les différents phonons replicas dans h-BN proviennent uniquement des variations de la vitesse du groupe des phonons aux points T de la zone de Brillouin. En termes simples, nous dirons qu'une grande vitesse du groupe du phonon, a pour conséquence un grande largeur de la raie de PL à laquelle il contribue. L'accord entre ce modèle théorique de la forme des raie de fluorescence requière la considération d'une forme de raie Gaussi-

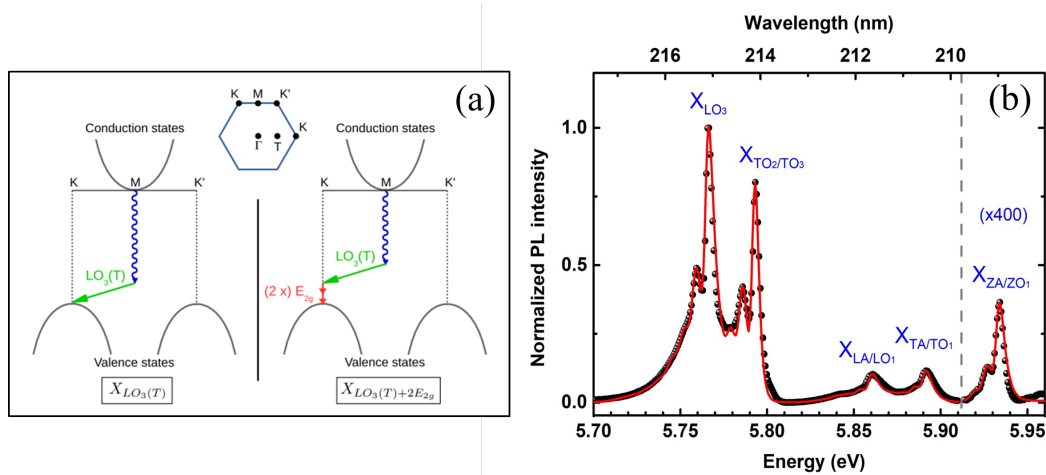


Figure R.3: Représentation schématique de l'origine de la structure fine du spectre PL dans h-BN (a), et spectres de photoluminescence en sphère noire avec l'ajustage de la forme obtenu en utilisant le modèle théorique en ligne rouge (b).

enne plutôt que Lorentzienne pour la raie de fluorescence assistée par phonon, ce qui fait penser à une interaction électron-phonon s'opérant en régime dit de couplage fort (figure R.3(b)) et il impose aussi de calculer l'élargissement des répliques Raman d'une manière cumulative avec l'ordre des harmoniques de fréquence E_{2g} .

Le fait que l'analyse des forme de raies privilégie une distribution spectrale gaussienne interpelle car il s'intègre particulièrement bien au sein de la prédiction théorique de Toyozawa de la forme des raies d'absorption excitoniques en régime de couplage fort de l'interaction exciton-phonon [61, 63]. Pour aller plus loin dans la validation de cette prédiction théorique dont aucune preuve expérimentale n'était disponible avant notre travail, nous avons cherché une seconde preuve. Nous avons donc complété la première preuve obtenue à savoir la comparaison entre les fonctions gaussiennes et lorentziennes dans les fits du spectre PL à basses température (8 K) par des mesures à plus hautes températures (de 8K à 300K) et par leurs analyses (figure R.4 (a&b)). Nous obtenons une variation de la largeur de raie en racine carrée de la température, conformément à la théorie de Toyozawa pour le régime de couplage fort (figure R.4(c)). En ajustant nos données, Nous avons interprété, l'élargissement thermique des raies sur la base de la diffusion quasi-élastique par phonons acoustiques à basse température suivie de la diffusion inélastique par absorption de phonons optiques correspondant aux modes ZA et ZO₁ dans h-BN.

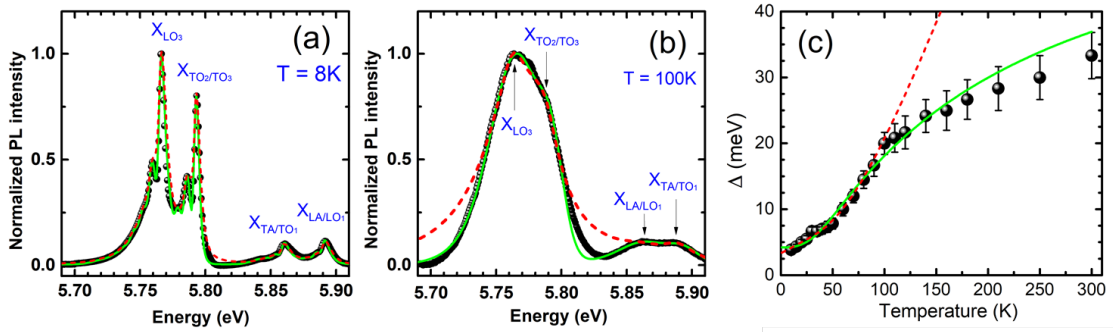


Figure R.4: Spectres de photoluminescence du h-BN à basses température (a) et à haute température (b). L'élargissement thermique en fonction de la température (c). Les données expérimentale sont tracées en sphères noires, l'ajustage théorique pour le régime de couplage fort est en vert, celui pour le régime de couplage faible est en rouge.

Ingénierie isotopique en nitrure de bore hexagonal

L'originalité du bore est qu'à l'état naturel ${}^{\text{Na}}\text{B}$ est qu'il est composé de l'isotope ${}^{11}\text{B}$ à 80 pourcents et de l'isotope ${}^{10}\text{B}$ à 20 pourcents. Les noyaux de ces deux isotopes ne réagissent pas de la même manière lors de l'éclairage par un flux de neutrons auxquels le ${}^{11}\text{B}$ est indifférent mais pas le ${}^{10}\text{B}$, ce qui est intéressant, mais constitue un phénomène auquel nous avons préféré le changement de la masse nucléaire de l'ordre de 10 pourcents qui va avoir des conséquences sur les énergies des phonons, au premier ordre. La dépendance des fréquences phononiques et des largeurs de raies avec la composition isotopique de bore : Les mesures Raman réalisées sur trois échantillons aux compositions isotopiques contrôlées en bore qui ont été effectuées par nos collègues de Barcelone et Thierry Michel ont démontré la dépendance de l'énergie des phonons avec la masse « moyenne » de BN (figure R.5(a)). S'agissant du mode raman actif à haute fréquence nous avons observé le décalage de la énergie Raman de ${}^{11}\text{BN}$ et ${}^{10}\text{BN}$, par rapport à ${}^{\text{Na}}\text{BN}$ et l'effet du désordre de masse isotopique conduisant à un déplacement d'énergie non linéaire avec les proportions relatives des deux isotopes et produisant à un élargissement spectaculaire de la raie de ${}^{\text{Na}}\text{BN}$ par rapport à celles de ${}^{10}\text{BN}$ et ${}^{11}\text{BN}$.

Un second effet plus subtil est celui de la renormalisation de l'énergie des états électroniques : Les mesures PL ont été effectuées pour les trois échantillons isotopiques contrôlés de bore. Nous avons observé le décalage vers le rouge global des spectres de PL de ${}^{11}\text{BN}$ à ${}^{10}\text{BN}$ comme anticipé à partir de l'augmentation des énergies des phonons. Les mesures Raman dépendant de la température du second mode actif Raman qui se situe dans la

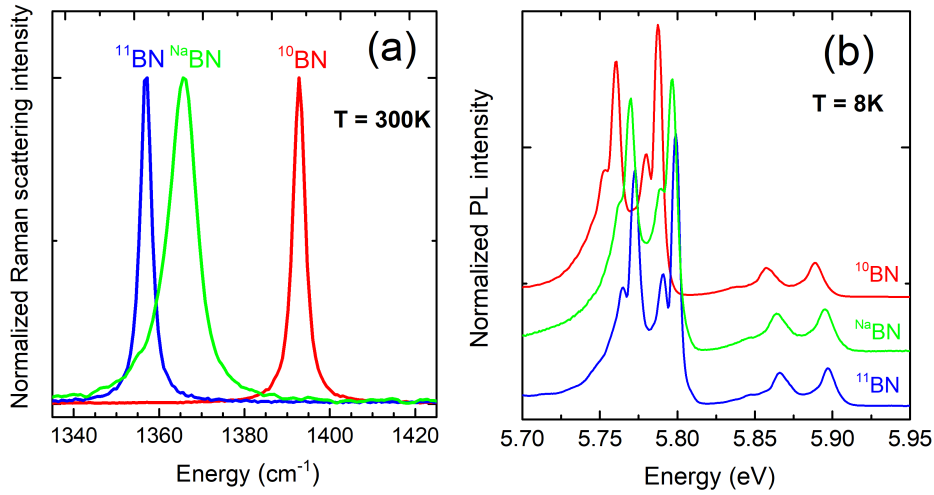


Figure R.5: Spectres des Raman (a) et photoluminescence (b) du ^{10}BN , $^{\text{Na}}\text{BN}$ and ^{11}BN .

région des basses fréquences à 52.5 cm^{-1} à basse énergie et correspond aux mouvements de cisaillement entre les plans ont été effectuées de 10 à 600K (figure R.6(a)). En augmentant la température, le paramètres du réseau c augmente avec la température et l'énergie de ces modes Raman diminue. Connaissant $c(T)$ une loi de variation en puissance a été utilisée pour analyser nos données. On obtient une modification de l'exposant de cette loi de puissance d'un échantillon à l'autre, ce qui montre une première fois que le couplage de van de Waals, varie avec la composition isotopique. Une deuxième preuve a été obtenue en étudiant l'élargissement des raies de PL en raison de la contribution du mode ZO_1 (figure R.6(b)). De même que pour le mode de cisaillement inter feuillets, on obtient une augmentation de la force de couplage de cette mode de ^{11}BN à ^{10}BN en passant par une valeur intermédiaire pour $^{\text{Na}}\text{BN}$. Nous en déduisons que l'ingénierie isotopique en BN affecte les vibrations du réseau contrôlées par le faible couplage de van der Waals entre les couches adjacentes.

Finalement nous avons demandé à notre collègue Arie van der LEE de l'Institut Européen des membranes des mesures de diffraction des rayons X pour ^{11}BN à ^{10}BN par notre collègue afin de révéler des différences. Le résultat est que la distribution de la densité électronique est plus diffuse entre les couches adjacentes dans ^{11}BN que dans les cristaux ^{10}BN . Par conséquent, nous pouvons conclure par une observation directe que la distribution électronique de couche intermédiaire elle-même est affectée par la substitution isotopique qui contribue à la modification de l'interaction de van de Waals.

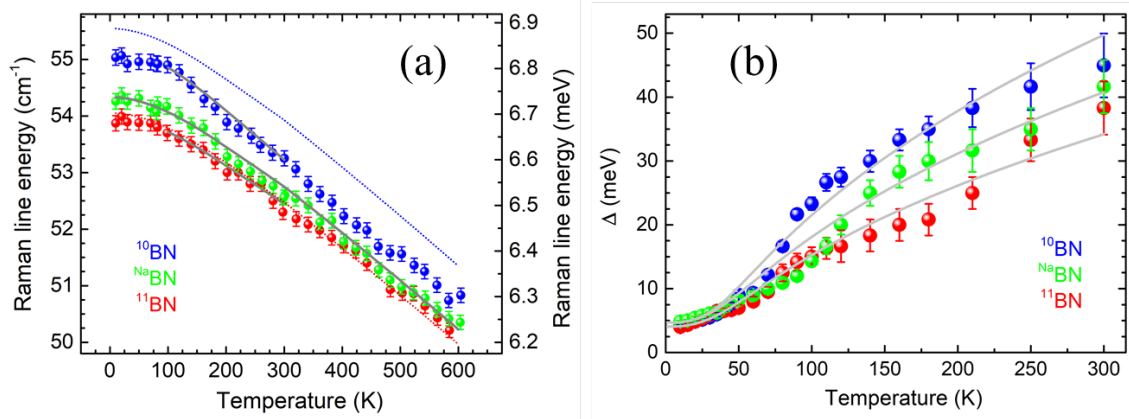


Figure R.6: (a) Adoucissement thermique du mode Raman basse fréquence pour ^{10}BN , $^{\text{Na}}\text{BN}$ and ^{11}BN ; (b) Elargissement thermique des raies de PL en fonction de la température pour ^{10}BN , $^{\text{Na}}\text{BN}$ and ^{11}BN .

Le nitrure de bore hexagonal crû par Epitaxie sous Jets Moléculaires (MBE).

Nous avons étudié deux séries d'épitaxies de h-BN crûes par MBE sur différents substrats: le saphir et le graphite pyrolytique hautement ordonné (HOPG), pour des températures de croissance différentes allant de 1390°C , 1480°C , 1560°C , et 1690°C .

Les premières mesures PL, que nous avons publiées concerne un signal de PL dans la région de 5.4 à 5.5 eV dans l'ultraviolet (UV) aussi bien pour des épitaxies h-BN minces crûes par MBE sur des substrats de saphir que de graphite (figures R.7. Cette signaux de PL sont centrés autour de la bande d'émission correspondant aux fautes d'empilement déjà identifiées dans le cristal massif h-BN. Nous constatons pour la série crûe sur le saphir, une forte augmentation de l'intensité PL avec la température de croissance. Des mesures d'imagerie par AFM montrent que ces épitaxies de h-BN sont constituées de domaines nanocristallins, et que l'épaisseur moyenne par fournie par la mesure AFM (de 5 à 17.5 nm) diminue avec la température de croissance. Les images de microscopie à force atomique (AFM) indiquent que l'épaisseur moyenne de la série crûe sur graphite est nettement inférieure à celle de la série cultivée sur saphir (de 0,03 à 0.38 nm) à comparer avec les valeurs allant de 5 à 17.5 nm citées plus haut). La dépendance de l'intensité de PL avec la température de croissance est totalement différente. Pour les deux échantillons crûs sur graphite avec les températures de croissance les plus basses de 1390°C et 1480°C , nous avons observé les pics PL aux énergies de 5.88 eV et 5.91 eV qui correspondent aux deux répliques phonons LA/ LO_1 et TA/ TO_1 . Ces raies de PL n'ont jamais été

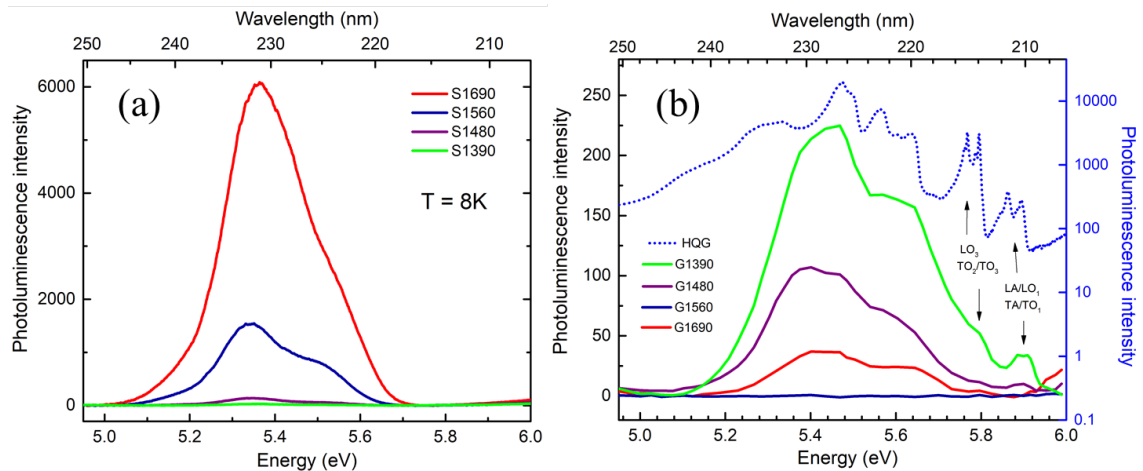


Figure R.7: (a): Spectres de PL des épitaxies de h-BN crûes sur saphir; (b) Spectres de PL des épitaxies de h-BN crûes sur graphite. En bleu un spectre de PL mesuré sur du matériau massif.

observées dans des épitaxies de BN minces crûes soit par CVD, soit par MBE. Nous montrons pour la première fois, l'évidence de photoluminescence assistée par phonons dans des couches épitaxiales minces de h-BN. C'est une signature directe pour l'excellente qualité cristalline de nos échantillons crûe par MBE à haute température. La comparaison entre les spectres PL des deux séries du h-BN indique que la qualité des échantillons cru sur des substrats graphite est meilleure que celle des substrats de saphir. Nous concluons que la croissance MBE à haute température peut produire des couches épitaxiées de h-BN de haute qualité.

Abstract

Hexagonal boron nitride (h-BN) is a wide bandgap (~ 6 eV) semiconductor with a very high thermal and chemical stability often used in devices operating under extreme conditions. The indirect nature of the bandgap in h-BN is investigated by both theoretical calculations and experiments. An indirect excitation and phonon-assisted recombinations in h-BN are observed in photoluminescence spectroscopy. This thesis focuses on the optical properties of bulk and epilayers of h-BN. We investigated samples from different sources grown by different methods in order to confirm the intrinsic optical properties of h-BN. We report the impact of the phonon symmetry on the optical response of h-BN by performing polarization-resolved PL measurements. From them, we will measure the contribution of all the phonon-assisted recombination which was not detected before this thesis. We follow by addressing the origin of the fine structure of the phonon-assisted recombinations in h-BN. It arises from overtones involving up to six low-energy interlayer shear phonon modes, with a characteristic energy of about 6.8 meV. Raman and photoluminescence measurements are recorded to quantify the influence of isotope effects on optical properties of h-BN as well as the modifications of van der Waals interactions linked to utilization of ^{10}B and ^{11}B or natural Boron for the growth of bulk h-BN crystals. Finally, we study h-BN thin epilayers grown by Molecular Beam Epitaxy at Nottingham University, atomic force microscopy (AFM) images and photoluminescence features are combined to confirm the first observation of phonon-assisted recombination in high quality thin h-BN epilayers grown on c-plane sapphire and Highly Ordered Pyrolytic Graphite. This demonstrates that large scale growth of h-BN by epitaxy is getting a technologically required maturity.

Résumé

Le nitrure de bore hexagonal (h-BN) est un semiconducteur à large bande interdite (~ 6 eV) avec une stabilité thermique et chimique très élevées lui offrant la possibilité d'être utilisé dans des dispositifs fonctionnant dans des conditions de fonctionnements extrêmes. La nature indirecte de la bande interdite dans h-BN a été étudiée à la fois par des calculs théoriques et par des expériences. Un exciton indirect et des recombinaisons assistées par phonons dans h-BN ont été observées par photoluminescence. Durant cette thèse, nous avons étudié les propriétés optiques de cristaux massifs et de couches hétéro-épitaxiales de nitrure de bore hexagonal. Nous avons étudié des échantillons provenant de différentes sources et des cristaux qui ont été fabriqués en utilisant différentes méthodes de croissance pour nous permettre de mesurer les propriétés optiques intrinsèques de h-BN. Nous rapportons l'impact des symétries des phonons sur la réponse optique du h-BN en effectuant des mesures photoluminescence résolues par polarisation. L'analyse des données en polarisation, nous permet de mesurer la contribution du phonon manquant, celui qui n'a pas été détectée avant cette thèse. En suite, nous démontrons que l'origine de la structure fine du spectre de PL provient pour chaque réplique phonon d'une diffusion complémentaire de type Raman faisant intervenir le mode de phonon E_{2g} à basse énergie (mode de cisaillement inter-feuillets). Les spectroscopies de photoluminescence et de diffusion inélastique Raman ont été combinées pour quantifier l'influence des effets isotopiques sur les propriétés optiques de h-BN ainsi pour révéler que les modifications des interactions de van de Waals liées à l'utilisation de ^{10}B et 11 ou du bore naturel pour la croissance de cristaux h-BN massifs. Enfin, nous étudions des épitaxies de h-BN crûes par Epitaxie sous Jets Moléculaires. L'utilisation conjointe de l'imagerie par microscopie à force atomique (AFM) et de la spectroscopie de photoluminescence permet de comprendre la première observation de recombinaison assistée par phonons dans des épitaxies de h-BN sur le saphir et le graphite. Ce résultat indique que la croissance de h-BN à large échelle par méthode épitaxiales est en voie d'acquérir la maturité nécessaire au développement technologique de h-BN.